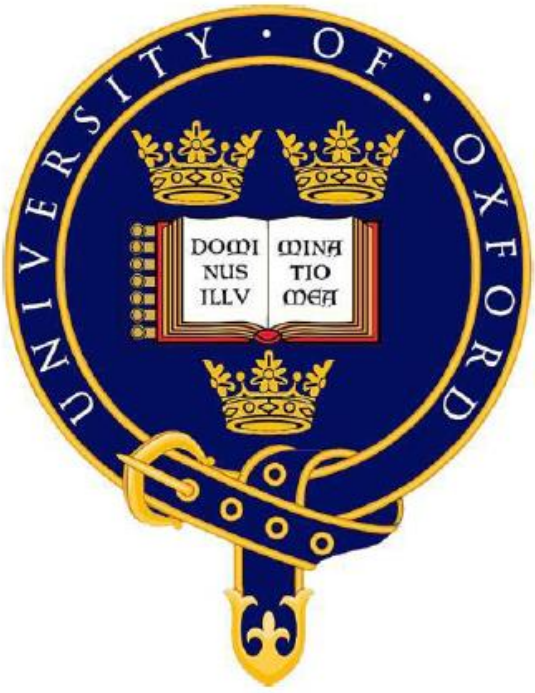
The University of Oxford

Department of Chemistry



Modifying UiO-series Metal-Organic Frameworks for Fuel-Forming Photocatalysis

Bryan Kit Yue, NG

Trinity College

Hilary 2024

A thesis submitted for the degree of
DPhil in Inorganic Chemistry

Declaration

I confirm that all research described in this thesis is my own work unless otherwise stated.

All the materials used in this thesis from other sources have been properly cited and fully acknowledged.

Acknowledgement

I would like to express my gratitude towards a lot of people who helped me in various ways throughout the years of my DPhil.

First and foremost, I would like to thank Prof. Edman Tsang as my DPhil supervisor. In the countless conversations between Edman and I, I have evolved from a part II student not knowing whatever I was doing with science in 2019 to where I am now. He has always been supportive towards my work and provided feedback for me on the presentation of my scientific work, for publishing in better journals. I am grateful for his trust in supervising part II students since the first year of my DPhil journey, when I could learn about how to do research as I teach my Part II students.

Secondly, my gratitude goes towards my family, including my parents and my wife. They have supported me in the hard times and aided me emotionally and financially. I would never be in the position I am now without them.

Thirdly, I would like to thank all the collaborator who contributed to the scientific research I am doing, including:

Dr. Tai-Sing Wu and Prof. Yun-Liang Soo, for hosting me two months in 2021 in National Tsing Hua University (Taiwan) and National Synchrotron Radiation Research Centre (NSRRC) during COVID. I was especially grateful for Dr. Tai-Sing Wu for teaching all the techniques he knows to me with no reservation, on theories of X-ray absorption spectroscopy. I also gained hands-on experience on running X-ray absorption spectroscopy experiments on all the different catalyst samples sent from our research group.

Dr. Benedict Lo, for hosting me more than 6 months in Hong Kong Polytechnic University in 2020-21 and teaching me the thinking process behind doing research. I would also like to thank his students, Dr. Qi Xue, Dr. Tianxiang Chen, Hao Zhang and Tommy Chen

for good company. Without them, I will likely still have little clue what I have to present when writing a paper.

Prof. Xin-Ping Wu and his students, for the DFT calculations in chapter 3-5

Dr. Guangchao Li for solid-state NMR studies

Dr. Robert Taylor for TRPL measurements

Dr. Mingjie Li and Mr. Qi Wei for TAS measurements in chapter 5

Current and previous members of the Tsang group, including Dr. Tatchamapan Yoskamtorn, who has been an excellent colleague as well as a wonderful collaborator. Dr. Jianwei Zheng, Dr. Pu Zhao, Dr. Tugce Ayvali and Dr. Yiyang Li for their guidance towards the beginning of my DPhil. Also Baron Ho for his microscopic images; Leo for his guidance on XRD capillaries; Wentian for his guidance in XPS; Yifei, Tommy, Konstant, Haokun, Xiang, Dongpei, Dori, Haozhe, Mengqi, Renzo, Joseph, Amy, Ati, and Jiasi for the different scientific discussions.

I would also like to thank Mengjiang Lin, Daniel Woodside and Xiyu Zhang who helped on performing experiments of various parts of my work as part II students.

Abstract

Metal-Organic Frameworks (MOFs) are porous structures built from metal-oxo clusters and organic linkers, and have recently emerged as a new class of inorganic material for various applications. These materials have wide chemical tuneability and high surface area, which has given rise to a wide range of applications. Specifically, the Universitet i Oslo (UiO) series have attracted much interest in the field of photocatalysis due to the strong ionic interaction between the highly charged Zr^{4+} and O^{2-} in the zirconium building blocks and terephthalic acid.

This thesis explores three different strategies of modifying UiO-series MOFs for improving the activity for three different photocatalytic fuel-forming reactions, namely hydrogen production from water splitting, methane from CO_2 hydrogenation as well as hydrogen-deuterium exchange reaction. The series of photocatalysts were characterized thoroughly via Rietveld refinement of Synchrotron X-ray diffraction (SXRD) and X-ray absorption spectroscopy (XAS). The optical characteristics and catalytic activity will then be discussed with respect to their structural properties in a systematic manner.

Chapter 1 has introduced MOFs as a materials, along of the various strategies for further enhancing the photocatalytic activity of UiO-series MOFs available in the literature. Chapter 2 includes the experimental details of both catalytic tests and characterization measurements, as well as the procedures for the treatment of data. These includes structural characterization (XRD, XAS etc.), optical characterization (UV-Vis, PL etc.), and computer simulations (DFT calculations).

Chapter 3 exploits the chemical stability and flexibility of UiO-series MOFs for the incorporation of Frustrated Lewis Pair-like active sites for the photocatalytic heterolytic activation of H_2 activation. Using organic linker with bipyridine functionality, a well-known chromophore $Ru(bpy)_3^{2+}$ can be partly heterogenized onto the MOF system as Ru-deposited

UiO-67-bpydc. Another Ru-deposited MOF with the amine functional group is also synthesized for comparison. The catalysts are structurally characterized via SXRD and XAS techniques, the charge transfer processes simulated by time-dependent density functional theory, and reactive intermediates upon the heterolytic cleavage of hydrogen molecules are clearly endorsed by FTIR and 2D NMR. This chapter concluded the importance of a bottom-up catalyst design approach to incorporate catalytic active sites into MOF materials.

Chapter 4 extends the ability of UiO-66-NH_2 acting as photocatalysts for CO_2 reduction by coupling with In_2S_3 semiconductor. The Lewis Acid-Base interactions between the amino group on the organic linker and the In_2S_3 species are evidenced by N 1s XPS and IR. A volcano trend can be observed towards the addition of In_2S_3 into UiO-66-NH_2, explained by the interplay between the efficient interface formation between the two species and the aggregation of In_2S_3 wrapping around the UiO-66-NH_2 particles. This chapter shed light on devising new synthesis methods for the design of interface between MOFs and co-catalysts for more efficient photocatalysts.

Chapter 5 explores the fundamental chemistries behind the increase in surface area of UiO-66-NH_2 upon CdS incorporation novel in the literature. Detailed characterizations such as XAS and XPS have been performed on the series of catalyst. Particularly, Rietveld refinement revealed the increase of dihedral angle of the organic linker upon CdS anchoring compared to virgin UiO-66-NH_2, indicating that the coordinated opening of organic linker has led to the increase in surface area. Moreover, DFT simulations revealed a similar observation driven by the charge transfer processes between UiO-66-NH_2 and the CdS species. More importantly, it has been shown that this increase in surface area correlates well towards the rate of photocatalytic water splitting. This chapter provides an atomic understanding of the rotational dynamics in UiO-66-NH_2.

Chapter 6 concludes this thesis by summarizing the findings in the experimental chapters, and suggests future work on further engineering UiO-series of MOFs for fuel-forming photocatalysis.

List of Abbreviations

2D	2-Dimensional
3D	3-Dimensional
BDC	Benzene-1,4-dicarboxylic acid
BET	Brunauer-Emmett-Teller
BPDC	biphenyl-4,4'-dicarboxylate
CC	Column Chromatography
CN	Coordination Number
DFT	Density Functional Theory
DI	Deionized
DMF	Dimethylformamide
D-W	Debye-Waller
EDX	Energy Dispersive X-ray
EPR	Electron Paramagnetic Resonance
ES	Excited State
ESA	Excited State Absorption
EXAFS	Extended X-ray Absorption Fine Structure
FID	Flame Ionization Detector
FLP	Frustrated Lewis Pair
FTIR	Fourier Transformed-Infra Red
GC	Gas Chromatography
GOF	Goodness of Fit
GS	Ground State
HAADF-STEM	High-angle Annular Dark-field Scanning Transmission Electron Microscopy

HER	Hydrogen Evolution Reaction
HKUST	Hong Kong University of Science and Technology
HRTEM	High Resolution-Transmission Electron Microscopy
ICP	Inductively-Coupled Plasma
ICP-MS	Inductively-Coupled Plasma-Mass Spectrometry
IEA	International Energy Agency
IR	Infra-red
LC	Liquid Chromatography
LLCT	Linker-linker Charge Transfer
LMCT	Ligand-to-Metal Charge Transfer
m/z	Mass to charge ratio
MAS	Magic Angle Spinning
MLCT	Metal to ligand Charge Transfer
MOF	Metal-Organic Frameworks
Mt	Million ton
NMR	Nuclear Magnetic Resonance
NOESY	Nuclear Overhauser Effect Spectroscopy
NP	Nanoparticle
NSRRC	National Synchrotron Radiation Research Centre
OER	Oxygen Evolution Reaction
PL	Photoluminescence
POM	Polyoxometalates
ppb	parts per billion
ppm	parts per million
ppt	parts per trillion

PSE	Post-synthetic exchange
PVP	Polyvinylpyrrolidone
PXRD	Powdered X-ray Diffraction
QMS	Quadrupole Mass Spectrometer
SBU	Secondary Building Unit
SEM	Scanning Electron Microscopy
SHE	Standard Hydrogen Electrode
SSNMR	Solid-State Nuclear Magnetic Resonance
SXRD	Synchrotron X-ray Diffraction
TAA	Thioacetamide
TAS	Transient Absorption Spectroscopy
TCD	Thermal Conductivity Detector
TDDFT	Time Dependent-Density Functional Theory
TEM	Transmission Electron Microscopy
TEOA	Triethanolamine
TGA	Thermogravimetric Analysis
TMA	benzene-1,3,5-tricarboxylate
TRPL	Time-resolved Photoluminescence
UiO	Universitet i Oslo
UV	Ultra Violet
UV-Vis	Ultra Violet-Visible
VASP	Vienna ab initio Simulation Package
XANES	X-ray Absorption Near-Edge Structures
XAS	X-ray Absorption Spectroscopy
XPS	X-ray Photoelectron Spectroscopy

List of Figures

Figure 1 . 1 | Combination of inorganic units and organic linkers to form extending 3-dimensional network 1
Figure 1 . 2 | Secondary building units of $Cu_3(TMA)_2(H2O)_3$ and its relation to the framework structure of HKUST-1. Figure reproduced from Ref [10]. Reprinted with permission from AAAS 3
Figure 1 . 3 | Examples of different topologies of inorganic units and organic linkers. Colour scheme: Red = O, green = N, black = C. Figure reproduced from Ref [11]. Reproduced with permission from Springer Nature 4
Figure 1 . 4 | (a) Inorganic unit of UiO-66, $Zr_6O_4(OH)_4$, with the hydrogen omitted for clarity. (b) the Secondary Building Unit and the organic linker of terephalic acid of UiO-66. (c) The combination of both the inorganic unit and organic linker into the framework of UiO-66. Colour scheme: Dark blue = Zr, Light blue = O, Pink = C. Hydrogen are omitted for clarity. Figure reproduced from [18]. Reproduced with permission from Springer Nature 6
Figure 1 . 5 | Summary of purpose of modulator and deprotonating agent added during MOF synthesis procedures. Figure reproduced from Ref [20]. Copyright © 2020 American Chemical Society 9
Figure 1 . 6 | Structure formed from the $Zr_6O_4(OH)_4$ inorganic unit with terephthalic acid / benzene-1,4-dicarboxylic acid (BDC) to yield UiO-66; with biphenyl-4,4’-dicarboxylate (BPDC) to yield UiO-67; and with [1,1':4',1"-terphenyl]-4,4"-dicarboxylic acid to yield UiO-68. Figure reproduced from Ref [21]. Copyright © 2008, American Chemical Society 10
Figure 1 . 7 | (a) Structure of UiO-66 without organic linkers, as cubic close packed $Zr_6O_4(OH)_4(CO_2)_{12}$ SBUs. (blue polyhedra) (b) Structure of CaF_2, with the position of Ca^{2+} (blue) and F^- (green) analogous to that of tetrahedral pores and SBUs, respectively. (c) Structure of NaCl, with the position of Na^+ (green) and Cl^- (blue) analogous to that of octahedral pores and SBUs, respectively. 11
Figure 1 . 8 | (a) Diagram showing the reactions during water splitting on a semiconductor photocatalyst: (i) light absorption and formation of electron-hole pair; (ii) charge diffusion and transport; (iii) redox reaction. (b) Energy diagram for photocatalytic water splitting based on one-step excitation. Figures reproduced from Ref [45]. Copyright © 2020 American Chemical Society. 14
Figure 1 . 9 | Homolytic and Heterolytic cleavage of H-H bond 17

Figure 1 . 10 | Isoreticular synthesis of UiO-66-NH_2 and UiO-67-bpydc from UiO-66 with varied organic linker 20
Figure 1 . 11 | (a) Isoreticular synthesis of UiO-66 with terephthalic acid, and UiO-66-NH_2 with 2-amino-terephthalic acid. (b) UV-Vis spectra of UiO-66 and UiO-66-NH_2. Figures reproduced from [22] and [75]. Copyright © 2010, American Chemical Society. Copyright © 2010 WILEY-VCH Verlag GmbH & Co. KGaA, Weinheim 21
Figure 1 . 12 | Synthesis procedures of Cu^{II}@Ru-UiO-bpydc catalyst for the selective reduction of CO_2 to ethanol. Figures reproduced from Ref [80]. 23
Figure 1 . 13 | Total (Black) and projected (red and blue) density of states of the pristine UiO-66(M) with M=Zr, Hf, Th, Ti, U, and Ce. For U, only the most stable ferromagnetic state is shown. The unoccupied Zr 4d, Hf 5d, Th 6d and 5f, Ti 3d, U 5f and Ce 4f orbitals are highlighted with a yellow background. The plot for U also shows at higher energy some unoccupied 6d orbitals. Figure reproduced from Ref [87]. Copyright © 2018, American Chemical Society 26
Figure 1 . 14 | Proposed coordination sites of Ti in the Zr_6 inorganic units of UiO-series MOF. (a) inclusion of Ti^{4+} in the cluster through metal exchange in place of Zr^{4+}. (b) Appendage of Ti^{4+} to the surface of the cluster at a missing linker defect site. Colour scheme: Grey polyhedra: ZrO_8, Blue polyhedra: TiO4, Black = C, Red = O, White = H. (c) Photocatalytic hydrogen evolution reaction activity of metal exchanged Ti^{4+}, Ti^{4+} on missing linker defect, pristine and defective UiO-66-NH_2. Reaction condition: 30 mg MOFs suspended in 23.5 mL CH_3CN, 4.7 mL Triethylamine, 0.5 mL H2O at 40°C. Figure reproduced from Ref [89]. Copyright © 2017, American Chemical Society 27
Figure 1 . 15 | (a) Schematic illustration for the synthesis of Ru nanoparticles encapsulated by the UiO-66 framework. (b,c) HRTEM images of Ru@UiO-66. (c) Size distribution of Ru NPs. (d) TEM image and its EDX mapping of (e) C, (f) O, (g) Zr, and (h) Ru. Figure reproduced from Ref [90]. 28
Figure 1 . 16 | TEM images of (a) Au@Pd@UiO-66, (b, c) Pt/Au@UiO-66, (d) EDX elemental mapping image of Au@Pd@UiO-66. © 2017 WILEY-VCH Verlag GmbH & Co. KGaA, Weinheim 30
Figure 1 . 17 | (a) Schematic representation of the two-step encapsulation of PW12 POM into UiO-67, followed by the introduction of RhCp* complex via linker post-synthetic exchange. Colour scheme: Blue polyhedral = WO6, pink polyhedral = PO4. (b) SEM image of (PW12, Cp*Rh)@UiO-67 and the corresponding EDX mapping of Rh from Rh*Cp, W from POM

and Zr from UiO-67. Figure reproduced from Ref [92]. Copyright © 2020, American Chemical Society.....31

Figure 2 . 1 | Illustration of the derivation of Bragg's Law, with blue lines indicating incident X-rays with angle θ, and red lines indicating reflected X-rays also with angle θ.....51
Figure 2 . 2 | (a) (100), (b) (110), and (c) (111) lattice planes of UiO-66 54
Figure 2 . 3 | An Mn K-edge XAS spectrum for Ramsdellite.....57
Figure 2 . 4 | Methods of determination of valence states from XANES spectra. (a) First derivative, (b) Half height intensity, (c) Integral method and (d) Linear Combination Fitting. 59
Figure 2 . 5 | Cu K-edge XAS data transformation to EXAFS process. (a) Raw XAS data. (b) raw k-space EXAFS data. (c) k^3-weighted k-space EXAFS data. (d) k^3-weighted R-space EXAFS data. 60
Figure 2 . 6 | EXAFS fitting for a Ru doped UiO-series MOF, attempted with (a) Ru-Si, (b) Ru-S and (c) Ru-Cl scattering paths. 63
Figure 2 . 7 | Wavelet transform for Cu K-edge XAS data of CuO.....64
Figure 2 . 8 | (a) Binding energy for sulphur with various oxidation states. (b) an XPS survey scan 66
Figure 2 . 9 | Calibration curve for ^{115}In and ^{90}Zr for ICP 69
Figure 2 . 10 | Magnetic field lifting degeneracy for nuclei with opposite spin 72
Figure 2 . 11 | Simplified Jablonski diagram showing the light absorption, fluorescence, phosphorescence processes. S_0, S_1 and S_2 are arbitrary singlet states, while T_1 is arbitrary triplet states. 78
Figure 2 . 12 | Schematic diagram of a Transient Absorption Spectroscopy experiment, reproduced from ref [25].....81

Figure 3 . 1 | Fourier-transformed magnitude of the experimental Ru K-edge k^3-weighted R-space EXAFS data and fit of (a) Ru/bpy and (b) Ru/NH_2, where |χ(R)| and Re[χ(R)] denote the magnitude and real part of the Fourier transformed k-space data. k^3-weighted k-space EXAFS data and fit for (c) Ru/bpy and (d) Ru/NH_2. Dr. Tai-Sing Wu and Prof. Yun-Liang Soo are gratefully acknowledged for their assistance in EXAFS data collection.....98
Figure 3 . 2 | Comparison of scattering paths generated by Ru-N, Ru-O, Ru-Cl and Ru-Ru. 100

Figure 3 . 3 | High-throughput X-ray diffraction of (a) Ru/bpy and UiO-67-bpydc, (b) Ru/NH_2 and UiO-66-NH_2. Crystal structures built from Rietveld Refinement of SXRD data with EXAFS fitting parameters of (c) Ru/bpy and (d) Ru/NH_2. Colour scheme: Zr = light blue polyhedra, O = red, C = black, N = blue, Ru = pink and Cl = light green. Hydrogen and adsorbed water O-atoms have been omitted for clarity. (e) Rietveld refinement of Ru/bpy and (f) Rietveld refinement of Ru/NH_2. Assistance from Dr. Tatchamapan Yoskamtorn is gratefully acknowledge for the Rietveld refinement 106
Figure 3 . 4 | Reactivities of Ru/bpy and Ru/NH_2 under illuminated and dark conditions on the hydrogen-deuterium exchange reaction 109
Figure 3 . 5 | Calibration curve of QMS signal with HD gas.....109
Figure 3 . 6 | Arrheniusm plot of Ru/bpy illuminated of the natural log of catalytic activity against the inverse of temperature 110
Figure 3 . 7 | FTIR spectra of Ru/bpy in dark and illuminated in reaction conditions 111
Figure 3 . 8 | (a) ^1H NMR spectra of Ru/bpy illuminated and in dark. (b) Deconvoluted 1D ^1H SSNMR spectra of Ru/bpy in dark. Assistance from Dr. Guangchao Li for obtaining the solid state-NMR spectra is gratefully acknowledged. 112
Figure 3 . 9 | Deconvoluted 1D ^1H SSNMR spectra of Ru/bpy illuminated 116
Figure 3 . 10 | Thermogravimetric analysis (TGA) of UiO-67-bpydc.....118
Figure 3 . 11 | (a) ^1H-^1H COSY NMR spectrum of Ru/bpy in dark (blue) and illuminated (brown). (b) Proposed mechanism of heterolytic activation of H-H bond by transient frustrated Lewis acid-base like pair. 119
Figure 3 . 12 | UV-Vis absorbance spectra comparison for (a) Ru/bpy, UiO-67-bpydc, (b) Ru/NH_2, UiO-66-NH_2.....121
Figure 3 . 13 | UV-Vis spectra of UiO-67-bpydc and 2,2'-bipyridine5,5'-dicarboxylic acid121
Figure 3 . 14 | Photoluminescence spectra of (a) Ru/bpy and (b) Ru/NH_2 along with their parent MOFs excited at 375 nm.....121
Figure 3 . 15 | TRPL of (a) UiO-67-bpydc and Ru/bpy. (b) UiO-66-NH_2 and Ru/NH_2. Assistance from Dr. Yiyang Li for obtaining the TRPL spectra is gratefully acknowledged. 124
Figure 3 . 16 | Transient Absorption Spectroscopy (TAS) of Ru/bpy 126
Figure 3 . 17 | Optimized structures of (a) the UiO-66-NH_2 and (b) UiO-67-bpydc frameworks with Ru species anchored on the linkers. Prof. Xin-Ping Wu is gratefully acknowledged for the DFT optimization of the structures. 128

Figure 3 . 18 | Cluster models of (a) the Ru/NH_2 and (b) Ru/bpy structures.....129
Figure 3 . 19 | Electron-hole distributions (isosurface:0.001 e/$Å^3$) of the electronic transitions with oscillator strength being larger than 0.01 in the cluster models of Ru/bpy and Ru/NH_2 structures. S and D denote singlet and doublet, respectively. Structure colour scheme: C = black, N = blue, O = red, H = white, Ru = grey, Cl = green. Isosurface colour scheme: Electron = yellow, hole = blue.....132

Figure 4 . 1 | Photocatalytic activity of CO_2 reduction for the series of UiO-66-NH_2 and InS-deposited UiO-66-NH_2. The yellow and blue bars correspond to the amount of CO and CH_4 formed in μmol h^{-1} g_{cat}^{-1}, respectively. The CO_2 reduction was performed with 1:3 CO_2/H_2 mixture at 180ºC. The catalytic activity was measured with the assistance of Ms. Xiyu Zhang. 143
Figure 4 . 2 | Control experiments of In-2 sample with light, dark (without light) and under N_2 (in place of CO_2). 145
Figure 4 . 3 | X-ray diffraction pattern of the series of catalysts, with the peaks of In_2S_3 phases in In-5 labelled. 148
Figure 4 . 4 | (a) High-resolution In 3d XPS spectra, (b) Normalized $3d_{5/2}$ peak of In-1 to In-5 151
Figure 4 . 5 | (a) S 2p XPS of In-1 to In-5 samples, (b) In-5 S 2p XPS fitted with two Gaussian peaks corresponding to $2p_{1/2}$ and $2p_{3/2}$ peaks. 152
Figure 4 . 6 | (a) N 2p XPS of In-1 to In-5 samples, (b) Normalized N 2p XPS fitted with a Gaussian peak. The lower R-factor obtained for In-4 and In-5 is due to the lower signal-to-noise ratio. 153
Figure 4 . 7 | (a) FT-IR full spectra of the series of catalyst and (b) N-H bending at 1659 cm^{-1} 155
Figure 4 . 8 | In K-edge X-ray Absorption Spectra of In-1 to In-5. Dr. Tai-Sing Wu and Prof. Yun-Liang Soo are gratefully acknowledged for their assistance in XAS data collection....156
Figure 4 . 9 | Wavelet analysis of XAS data for (a) In-1, (b) In-2, (c) In-3, (d), In-4, and (e) In-5.....158
Figure 4 . 10 | Data and fit of (a) R-space and (b) k-space of In K-edge EXAFS data for In-1 to In-5.....161
Figure 4 . 11 | TEM image of UiO-66-NH_2. Mr. Ping-Luen Ho is gratefully acknowledged for his assistance in collecting the TEM images and their EDX mappings. 162

Figure 4 . 12 | TEM image of In-1 163
Figure 4 . 13 | TEM image of In-2 163
Figure 4 . 14 | TEM image of In-3 164
Figure 4 . 15 | (a) TEM image of In-3 and its EDX mapping of (b) Zr, (c) C, (d) N, (e) O, (f) In and (g) S 165
Figure 4 . 16 | TEM image of In-4 165
Figure 4 . 17 | TEM image of In-5 166
Figure 4 . 18 | BET Surface area of In-1 to In-5 compared with UiO-66-NH_2 166
Figure 4 . 19 | N_2 Adsorption-Desorption isotherm of In-1 to In-5 compared to UiO-66-NH_2. 168
Figure 4 . 20 | UV-Vis Spectra of UiO-66-NH_2, In-1 to In-5 170
Figure 4 . 21 | Tauc plot of In-1 to In-5 compared to UiO-66-NH_2 171
Figure 4 . 22 | PL spectra of In-1 to In-5 173
Figure 4 . 23 | TRPL spectra for In-1 to In-5. Dr. Yiyang Li is gratefully acknowledged for his assistance in collecting the TRPL spectra. 174
Figure 4 . 24 | Activation of H_2 and CO_2 via an FLP-like manner by In_2S_3 materials upon light irradiation 176

Figure 5 . 1 | Photocatalytic water splitting activities performed at 120°C with 10% v/v TEOA. The catalytic activity was measured with the assistance of Mr. Daniel Woodside. . 188
Figure 5 . 2 | BET surface area for the series of catalysts 190
Figure 5 . 3 | (a) Total pore volume and (b) Adsorption and desorption isotherm of the series of catalysts 191
Figure 5 . 4 | Plot of photocatalytic activity against BET surface area for the series of catalysts 192
Figure 5 . 5 | XRD pattern for the series of catalysts 193
Figure 5 . 6 | Zr 3d XPS data. The Zr 3d data is offset by 1000 units in the y-axis 195
Figure 5 . 7 | (a) TGA analysis and (b) Weight derivative at 280-380°C obtained from TGA 196
Figure 5 . 8 | Cd K-edge X-ray absorption Spectroscopy of the series of catalysts. Dr. Tai-Sing Wu and Prof. Yun-Liang Soo are gratefully acknowledged for their assistance in collection of XAS spectra. 197
Figure 5 . 9 | Wavelet transform for (a) 0.1Cd, (b) 0.2Cd, (c) 1.8Cd, and (d) 2.3Cd 198

Figure 5 . 10 | k^2-weighted (a) R-space and (b) k-space data and fit for the series of catalyst 200
Figure 5 . 11 | SEM images for UiO-66-NH_2. Mr. Zhiyang Zhong is gratefully acknowledged for his assistance in obtaining the SEM images.....202
Figure 5 . 12 | TEM images for 0.2Cd. Mr. Ping-Luen Ho is gratefully acknowledged for his assistance in obtaining the TEM images and their EDX mappings.....203
Figure 5 . 13 | TEM images for 1.8Cd 203
Figure 5 . 14 | TEM images for 2.3Cd 204
Figure 5 . 15 | TEM image of 1.8CdS at higher resolution, showing CdS particles on the surface of UiO-66-NH_2, with the fringes clearly seen with spacing corresponds to the [111] face of CdS at 3.3Å.....205
Figure 5 . 16 | EDX mapping of 0.2Cd/UiO-66-NH_2 206
Figure 5 . 17 | EDX mapping of 1.8Cd/UiO-66-NH_2 207
Figure 5 . 18 | EDX mapping for 2.3Cd/UiO-66-NH_2.....208
Figure 5 . 19 | Particle size distribution of CdS in (a) 1.8Cd and (b) 2.3Cd.....209
Figure 5 . 20 | Observed, calculated and difference in SXRD intensity for Rietveld Refinement of pristine UiO-66-NH_2.....213
Figure 5 . 21 | Rietveld refined UiO-66-NH_2, showing (a) the tetrahedral pore and (b) the rotation viewed in the plane of the carboxylate of the organic linker on top. Colour scheme: Zr = light green polyhedra, O = red, C = black, N = blue. Hydrogen and adsorbed water O-atoms have been omitted for clarity.....213
Figure 5 . 22 | Observed, calculated and difference in SXRD intensity for Rietveld Refinement of 1.8Cd.....216
Figure 5 . 23 | Rietveld refined 1.8Cd, showing (a) the tetrahedral pore and (b) the rotation viewed in the plane of the carboxylate of the organic linker on top. Colour scheme: Zr = light green polyhedra, O = red, C = black, N = blue, Cd = pink, S = yellow. Hydrogen and adsorbed water O-atoms have been omitted for clarity. 216
Figure 5 . 24 | Energy of UiO-66-NH_2 with varying dihedral angles. The assistance of Prof.. Xin-Ping Wu on the DFT calculations are gratefully acknowledged. 218
Figure 5 . 25 | Addition of Cd_4S_4 cluster onto UiO-66-NH_2 for Cd_4S_4/UiO-66-NH_2, a structural model for CdS-deposited UiO-66-NH_2.....220
Figure 5 . 26 | (a) UV-Vis absorbance spectra and (b) Tauc plot of the series of catalyst ...223

Figure 5 . 27 | Simulated Absorption Spectra of (a) UiO-66-NH_2 and (b) Cd_4S_4/UiO-66-NH_2 224
Figure 5 . 28 | Normalized UV-Vis spectra of UiO-66-NH_2 and 2.3Cd, and their normalized difference 226
Figure 5 . 29 | (a) PL intensity of the series of catalyst and (b) Stern-Volmer plot of I_0/I against combined mol% of Cd from ICP 227
Figure 5 . 30 | Normalized PL spectra for series of catalyst 227
Figure 5 . 31 | Deconvoluted Gaussian peaks from PL data for 1.8Cd and 2.3Cd 228
Figure 5 . 32 | Transient Absorption Spectroscopy (TAS) for selected catalysts. Dr. Mingjie Li and Mr. Qi Wei are gratefully acknowledged for their assistance in collection of TAS spectra. 230
Figure 5 . 33 | TAS for selected catalysts probed at 200fs.....231
Figure 5 . 34 | Activation of H_2O via an FLP-like manner by Cd-S acid-base pair upon light irradiation. 232

List of Tables

Table 1 . 1 | Examples of MOFs reported in the literature for various applications.....2

Table 2 . 1 | Mass of indium nitrate hydrate and thioacetamide added in the synthesis procedures for In_2S_3/UiO-66-NH_2 48
Table 2 . 2 | Mass of thioacetamide added in the synthesis procedures for CdS/UiO-66-$NH_2$48

Table 3 . 1 | Amount of Ru and Zr as determined by ICP-MS analysis 95
Table 3 . 2 | EXAFS fitting parameters of Ru/bpy.....99
Table 3 . 3 | EXAFS fitting parameters of Ru/NH_2 99
Table 3 . 4 | Atomic parameters from Rietveld refinement of SXRD measurement for Ru/bpy 107
Table 3 . 5 | Atomic parameters from Rietveld refinement of SXRD measurement for Ru/NH_2 108
Table 3 . 6 | Fitting of NMR spectrum of Ru/bpy in dark by a mixture of Gaussian/Lorentz peaks 113
Table 3 . 7 | Fitting of NMR spectrum of Ru/bpy in dark by a mixture of Gaussian/Lorentz peaks 117
Table 3 . 8 | Calculation of Linker to Zr ratio based on TGA data.....118
Table 3 . 9 | Ratio of N(H^+) proton on Ru-N pair relative to bipyridinic linker protons 119
Table 3 . 10 | Gaussian fitting parameters of PL of Ru/bpy and UiO-67-bpydc 123
Table 3 . 11 | Fitting parameters of TRPL data against a bi-exponential decay function.....125
Table 3 . 12 | Relative energies (ΔE) of the cluster model of the Ru/bpy with various spin states.....130
Table 3 . 13 | Relative energies (ΔE) of the cluster model of the Ru/NH_2 with various spin states.....130
Table 3 . 14 | Electronic transitions with oscillator strength being larger than 0.01 in the cluster models of Ru/bpy and Ru/NH_2 structures.....133

Table 4 . 1 | Amount of In and Zr present in series of In_2S_3/UiO-66-NH_2 catalysts quantified by ICP 142

Table 4 . 2 | Catalytic performance of In-2 in CO_2 reduction to CH_4 compared to the literature. 146
Table 4 . 3 | Lattice parameters from Le Bail refinement of SXRD 150
Table 4 . 4 | Peak binding energy of In $3d_{5/2}$ and $3d_{3/2}$ XPS for the series of catalyst 151
Table 4 . 5 | Peak binding energy of N 2p XPS, and the R-factor of Gaussian Fit for the series of catalyst 154
Table 4 . 6 | EXAFS fitting parameters for In-1 to In-5 161
Table 4 . 7 | Fitting parameters of TRPL on a bi-exponential decay function for In-1 to In-5. 174

Table 5 . 1 | ICP-MS results for Cd and S in the series of catalyst 186
Table 5 . 2 | Catalytic performance of 1.8CdS/UiO-66-NH_2 in photocatalytic water splitting compared to the literature. 189
Table 5 . 3 | Parameters for the linear fit of catalytic activity against BET surface area 192
Table 5 . 4 | Lattice parameter of UiO-66-NH_2, 1.8CdS/UiO-66-NH_2 and 2.3CdS/UiO-66-NH_2 obtained from SXRD. 194
Table 5 . 5 | Binding energy determined by Zr XPS 195
Table 5 . 6 | Fitting parameters for Cd K-edge EXAFS 200
Table 5 . 7 | Crystallographic data and details of UiO-66-NH_2 and 1.8Cd based on SXRD. The assistance of Dr. Guangchao Li is gratefully acknowledged in the Refinement. 211
Table 5 . 8 | Atomic parameters from Rietveld Refinement of UiO-66-NH_2 214
Table 5 . 9 | Atomic parameters from Rietveld Refinement of 1.8Cd 217
Table 5 . 10 | Energy of UiO-66-NH_2 with varying dihedral angles 219
Table 5 . 11 | Energy of Cd_4S_4/UiO-66-NH_2 with varying dihedral angles, and their structural model 222
Table 5 . 12 | First 10 excited states in Cd_4S_4/UiO-66-NH_2 simulated by TD-DFT 225
Table 5 . 13 | Gaussian peak fitting parameters for PL data of 1.8Cd and 2.3Cd 228

List of Publications

Journal Articles

1. Photo-Induced Active Lewis Acid-Base Pairs in Metal-Organic Framework for H_2 Activation.
   Ng, B. K. Y.; Zhou, Z.-J.; Liu, T.-T.; Yoskamtorn, T.; Li, G.; Wu, T.-S.; Soo, Y.-L.; Wu, X.-P.; Tsang, S. C. E.,
   J. Am. Chem. Soc. **2023**, 145, 35, 19312-19320
2. Molecular Layer-by-layer Re-stacking of MoS_2-In_2Se_3 by Electrostatic means: Assembly of a New Layered Photocatalyst.
   Ng, B. K. Y.‡; Wong, C. C. Y. ‡; Niu, W.; Garcia, H. P.; Li, Y.; Ho, P-L.; Kuo, W. C. H.; Taylor, R. A.; Taniya, K.; Wei, Q.; Li, M.; Stamatakis, M.; Tsang, S. C. E.,
   Mater. Chem. Front., **2023**, 7, 937-945
3. In-Situ Grown Cu Dendrites Plasmonically Enhance Electrocatalytic Hydrogen Evolution of Facet-Engineered Cu_2O
   Zhang, H.; Diao, J.; Liu, Y.; Zhao, H.; **Ng, B. K. Y.**; Ding, Z.; Guo, Z.; Li, H.; Jia, J.; Yu, C.; Guo, Y.; Henkelman, G.; Titirici, M.-M.; Robertson, J.; Nellist, P.; Qiu, J.; Xie, F.; Riley, J.,
   Adv. Mater., **2023**, 2305742
4. Confined Ru sites in 13X zeolite for ultra-high H_2 production from NH_3 decomposition.
   Leung, K. C.; Hong, S.; Li, G.; Xing, Y.; **Ng, B. K. Y.**; Ye, D.; Zhao, P.; Tan, E.; Safonova, O.; Wu, T.-S.; Li, M. M.-J.; Mpourmpakis, G.; Tsang, S. C. E.,
   J. Am. Chem. Soc. **2023**, 145, 26, 14548-14561
5. Metal-Loaded Zeolites in Ammonia Decomposition Catalysis.
   Leung, K. C.; Tan, E.; Li, G.; **Ng, B. K. Y.**; Ho, B.; Lebedev, K.; Tsang S. C. E.
   Faraday Discuss. **2023**, 243, 520-548
6. Investigating porous catalysts with synchrotron X-rays and neutrons
   Mo, S.; Wang, G.; **Ng, B. K. Y.**; Zhao, P.,
   Chem Catalysis **2022**, 2, 12, 3290-3303
7. Controlled synthesis of Bi- and tri-nuclear Cu-oxo nanoclusters on metal-organic frameworks and the structure-reactivity correlations.
   Xue, Q.; **Ng, B. K. Y.**; Man, H. W.; Wu, T. S.; Soo, Y. L.; Li, M. M.; Kawaguchi, S.; Wong, K. Y.; Tsang, S. C. E.; Huang, B.; Lo, T. W. B.,
   Chem. Sci. **2021**, 13 (1), 50-58.
8. Guest-Anion-Induced Rotation-Restricted Emission in UiO-66-NH2 and Advanced Structure Elucidation.
   Xue, Q.; Chan, K. H.; Yim, C. K.; **Ng, B. K. Y.**; Chen, T.; Day, S. J.; Tang, C.; Kawaguchi, S.; Wong, K.-Y.; Lo, T. W. B.,
   Chem. Mater. **2021**, 33 (13), 5422-5429.

9. Recent Advances in the Engineering of Single-Atom Catalysts Through Metal-Organic Frameworks.
   Xue, Q.; Zhang, Z.; **Ng, B. K. Y.**; Zhao, P.; Lo, B. T. W.,
   Top. Curr. Chem. **2021**, 379 (2), 11
10. Ce-promoted PtSn based catalysts for hydrocracking of thermoplastic wastes into gasoline range products
    Wang, H.; Yoskamtorn, T.; Zheng, J.; Ho, P.-L., **Ng, B. K. Y.**, Tsang, S. C. E.,
    ACS Catal. **2023**, 13, 15886-15898
11. Stabilization of Ni-containing Keggin-type Polyoxometalates with Variable Oxidation States as Novel Catalysts for Electrochemical Water Oxidation
    Li, X.; **Ng, B. K. Y.**; Ho, P.-L.; Jia, C.; Shang, J.; Yoskamtorn, T.; Pan, X.; Li, Y.; Li, G.; Wu, T.-S.; Soo, Y.-L.; He, H.; Yue, B.; Tsang, S. C. E.,
    (Submitted)

Conferences

1. **Ng, B. K. Y.**, Wu, X.-P., Tsang, S. C. E.; Photo-Induced Active Lewis Acid-Base Pairs in Metal-Organic Framework for H_2 Activation. Poster Presentation for UK Porous Material Conference (UKPorMat) 2023 in Sheffield. **Awarded Poster Prize**
2. **Ng, B. K. Y.**, Wu, X.-P., Tsang, S. C. E.; Photo-Induced Active Lewis Acid-Base Pairs in Metal-Organic Framework for H_2 Activation. Poster Presentation for European Catalysis Conference (EuropaCat) 2023 in Prague. **Awarded Poster Prize**

Table of Contents

Declaration II

Acknowledgement III

Abstract V

List of Abbreviations VIII

List of Figures XI

List of Tables XIX

List of Publications XXI

Journal Articles XXI

Conferences XXII

1 Chapter 1 | Introduction 1

1.1 Metal-Organic Frameworks (MOFs) 1

1.1.1 Inorganic Units 2

1.1.2 Organic linker 5

1.1.3 UiO-series 5

1.1.4 Synthesis of UiO-66 7

1.1.5 Tetrahedral and Octahedral pores 10

1.2 Catalysis with light 11

1.2.1 Hydrogen gas as an energy carrier 12

1.2.2 Hydrogen from water splitting 13

1.2.3 Hydrogen activation and utilization 15

1.2.4 The use of H_2 in CO_2 reduction 17

1.2.5 Heterolytic cleavage of H-H 18

1.2.6 Metal-organic frameworks as Catalysts 18

1.3 Engineering UiO-series MOFs as photocatalysts 20

1.3.1 Functionalizing the organic linker 20

1.3.2 Decoration onto the inorganic units 23

1.3.3 Modifying the metals in the Zr_6 inorganic units 25

1.3.4 Encapsulation into UiO-series MOFs 28

1.3.5 Enhancing the surface area 31

1.4 Aim of this thesis 32
1.5 Thesis overview 33
1.6 References 36
2 Chapter 2 | Experimental Methods 46
2.1 Chemicals 46
2.2 Synthesis of catalysts 46
2.2.1 Synthesis of UiO-67-bpydc 46
2.2.2 Synthesis of UiO-66-NH_2 46
2.2.3 Synthesis of Ru/UiO-67-bpydc (Ru/bpy) 47
2.2.4 Synthesis of Ru/UiO-66-NH_2 (Ru/NH_2) 47
2.2.5 Synthesis of In_2S_3/UiO-66-NH_2 47
2.2.6 Synthesis of CdS/UiO-66-NH_2 48
2.3 Catalytic activity measurement 48
2.3.1 Chapter 3 – Hydrogen-Deuterium Exchange 49
2.3.2 Chapter 4 – CO_2 reduction 49
2.3.3 Chapter 5 – Water splitting 50
2.4 Structural Characterization 50
2.4.1 X-ray diffraction (XRD) 50
2.4.2 X-ray absorption spectroscopy (XAS) 56
2.4.3 X-ray photoelectron spectroscopy (XPS) 65
2.4.4 Inductively Coupled Plasma Mass Spectrometry (ICP-MS) 68
2.4.5 N_2 adsorption-desorption experiments 70
2.4.6 Thermogravimetric Analysis (TGA) 70
2.4.7 Infra-red Spectroscopy (IR) 71
2.4.8 Nuclear Magnetic Resonance (NMR) 72
2.4.9 Scanning / Transmission Electron Microscopy (S/TEM) 74
2.4.10 Energy dispersive X-ray (EDX) 75
2.5 Optical Characterization 76
2.5.1 Ultra-Violet-Visible (UV-Vis) 76
2.5.2 Photoluminescence (PL) 77

2.5.3 Time-resolved photoluminescence (TRPL) 79
2.5.4 Transient Absorption Spectroscopy (TAS) 80
2.6 Fuel-forming photocatalysis quantification 82
2.6.1 Quadrupole Mass Spectrometry (QMS) 82
2.6.2 Gas chromatography (GC) 82
2.7 Density Functional Theory (DFT) Calculations 85
2.8 References 88
3 Chapter 3 | Designing UiO-based catalysts for photocatalytic heterolytic hydrogen activation 92
3.1 Graphical abstract 92
3.2 Introduction 92
3.3 Results and Discussion 94
3.3.1 Structural Characterization 94
3.3.2 Structure-activity relationship 109
3.3.3 Optical Characterization 120
3.3.4 Excited-state Calculations 126
3.4 Conclusion 133
3.5 References 134
4 Chapter 4 | Designing UiO-based catalysts for photocatalytic CO_2 reduction 140
4.1 Introduction 140
4.2 Results and Discussion 142
4.2.1 Photocatalytic CO_2 Reduction 142
4.2.2 Structural Characterization 146
4.2.3 Structure-Reactivity Relationship 168
4.2.4 Optical Characterization 169
4.2.5 Mechanism of photocatalytic CO_2 reduction 175
4.3 Conclusion 177
4.4 Reference 178
5 Chapter 5 | Enhancing photocatalytic water splitting via Gate-Opening Effect of UiO MOFs 184
5.1 Introduction 184

5.2 Results and Discussion 185
5.2.1 Photocatalytic performance 187
5.2.2 Structural Characterization 193
5.2.3 Structure-reactivity relationship 209
5.2.4 Mechanism of photocatalytic water splitting 231
5.3 Conclusion 232
5.4 References 234
6 Chapter 6 | Conclusion & Future Works 239
6.1 Conclusion 239
6.2 Future Work 240
6.2.1 Catalytic testing 240
6.2.2 Mechanistic studies 241
6.2.3 Post mortem analysis 241
6.2.4 In-situ characterization 241
6.2.5 Applying MOFs as photocatalysts at industrial scales 242

1 Chapter 1 | Introduction

1.1 Metal-Organic Frameworks (MOFs)

Metal-Organic Frameworks are extending frameworks formed by coordination of metal ions or clusters (inorganic units) with polyfunctional organic ligands, which are held together by electrostatic force. They have attracted considerable attention due to their outstanding properties including high specific surface area, tunable pore sizes and adjustable functional groups. Topologically, the metal cluster and organic linkers are similar as dots and lines, for the construction of 3D materials as depicted in Figure 1 . 1. These MOF materials have possible applications in the fields of adsorption[1], separation[2,3], sensing[4], and catalysis[5-7], and which have been tabulated in Table 1 . 1. The wide range of inorganic units and organic linkers available combined to let one thousand MOF bloom. The inorganic units and organic linkers will be separately introduced in this thesis, before delving into the UiO-series of MOFs.

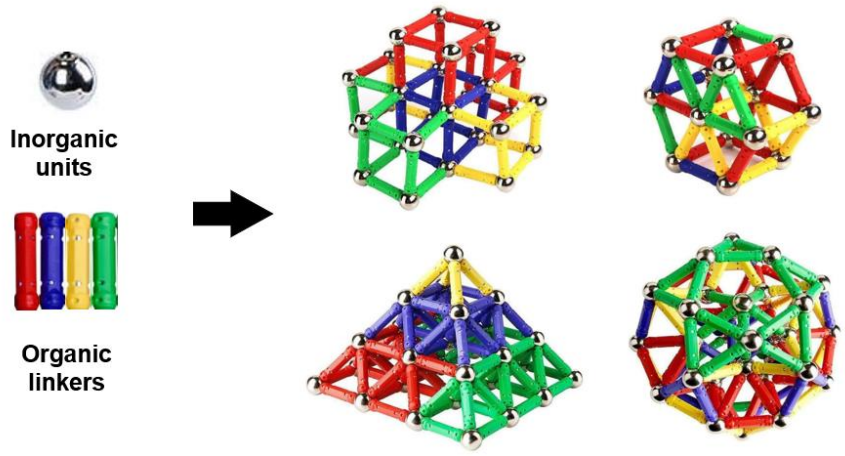


Figure 1 . 1 | Combination of inorganic units and organic linkers to form extending 3-dimensional network

MOF	Application	Structural properties exploited	Ref
UiO-67 and UiO-67-bpydc	Adsorption of NH_3 molecule	Structural flexibility of bipyridine dicarboxylic linker in UiO-67-bpydc	1
Fe-MOF-74	Separation of CH_4 from mixtures of light hydrocarbons	Open Fe metal sites from the porous framework	2
ZIF-90	Separation of H_2 from CH_4	Tunable pore sizes in correlation to the difference in kinetic diameter	3
UiO-66-NH_2	Sensing of F^- or CO_3^{2-} ion	Hydrogen bonding restricting rotation of organic linker, enhancing photoluminescence	4
UiO-66-NH_2	Catalysis of formic acid decomposition	Tunable Cu-oxo nanoclusters for formic acid dehydrogenation and dehydration	5
MIL-101(Cr)	Catalytic addition of HBpin across imines	Open Cr metal sites for incorporation of Lewis Base for activation of HBpin	6
NENU-500 and NENU-501	Catalytic hydrogen evoluation reaction	Tunable pore sizes for incorporation of polyoxometalate $PMo_{12}O_{36}(OH)_4Zn_4$	7

Table 1 . 1 | Examples of MOFs reported in the literature for various applications

1.1.1 Inorganic Units

Inorganic units are commonly formed with positively charged metals and oxide ions. The first MOF reported in 1989 by Robson[8] has only got a single singly charged Cu^+ as the connecting node. Later in 1995, O. M. Yaghi used the term Metal-Organic Framework for the first time as he reported a copper-bipyridine structure, also containing one singly charged Cu ion to hold the structure together[9]. The complexity of MOF is limited by the tetrahedral or octahedral coordination of single metal ions. Such MOFs are yet to receive more attention, as the positive

charge on the Cu metal is unbalanced by the cyanide / pyridine based organic linker. The need for charge balancing anion such as BF_4^- or NO_3^- limits the purification of the MOF material.

The complexity of inorganic units grew by the report of the HKUST-1 MOF by Williams in 1999[10], by having a $Cu_2(OH)_2$ dimer connecting bezene-1,3,5-tricarboxylate (TMA). The concept of secondary building units (SBUs) is also proposed. By viewing the 3D structure of HKUST-1 as corner-sharing $Cu_3(TMA)_2(H_2O)_3$ octahedra as depicted in Figure 1 . 2, the topology and connectivity of metal-organic frameworks resembles how polyethylene can be formed from the polymerization of ethylene.

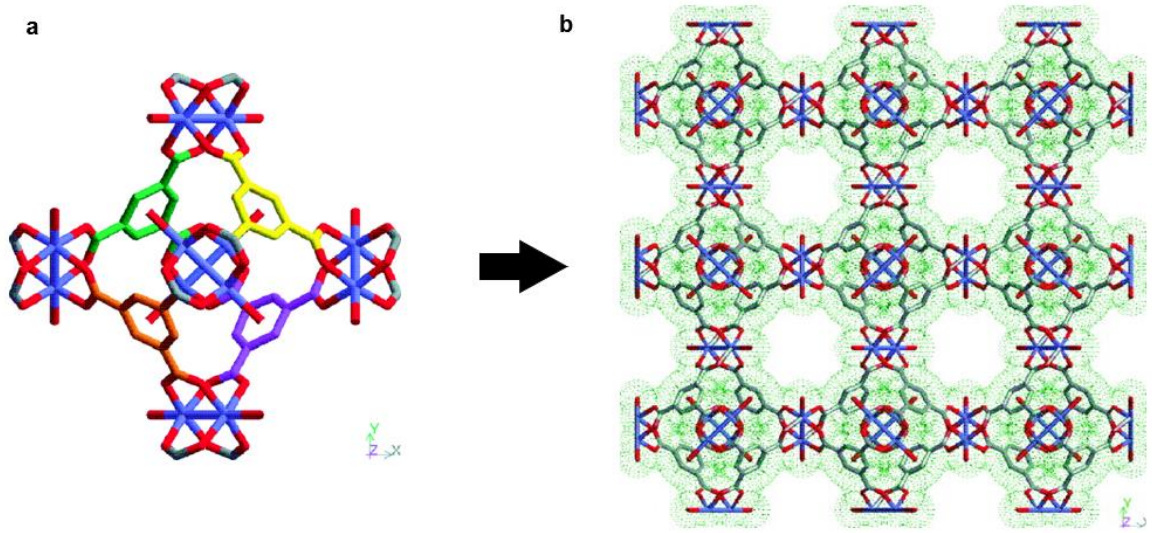


Figure 1 . 2 | Secondary building units of $Cu_3(TMA)_2(H2O)_3$ and its relation to the framework structure of HKUST-1. Figure reproduced from Ref [10]. Reprinted with permission from AAAS

Moreover, William's report of HKUST-1 structure has included the +2 charged copper species, which laid the foundation of the exponential increase of reports of MOF materials. Currently, the inorganic units in MOFs often compose of metals ranging with charge +2, such as Fe, Co, Cu and Zn, to +3, such as Al and In, to +4, such as Zr, Ce and Hf. The variety in metal species and valence results in different topology available for the inorganic units, which are summarized in Figure 1 . 3 a-e.

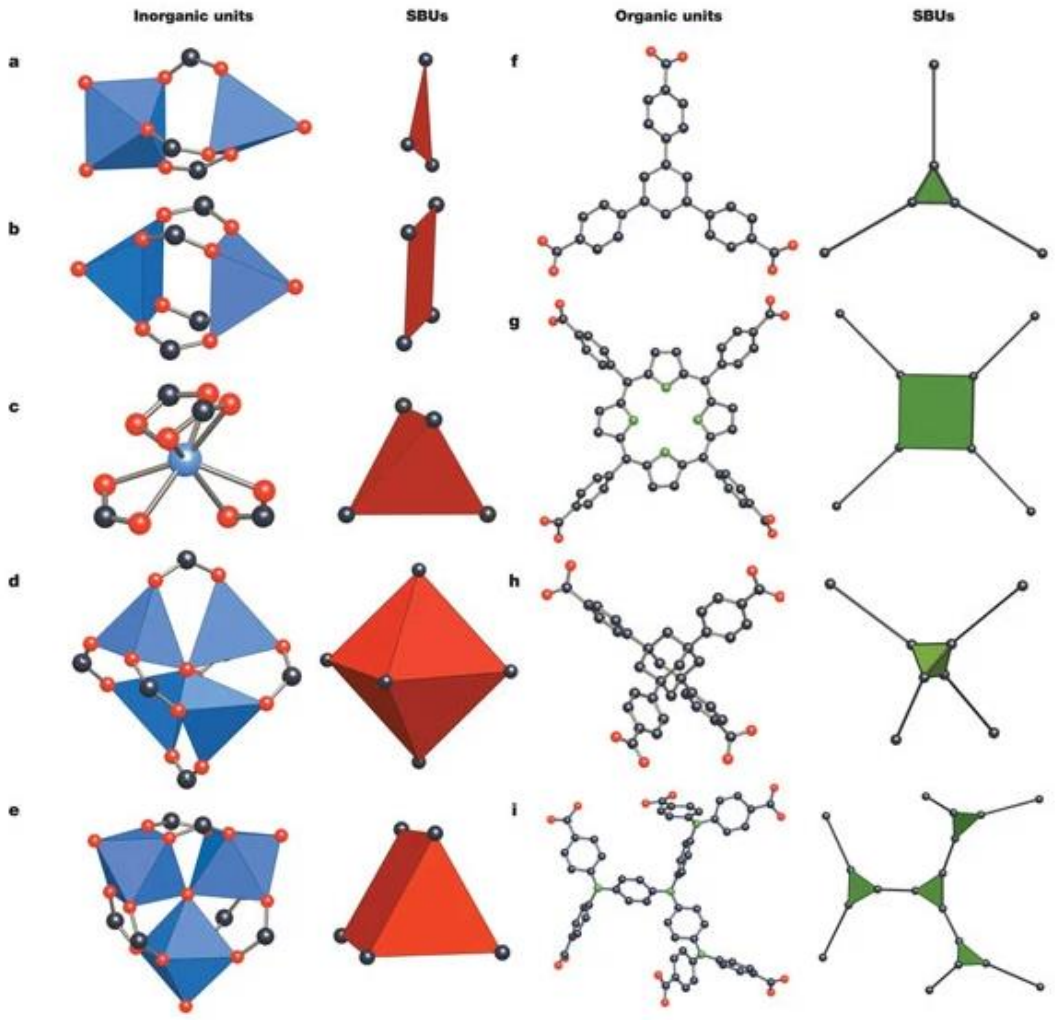


Figure 1 . 3 | Examples of different topologies of inorganic units and organic linkers. Colour scheme: Red = O, green = N, black = C. Figure reproduced from Ref [11]. Reproduced with permission from Springer Nature

1.1.2 Organic linker

Suggested by its name, organic linkers are organic species with the purpose of connecting the inorganic units together for the formation of 3D frameworks. Common ingredients of the organic linkers are aromatic rings such as benzene[12], imidazole[13], thanks to their rigidity. Cubanes have also been incorporated into organic linkers in recent reports by Macreadie[14]. The organic linkers commonly connect to the inorganic units via oxygen or nitrogen-based ligands. Nitrogen on imidazole rings or pyridine rings have been used to connect to the positively charged metal ions, such as aforementioned Yaghi's report of $Cu(4,4'\text{-bpy})_{1.5}{\cdot}NO_3(H_2O)_{1.5}$[9]. By far the most frequently used ligand is the carboxylate group, which can chelate onto the metal ions to provide extra stability.

One of the varieties in MOFs stem from the divergence of the topologies of the organic linker. Most common organic linkers have linear topology, have two carboxylate groups to join two inorganic units together, such as benzene-1,4-dicarboxylic acid otherwise known as terephthalic acid. Triangular, square, tetrahedral, and other topologies are also possible with different organic linker. In the HKUST-1 MOF reported by Williams, the benzene-1,3,5-tricarboxylate organic linker results in a triangular topology[10]. Organic linker with square, tetrahedral or other more complex organic linker topology has also been reported. The different topologies and connectivities of organic linkers are shown in Figure 1 . 3 f-j.

1.1.3 UiO-series

UiO stands for Universitet i Oslo, where Cavka and coworkers first reported the zirconium inorganic building block, $Zr_6O_4(OH)_4$ to be exceptionally stable for the construction of metal-organic framework materials[15]. This building block contains 6 Zr^{4+} ions arranged in the corner of an octahedron, with each face of the octahedron capped by either μ_3-O or μ_3-OH. Each Zr_6 inorganic unit connects to 12 organic linkers. The difference between terms "Inorganic units"

and “Secondary building units” are sometimes confusingly used in the literature. UiO-66 MOF is used as an example to illustrate the difference between inorganic units, secondary building units and the UiO-66 framework in Figure 1 . 4. The four charge-balancing proton from $(OH)_4$ has been omitted for clarity.

The inorganic unit, or inorganic building block, is the $Zr_6O_4(OH)_4$ in Figure 1 . 4 a. The secondary building block includes the whole of the inorganic unit, and also the carboxylates from the terephthalic acid (organic linker) that are directly bonded to the inorganic unit, as shown in Figure 1 . 4 b. The concept of secondary building units is introduced for the classification of MOFs according to the connectivity of the inorganic units, in spite of the risk of double-counting the ($-CO_2$) carboxylate units[16,17]. Without the carboxylate ($-CO_2$) in the SBUs, the 12-fold connectivity is not immediately obvious simply by observing the $Zr_6O_4(OH)_4$ in Figure 1 . 4 a. The connection of inorganic units and organic linker would result in the UiO-66 framework (Figure 1 . 4 c).

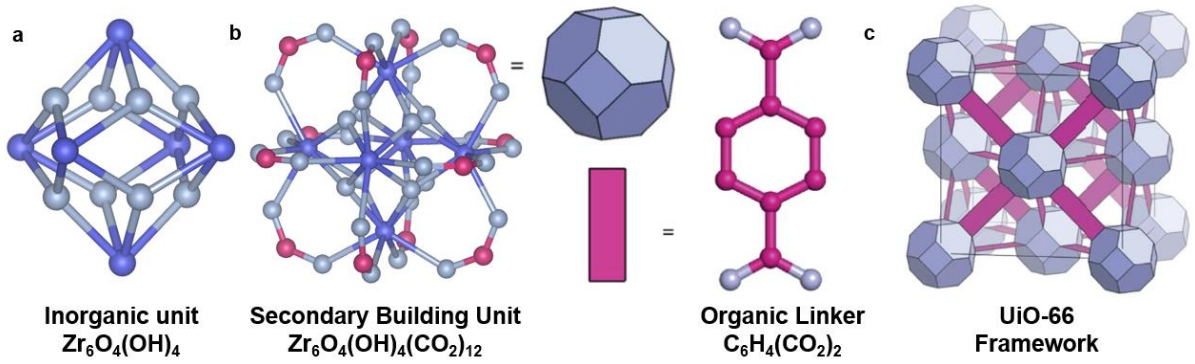


Figure 1 . 4 | (a) Inorganic unit of UiO-66, $Zr_6O_4(OH)_4$, with the hydrogen omitted for clarity. (b) the Secondary Building Unit and the organic linker of terephalic acid of UiO-66. (c) The combination of both the inorganic unit and organic linker into the framework of UiO-66. Colour scheme: Dark blue = Zr, Light blue = O, Pink = C. Hydrogen are omitted for clarity. Figure reproduced from [18]. Reproduced with permission from Springer Nature

1.1.4 Synthesis of UiO-66

In a typical synthesis of UiO-66, $ZrCl_4$, terephthalic acid, modulators (such as ethanoic acid) will be added into dimethylformamide (DMF). In some synthesis some deprotonating agent such as triethylamine will be added. $ZrCl_4$ and terephthalic acid are the building blocks of UiO-66, with HCl as side products during the reaction. The high concentration of only these two reagents will lead to a rapid reaction that produces a gel product instead of powder MOFs. The reason stems from the lack of long-range order in the 3D network, due to rapid nucleation and interconnection without achieving full 8-fold coordination for Zr^{4+} ions.

The addition of modulators is commonly used to assist the production of powder MOFs. They take the form R-COOH where R can be a -H (formic acid), $-CH_3$ (acetic acid), $-C_6H_5$ (benzoic acid) and others. They bind to the Zr^{4+} competitively and reversibly, which slows the crystallization process and allows for more control in structure growth. The concentration of modulators needs to be optimized, as too much modulator present would inhibit crystallization as they surround the Zr^{4+}. It has also been hypothesized that the modulator can accelerate the crystallization process by enhancing the hydrolysis of $ZrCl_4$[19].

Deprotonating agents are sometimes added to activate the carboxylic acid functionality on the organic linker by deprotonation. The interaction between the deprotonated carboxylate with the Zr^{4+} can be promoted. However, with excessive deprotonating agents the modulators can get deprotonated and inhibits nucleation[20]. A summary of the purpose of each reagents on MOF structure growth is illustrated in Figure 1 . 5.

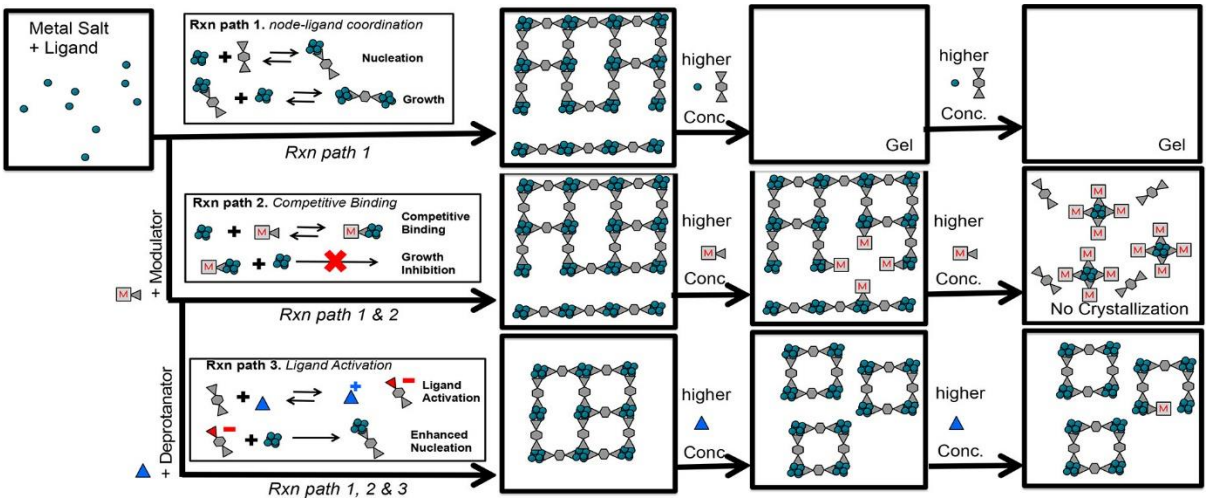


Figure 1 . 5 | Summary of purpose of modulator and deprotonating agent added during MOF synthesis procedures. Figure reproduced from Ref [20]. Copyright © 2020 American Chemical Society

In the simplest MOF in the family, UiO-66, each terephthalic acid molecule has its carboxylate group coordinated to an edge of the Zr_6 octahedron. The structure of UiO-66 is held strongly together by the electrostatic charge between highly charged Zr^{4+} and O^{2-} from the Zr-oxo clusters and terephthalic acid, respectively. Such strong forces have resulted in exceptionally stable structures with wide chemical tunability of the organic linker. More specifically, the chemical stability of the UiO-series MOFs is attributed to the ability of μ_3-OH groups to rearrange reversibly upon dehydroxylating, without any changes in the connecting carboxylates[21]. Increasing the number of phenyl rings on the organic linker results in the structure of UiO-67 and UiO-68, as shown in Figure 1 . 6 below. The structure of these MOFs can be seen as cubic close packed of $Zr_6O_4(OH)_4$ units with organic linkers connecting the nodes together.

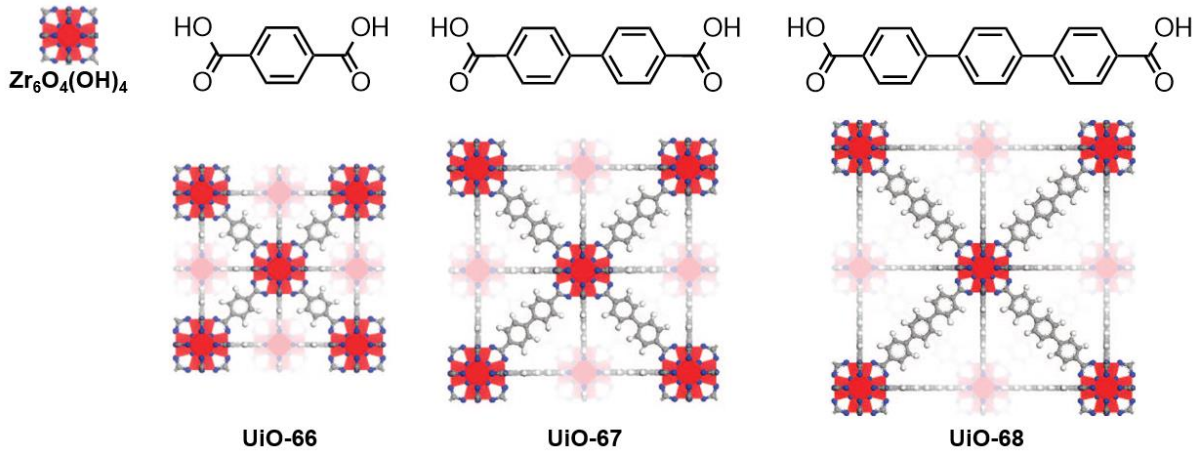


Figure 1 . 6 | Structure formed from the $Zr_6O_4(OH)_4$ inorganic unit with terephthalic acid / benzene-1,4-dicarboxylic acid (BDC) to yield UiO-66; with biphenyl-4,4'-dicarboxylate (BPDC) to yield UiO-67; and with [1,1':4',1"-terphenyl]-4,4"-dicarboxylic acid to yield UiO-68. Figure reproduced from Ref [21]. Copyright © 2008, American Chemical Society

In a subsequent paper, Lillerud and coworkers functionalized the organic linker with amine, nitro and bromine and characterized such MOF structures with FTIR, PXRD, TGA and N_2 adsorption measurements[22]. The introduction of such functional group brought changes to the structural and optical properties of the MOFs, which allows the use of the UiO-series MOFs on a wider range of applications. The introduction of functional groups without changing the topology or connectivity between the inorganic units and organic linkers is termed isoreticular synthesis[23].

1.1.5 Tetrahedral and Octahedral pores

The construction of framework by Zr_6 inorganic units and terephthalic acid gave rise to the porous nature of UiO-66. Two types of pores exist in UiO-66, and are termed tetrahedral pores and octahedral pores. Understanding the differences between the two types of pores is easier by viewing the structure of UiO-66 as cubic close packed $Zr_6O_4(OH)_4(CO_2)_{12}$ SBUs, with the linkers omitted for clarity as illustrated in Figure 1 . 7 a. The location of tetrahedral pores is similar to the location of tetrahedral holes, at the position of F^- (green spheres) viewing the

fluorite structure of CaF_2 as cubic close packed Ca^{2+} ions (blue spheres) in Figure 1 . 7 b. Tetrahedral pores are surrounded by 4 organic linkers in a tetrahedral manner. On another hand, the location of octahedral pores is similar to the location of octahedral holes, at the position of Na^+ (green spheres) viewing the NaCl rocksalt structure as cubic close packed Cl^- ions (blue spheres) in Figure 1 . 7 c. Octahedral pores are surrounded by 6 organic linkers in an octahedral manner. It follows that the octahedral pores are larger than the tetrahedral pores, with diameters 8Å and 11Å, respectively in UiO-66. As the length of linker grows the pore sizes grows to 12Å and 16Å[24]. In every unit cell of UiO-series MOFs containing 24 Zr^{4+} ions (4 Zr_6 inorganic units), there are 8 tetrahedral pores and 4 octahedral pores.

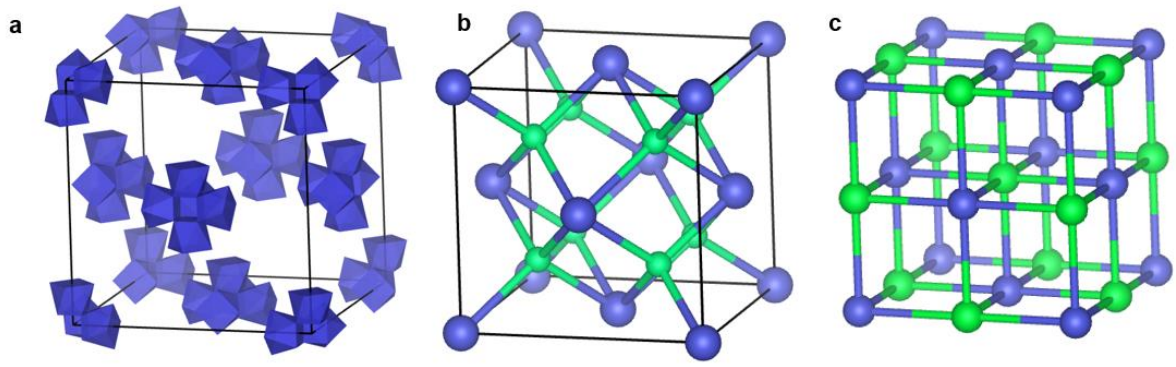


Figure 1 . 7 | (a) Structure of UiO-66 without organic linkers, as cubic close packed $Zr_6O_4(OH)_4(CO_2)_{12}$ SBUs. (blue polyhedra) (b) Structure of CaF_2, with the position of Ca^{2+} (blue) and F^- (green) analogous to that of tetrahedral pores and SBUs, respectively. (c) Structure of NaCl, with the position of Na^+ (green) and Cl^- (blue) analogous to that of octahedral pores and SBUs, respectively.

1.2 Catalysis with light

Catalysis speeds up reaction by providing an alternative pathway with a lower activation energy, as any secondary school chemistry textbook would write. This reduction in activation energy translates to a reduction in reaction time. As the reaction finishes, the catalysts will be regenerated and not be consumed, and can be used in subsequent reactions. Heterogeneous catalysis, where the catalysts and the reactants are in different phases, is of significant industrial

importance[25,26]. One well-known example is the Haber-Bosch process, where solid iron oxide catalysts catalyze gaseous nitrogen and hydrogen mixture into ammonia[27]. In such a process, the catalyst will not be consumed and can therefore be reused for further reaction. On top of that, due to the difference in phase, the catalyst can be easily separated from the reactant/product mixture. Therefore, the chemical process can become significantly more environmentally friendly[28-31].

Photocatalysis is a branch of catalysis where the catalytic process is promoted by photoexcited electrons and holes. Upon light illumination, electrons can be promoted from valence band to the conduction band, which creates electron vacancy (or hole, h^+) in the valence band and an extra electron (e^-) in the conduction band. The excited electron-hole pair can then participate in redox reactions[32,33]. Unfortunately, it is also possible for such generated electron-hole pair to recombine and release the energy as light, heat, or molecular vibration[34,35]. Upon the formation of electron-hole pair with light irradiation, a good photocatalyst can diffuse the excited electron or hole to the surface of the catalysts, where it can come into contact with reactant[36,37]. The catalytic performance of the catalysts is dependent on the thermodynamics of the reaction. The separated electrons and holes need to satisfy certain energy criteria, such that the excited electrons and holes have sufficient energy to reduce and be reduced, respectively[38,39]. The fundamental steps of photocatalysis are summarized in Figure 1 . 8 a below. The thermodynamics of the fuel-forming reactions will be discussed in greater details in subsequent discussions.

1.2.1 Hydrogen gas as an energy carrier

Hydrogen is the lightest element in the periodic table. Containing only one proton and one electron, its affinity towards pairing up its electron gave rise to a wide range of chemical reactivity. The simplest compound for hydrogen element is hydrogen gas, H_2. The two hydrogen atoms are bonded with a single bond with a bond enthalpy of 436 kJ mol^{-1},[40]. To

avoid confusion, in subsequent discussions the word “hydrogen” will refer to the H_2 hydrogen gas, rather than the element.

The vast use and exploitation of fossil fuels have become one of the greatest energy challenges for the 21st century due to anthropogenic carbon dioxide emissions, responsible for global warming. It is essential to find alternative fuels and develop sustainable energy systems with reduced carbon emissions. Hydrogen has emerged as a major carbon independent energy carrier, has proven itself to be one of the ideal candidates for achieving a greener chemical industry. Its combustion releases energy ($H_2 + ½ O_2 \rightarrow H_2O$, $\triangle H = -286$ kJ mol^{-1}) and forms water as a product, without any carbon emissions[41,42].

According to the IEA, hydrogen demand reached 94 million tonnes in 2021, and contains energy equal to about 2.5% of global final energy consumption[43]. Despite an increase in technology allowing hydrogen to be used as an energy source alternative to fossil fuels, there will be no benefit in mitigating climate change if the hydrogen production causes significant carbon emissions. Hydrogen is produced via the steam reforming of methane $CH_4 + H_2O \rightarrow CO + 3H_2$, which happens at high temperature of 700-1100°C and is energy intensive. Currently, less than 1 Mt of hydrogen is produced via low-emissions means.

1.2.2 Hydrogen from water splitting

Water splitting is the reverse reaction to the combustion of water, that is, $H_2O \rightarrow H_2 + ½ O_2$, which is an endothermic process with $\triangle H = +286$ kJ mol^{-1}. In 1972 Fujishima and Honda published the use of TiO_2 as a catalyst for water splitting reaction, which was frequently referred to as the first demonstration of photocatalytic water splitting[44]. Until now, the photocatalytic water splitting reaction has been studied for decades, and significant progress has been made[45-47].

Considering the thermodynamics, for overall water splitting $H_2O \rightarrow H_2 + ½ O_2$, the electron in conduction band will need to reduce H^+ in the hydrogen evolution reaction (HER) half reaction $H^+ + e^- \rightarrow ½ H_2$, which has a standard electrode potential of +0.00 V against SHE. Similarly, the hole in the valence band will oxidize H_2O in the oxygen evolution reaction (OER) half reaction $H_2O \rightarrow ½ O_2 + 2 H^+ + 2 e^-$, which has a standard electrode potential of +1.23 V. As a result, for both half reactions to happen simultaneously to produce hydrogen and oxygen, the valence band maximum will need to be more positive than +1.23 V, while the conduction band minimum should be more negative than 0.00 V, depicted according to Figure 1 . 8 b below.

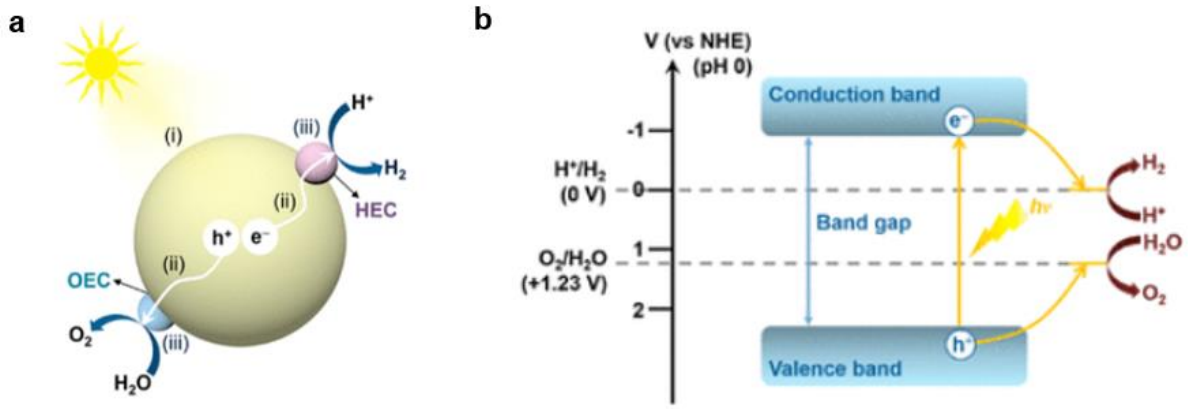


Figure 1 . 8 | (a) Diagram showing the reactions during water splitting on a semiconductor photocatalyst: (i) light absorption and formation of electron-hole pair; (ii) charge diffusion and transport; (iii) redox reaction. (b) Energy diagram for photocatalytic water splitting based on one-step excitation. Figures reproduced from Ref [45]. Copyright © 2020 American Chemical Society.

Sacrificial reagent

Limitations in catalysts restrict efficient catalysis of the full process, which may be due to a variety of factors. As such, sacrificial reagents can be added to the reaction system in order to enhance the activity for a more thorough investigation of either HER or OER. Methanol or triethanolamine (TEOA) are common sacrificial reagents for the study of photocatalytic

HER[48,49]. TEOA is irreversibly oxidized by the photogenerated holes, therefore suppressing charge recombination, and enhancing HER[50].

1.2.3 Hydrogen activation and utilization

Hydrogen utilization was one of the first processes found that can be catalytically promoted by Sabatier in 1897, hydrogenating ethylene into ethane using a Ni catalyst[51]. It is still extensively used in a wide range of chemical processes, such as the aforementioned Haber-Bosch process for the synthesis of ammonia $N_2 + 3\ H_2 \rightarrow 2\ NH_3$, and the synthesis of methanol $CO_2 + 3\ H_2 -> CH_3OH + H_2O$. Hydrogen is also involved in a variety of carbon capture and usage, as hydrogen is used to reduce the carbon in carbon dioxide to more desired fuel-like products such as methane CH_4 and methanol CH_3OH.

In the first step of hydrogen utilization, the H-H single bond has to be broken. There are two separate pathways for such cleavage of H-H bonds: Homolytic and heterolytic. Homolytic cleavage of H-H bonds results in 2 hydrogen radicals $H\cdot$, and can be stabilized by metals. It is generally understood that Group 10 metals such as Ni and Pt are good at stabilized the hydrogen radicals[52]. Upon reaction with small molecules such as CO_2, radicals would be generated as high energy intermediates. Alternatively, heterolytic cleavage of H-H bonds results in a protonic H^+ and a hydridic H^-, which is typically stabilized by two distinct active sites and has preferential sites of reaction. Exemplifying with CO_2, the hydridic H^- will add to the electrophilic carbon, while the protonic H^+ will add to the nucleophilic oxygen. These two different pathways for hydrogen activation is summarized in Figure 1 . 9. In the case of Ru single atoms supported on MgO (111) surface, upon heterolytic cleavage of hydrogen molecule, the protonic hydrogen is adsorbed by the oxide of MgO, converting into a hydroxyl group, while the hydridic hydrogen is adsorbed on Ru[53].

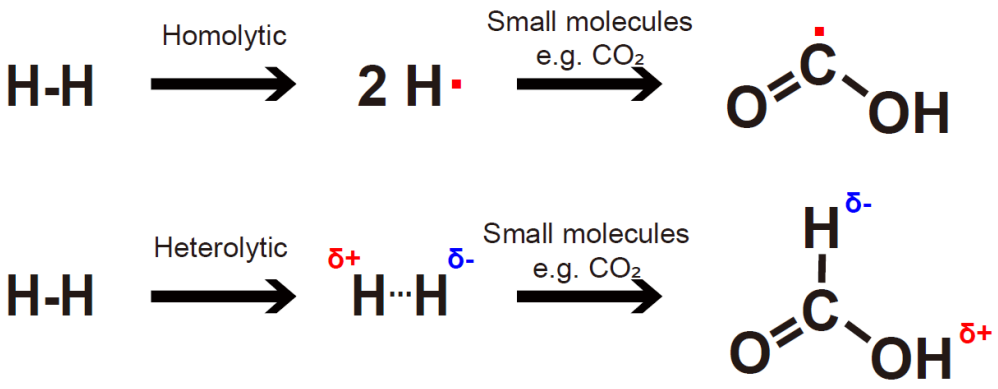


Figure 1 . 9 | Homolytic and Heterolytic cleavage of H-H bond

1.2.4 The use of H_2 in CO_2 reduction

Currently, 62 % of the global electricity generation comes from fossil fuels, such as coal and natural gas[54]. The combustion of fossil fuels generates carbon dioxide, which enhances the greenhouse effect by absorbing as vibrations of the C=O bonds and re-radiating them in all directions including back toward the surface of the Earth. CO_2 capture and utilization has emerged to be one potential solution: CO_2 would be captured and converted via reduction with H_2 into fuels such as methanol CH_3OH or methane CH_4. This would resemble the photosynthesis process and would be a sustainable and carbon-neutral strategy towards the enhanced greenhouse effect due to increased carbon emissions.

A certain relationship between the mode of hydrogen activation and its reactivity has been suggested by several researchers. In the process of CO_2 reduction by hydrogen, the formation of either formate (HCOO*) or carboxyl (*COOH) intermediate can be dependent on the active sites present in the catalysts. In a paper by Nelson and Szanyi, a divergent chemical behaviour of homolytically and heterolytically activated hydrogen towards CO_2 has been observed, exemplified by the formation of the formate and carboxyl intermediates, respectively[55].

1.2.5 Heterolytic cleavage of H-H

Various methods of designing Frustrated Lewis Pair (FLP)-based catalysts have been developed specifically for hydrogenation reactions. Frustrated Lewis Pairs was first termed by

Welch and Stephan in 2006 as they report the activation of hydrogen via a bulky borane and phosphine[56]. This concept has then been extended to heterogeneous catalysis by Guo, Wang and coworkers in 2014[57], combining imines and nitriles as Lewis base and gold as Lewis acid for the heterolytic activation of hydrogen. After 2020, the concept of FLPs have also been used to explain geometrically separated Lewis acidic and basic sites for catalysis, such as anion vacancies and hydroxyl groups, which have demonstrated pivotal effect in the process of CO_2 reduction[58]. Heterolytic cleavage of H-H is generally beneficial towards activating polarized double bonds such as C=O in CO_2 or carbonyls, and C=N in imines, with the hydridic hydrogen attacking the electrophilic carbon in carbonyls or imines and protonic hydrogen bonding to the oxygen or nitrogen in a concerted manner[59-62].

1.2.6 Metal-organic frameworks as Catalysts

The structure of MOFs has been likened to zeolites mainly due to their porous nature, with their high chemical tunability allowing for an increased control and modulation of electronic properties[63]. Zeolite has been the most successful type of solid catalyst (e.g. the use of zeolite ZSM-5 in catalytic cracking of crude oil)[64], to which new applications can still be discovered[65-67]. Although it could be anticipated that MOFs can be designed as great catalysts, their application towards catalysis has still been relatively limited due to the combination of two factors[68,69].

Firstly, the electrostatic forces between the inorganic units and organic linkers still falls weaker compared to the covalent bonds between Si-O or Al-O present in zeolites. The stronger covalent interaction allows zeolites to be stable under moisture and high temperatures (can be up to 600 °C or higher). Majority of the MOFs decompose at around 300 °C, and a portion of the MOFs whose structural integrity weakens at the presence of water. Their low thermal stability has limited their application as thermal catalysts.

Secondly, in commonly seen MOF structures, the metal ions in the inorganic units are in full coordination. In MOF-5 the Zn^{2+} ions are tetrahedrally coordinated[70], in HKUST-1 the Cu^{2+} ions are octahedrally coordinated[10], and in UiO-66 the Zr^{4+} ions are 8-coordinated. Catalysis requires unsaturated coordination positions, commonly at the edge sites of bulk materials. The fully coordinated metal sites present in MOFs leaves no room for reactants to bond, and subsequently be catalysed.

Nevertheless, MOFs have attracted significant attention in the field of photocatalysis. With the aid of light irradiation, the temperature required for chemical reactions to run can be lowered, and their thermal stability still allows their application as photocatalysts. Moreover, the organic linkers have accessible band gaps to absorb light and initiate charge transfer reactions. Their high surface area allows reactants to adsorb and subsequently react with the excited electron and holes that are formed[71,72].

The lack of coordination sites in MOFs can be mitigated in several ways. In the case of HKUST-1, one of the coordination sites around the Cu^{2+} ions in the inorganic units are water, and can be removed upon thermal activation[73]. Co-catalysts can also be added with MOFs acting as a support material, so that the charge generated in the MOF upon illumination can be transferred and initiate redox reactions. Wang has reported the incorporation of Pt nanoparticles into a phosphorescent MOF, which has a turnover number of 7000 in the hydrogen evolution reaction. The high catalytic activity has been ascribed to the facile electron transfer from the photoreduced Ir anchored on the organic linker onto entrapped Pt nanoparticles[74].

1.3 Engineering UiO-series MOFs as photocatalysts

1.3.1 Functionalizing the organic linker

The isoreticular synthesis of UiO-66, replacing the organic linker terephthalic acid with 2-aminoterephthalic acid, yields UiO-66-NH_2. Replacing the organic linker with 2,2-bipyridine-5,5-dicarboxylic acid, yields UiO-67-bpydc. Such changes are encapsulated in Figure 1 . 10 below. These are the two MOFs investigated in this thesis, with the rationale behind such modification explained subsequently with respect to their application as photocatalysts.

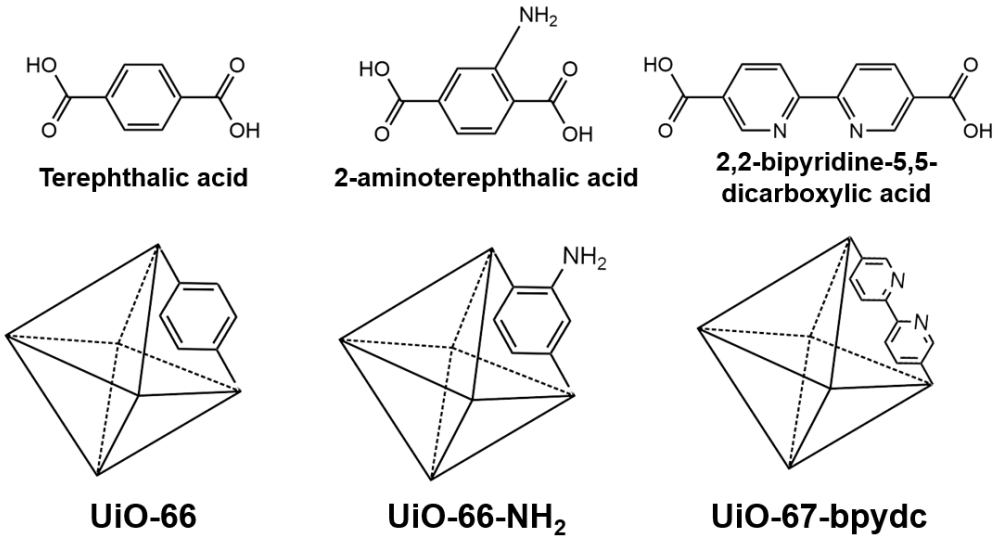


Figure 1 . 10 | Isoreticular synthesis of UiO-66-NH_2 and UiO-67-bpydc from UiO-66 with varied organic linker

Other than the advantages and disadvantages of MOFs as catalysts discussed above, two other factors affect the application of UiO-series MOFs as photocatalysts. The strong electrostatic force between the highly charged Zr^{4+} metal ions and carboxylate groups in the terephthalic acid in the structure increases the thermal stability of the UiO-series MOF, with UiO-66 stable until 550 °C. At the same time, the highly charged Zr^{4+} metal ions gave rise to a high band gap that is in the UV region, and reduced exciton lifetime upon light irradiation. Few papers report the direct use of UiO-66 as photocatalysts. Some sort of modifications, either to the inorganic

units or the organic linkers, is always presented simultaneously with UiO-66 as photocatalysts. The deposition of co-catalyst onto UiO-66 MOFs also proved to be difficult, as the aromatic ring in terephthalic acid contains no Lewis acidic / basic sites for chemical anchoring of co-catalysts.

The most used tactic to engineer UiO-series MOF for photocatalysis is via isoreticular synthesis. Replacing the terephthalic acid with 2-aminoterephthalic acid to introduce an amino group as UiO-66-NH_2 has numerous advantages (Figure 1 . 11 a). The amino group is an electron donating group in an aromatic system, and in the case of UiO-66-NH_2, the energy of the valence band can be raised, shifting the regions of light absorption into the visible region. This effect is manifested via the UV-Vis spectra of UiO-66-NH_2 compared to UiO-66 as shown in Figure 1 . 11 b. Absorption peaks between 200-300 nm corresponds to the π to π* transition of the aromatic ring. The peak centred on 375 nm corresponds to absorption from the lone pair from amino group n to π* transition.

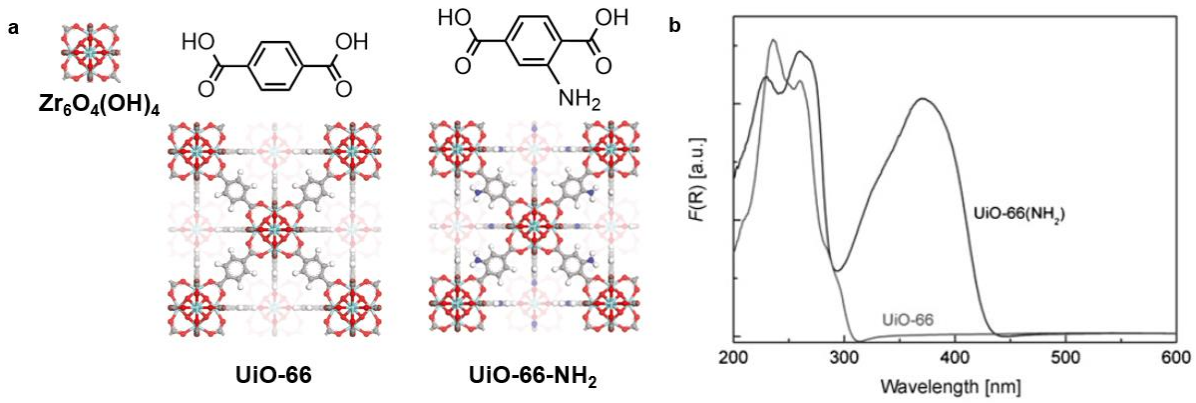


Figure 1 . 11 | (a) Isoreticular synthesis of UiO-66 with terephthalic acid, and UiO-66-NH_2 with 2-amino-terephthalic acid. (b) UV-Vis spectra of UiO-66 and UiO-66-NH_2. Figures reproduced from [22] and [75]. Copyright © 2010, American Chemical Society. Copyright © 2010 WILEY-VCH Verlag GmbH & Co. KGaA, Weinheim

Additionally, the amino group in UiO-66-NH_2 is Lewis basic. This allows the deposition of co-catalysts, further expanding its catalytic possibilities. The anchoring of Cu^{2+} onto the amino

sites of UiO-66-NH_2 has facilitated the reduction of CO_2 into methanol as reported by Li and coworkers, via the stabilization of CHO* and CO* intermediates[76]. The Lewis basic amino functionality also enabled the deposition of semiconductor materials. According to the report by Su, $Cd_{0.2}Zn_{0.8}S$@UiO-66-NH_2 nanocomposites synthesized via a solvothermal method allows an efficient charge separation and transfer between UiO-66-NH_2 and the sulphide material. As a result, a H_2 production rate of 5846.5 μmol h^{-1} g^{-1} can be obtained[77].

The isoreticular synthesis of using a bipyridine based ligand from UiO-67 to UiO-67-bpydc allows the introduction of chelating bipyridine ligands, as the two nitrogen atoms on the pyridine rings have lone pairs of electrons that are orthogonal to the π system. Such bipyridine ligands are exceptionally good at stabilizing single atoms. Numerous reports of UiO-67-bpydc supported catalysts have utilized the chelating properties of the bipyridine organic linker. Efficient acidic water oxidation on Ru loaded UiO-67-bpydc has been attributed to the stabilization of the *Vo-RuO_4^{2-} intermediate, which contributed to the enhanced OER performance and long-term stability of up to 115h[78]. The bipyridine-based organic linker is also used to stabilize Pt^{2+} precursors in the synthesis of Pt@UiO-67 catalysts, which aggregates into Pt nanoparticles upon reduction at 350 °C for 4 h by 10 % H_2/N_2[79].

The proximity between the bipyridine linker of UiO-67-bpydc with the well-known chromophore $Ru(bpy)_3^{2+}$ has sparked its incorporation into MOF. By first synthesizing $[Ru^{II}(bpy)_2(H_2bpydc)]Cl_2$ combining $Ru(bpy)_2Cl_2$ and H_2bpydc, and in the next step mixing with more H_2bpydc and $ZrCl_4$, a UiO-series MOF with both undeposited H_2bpydc and Ru-H_2bpydc can be achieved. Figure 1 . 12 has been drawn to visualize this complex synthesis procedure. Via subsequent introduction of Cu sites, photocatalytic CO_2 reduction to ethanol with selectivity higher than 99 % has been achieved, which are attributed to the single electron transfer enabled by the $Ru(bpy)_3^{2+}$ based chromophores to stabilize metal centres of intermediate oxidation state[80].

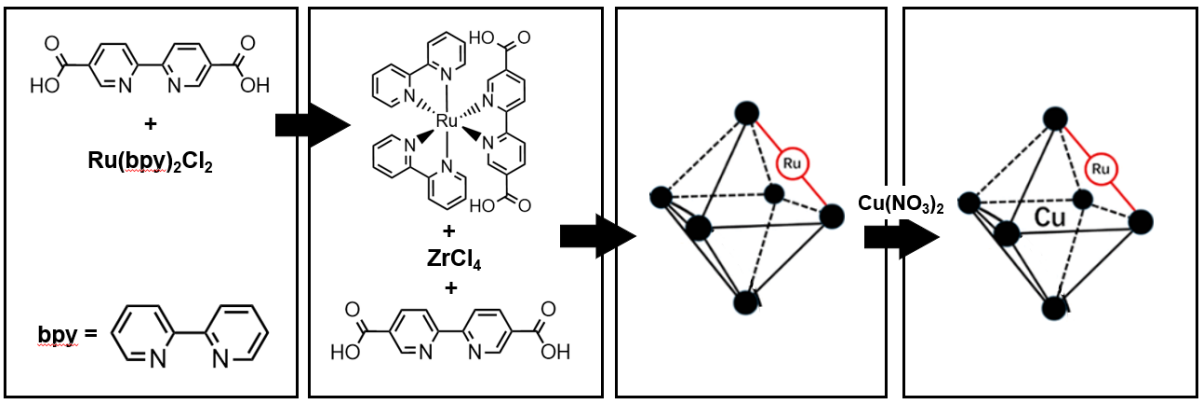


Figure 1 . 12 | Synthesis procedures of Cu^{II}@Ru-UiO-bpydc catalyst for the selective reduction of CO_2 to ethanol. Figures reproduced from Ref [80].

The pre-functionalization of organic linker prior to the construction of the extended UiO MOF framework is not limited to the introduction of metals. Gomez-Aviles functionalized the amino group in UiO-66-NH_2 via cyclopentyl and cyclohexyl group via reductive amination to reduce the band gap energy. The reduced bandgap lead to enhanced separation of photogenerated charges due to inductive electron effect of the cycloalkyl substituent, and consequently showed a more efficient photocatalytic degradation of acetaminophen[81].

Other than metal co-catalysts such as Ru and Cu, it is also possible to introduce other band gap materials such as semiconductors as co-catalysts to improve the photocatalytic activities of UiO-series MOFs. Thiol functionalized organic linker in UiO-66 to UiO-66-$(SH)_2$ has been used to stabilize CdS quantum dots for efficient photocatalytic water splitting. The thiol linkage between MOF and CdS quantum dots have been reported as effective transfer bridge of charge carriers, as revealed by ultrafast transient absorption spectroscopy[82].

1.3.2 Decoration onto the inorganic units

Some of the 12 organic linkers connected to the Zr_6 inorganic units can go missing due to interplay between enthalpy and entropy effects during the synthesis process of UiO-series MOFs. Ratios between Zr and organic linkers evidenced by thermogravimetric analysis reveals

the presence of missing-linker defects[83]. The crystal structure of the UiO-66 MOFs is still unaffected despite the presence of such missing-linker defects, due to the high connectivity between the Zr_6 inorganic units which are not possible in other MOFs. Wu and coworkers investigated how the extent of missing-linker defects can be tuned via the addition of acetic acid as modulator during the synthesis process. The authors also examined the gas adsorption behaviour of MOFs as a function of missing-linker defects present and reported an increase in both pore volume and surface area upon formation of missing-linker defects[84].

Absence of organic linkers in UiO-66 will expose a highly charged Zr^{4+}, which is terminated by either -OH/OH_2 groups from moisture in the air, or acetate or other modulators that are added during synthesis procedures. Researchers in the field of catalysis exploited the -OH/OH_2 groups terminating the missing-linker defects for the stabilization of metal species. Abdel-Mageed reported a highly active and stable single-atom Cu stabilized by the -OH group at the missing-linker sites characterized structurally by single crystal XRD and XAS. This catalyst proved to be selective catalysts towards CO oxidation reaction even in O_2-rich reaction atmospheres at temperatures up to 350 °C[85].

The chemical similarity between the $Zr_6O_4(OH)_4$ inorganic unit and ZrO_2, which are utilized industrially as support for Cu metals as Cu/ZrO_2 catalysts for CO_2 reduction into methanol. Zhu and coworkers reported Cu/UiO-66 catalysts via ion exchange of Cu^{2+} ions at the -OH groups resulted from missing linker defects, which forms Cu nanoparticles present in the pores upon reduction in 25 % H_2/N_2 at 200 °C. From thorough catalytic testing, the authors concluded that the Zr-O-Cu interface are part of the active sites for CO_2 chemisorption and consequently for high activity of CO_2 reduction towards methanol[86].

1.3.3 Modifying the metals in the Zr_6 inorganic units

The strong electrostatic force between Zr^{4+} and the carboxylate functional group of the organic linker gave rise to the high chemical stability of UiO-series MOFs. Nevertheless, modifications on the inorganic units have been reported for improving photocatalytic activities. It is noted that reports on the modification of Zr_6 inorganic units were only seen on pristine UiO-66, likely because of the weakened chemical stability upon any isoreticular synthesis with functionalized organic linkers. A theoretical study by Wu, Gagliardi and Truhlar has recognized ligand-to-metal charge transfer (LMCT) as the pathway of charge separation upon light irradiation in UiO-66. From density of states calculation replacing Zr with Hf, Th, Ti, U and Ce all in +4 state, they revealed that with Ce^{4+} the LMCT can be greatly facilitated due to the presence of low-lying empty 4f orbitals (Figure 1 . 13). With further tuning of the LMCT energy via linker functionalization, it is possible to engineer the electronic structure of Ce-based MOF to tailor for photocatalytic reactions[87].

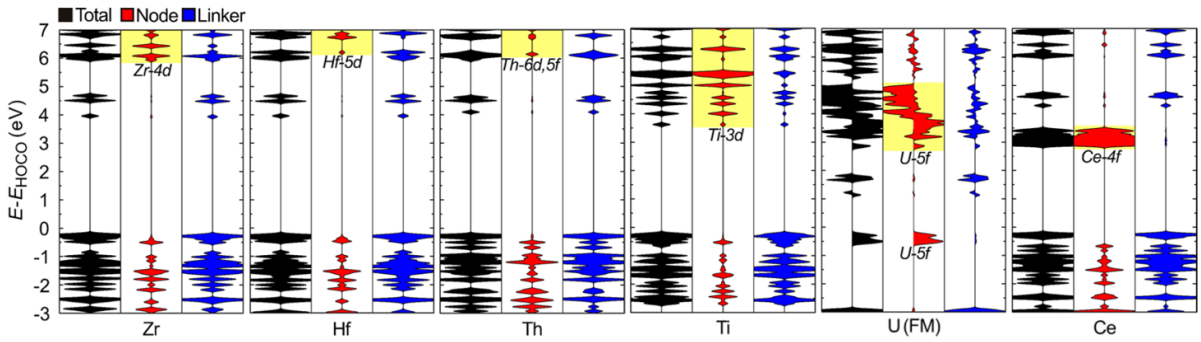


Figure 1 . 13 | Total (Black) and projected (red and blue) density of states of the pristine UiO-66(M) with M=Zr, Hf, Th, Ti, U, and Ce. For U, only the most stable ferromagnetic state is shown. The unoccupied Zr 4d, Hf 5d, Th 6d and 5f, Ti 3d, U 5f and Ce 4f orbitals are highlighted with a yellow background. The plot for U also shows at higher energy some unoccupied 6d orbitals. Figure reproduced from Ref [87]. Copyright © 2018, American Chemical Society

Melillo and coworkers attempted to verify the findings of Wu experimentally, by exchanging partly the Zr^{4+} metals in the inorganic units of UiO-66 with Ce^{4+} and Ti^{4+} for overall water splitting reaction. They also synthesized UiO-66 with only Ce^{4+} as suggested by Wu's conclusion for comparison. It is found that a mixed-metal UiO-66 (Zr/Ce/Ti) with a Zr:Ce:Ti metal content ratio of 8.3:1.0:2.4 achieves the best photocatalytic water splitting, outperforming the UiO-66(Ce) as suggested by Wu, Gagliardi and Truhlar. The authors attributed the enhancement of photocatalytic water splitting activity to the collective cooperation of trimetallic clusters favouring the kinetics of the four electrons-four proton process resulting in oxygen evolution. The mixed-metal UiO-66 (Zr/Ce/Ti) has also indicated a lesser extent of charge recombination upon light irradiation[88].

Exchanging the Zr^{4+} ions in the inorganic unit can be challenging experimentally, as a paper by Santaclara and coworkers revisits the synthesis procedures of metal exchange versus grafting onto Zr_6 inorganic units, along with their implications on photocatalysis, as depicted in Figure 1 . 14 a-b. From density of states calculations, they showed that the Ti^{4+} grafted on missing linker defect with 3 chlorides completing the coordination environment would have a

band gap 2.2 eV, which is smaller than the 2.7 eV if the Ti^{4+} is in the inorganic unit replacing Zr^{4+}. More importantly, the separate synthesis of the two Ti^{4+} included UiO-66-NH_2 along with characterization via IR, EPR and TGA, have resulted in widely different photocatalytic activities for water splitting. It is observed that with Ti^{4+} grafted on missing linker defect is 14x more active compared to that with Ti^{4+} incorporated in the node (Figure 1 . 14 c). The dramatic difference of catalytic activity simply stems from the different choice of Titanium source during the synthesis procedures, and highlighted the challenges associated with chemical modification of the Zr_6 inorganic units[89].

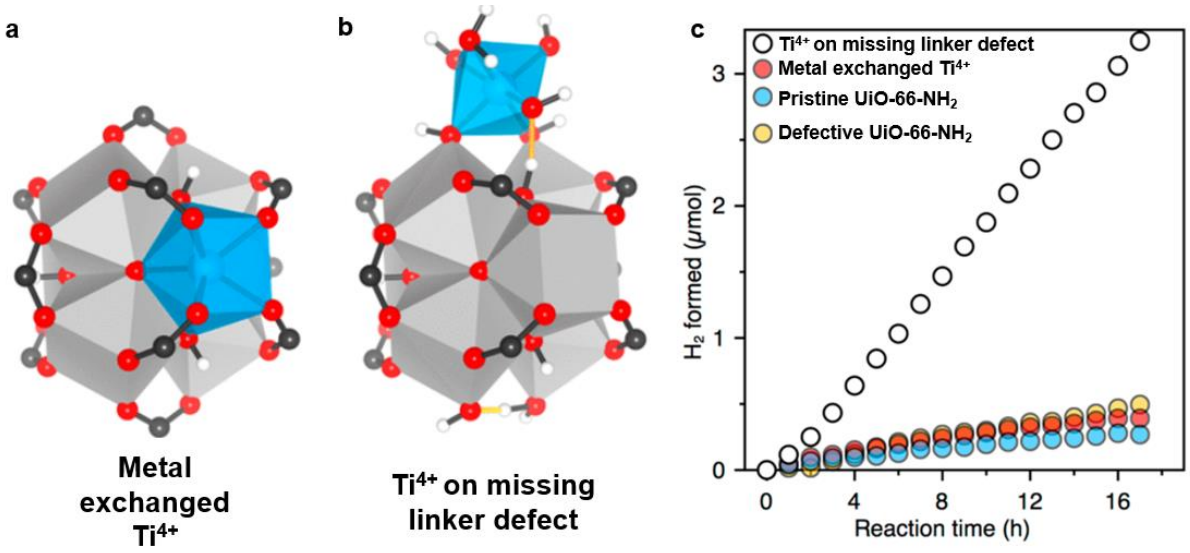


Figure 1 . 14 | Proposed coordination sites of Ti in the Zr_6 inorganic units of UiO-series MOF. (a) inclusion of Ti^{4+} in the cluster through metal exchange in place of Zr^{4+}. (b) Appendage of Ti^{4+} to the surface of the cluster at a missing linker defect site. Colour scheme: Grey polyhedra: ZrO_8, Blue polyhedra: TiO4, Black = C, Red = O, White = H. (c) Photocatalytic hydrogen evolution reaction activity of metal exchanged Ti^{4+}, Ti^{4+} on missing linker defect, pristine and defective UiO-66-NH_2. Reaction condition: 30 mg MOFs suspended in 23.5 mL CH_3CN, 4.7 mL Triethylamine, 0.5 mL H2O at 40°C. Figure reproduced from Ref [89]. Copyright © 2017, American Chemical Society

1.3.4 Encapsulation into UiO-series MOFs

One of the advantages of MOF materials is their high surface area which stems from their porosity. Various studies attempted to impregnate co-catalysts into the pores of UiO MOFs, which are added along with the $ZrCl_4$ and organic linkers to be encapsulated. Xu presented a simple and efficient method for encapsulating Ru nanoparticles (NPs) in UiO-66 illustrated in Figure 1 . 15 a. By adding $RuCl_3$ along with $ZrCl_4$ and terephthalic acid, Ru can be deposited, reduced and aggregated during the synthesis procedures, and trapped within the porosity of UiO-66. From the HRTEM images, the size of Ru NPs shows a homogeneous distribution with an average diameter of 1.66 ± 0.24 nm (Figure 1 . 15 b-c), comparable to the size of 0.8 and 1.1 nm for tetrahedral and octahedral pores, respectively. Such comparable size of the Ru NPs is possible to be encapsulated into the pores of the UiO-66 framework, observed in the EDX mapping as shown in Figure 1 . 15 d-h[90].

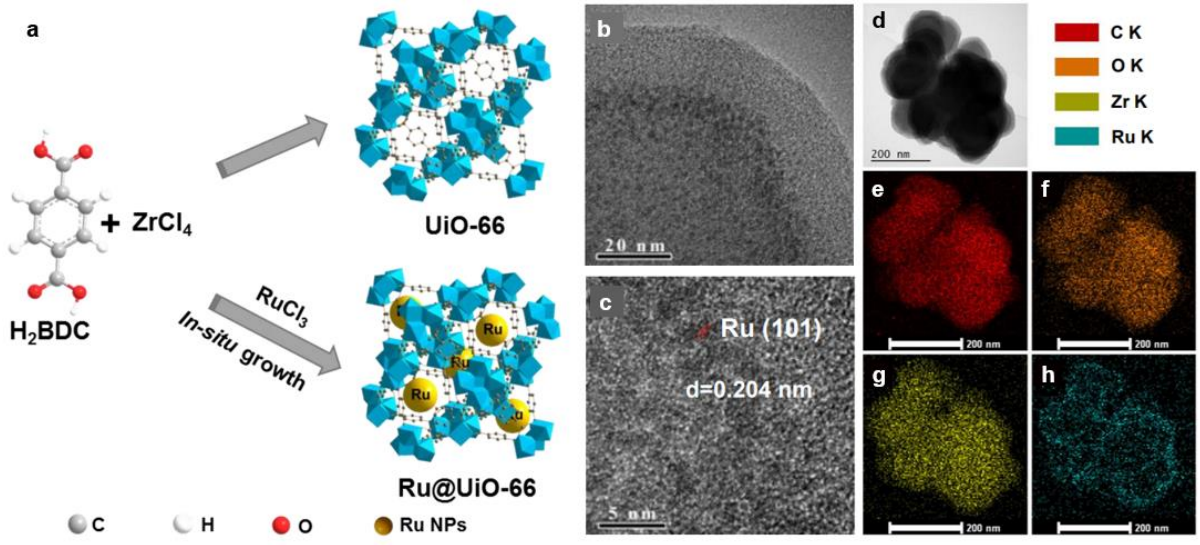


Figure 1 . 15 | (a) Schematic illustration for the synthesis of Ru nanoparticles encapsulated by the UiO-66 framework. (b,c) HRTEM images of Ru@UiO-66. (c) Size distribution of Ru NPs. (d) TEM image and its EDX mapping of (e) C, (f) O, (g) Zr, and (h) Ru. Figure reproduced from Ref [90].

It is also possible to encapsulate metal nanoparticles of larger sizes into MOFs. Zheng, has prepared a catalyst comprising an Au@Pd core-shell encapsulated in a UiO-66 centre for CO_2 hydrogenation. The authors controlled the size of the Au@Pd core-shell via the amount of polyvinylpyrrolidone (PVP) surfactant added, and were able to synthesized Au@Pd nanoparticles with an average size of 17.0 ± 1.1 nm. Via further PVP addition, a heterostructure of core-shell Au@Pd@UiO-66 (Au@Pd as core, UiO-66 as shell) can be synthesized without aggregation. In spite of the similar synthesis procedures with Xu and coworkers as discussed previously, the significantly larger size of the Au@Pd nanoparticles (17.0 nm) compared to the pores of UiO-66 (1 nm) lead to the direct synthesis of the UiO-66 framework on top of the Au@Pd nanoparticle is observed. Further Pt deposition onto the surface of the Au@Pd@UiO-66 has yielded the optimal catalysts Pt/Au@Pd@UiO-66, with a CO_2 conversion of 7.30 % at 300 °C for 4 hours with hourly space velocity of H_2:CO_2 3:1 gas of 24000 mL g^{-1} h^{-1}. The core-shell structure can be clearly seen in the HAADF-STEM, TEM images and their corresponding EDX elemental mapping in Figure 1 . 16. In this study, it is noted that the average size of the Au@Pd nanoparticles is much larger than the pore sizes of UiO-66, which is a possible explanation for the Au@Pd core – UiO-66 shell structure[91].

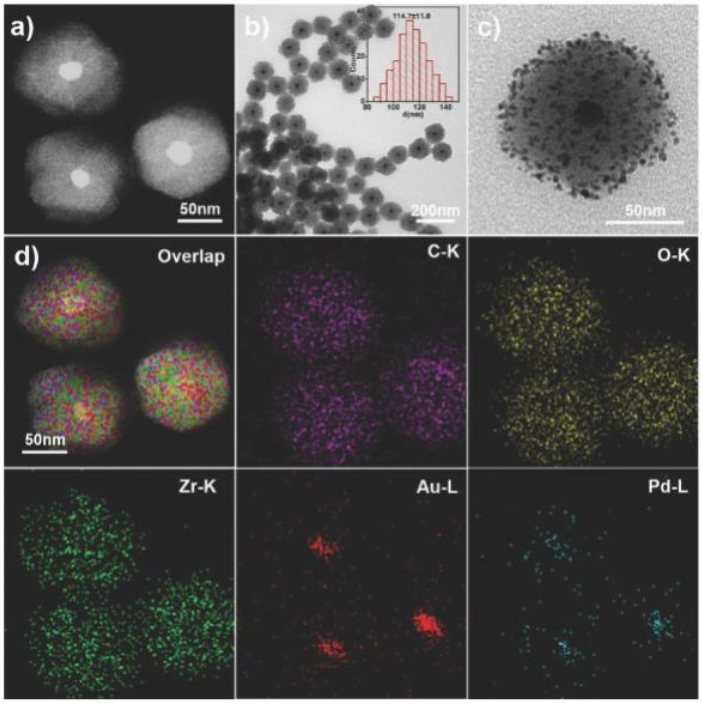


Figure 1 . 16 | TEM images of (a) Au@Pd@UiO-66, (b, c) Pt/Au@UiO-66, (d) EDX elemental mapping image of Au@Pd@UiO-66. © 2017 WILEY-VCH Verlag GmbH & Co. KGaA, Weinheim

Polyoxometalates (POMs) are soluble anionic metal oxide clusters of d-block transition metals in high oxidation states (typically W^{6+}, Mo^{6+} and V^{5+}), which exhibit remarkable redox or acid-base properties crucial to efficient catalysis. Encapsulation of $PW_{12}O_{40}^{3-}$ POMs with a diameter approximately equal to 12 Å into UiO-67, with a pore size of 12 and 16 Å was performed by Benseghir The $PW_{12}O_{40}^{3-}$ was added along with $ZrCl_4$ and BPDC linkers, and subsequently a RhCp* complex was introduced as part of a linker post-synthetic exchange (PSE), as represented schematically in Figure 1 . 17 a. Characterization by microscopy shows clearly the encapsulation of PW_{12} in the pores (Figure 1 . 17 b). The (PW_{12}, Cp*Rh)@UiO-67 catalysts showed photoreduction activity of CO_2 into formate and H_2 in the presence of TEOA as a sacrificial reagent, and that the photocatalytic activity is reduced in the absence of the POM or Cp*Rh[92].

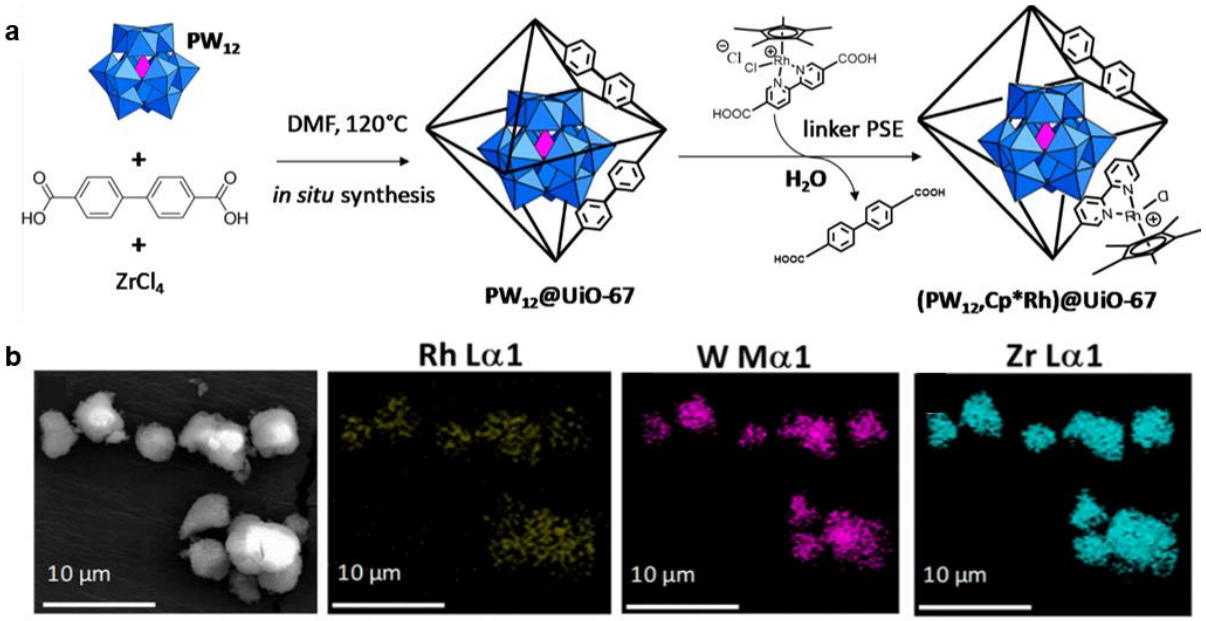


Figure 1 . 17 | (a) Schematic representation of the two-step encapsulation of PW12 POM into UiO-67, followed by the introduction of RhCp* complex via linker post-synthetic exchange. Colour scheme: Blue polyhedral = WO6, pink polyhedral = PO4. (b) SEM image of (PW12, Cp*Rh)@UiO-67 and the corresponding EDX mapping of Rh from Rh*Cp, W from POM and Zr from UiO-67. Figure reproduced from Ref [92]. Copyright © 2020, American Chemical Society

1.3.5 Enhancing the surface area

The high surface area of UiO-series MOFs (e.g. >1000 m^2 g^{-1} for UiO-66) is one of the reasons for its popular application as photocatalysts, as the adsorption of reactants is one of the crucial steps for efficient photocatalysts. It is generally understood that the surface areas of MOFs decreases upon incorporation of co-catalysts, either due to pore blockages or reduction in crystallinity of the MOF[93-96].

Nevertheless, Cao and coworkers have synthesized a composite material containing UiO-66 and graphene oxide (GO), with the graphene oxide added along with the $ZrCl_4$ and terephthalic acid and heated under 120 °C for 24 hours. Limited characterization of the UiO-66/GO composite using XRD and IR shows the retained crystal structure. Interestingly, an increase in

the BET surface area derived from CO_2 adsorption isotherms have been observed for the UiO-66/GO composite (1184 m^2 g^{-1}) compared to UiO-66 (838 m^2 g^{-1}) with limited explanation with respect to the structure of the composite given[97].

Additionally, in a recently published paper in 2023, Li reported a BiOCl/UiO-66 composite as photocatalysts for Cr^{6+} removal. In a one-pot synthesis similar to above, $Bi(NO_3)_2 \cdot 5H_2O$, $ZrCl_4$ and terephthalic acid are mixed together for the fabrication of BiOCl/UiO-66 composite. A significant increase in BET surface area can be observed for UiO-66 upon BiOCl decoration from 579 m^2 g^{-1} to 1530 m^2 g^{-1}. The authors have hypothesized that the much-increased surface area originates from the decreased pH value during synthesis, albeit with limited evidence[98]. The value for BET surface area reported in this work is lower than the expected. However, it is worth noting that the BET surface area for the same material reported using the same synthesis procedures can still vary significantly due to variance of algorithms in BET surface area from adsorption isotherms[99]. Nevertheless, the increase in value of BET surface area should still be reliable, assuming the same algorithm is used for the generation of BET surface area from the adsorption isotherms. To the best of my knowledge, the two papers discussed above are the only two papers to report an increase in BET surface area upon coupling of UiO-series MOF to other materials. More work will be needed to shed light on the chemistries underlying such increase in surface areas.

1.4 Aim of this thesis

The application of UiO-series MOFs towards photocatalysis has been thoroughly reviewed. The structure of UiO-66 MOF composed of Zr_6 inorganic units and terephthalic acid has gifted the MOF with exceptional chemical stability and tunability. The flexibility of the organic and inorganic building block allows structural engineering tailored for photocatalytic applications as reviewed previously, with strategies modifying the inorganic units and organic linker

directly, encapsulating co-catalysts into the MOF, and enhancing the surface area providing extra sites of adsorption. In my DPhil journey, it had been my aims to build on the previous works, to design, synthesise and characterize UiO-series MOFs for fuel-forming photocatalytic applications. Based on the chemical intuition I developed from undergraduate studies in Oxford, I would choose co-catalysts to be coupled with MOF materials, and go on to optimize the parameters for the corresponding catalysis reaction. Having identified a trend of catalytic reactivity, I would use various structural and optical characterization techniques to understand the changes induced by the incorporation of the co-catalysts. The improvement in catalytic activity can then be explained clearly via the structural and optical changes present in the catalysts. Density Functional Theory (DFT) simulations are sometimes used to exceed the limitation of experiments, for providing an explanation based on the interactions between the various potentials of elements present in the catalysts.

1.5 Thesis overview

Chapter 1 has introduced MOFs as a material, the use of highly charged Zr^{4+} as inorganic units along with phenyl rings-based organic linker to create UiO-series of MOFs. The structural advantages of UiO-series MOFs have been introduced with respect to the principles of fuel-forming photocatalysis. The various strategies for further enhancing the photocatalytic activity of UiO-series MOFs available in the literature have also been reviewed.

Chapter 2 will include the details of the synthesis procedures of all the catalysts along with catalytic testing procedures. It will also introduce the various characterization techniques that have been employed in this thesis. These includes structural characterization (XRD, XAS etc.), optical characterization (UV-Vis, PL etc.), and computer simulations (DFT calculations).

In the following 3 experimental chapters, **chapter 3** exploits the chemical stability and flexibility of UiO-series MOFs for the incorporation of Frustrated Lewis Pair-like active sites

for the photocatalytic heterolytic activation of H_2 activation. Using organic linker with bipyridine functionality, a well-known chromophore $Ru(bpy)_3^{2+}$ can be partly heterogenized onto the MOF system as Ru-deposited UiO-67-bpydc. Another Ru-deposited MOF with the amine functional group is also synthesized for comparison. The catalysts are structurally characterized via SXRD and XAS techniques, the charge transfer processes simulated by time-dependent density functional theory, and reactive intermediates upon the heterolytic cleavage of hydrogen molecules are clearly endorsed by FTIR and 2D NMR. This chapter concluded the importance of a bottom-up catalyst design approach to incorporate catalytic active sites into MOF materials.

In the second experimental chapter, **chapter 4** extends the ability of UiO-66-NH_2 acting as photocatalysts for CO_2 reduction by coupling with In_2S_3 semiconductor. The Lewis Acid-Base interactions between the amino group on the organic linker and the In_2S_3 species are evidenced by N 1s XPS and IR. A volcano trend can be observed towards the addition of In_2S_3 into UiO-66-NH_2, explained by the interplay between the efficient interface formation between the two species and the aggregation of In_2S_3 wrapping around the UiO-66-NH_2 particles. This chapter shed light on devising new synthesis methods for the design of interface between MOFs and co-catalysts for more efficient photocatalysts.

In the third experimental chapter, **chapter 5** explores the fundamental chemistries behind the increase in surface area of UiO-66-NH_2 upon CdS incorporation novel in the literature. Detailed characterizations such as XAS and XPS have been performed on the series of catalyst. Particularly, Rietveld refinement revealed the increase of dihedral angle of the organic linker upon CdS anchoring compared to virgin UiO-66-NH_2, indicating that the coordinated opening of organic linker has led to the increase in surface area. Moreover, DFT simulations revealed a similar observation driven by the charge transfer processes between UiO-66-NH_2 and the CdS

species. More importantly, it has been shown that this increase in surface area correlates well towards the rate of photocatalytic water splitting. This chapter provides an atomic understanding of the rotational dynamics in UiO-66-NH_2.

Chapter 6 concludes this thesis by summarizing the findings in the experimental chapters, and suggests future work on further engineering UiO-series of MOFs for fuel-forming photocatalysis.

1.6 References

1 Yoskamtorn, T., Zhao, P., Wu, X. P., Purchase, K., Orlandi, F., Manuel, P., Taylor, J., Li, Y., Day, S., Ye, L., Tang, C. C., Zhao, Y. & Tsang, S. C. E. Responses of Defect-Rich Zr-Based Metal-Organic Frameworks toward NH(3) Adsorption. J Am Chem Soc 143, 3205-3218 (2021).

2 Cui, W. G., Hu, T. L. & Bu, X. H. Metal-Organic Framework Materials for the Separation and Purification of Light Hydrocarbons. Adv Mater 32, e1806445 (2020).

3 Qiu, S., Xue, M. & Zhu, G. Metal-organic framework membranes: from synthesis to separation application. Chem Soc Rev 43, 6116-6140 (2014).

4 Xue, Q., Chan, K. H., Yim, C. K., Ng, B. K. Y., Chen, T., Day, S. J., Tang, C., Kawaguchi, S., Wong, K.-Y. & Lo, T. W. B. Guest-Anion-Induced Rotation-Restricted Emission in UiO-66-NH2 and Advanced Structure Elucidation. Chem Mater 33, 5422-5429 (2021).

5 Xue, Q., Ng, B. K. Y., Man, H. W., Wu, T. S., Soo, Y. L., Li, M. M., Kawaguchi, S., Wong, K. Y., Tsang, S. C. E., Huang, B. & Lo, T. W. B. Controlled synthesis of Bi- and tri-nuclear Cu-oxo nanoclusters on metal-organic frameworks and the structure-reactivity correlations. Chem Sci 13, 50-58 (2021).

6 Niu, Z., Bhagya Gunatilleke, W. D. C., Sun, Q., Lan, P. C., Perman, J., Ma, J.-G., Cheng, Y., Aguila, B. & Ma, S. Metal-Organic Framework Anchored with a Lewis Pair as a New Paradigm for Catalysis. Chem 4, 2587-2599 (2018).

7 Zhu, B., Zou, R. & Xu, Q. Metal–Organic Framework Based Catalysts for Hydrogen Evolution. Adv Energy Mater 8 (2018).

8 Hoskins, B. F. & Robson, R. Infinite polymeric frameworks consisting of three dimensionally linked rod-like segmants. J Am Chem Soc 111, 5962-5964 (1989).

9 Yaghi, O. & Li, H. Hydrothermal Synthesis of a Metal-Organic Framework Containing Large Rectangular Channels. J Am Chem Soc 117, 10401-10402 (1995).

10 Chui, S. S.-Y., Lo, S. M.-F., H., C. J. P., Orpen, A. G. & Williams, I. D. A Chemically Functionalizable Nanoporous Material [Cu3(TMA)2(H2O)3]n. Science 283, 1148-1150 (1999).

11 Yaghi, O., O'Keeffe, M., Ockwig, N. W., Chae, H. K., Eddaoudi, M. & Kim, J. Reticular Synthesis and the Design of New Materials. Nature 423, 705-714 (2003).

12 Katz, M. J., Brown, Z. J., Colon, Y. J., Siu, P. W., Scheidt, K. A., Snurr, R. Q., Hupp, J. T. & Farha, O. K. A facile synthesis of UiO-66, UiO-67 and their derivatives. Chem Commun (Camb) 49, 9449-9451 (2013).

13 Zhao, P., Lampronti, G. I., Lloyd, G. O., Suard, E. & Redfern, S. A. T. Direct visualisation of carbon dioxide adsorption in gate-opening zeolitic imidazolate framework ZIF-7. J. Mater. Chem. A 2, 620-623 (2014).

14 Macreadie, L. K., Idrees, K. B., Smoljan, C. S. & Farha, O. K. Expanding Linker Dimensionality in Metal-organic Frameworks for sub-Angstrom Pore Control for Separation Applications. Angew Chem Int Ed Engl 62, e202304094 (2023).

15 Cavka, J. H., Jakobsen, S., Olsbye, U., Guillou, N., Lamberti, C., Bordiga, S. & Lillerud, K. P. A new zirconium inorganic building brick forming metal organic frameworks with exceptional stability. J Am Chem Soc 130, 13850-13851 (2008).

16 Tranchemontagne, D. J., Mendoza-Cortes, J. L., O'Keeffe, M. & Yaghi, O. M. Secondary building units, nets and bonding in the chemistry of metal-organic frameworks. Chem Soc Rev 38, 1257-1283 (2009).

17 O'Keeffe, M., Peskov, M. A., Ramsden, S. J. & Yaghi, O. The Reticular Chemistry Structure Resource (RCSR) Database of, and Symbols for, Crystal Nets. Accounts of chemical Research 41, 1782-1789 (2008).

18 Cliffe, M. J., Wan, W., Zou, X., Chater, P. A., Kleppe, A. K., Tucker, M. G., Wilhelm, H., Funnell, N. P., Coudert, F. X. & Goodwin, A. L. Correlated defect nanoregions in a metal-organic framework. Nat Commun 5, 4176 (2014).

19 Ren, J., Langmi, H. W., North, B. C., Mathe, M. & Bessarabov, D. Modulated synthesis of zirconium-metal organic framework (Zr-MOF) for hydrogen storage applications. International Journal of Hydrogen Energy 39, 890-895 (2014).

20 Winarta, J., Shan, B., McIntyre, S. M., Ye, L., Wang, C., Liu, J. & Mu, B. A Decade of UiO-66 Research: A Historic Review of Dynamic Structure, Synthesis Mechanisms, and Characterization Techniques of an Archetypal Metal–Organic Framework. Crystal Growth & Design 20, 1347-1362 (2019).

21 Cavka, J. H., Jakobsen, S., Olsbye, U., Guillou, N., Lamberti, C., Bordiga, S. & Lillerud, K. P. A New Zirconium Inorganic Building Brick Forming Metal Organic Frameworks with Exceptional Stability J Am Chem Soc 130, 13850-13851 (2008).

22 Kandiah, M., Nilsen, M. H., Usseglio, S., Jakobsen, S., Olsbye, U., Tilset, M., Larabi, C., Quadrelli, E. A., Bonino, F. & Lillerud, K. P. Synthesis and Stability of Tagged UiO-66 Zr-MOFs. Chem Mater 22, 6632-6640 (2010).

23 Garibay, S. J. & Cohen, S. M. Isoreticular synthesis and modification of frameworks with the UiO-66 topology. Chem Commun 46, 7700-7702 (2010).

24 Zhao, W., Zhang, C., Yan, Z., Zhou, Y., Li, J., Xie, Y., Bai, L., Jiang, L. & Li, F. Preparation, characterization, and performance evaluation of UiO-66 analogues as stationary phase in HPLC for the separation of substituted benzenes and polycyclic aromatic hydrocarbons. PLoS One 12, e0178513 (2017).

25 Hattori, H. Heterogeneous Basic Catalysis. Chem Rev 95, 537-558 (1995).

26 N., A. J. Environmental Catalysis. Appl Catal B-Environ 1, 221-256 (1992).

27 Haber, F. The Synthesis of Ammonia from its Elements. Nobel Lecture (1920).

28 Bell, A. T. The Impact of Nanoscience on Heterogeneous Catalysis. Science 299, 1688-1691 (2003).

29 Astruc, D., Lu, F. & Aranzaes, J. R. Nanoparticles as Recyclable Catalysts: The Frontier between Homogeneous and Heterogeneous Catalysis. Angew Chem Int Ed 44, 7852-7872 (2005).

30 Sheldon, R. A. & Downing, R. S. Heterogeneous Catalytic Transformations for Environmentally Friendly Production. Appl Catal A Gen 189, 163-183 (1999).

31 Christopther, P. & Linic, S. Engineering Selectivity in Heterogeneous Catalysis: Ag Nanowires as Selective Ethylene Epoxidation Catalysis. J Am Chem Soc 130, 11264-11265 (2008).

32 Zhang, L., Zhang, J., Yu, H. & Yu, J. Emerging S-Scheme Photocatalyst. Adv Mater 34, 2107668 (2022).

33 Chen, S., Hu, Y., Meng, S. & Fu, X. Study on the separation mechanisms of photogenerated electrons and holes for composite photocatalysts g-C3N4-WO3. Appl Catal B-Environ 150-151, 564-573 (2014).

34 Xiao, M., Wang, Z., Luo, B., Wang, S. & Wang, L. Enhancing Photocatalytic activity of tantalum nitride by Rational Suppression of Bulk, Interface and Surface Charge Recombination. Appl Catal B-Environ 246, 195-201 (2019).

35 Li, A., Chang, X., Huang, Z., Li, C. M., Wei, Y., Zhang, L., Wang, T. & Gong, J. Thin Heterojunctions and Spatially Separated Cocatalysts to Simultaneous Reduce Bulk and Surface Recombination in Photocatalysts. Angew Chem 128, 13938-13942 (2016).

36 Chen, F., Ma, T., Zhang, T., Zhang, Y. & Huang, H. Atomic-Level Charge Separation Strategies in Semiconductor-Based Photocatalysts. Adv Mater 33, 2005256 (2021).

37 Chen, R., Pang, S., An, H., Zhu, J., Ye, S., Gao, Y., Fan, F. & Li, C. Charge Separation via Asymmetric Illumination in Photocatalytic Cu2O Particles. Nature Energy 3, 655-663 (2018).

38 Kubacka, A., Fernandez-Garcia, M. & Colon, G. Advanced Nanoarchitectures for Solar Photocatalytic Applications. Chem Rev 112, 1555-1614 (2011).

39 Yu, H., Irie, H. & Hashimoto, K. Conduction Band Energy Level Control of Titanium Dioxide: Toward an Efficient Visible-Light-Sensitive Photocatalyst. J Am Chem Soc 132, 6896-6899 (2010).

40 Navarro, R. M., Pena, M. A. & Fierro, J. L. G. Hydrogen Production Reactions from Carbon Feedstocks: Fossil Fuels and Biomass. Chem Rev 107, 3952-3991 (2007).

41 Mazloomi, K. & Gomes, C. Hydrogen as an energy carrier: Prospects and challenges. Renew Sustain Energy Rev 16, 3024-3033 (2012).

42 Midilli, A., Ay, M., Dincer, I. & Rosen, M. A. On hydrogen and hydrogen energy strategies I: current status and needs. Renew Sustain Energy Rev 9, 255-271 (2005).

43 Agency, I. E. Global Hydrogen Review 2022. (2022).

44 Fujishima, A. & Honda, K. Electrochemical Photolysis of Water at a Semiconductor Electrode. Nature 238, 37-38 (1972).

45 Wang, Q. & Domen, K. Particulate Photocatalysts for Light-Driven Water Splitting: Mechanisms, Challenges, and Design Strategies. Chem Rev 120, 919-985 (2020).

46 Takata, T., Jiang, J., Sakata, Y., Nakabayashi, M., Shibata, N., Nandal, V., Sekl, K., Hisatomi, T. & Domen, K. Photocatalytic water splitting with a quantum efficiency of almost unity. Nature 581, 411-414 (2019).

47 Ran, J., Zhang, J., Yu, J., Jaroniec, M. & Qiao, S. Z. Earth-abundant cocatalysts for semiconductor based photocatalytic water splitting. Chem Soc Rev 43, 7787-7812 (2014).

48 Fajrina, N. & Tahir, M. A critical review in strategies to improve photocatalytic water splitting towards hydrogen production. Int J Hydrogen Energy 44, 540-577 (2019).

49 Ni, M., Leung, M. K. H., Leung, D. Y. C. & Sumathy, K. A review and recent developments in photocatalytic water-splitting using TiO2 for hydrogen production. Renew Sustain Energy Rev 11, 401-425 (2007).

50 Kudo, A. & Miseki, Y. Heterogeneous photocatalyst materials for water splitting. Chem Soc Rev 38, 253-278 (2009).

51 Sabatier, P. & Senderens, J. Action of Nickel on Ethylene. Ethane Synthesis. C. R. Hebd. Seances Acad. Sci. 124, 1358 (1897).

52 Fouilloux, P. The Nature of Raney Nickel, its Adsorbed Hydrogen and its Catalytic Activity for Hydrogenation Reactions. Applied Catalysis 8, 1-42 (1983).

53 Wu, S., Tseng, K. Y., Kato, R., Wu, T. S., Large, A., Peng, Y. K., Xiang, W., Fang, H., Mo, J., Wilkinson, I., Soo, Y. L., Held, G., Suenaga, K., Li, T., Chen, H. T. & Tsang, S. C. E. Rapid Interchangeable Hydrogen, Hydride, and Proton Species at the Interface of Transition Metal Atom on Oxide Surface. J Am Chem Soc 143, 9105-9112 (2021).

54 Ember. Global Electricity Review 2022. (2022).

55 Nelson, N. C. & Szanyi, J. Heterolytic Hydrogen Activation: Understanding Support Effects in Water–Gas Shift, Hydrodeoxygenation, and CO Oxidation Catalysis. ACS Catalysis 10, 5663-5671 (2020).

56 Welch, G. C., Juan, R. R. S., Masuda, J. D. & Stephan, D. W. Reversible, Metal-Free Hydrogen Activation. Science 314, 1124-1126 (2006).

57 Lu, G., Zhang, P., Sun, D., Wang, L., Zhou, K., Wang, Z.-X. & Guo, G.-C. Gold catalyzed hydrogenations of small imines and nitriles: enhanced reactivity of Au surface toward H2via collaboration with a Lewis base. Chem. Sci. 5, 1082-1090 (2014).

58 Liang, X., Wang, X., Zhang, X., Lin, S., Ji, M. & Wang, M. Frustrated Lewis Pairs on In(OH)3–x Facilitate Photocatalytic CO2 Reduction. ACS Catal. 13, 6214-6221 (2023).

59 Mahdi, T. & Stephan, D. W. Enabling catalytic ketone hydrogenation by frustrated Lewis pairs. J Am Chem Soc 136, 15809-15812 (2014).

60 Scott, D. J., Simmons, T. R., Lawrence, E. J., Wildgoose, G. G., Fuchter, M. J. & Ashley, A. E. Facile Protocol for Water-Tolerant "Frustrated Lewis Pair"-Catalyzed Hydrogenation. ACS Catal 5, 5540-5544 (2015).

61 Li, S., Li, G., Meng, W. & Du, H. A Frustrated Lewis Pair Catalyzed Asymmetric Transfer Hydrogenation of Imines Using Ammonia Borane. J Am Chem Soc 138, 12956-12962 (2016).

62 Xie, Y., Chen, J., Wu, X., Wen, J., Zhao, R., Li, Z., Tian, G., Zhang, Q., Ning, P. & Hao, J. Frustrated Lewis Pairs Boosting Low-Temperature CO2 Methanation Performance over Ni/CeO2 Nanocatalysts. ACS Catalysis 12, 10587-10602 (2022).

63 Corma, A., Garcia, H. & Llabres i Xamena, F. X. Engineering Metal Organic Frameworks for Heterogeneous Catalysis. Chem. Rev. 110, 4606-4655 (2010).

64 Weckhuysen, B. M. & Yu, J. Recent advances in zeolite chemistry and catalysis. Chem Soc Rev 44, 7022-7024 (2015).

65 Leung, K. C., Hong, S., Li, G., Xing, Y., Ng, B. K. Y., Ho, P.-L., Ye, D., Zhao, P., Tan, E., Safonova, O. V., Wu, T. S., Li, M. M. J., Mpourmpakis, G. & Tsang, S. C. E. Confined Ru Sites in a 13X Zeolite for Ultrahigh H2 Production from NH3 decomposition. J Am Chem Soc 145, 14548-14561 (2023).

66 Leung, K. C., Tan, E., Li, G., Ng, B. K. Y., Ho, P.-L., Lebedev, K. & Tsang, S. C. E. Metal-loaded zeolites in ammonia decomposition catalysis. Faraday Discuss. 243, 520-548 (2023).

67 Sun, Q., Wang, N. & Yu, J. Advances in Catalytic Applications of Zeolite-Supported Metal Catalysts. Adv Mater 33, 2104442 (2021).

68 Llabresixamena, F., Abad, A., Corma, A. & Garcia, H. MOFs as catalysts: Activity, reusability and shape-selectivity of a Pd-containing MOF. Journal of Catalysis 250, 294-298 (2007).

69 Llabres i Xamena, F. X., Corma, A. & Garcia, H. Applications for Metal-Organic Frameworks (MOFs) as Quantum Dot Semiconductors. J Phys Chem C 111, 80-85 (2007).

70 Eddaoudi, M., Kim, J., Rosi, N., Vodak, D., Wachter, J., O'Keeffe, M. & Yaghi, O. M. Systematic Design of Pore Size and Functionality in Isoreticular MOFs and Their Application in Methane Storage. Science 295, 469-472 (2002).

71 Wang, S. & Wang, X. Multifunctional Metal-Organic Frameworks for Photocatalysis. Small 11, 3097-3112 (2015).

72 Alvaro, M., Carbonell, E., Ferrer, B., Xamena, F. X. L. I. & Garcia, H. Semiconductor behavior of a metal-organic framework (MOF). Chem-Eur J 13, 5106-5112 (2007).

73 Alaerts, L., Seguin, E., Poelman, H., Thibault-Starzyk, F., Jacobs, P. A. & De Vos, D. E. Probing the Lewis acidity and catalytic activity of the metal-organic framework [Cu3(btc)2] (BTC=benzene-1,3,5-tricarboxylate). Chemistry 12, 7353-7363 (2006).

74 Wang, C., deKrafft, K. E. & Lin, W. Pt nanoparticles@photoactive metal-organic frameworks: efficient hydrogen evolution via synergistic photoexcitation and electron injection. J Am Chem Soc 134, 7211-7214 (2012).

75 Gomes Silva, C., Luz, I., Llabres i Xamena, F. X., Corma, A. & Garcia, H. Water stable Zr-benzenedicarboxylate metal-organic frameworks as photocatalysts for hydrogen generation. Chemistry 16, 11133-11138 (2010).

76 Wang, G., He, C. T., Huang, R., Mao, J., Wang, D. & Li, Y. Photoinduction of Cu Single Atoms Decorated on UiO-66-NH(2) for Enhanced Photocatalytic Reduction of CO(2) to Liquid Fuels. J Am Chem Soc 142, 19339-19345 (2020).

77 Su, Y., Zhang, Z., Liu, H. & Wang, Y. Cd0.2Zn0.8S@UiO-66-NH2 nanocomposites as efficient and stable visible-light-driven photocatalyst for H2 evolution and CO2 reduction. Applied Catalysis B: Environmental 200, 448-457 (2017).

78 Yao, N., Jia, H., Zhu, J., Shi, Z., Cong, H., Ge, J. & Luo, W. Atomically dispersed Ru oxide catalyst with lattice oxygen participation for efficient acidic water oxidation. Chem 9, 1882-1896 (2023).

79 Gutterod, E. S., Lazzarini, A., Fjermestad, T., Kaur, G., Manzoli, M., Bordiga, S., Svelle, S., Lillerud, K. P., Skulason, E., Oien-Odegaard, S., Nova, A. & Olsbye, U. Hydrogenation of CO(2) to Methanol by Pt Nanoparticles Encapsulated in UiO-67: Deciphering the Role of the Metal-Organic Framework. J Am Chem Soc 142, 999-1009 (2020).

80 Zeng, L., Wang, Z., Wang, Y., Wang, J., Guo, Y., Hu, H., He, X., Wang, C. & Lin, W. Photoactivation of Cu Centers in Metal-Organic Frameworks for Selective CO(2) Conversion to Ethanol. J Am Chem Soc 142, 75-79 (2020).

81 Gómez-Avilés, A., Solís, R. R., García-Frutos, E. M., Bedia, J. & Belver, C. Novel isoreticular UiO-66-NH2 frameworks by N-cycloalkyl functionalization of the 2-aminoterephtalate linker with enhanced solar photocatalytic degradation of acetaminophen. Chemical Engineering Journal 461 (2023).

82 Mao, S., Zou, Y., Sun, G., Zeng, L., Wang, Z., Ma, D., Guo, Y., Cheng, Y., Wang, C. & Shi, J. W. Thio linkage between CdS quantum dots and UiO-66-type MOFs as an effective transfer bridge of charge carriers boosting visible-light-driven photocatalytic hydrogen production. J Colloid Interface Sci 581, 1-10 (2021).

83 Valenzano, L., Civalleri, B., Chavan, S., Bordiga, S., Nilsen, M. H., Jakobsen, S., Lillerud, K. P. & Lamberti, C. Disclosing the Complex Structure of UiO-66 Metal Organic Framework: A Synergic Combination of Experiment and Theory. Chemistry of Materials 23, 1700-1718 (2011).

84 Wu, H., Chua, Y. S., Krungleviciute, V., Tyagi, M., Chen, P., Yildirim, T. & Zhou, W. Unusual and highly tunable missing-linker defects in zirconium metal-organic framework UiO-66 and their important effects on gas adsorption. J Am Chem Soc 135, 10525-10532 (2013).

85 Abdel-Mageed, A. M., Rungtaweevoranit, B., Parlinska-Wojtan, M., Pei, X., Yaghi, O. M. & Behm, R. J. Highly Active and Stable Single-Atom Cu Catalysts Supported by a Metal-Organic Framework. J Am Chem Soc 141, 5201-5210 (2019).

86 Zhu, Y., Zheng, J., Ye, J., Cui, Y., Koh, K., Kovarik, L., Camaioni, D. M., Fulton, J. L., Truhlar, D. G., Neurock, M., Cramer, C. J., Gutierrez, O. Y. & Lercher, J. A. Copper-zirconia interfaces in UiO-66 enable selective catalytic hydrogenation of CO2 to methanol. Nat Commun 11, 5849 (2020).

87 Wu, X. P., Gagliardi, L. & Truhlar, D. G. Cerium Metal-Organic Framework for Photocatalysis. J Am Chem Soc 140, 7904-7912 (2018).

88 Melillo, A., Cabrero-Antonino, M., Navalón, S., Álvaro, M., Ferrer, B. & García, H. Enhancing visible-light photocatalytic activity for overall water splitting in UiO-66 by controlling metal node composition. Applied Catalysis B: Environmental 278 (2020).

89 Santaclara, J. G., Olivos-Suarez, A. I., Gonzalez-Nelson, A., Osadchii, D., Nasalevich, M. A., van der Veen, M. A., Kapteijn, F., Sheveleva, A. M., Veber, S. L., Fedin, M. V., Murray, A. T., Hendon, C. H., Walsh, A. & Gascon, J. Revisiting the Incorporation of Ti(IV) in UiO-type Metal–Organic Frameworks: Metal Exchange versus Grafting and Their Implications on Photocatalysis. Chemistry of Materials 29, 8963-8967 (2017).

90 Feiyan Xu, K. M., Bicheng Zhu, Huibiao Liu, Jingsan Xu, and Jiaguo Yu. Graphdiyne: A New Photocatalytic CO2 Reduction Cocatalyst. Advanced Functional Materials 29, 1904256 (2019).

91 Zheng, Z., Xu, H., Xu, Z. & Ge, J. A Monodispersed Spherical Zr-Based Metal-Organic Framework Catalyst, Pt/Au@Pd@UIO-66, Comprising an Au@Pd Core-Shell Encapsulated in a UIO-66 Center and Its Highly Selective CO(2) Hydrogenation to Produce CO. Small 14 (2018).

92 Benseghir, Y., Lemarchand, A., Duguet, M., Mialane, P., Gomez-Mingot, M., Roch-Marchal, C., Pino, T., Ha-Thi, M. H., Haouas, M., Fontecave, M., Dolbecq, A., Sassoye, C. & Mellot-Draznieks, C. Co-immobilization of a Rh Catalyst and a Keggin Polyoxometalate in the UiO-67 Zr-Based Metal-Organic Framework: In Depth Structural Characterization and Photocatalytic Properties for CO(2) Reduction. J Am Chem Soc 142, 9428-9438 (2020).

93 Li, G., Yoskamtorn, T., Chen, W., Foo, C., Zheng, J., Tang, C., Day, S., Zheng, A., Li, M. M. & Tsang, S. C. E. Thermal Alteration in Adsorption Sites over SAPO-34 Zeolite. Angew Chem Int Ed Engl 61, e202204500 (2022).

94 Molavi, H., Eskandari, A., Shojaei, A. & Mousavi, S. A. Enhancing CO2/N2 adsorption selectivity via post-synthetic modification of NH2-UiO-66(Zr). Microporous and Mesoporous Materials 257, 193-201 (2018).

95 Wang, R., Wan, J., Jia, J., Xue, W., Hu, X., Liu, E. & Fan, J. Synthesis of In2Se3 homojunction photocatalyst with α and γ phases for efficient photocatalytic performance. Materials & Design 151, 74-82 (2018).

96 Liu, T., Gu, A., Wei, T., Chen, M., Guo, X., Tang, S., Yuan, Y. & Wang, N. Ligand-Assistant Iced Photocatalytic Reduction to Synthesize Atomically Dispersed Cu Implanted Metal-Organic Frameworks for Photo-Enhanced Uranium Extraction from Seawater. Small 19, e2208002 (2023).

97 Cao, Y., Zhao, Y., Lv, Z., Song, F. & Zhong, Q. Preparation and enhanced CO2 adsorption capacity of UiO-66/graphene oxide composites. Journal of Industrial and Engineering Chemistry 27, 102-107 (2015).

98 Li, X., Almatrafi, E., Wang, H., Liu, X., Yang, Y., Zhou, C., Tang, X., Ren, X., Yin, L., Zeng, G. & Wang, D. Novel synthesis strategy for Z-scheme BiOCl/UiO-66 photocatalyst: Enhanced surface area and improved Cr(VI) removal efficiency. Chemical Engineering Journal 457 (2023).

99 Osterrieth, J. W. M., Rampersad, J., Madden, D., Rampal, N., Skoric, L., Connolly, B., Allendorf, M. D., Stavila, V., Snider, J. L., Ameloot, R., Marreiros, J., Ania, C., Azevedo, D., Vilarrasa-Garcia, E., Santos, B. F., Bu, X. H., Chang, Z., Bunzen, H., Champness, N. R., Griffin, S. L., Chen, B., Lin, R. B., Coasne, B., Cohen, S., Moreton, J. C., Colon, Y. J., Chen, L., Clowes, R., Coudert, F. X., Cui, Y., Hou, B., D'Alessandro, D. M., Doheny, P. W., Dinca, M., Sun, C., Doonan, C., Huxley, M. T., Evans, J. D., Falcaro, P., Ricco, R., Farha, O., Idrees, K. B., Islamoglu, T., Feng, P., Yang, H., Forgan, R. S., Bara, D., Furukawa, S., Sanchez, E., Gascon, J., Telalovic, S., Ghosh, S. K., Mukherjee, S., Hill, M. R., Sadiq, M. M., Horcajada,

P., Salcedo-Abraira, P., Kaneko, K., Kukobat, R., Kenvin, J., Keskin, S., Kitagawa, S., Otake, K. I., Lively, R. P., DeWitt, S. J. A., Llewellyn, P., Lotsch, B. V., Emmerling, S. T., Putz, A. M., Marti-Gastaldo, C., Padial, N. M., Garcia-Martinez, J., Linares, N., Maspoch, D., Suarez Del Pino, J. A., Moghadam, P., Oktavian, R., Morris, R. E., Wheatley, P. S., Navarro, J., Petit, C., Danaci, D., Rosseinsky, M. J., Katsoulidis, A. P., Schroder, M., Han, X., Yang, S., Serre, C., Mouchaham, G., Sholl, D. S., Thyagarajan, R., Siderius, D., Snurr, R. Q., Goncalves, R. B., Telfer, S., Lee, S. J., Ting, V. P., Rowlandson, J. L., Uemura, T., Iiyuka, T., van der Veen, M. A., Rega, D., Van Speybroeck, V., Rogge, S. M. J., Lamaire, A., Walton, K. S., Bingel, L. W., Wuttke, S., Andreo, J., Yaghi, O., Zhang, B., Yavuz, C. T., Nguyen, T. S., Zamora, F., Montoro, C., Zhou, H., Kirchon, A. & Fairen-Jimenez, D. How Reproducible are Surface Areas Calculated from the BET Equation? Adv Mater 34, e2201502 (2022).

2 Chapter 2 | Experimental Methods

2.1 Chemicals

All chemicals were obtained from commercial sources and used as received. $ZrCl_4$ (Alfa Aesar, 98 %, cont. 1-2 % hafnium (IV) chloride), 2,2'-Bipyridine-5,5'-dicarboxylic acid (Sigma-Aldrich, 97 %), 2-aminoterephthalic acid (Merck, 99 %), Ruthenium (III) chloride hydrate (Merck, 99.98 %), Cadmium (II) nitrate hydrate (≥9 9%), Indium (III) nitrate hydrate (99.99 %), thioacetamide (98 %), acetonitrile (99.9 %), triethanolamine (Sigma Aldridge, 98 %)

2.2 Synthesis of catalysts

2.2.1 Synthesis of UiO-67-bpydc

In a 20 mL scintillation vial, 0.150 mmol of $ZrCl_4$, 0.138 mmol of 2,2-bipyridine-5,5'-dicarboxylic acid, 0.7 mL of ethanoic acid were added into 10 mL of DMF. The reaction mixture was sonicated for 10 minutes, and then heated in an oven at 120°C for 24 hours. The formed UiO-67-bpydc powder was collected by centrifugation at 5000 rpm for 5 minutes, washed by DMF for 3 times. Subsequently, the synthesized UiO-67-bpydc is soaked in ethanol for 24 hours to exchange all the DMF solvent present within the sample, with the ethanol exchanged 3 times. The products were then dried overnight in a vacuum oven at 80°C.

2.2.2 Synthesis of UiO-66-NH_2

UiO-66-NH_2 was synthesised based on the method reported by Cavka.[1] In a 20 mL scintillation vial, 0.150 mmol of $ZrCl_4$ and 0.138 mmol of 2-aminoterephthalic acid, 0.7 mL of ethanoic acid were added into 10 mL of DMF. The reaction mixture was sonicated for 10 minutes, and then heated in an oven at 120 °C for 24 hours. The formed UiO-66-NH_2 powder was collected by centrifugation at 5000 rpm for 5 minutes, washed by DMF for 3 times. Subsequently, the synthesized UiO-66-NH_2 is soaked in ethanol for 24 hours to exchange all the DMF solvent

present within the sample, with the ethanol exchanged 3 times. The products were then dried overnight in a vacuum oven at 80°C.

2.2.3 Synthesis of Ru/UiO-67-bpydc (Ru/bpy)

200 mg of dried UiO-67-bpydc was put into activation at 120°C overnight, then added into 20 mL of ethanol. 107.6 mg of $RuCl_3$ was added to the UiO-67-bpydc mixture under stirring at room temperature for 24 hours. The product was collected by centrifugation at 5000 rpm for 5 minutes, washed with ethanol for 3 times. The products were dried overnight in a vacuum oven at 80 °C.

2.2.4 Synthesis of Ru/UiO-66-NH_2 (Ru/NH_2)

200 mg of dried UiO-66-NH_2 was put into activation at 120°C overnight, then added into 20 mL of ethanol. 123.9 mg of $RuCl_3$ was then added into the UiO-66-NH_2 mixture under stirring at room temperature for 24 hours. The product was collected by centrifugation at 5000 rpm for 5 minutes, washed with ethanol for 3 times. The products were dried overnight in a vacuum oven at 80 °C.

2.2.5 Synthesis of In_2S_3/UiO-66-NH_2

200 mg of UiO-66-NH_2 was suspended in 20 mL of deionized (DI) water and sonicated for 30 minutes. Some amount of indium (III) nitrate hydrate according to Table 2 . 1 below was dissolved in 15 mL of DI water and added dropwise to the UiO-66-NH_2 suspension. Some other amount of TAA was dissolved in 10 mL of DI water before being added to the mixture dropwise. The solution was then heated for 3 hours at 60 °C in an oil bath before being cooled to room temperature. The resultant mixture was centrifuged at 5000 rpm for 5 minutes and washed sequentially three times with methanol and three times with DI water before being dried in a vacuum oven at 60 °C for 24 hours.

Catalysts	In-1	In-2	In-3	In-4	In-5
Mass of $In(NO_3)_3 \cdot xH_2O$ (mg)	250	500	750	2250	6750
Mass of TAA (mg)	23.58	47.16	70.74	212.22	636.66

Table 2 . 1 | Mass of indium nitrate hydrate and thioacetamide added in the synthesis procedures for In_2S_3/UiO-66-NH_2

2.2.6 Synthesis of CdS/UiO-66-NH_2

480 mg of UiO-66-NH_2 was suspended in 25 mL of Di water and stirred for 30 minutes. 1.744 g of $Cd(NO_3)_2 \bullet 4H_2O$ was dissolved separately in 15 mL of DI water and then added dropwise to the UiO-66-NH_2 suspension. A varying amount according to Table 2 . 2 below was dissolved in 10 mL of DI water and added dropwise to the mixture.

Catalysts	0.1Cd	0.2Cd	1.8Cd	2.3Cd
Mass of TAA (mg)	0	21.2	169.9	339.7

Table 2 . 2 | Mass of thioacetamide added in the synthesis procedures for CdS/UiO-66-NH_2

2.3 Catalytic activity measurement

The fuel-forming photocatalysis investigated in this thesis was conducted with a Sciencetech LH-S-300X Xe arc lamp, with a power output of 300 W and spectral distribution ranging from 250-2500 nm. All catalytic reactions were carried out in a 25 mL stainless steel batch reactor by Parr, equipped with two quartz windows with an illuminated area of 0.785 cm^2 which are

10 mm in diameter and 18 mm in thickness. The batch reactor is equipped with a thermocouple, capable of heating up to 300 °C.

2.3.1 Chapter 3 – Hydrogen-Deuterium Exchange

25mg of catalyst and a magnetic stirrer bar were added into a glass vial, subsequently into the Parr autoclave introduced above with magnetic stirring at 500 rpm. Prior to photocatalysis, the autoclave will be purged by 4 bar H_2 for 6 times to remove any residual air present, and 2 bar H_2 followed by another 2 bar of D_2 would be added. The autoclave would be allowed to heat to the desired temperature (50-100 °C). The light would then be switched on for light-on experments for 1.5 hours. Upon cool down, the autoclave was connected to the quadrupole mass spectrometer (QMS) for the quantitative determination of H_2, HD and D_2 present. Catalytic testing at each temperature is repeated for 3 times to minimize random error, and the standard deviation of the three tests were plotted as error bars.

2.3.2 Chapter 4 – CO_2 reduction

20 mg of catalyst will be dispersed in 10 mL of acetonitrile in a glass specimen tube of 25 mm diameter and 50 mm height. The mixture was sonicated for 10 minutes, then placed in the Parr autoclave introduced above. Prior to photocatalysis, the autoclave will be purged by 6 bar of 3:1 ratio of H_2:CO_2 for 8 times to remove any residual air dissolved in the solution. Afterwards the autoclave will be heated to 180 °C with magnetic stirring at 500 rpm. Upon reaching 180 °C, the lamp would be turned on for 2 hours. Upon cool down, the contents in the autoclave would be injected into the GC with hydrogen as the carrier gas coupled with FID detector. Catalytic testing at each temperature is repeated for 3 times to minimize random error, and the standard deviation of the three tests were plotted as error bars.

2.3.3 Chapter 5 – Water splitting

25 mg of catalyst and a magnetic stirrer bar were added into a glass specimen tube of 25 mm diameter and 50 mm height, along with 7.2 mL of DI water and 0.8 mL of TEOA, with the addition of TEOA as a sacrificial reagent according to the method by Zhang[2]. Upon sonication for 10 minutes, the glass vial would subsequently be put into the Parr autoclave introduced above. Prior to photocatalysis, the autoclave will be purged by 6 bar Ar for 6 times to remove any residual air dissolved in the solution. Afterwards the autoclave will be heated to 120 °C with magnetic stirring at 500 rpm. Upon reaching 120 °C, the lamp would be turned on for 1.5 hours. Upon cool down, the contents in the autoclave would be injected into the GC with nitrogen as the carrier gas coupled with TCD detector. Catalytic testing at each temperature is repeated for 3 times to minimize random error, and the standard deviation of the three tests were plotted as error bars.

2.4 Structural Characterization

2.4.1 X-ray diffraction (XRD)

X-Ray Diffraction is a simple and accurate method which is commonly used to probe the long-range order, and obtain information about the structure of the sample, including latticeype, lattice spacing and particle size. In 1912, Bragg reported that the wavelength of a homogeneous beam of X-rays can be found accurately in terms of the spacing of the elements of a NaCl crystal[3]. The formula was changed in 1913 to what was later termed Bragg's law of $n\lambda = 2d \sin\theta$, where n is the diffraction order, λ the wavelength, d the spacing between reflecting lattice planes and θ the scattering angle. It is now understood that X-ray constructively interfere with each other when the wavelength λ is comparable to the atomic spacing d between successive

layers of atoms in a crystalline structure, and become in phase to strike the imaging surface at a definite angle θ.

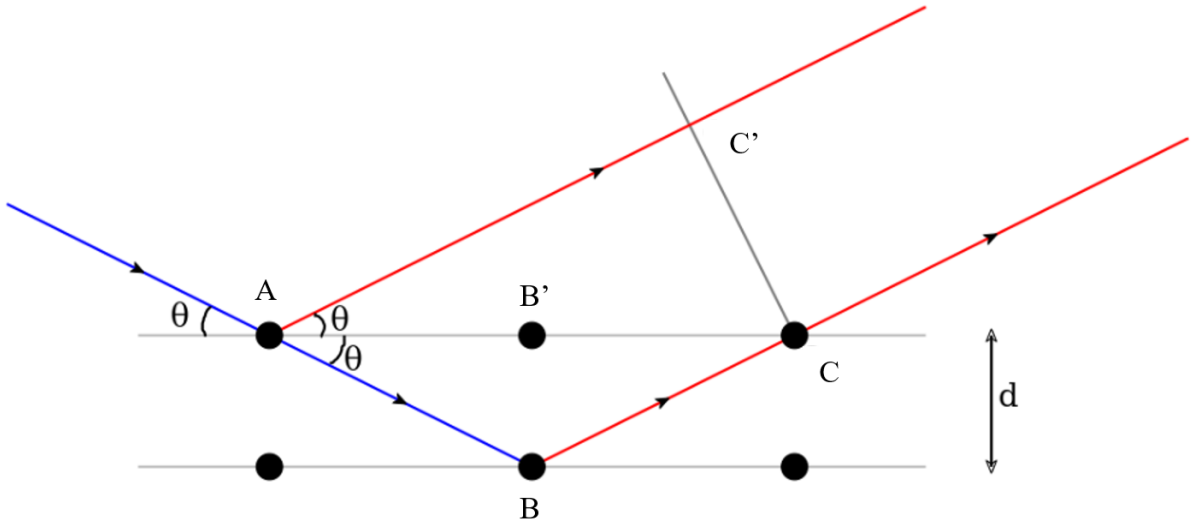


Figure 2 . 1 | Illustration of the derivation of Bragg's Law, with blue lines indicating incident X-rays with angle θ, and red lines indicating reflected X-rays also with angle θ.

For the waves to constructively interfere upon reflection of the crystal, the path difference between the two waves needs to equal an integer multiple n of the wavelength (nλ), in order for the reflected waves to be in phase. At the same time the path difference can be calculated in terms of the reflection angle θ with geometry as depicted in Figure 2 . 1. The path difference is AB + BC – AC' between the reflected rays from the two layers of atoms.

In this case, considering triangle ABB' and CBB', sin θ = d / AB = d / BC, rearranging to AB = BC = d / sin θ……(1)

Also, tan θ = d / AB' = d / CB', rearranging to AB' = CB' = d / tan θ.

AC can be expressed as AB' + CB'; AC = 2 AB' = 2 d / tan θ = 2 d cos θ / sin θ

Considering triangle ACC', cos θ = AC' / AC, which rearranges to AC' = AC cos θ = 2 d $\cos^2\theta$ / sin θ ……(2)

Substituting (1) and (2) into path difference of AB + BC – AC' gives

$$d / \sin\theta + d / \sin\theta - 2\,d\cos^2\theta / \sin\theta = 2\,d\,(1 - \cos^2\theta) / \sin\theta = 2\,d\,(\sin^2\theta) / \sin\theta = \underline{2\,d\sin\theta}$$

which is the results of Bragg's law shown above.

UiO-series of MOFs are a class of crystalline structures, with its long-range order well probed by X-ray diffraction. The (100), (110), and (111) planes of UiO-66 are shown in Figure 2 . 2 as an example. New peaks that are visible in XRD data not previously in the pristine MOF will indicate the incorporation of a different phase different to the MOF. In an experimental setup, electrons are produced by a hot Tungsten filament and accelerated through an applied voltage. These electrons subsequently bombard the target metal (e.g. Cu or Mo) to ionize an electron in the inner shells, X-ray will be produced as the electrons of higher energy fall into the newly generated hole. The generated X-rays will be filtered to give monochromatic radiation, which can be directed at the samples. The diffracted beams are measured at different angles to obtain an XRD spectrum. In this thesis, the diffraction patterns were obtained from a PANalytical X'pert PRO Diffractometer (PANalytical, Cambridge, UK), using Cu K_α where λ = 1.5148 Å with energy = 8.048 eV unless synchrotron X-ray diffraction (SXRD) is used. K_α indicates that X-ray generation is due to a transition from L-edge (with quantum number n = 2) to K-edge (with quantum number n = 1), and therefore 2p to 1s transition due to the selection rule of $\Delta l = \pm 1$. It is also possible for Mo K_α X-ray to be used on some lab-based XRD apparatus where λ = 0.7107 Å with energy = 17.45 keV.

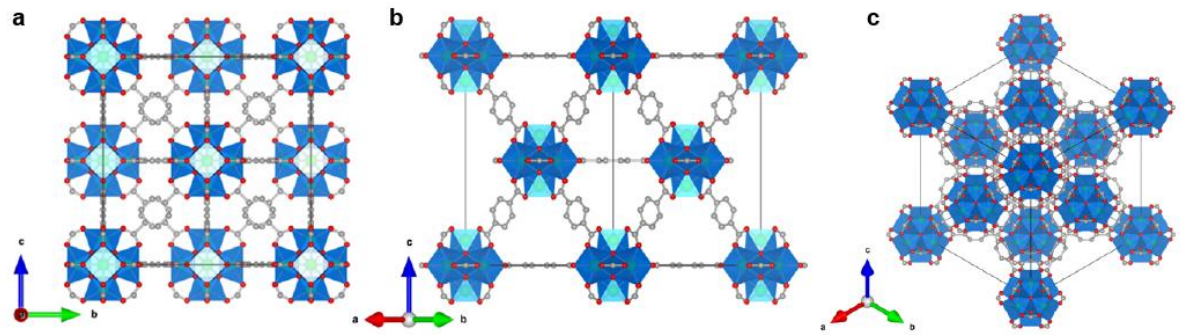


Figure 2 . 2 | (a) (100), (b) (110), and (c) (111) lattice planes of UiO-66

Rietveld refinement

Rietveld refinement is the most commonly used procedure for the structural determination of X-ray diffraction data developed by Rietveld[4]. This method of XRD data analysis compares a theoretical line profile to the experimental line profile via a least square approach with user-defined parameters such as lattice parameters, atomic coordinates, occupancies, and displacement from equilibrium positions.

Rietveld Refinement is a technique for use in the characterization of crystalline materials. It uses a least squares approach to refine a theoretical line profile until it matches the measured profile. With the non-linear least square method, Rietveld method fits a calculated profile based on a model including structural and instrumental parameter to the collected experimental data. Reasonable initial approximation is required for many free parameters, including unit cell dimensions, coordinates of all atoms in the crystal structure and the peak shape. The successful outcome of the refinement is dependent on the quality of model (including all initial approximations) and the quality of data.

Various R-factors are used in the Rietveld method to assess statistical agreement between the experimental and calculated profile. The most commonly used R-factor similar to other data fitting methods is the profile R-factor (R_p), which measures the difference between the experimental and the calculated data. Unfortunately, as an XRD profile have peaks of different

intensities, the R_p factor tends to overemphasize the influence of strong reflections and does not consider the experimental uncertainties. Both problems can be overcome by applying a weighting factor for every data point to generate weighted profile R-factor (R_{wp}). The weighting factor depends on the intensity of the XRD profile at a certain angle. Other corrections are done to remove the influence of the background in the XRD profile.

To avoid fitting limited data with too many parameters, an expected R-factor (R_{exp}) is determined by counting statistics, including observed data points and the number of parameters. The evaluation of the ratio χ, otherwise known as Goodness of Fit (GOF), the ratio between R_{wp} and R_{exp}, is used to evaluate the accuracy of the structural model. It is understood that R_{wp} value should be below 12% and GOF value should be equal to unity for a well-fitted Rietveld refinement[5]. However, for crystal structures with lower symmetry (e.g. monoclinic or triclinic) low R_{wp} can be challenging to obtain, and so the acceptable R_{wp} values can be up to 15 %[6].

Synchrotron X-ray diffraction (SXRD)

Resolution of XRD based on Cu K_α sources have relatively low signal-to-noise ratio, and for highly symmetric materials such as MOFs, can only be used for fingerprinting. In order to analyze the UiO-series MOFs with the Rietveld method, synchrotron X-ray diffraction with its much higher electron flux, orders of magnitude higher than the laboratory-based X-ray diffractometer have to be used. On top of that, the steps between individual data points are much smaller, allowing more parameters to be added into the fitting profile. With more data points, R_{exp} can be increased and consequently reducing the goodness of fit.

In this thesis, SXRD measurements were collected at beamline BL02B2 at SPring-8, Japan. The energy of the incident X-ray flux was set at 18 keV^2. The wavelength (λ = 0.689556(2) Å) and the 2θ zero-point (ZP = -0.000015(2)°) were calibrated using a diffraction pattern obtained from a high quality CeO_2 powder (NIST SRM674b). High-throughput SXRD data were obtained from the MOF samples (loaded in 0.5-mm borosilicate capillaries to reduce the

absorption of X-ray in the samples)) using the MYTHEN detector. The patterns were collected in the 2θ range 2-78° with 0.006° data binning. Each SXRD pattern was collected for 5 min for each MYTHEN-2θ step, i.e., 10 min in total for MYTHEN data summation. This produced patterns with a good signal-to-noise ratio (S/N).

2.4.2 X-ray absorption spectroscopy (XAS)

X-ray absorption spectroscopy is a widely used technique for determining the short-range order of a material. It is obtained by tuning the photon energy to excite core electrons of specific element present in the material (e.g. Ru in Ru/UiO-67-bpydc). In an XAS experiment, incidents X-ray of energy E is absorbed by a certain element present in the sample, destroying a core electron of binding energy of E_0, and emit a photoelectron with kinetic energy ($E-E_0$). The edges are named according to the principal quantum numbers n from which the core electron is excited. n = 1, 2 and 3 would correspond to (K-, L-, and M- edges respectively), and the transition is determined by the Fermi's Golden Rule. A fluorescent X-ray or an Auger electron will be ejected as the core state is eventually filled by decay of higher-lying electrons. The ejected photo-electron will scatter and interfere with its neighbouring atoms. As a result, the intensity of the XAS spectrum will depend on the density of states at the absorbing atom with energy ($E-E_0$).

An XAS spectrum is normally separated into 3 regions, which are considered as separate spectroscopic techniques and will be introduced separately. Using the Mn K-edge X-ray absorption spectroscopy of the Ramsdellite as an example as shown in Figure 2 . 3. With the K-edge energy at 6539 eV, the red-coloured region of 6539-6550 eV corresponds to the pre-edge region. The purple-coloured region of 6550-6560 eV corresponds to the X-ray Absorption Near-Edge Structures (XANES) region. The green region starting from 6560 eV corresponds to the Extended X-ray Absorption Fine Structure (EXAFS) region. The Pre-edge and the

XANES regions are used mainly for valence state determination, while the EXAFS region is mostly used for quantifying the coordination environment close to the absorbing elements.

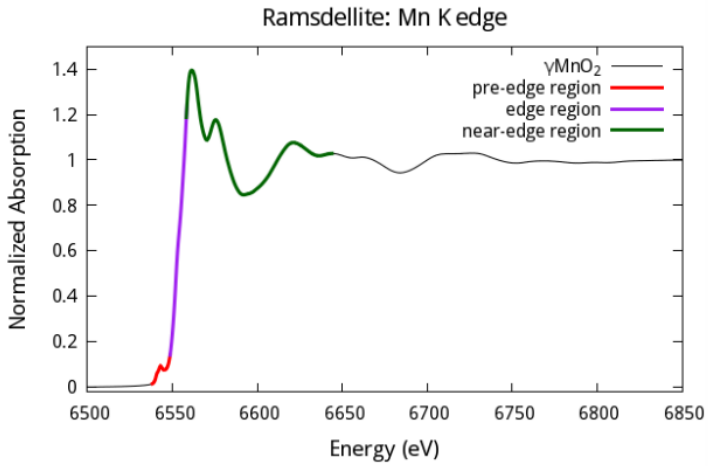


Figure 2 . 3 | An Mn K-edge XAS spectrum for Ramsdellite

Valence state determination from Pre-edge and XANES regions

As the valence of an element increases, the edge position will shift to higher energy. The pre-edge feature of XAS originates from the transitions between the core (in the case of Mn K-edge, 1s level) to the empty 3d levels with some hybridization with the 4p levels from the Mn ligands. XANES, on the other hand, stems from bound-state electronic transitions from deep core levels to valence levels, with the energy positions sensitive to changes in shielding of nuclear charge heavily influenced by the ligands[7]. The use of the pre-edge feature or XANES for the determination of valence state is concluded by the position of the feature against model compound with known valence states[8-10]. Quantification of valence state via comparison with model compounds can be performed via various methods, such as first derivative, half height intensity, integral method and linear combination fitting[11-14]. These methods of quantification are summarized in Figure 2 . 4.

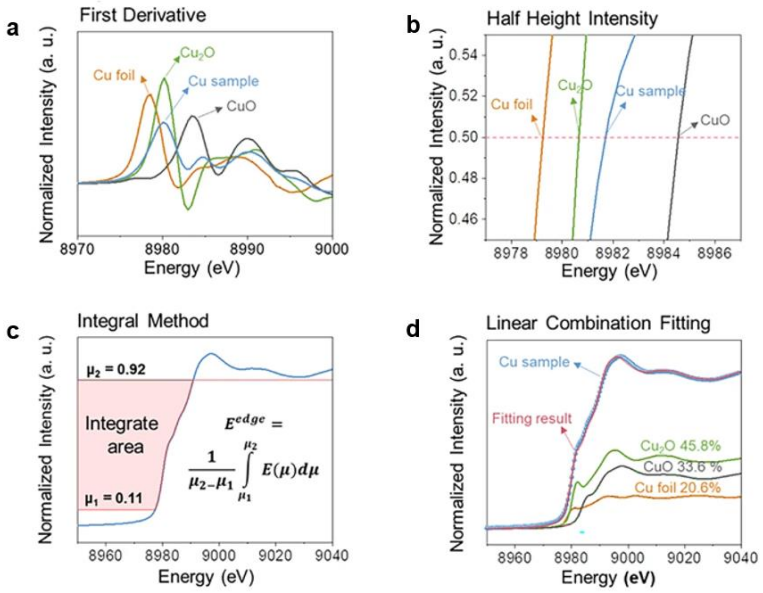


Figure 2 . 4 | Methods of determination of valence states from XANES spectra. (a) First derivative, (b) Half height intensity, (c) Integral method and (d) Linear Combination Fitting.

EXAFS region

The transformation from XAS spectra (Figure 2 . 5 a) to Cu K-edge EXAFS data of Cu metal foil is explained below. The oscillations starting from the edge position, commonly defined as the inflection point where the second derivative of the data is 0, is extracted from the data (Figure 2 . 5 b). A conversion from energy to wavenumber k via a conversion of Equation 2 . 1 below.

$$k = \sqrt{\frac{2m_e(E - E_0)}{\hbar}} \approx \sqrt{\frac{(E - E_0)}{3.81}}$$

Equation 2 . 1 | Conversion from energy E to wavenumber k

where $(E-E_0)$ kinetic energy of photo-electron,

m_e rest mass of electron,

$\hbar$ the reduced Planck's constant.

Next, the oscillations are weighted by a power of k, commonly k^2 or k^3 to generate the k-space EXAFS data otherwise known as χ(k) (Figure 2 . 5 c), which can then be fourier transformed into R-space EXAFS data (Figure 2 . 5 d) showing the coordination environments close to the absorbing elements with respect to the radial distance in Å. Due to phase shifts during fourier transformation of the data, the radial distance shown on the graph would be about 0.3-0.5 Å shorter than the actual distance. In this case, for the Cu present in metal foil, judging from the peak position at approximately 2.2 Å, it can be concluded that the distance between Cu and its neighbours are approximately 2.6 Å, which corresponds to the Cu-Cu distance.

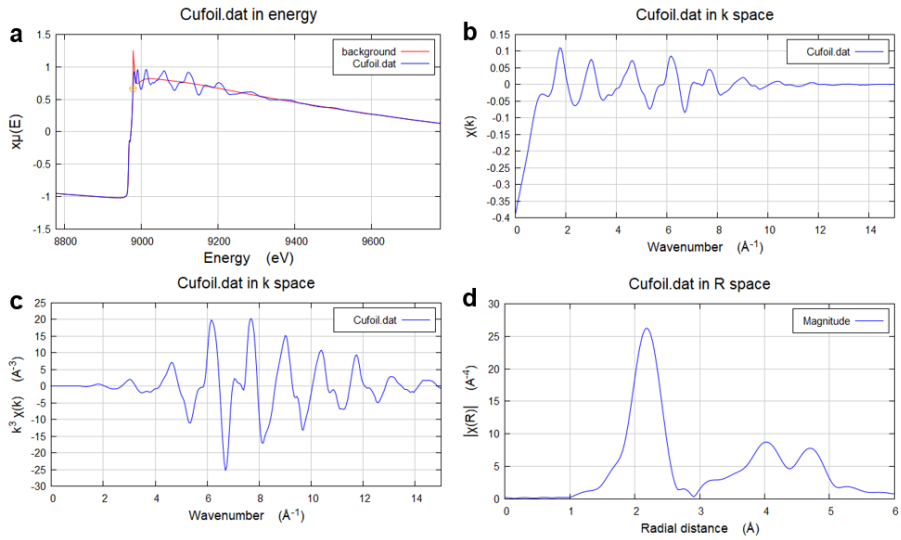


Figure 2 . 5 | Cu K-edge XAS data transformation to EXAFS process. (a) Raw XAS data. (b) raw k-space EXAFS data. (c) k^3-weighted k-space EXAFS data. (d) k^3-weighted R-space EXAFS data.

Quantifying coordination environments via EXAFS fitting

Based on multiple scattering theory, χ(k) (Figure 2 . 5 c) can be modelled by the EXAFS equation (Equation 2 . 2).

$$\chi(k) \sim \frac{(NS_0^2)F(k)}{2kR^2} \sin(2kR + \Phi(k))\, e^{-2\sigma^2 k^2} e^{-2R/\lambda}$$

Equation 2 . 2 | EXAFS equation

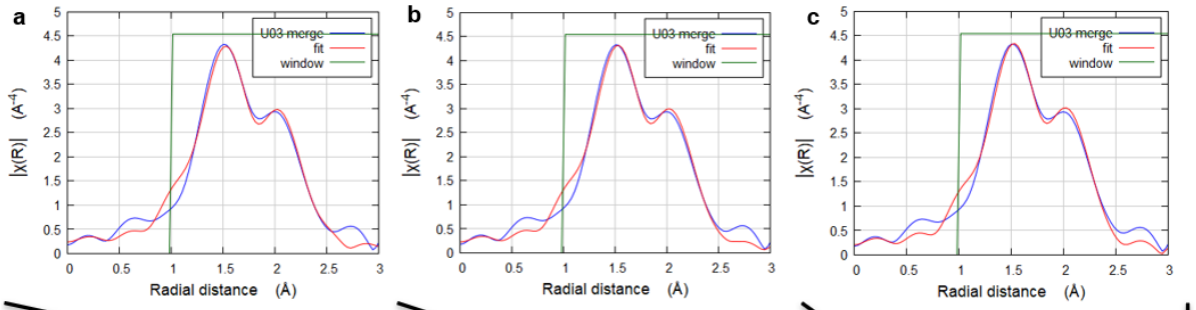
F(k), Φ(k), and λ (blue coloured) are the scattering functions dependent on atomic number of the scattering element. These scattering functions are derived from the multiple scattering theory from which the EXAFS equation emanates and considered by EXAFS fitting software. The red coloured are the parameters that can be altered for the quantification of coordination environment of the absorbing element: N is the degeneracy of the scattering path, chemically equivalent to the coordination number of a certain ligand. S_0^2 is the amplitude reduction factor and normally falls between the range of 0.7 and 1.0. Note that N and S_0^2 are directly correlated. For optimal accuracy of data fitting the amplitude reduction parameter shall be obtained from EXAFS data fitting of a model compound (such as the metal foil) with known coordination number to be used as a fixed input parameter in the data fitting. As a result, the coordination number of the absorption element can be accurately and reliably refined. R is the radial distance between the absorbing element and the scatterer or ligand. σ is the displacement from equilibrium position otherwise known as the Debye-Waller factor, quantifying disorder such as thermal motion of the scatterer or ligand. On a high level, N, R and σ can be assimilated to the peak height, peak position, and peak width of a Gaussian peak on data fitting.

Numerous software has been developed for EXAFS fitting purposes including WinXAS[15], PrestoPronto[16], Viper[17] and pyFitit[18]. These are in no way comparable to the popular DEMETER package developed by Ravel for EXAFS data processing with a citation of more than 15000[19]. Similar to the aforementioned evaluation of R_{exp} in Rietveld refinement, the

number of independent data point, N_{idp}, are determined by the Nyquist criterion, $N_{idp} = \frac{2\Delta k \Delta R}{\pi}$. Δk and ΔR are the fitting range selected for k-space and R-space data, respectively. A fitting range of [2:12] for k-space and [1:3] for R-space would result in an N_{idp} of $\frac{2 \times (12-2) \times (3-1)}{\pi} = 12.7$ as an upper bound for the number of parameters used in the fitting procedures.

In the fitting procedure, the amplitude reduction factor is used as a fixed input parameter as determined by EXAFS analysis of a model compound. A global parameter is used to refine the ΔE_0, where the beginning of the EXAFS region is considered in the whole XAS spectrum. For each individual scattering paths, three separate parameters will be used to refine the coordination number N, radial distance R, and the displacement from equilibrium position σ (Debye-Waller factor). For samples fitted with more parameters than the Nyquist criterion, certain constraints will be used to relate the parameters in order for the Nyquist criterion to be satisfied.

Prior knowledge of the sample is crucial for the data fitting, especially for EXAFS. Good fitting is possible for scattering paths in spite of a lack of chemical sense. The EXAFS data for a ruthenium doped UiO-series sample is shown in Figure 2 . 6 with $RuCl_3$ added as a precursor. The peak at 1.5 Å has been fitted with Ru-O scattering paths, while the peak at 2.0 Å is fitted with Ru-Si (Figure 2 . 6 a), Ru-S (Figure 2 . 6 b) and Ru-Cl (Figure 2 . 6 c) scattering paths respectively, each with acceptable fitting parameters and fitting quality. No Si or S source was added into the synthesis process, and so it is highly unlikely that any Ru-Si or Ru-S would be present. As a result, EXAFS fitting are commonly used with complimentary structural characterization techniques such as XRD, IR or ICP. To further improve the reliability of the EXAFS fitting, EXAFS fitting of the same sample at different edges are performed and cross-compared[20].



	Ru-Si	Ru-S	Ru-Cl
Degeneracy	2.24	1.76	1.45
R / Å	2.49	2.50	2.53
σ / 10^{-3}	4.9	6.3	6.5

Figure 2 . 6 | EXAFS fitting for a Ru doped UiO-series MOF, attempted with (a) Ru-Si, (b) Ru-S and (c) Ru-Cl scattering paths.

Wavelet transform of EXAFS data

The transformation of k-space into R-space data is via Fourier transform, and unfortunately suffers from several inherent limitations for EXAFS data analysis. Most importantly, the oscillations at different k value can correspond to scattering from elements with different atomic number. With Fourier transform such information will be lost as the resultant peak in R-space is independent of the position of the oscillation in k-space. Wavelet transform has emerged to be an improved way of visualizing EXAFS data in a 2-dimensional (R and k) way. Rather than using sine function as the basis function, a Morlet wavelet $\psi(k)$ is used as the basis function to compose the integral as in Equation 2 . 3:

$$\psi(k) = \frac{1}{\sqrt{2\pi}\sigma}(e^{i\kappa k} - e^{-\frac{\kappa^2}{2}})e^{-\frac{k^2}{2\sigma^2}}$$

Equation 2 . 3 | Morlet wavelet

where σ and κ are two free wavelet parameters. The sine function is periodic and by extension has complete resolution with respect to k, and upon Fourier transform would lead to no resolution of k in R-space. In the context of EXAFS, scattering paths due to different elements

with similar radial distance cannot be resolved. The Morlet wavelet function bypass this limitation by encompassing the sine and cosine functions ($e^{i\kappa k} - e^{-\frac{\kappa^2}{2}}$) in a Gaussian envelop $e^{-\frac{k^2}{2\sigma^2}}$ to reduce the resolution with respect to k. The free wavelet parameter κ controls the frequency of the sine and cosine function, while σ controls the width of the Gaussian envelop. As a result, scattering from different elements with similar radial distance can now be resolved, depicted by the second shell Cu-O and Cu-Cu at around 2.7 Å for the K-edge XAS of CuO in Figure 2 . 7. In this way, the difference between the second shell scattering Cu-O and Cu-Cu can be differentiated albeit positioned at similar radial distances[21].

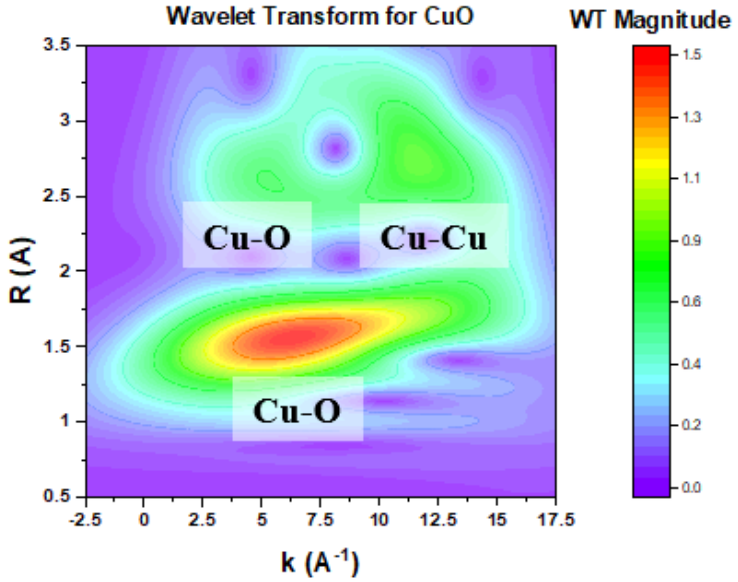


Figure 2 . 7 | Wavelet transform for Cu K-edge XAS data of CuO

In this thesis, XAS is used for the investigation of chemical coordination environments and oxidation states of the co-catalysts including Ru, Cd and In added onto UiO-66-NH_2 supports. XAS data performed are all measured at beamline BL07A of Taiwan Light Source at National Synchrotron Radiation Research Centre (NSRRC) in Taiwan. Fluorescence mode was used for the Ru K-edge (Chapter 3), Cd K-edge (Chapter 4) and In K-edge (Chapter 5) measurements and achieved by using a silicon drift detector. To ascertain the reproducibility of the

experimental data, at least 3 scan sets were collected and compared for each sample. The EXAFS data analysis was performed using IFEFFIT with Horae packages (Athena and Artemis). The spectra were calibrated with Ru metal foil as a reference to avoid energy shifts of the samples. And the amplitude reducing parameter was obtained from EXAFS data analysis of the Ru foil, which was used as a fixed input parameter in the data fitting to allow the refinement in the coordination number of the absorption element. Wavelet transform is performed on the XAS data in Chapter 4 and 5. A Morlet wavelet with free parameter $\sigma = 4$ and $\kappa = 2.5$ was used as the basis function. The R-range for the transformation is 0-6 Å, while the k-range is 0-14 $Å^{-1}$.

2.4.3 X-ray photoelectron spectroscopy (XPS)

XPS is a characterization technique for the identification of valence state of a certain element present on the surface of a material, which can provide information including state of hybridization and bonding environment. In contrast to the higher energy of Cu K_α X-ray (energy = 8047.8 eV), it uses the lower energy and less penetrating Al K_α X-ray (energy = 1486.7 eV). The first few atomic layer on the surface can be probed with its lower penetrating ability. XPS is largely based on the photoelectric effect, hence its name, where electrons of the target elements present in the sample can absorb X-ray photons and be excited and ejected as photoelectron with non-zero kinetic energy. Measuring the kinetic energy of such ejected photoelectrons can inquire about the binding energy of a certain elements present in the sample according to the photoelectric equation as shown in Equation 2 . 4.

$$E_{binding} = E_{photon} - E_{kinetic} + \phi$$

Equation 2 . 4 | The photoelectric equation

where $E_{binding}$ is the binding energy of the specific element on the sample,

E_{photon} the energy of the X-ray photons used (1486.7 eV for Al K_α X-ray),

$E_{kinetic}$ the kinetic energy of the electron measured by the apparatus,

ϕ the work function, which behaves as a constant to correct for certain parameters.

The binding energy can be indicative of the nuclear charge experienced by the element and can therefore give information about the oxidation states of the sample. Figure 2 . 8 a shows the relationship between binding energy and the rich variety of oxidation states for sulphur.

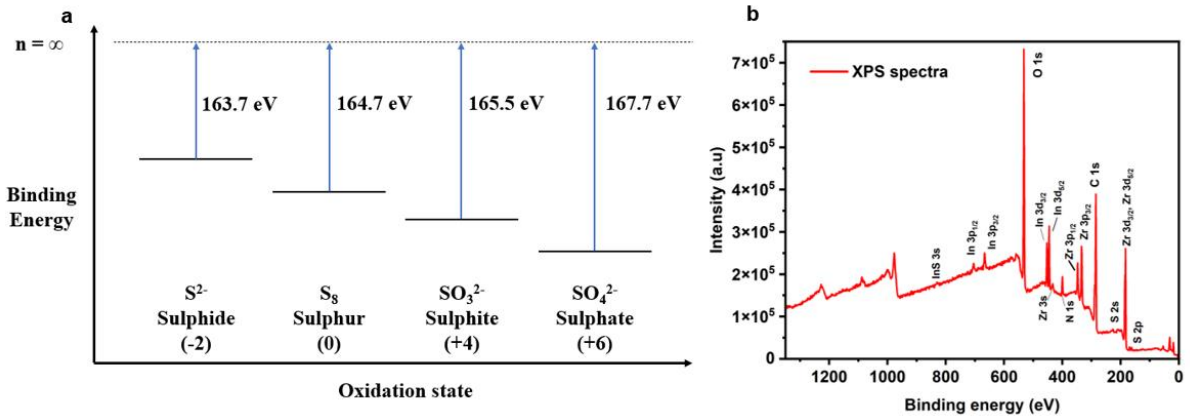


Figure 2 . 8 | (a) Binding energy for sulphur with various oxidation states. (b) an XPS survey scan

In an experimental set up, a survey scan will be taken by measuring the whole range of kinetic energy (Figure 2 . 8 b). The XPS measurement is commonly done under high vacuum conditions (~ 10^{-6} Pa) for the accurate detection of the kinetic energy of escaped photoelectron, preventing them from colliding with any molecules present in the chamber. At the same time, the sensitive microchannel plates in the detectors can be protected from moisture[22]. Since each element has a set of characteristic XPS peaks corresponding to the electron configuration of the elements. Peaks can be observed if the binding energy of that specific orbital falls below the energy of 1486.7 eV (Al K_α). If the intensities for each raw XPS peak can be corrected by dividing a relative sensitivity factor and subsequently normalized over all the elements detected, the atomic compositions of the sample can be quantified. The limitation of this method of

atomic composition quantification is the limiting penetration ability of the Al K_α X-ray, reducing its application on bulk materials.

Fitting the XPS data with Gaussian peaks is commonly performed for in-depth analysis. The raw XPS data can be noisy, which restricts the accurate comparison across different samples. Fitting with Gaussian peaks allows a more reliable determination of the peak maxima. Additionally, peaks arose from dissimilar oxidation states may overlap with each other, and fitting the combined peaks would allow for quantification of relative proportions of the different oxidation states present in the sample. To add to the complexity, spin-orbit coupling for certain energy levels (e.g. S 2p) would lead to the formation of 2 or more peaks present at some fixed ratio, which needs to be taken into account during peak fitting. For S 2p, the spin-orbit coupling results in two energy level of $2p_{1/2}$ (j = 1/2, energy level m_j = +1/2 and -1/2) and $2p_{3/2}$ (j = 3/2, energy level m_j = +3/2, +1/2, -1/2, -3/2). As the $2p_{3/2}$ has 4 energy levels while $2p_{1/2}$ has only two, the peak intensity for S $2p_{3/2}$ and $2p_{1/2}$ XPS would be in 2:1 ratio.

In this thesis, XPS is used to study the oxidation states and chemical environment of the CdS and In_2S_3 added as co-catalysts onto UiO-66-NH_2 as a support. XPS measurements were conducted using a Kratos Axis SUPRA XPS fitted with a monochromated Al kα X-ray source (1486.7 eV). A spherical sector analyser and 3 multichannel resistive plates, 128 channel delay line detectors. All data was recorded at 150 W and a spot size of 700 × 300 µm. Survey scans were recorded at pass energy of 160 eV, and high-resolution scans were recorded at pass energy of 20 eV. Electronic charge neutralization was achieved using a magnetic immersion lens. Filament current = 0.27 A, charge balance = 3.3 V, filament bias = 3.8 V. All sample data was recorded at a pressure below 10^{-8} Torr and a room temperature of 294 K. Data were analysed using CasaXPS software, and the spectra were calibrated with C 1s peak at 284.8 eV.

2.4.4 Inductively Coupled Plasma Mass Spectrometry (ICP-MS)

ICP-MS is an analytical technique that allows the quantification of certain elements in the periodic table down to parts per trillion (ppt) concentrations. Samples are digested in strong acid and subsequently diluted to generate a stabilized aqueous matrix. A plasma is generated by heating the gas (commonly Ar) with an electromagnetic coil inductively, and contains a certain concentration of ions and electrons in order for the gas to be electrically conductive. Upon injection into a nebulizer, where supersonic expansion of an inert gas is utilized to aerosolize the liquid. The Ar plasma with temperature up to 10,000 K is used to vaporize, atomize, and ionize the sample generating singly charged positive ions. Subsequently, the ion beam is directed into a quadrupole mass spectrometer, which separates the ions according to their mass to charge (m/z) ratio via the application of a varying magnetic field. ICP-MS is able to quantify the number of certain elements at ultra-low concentrations (ppt), and can detect different isotopes of the same element. However, the dependence of ICP-MS on mass limits the detection of certain elements due to interference from Ar in the plasma or molecules from air. This is exemplified by the difficulties in quantifying the amount of sulphur (^{32}S) which has identical mass with an O_2 molecule (m=32) present in air.

ICP-MS data in chapter 3 of this thesis was performed on Perkin Elmer NexION 2000B ICP-MS in Department of Geography, University of Oxford. Prior to measurement, approximately 20 mg of Ru deposited MOFs are digested in a Teflon-lined autoclave with 2 mL of concentrated HNO_3 and heated to 180 °C for 24 hours. Upon cool down, the samples are diluted to 2 % HNO_3 with 18 MΩ DI water. The calibrations were obtained using external calibration analysis with a series of standards of known concentrations prepared to form a calibration curve. The calibration standard was obtained from 10 ppm standards. QM mix was used to validate the calibration curve. Standards and samples were spiked with 1ng/g Rh, In, Ir, Re so that any general instrument drift could be normalised. All data results are reported as elemental

concentrations i.e. even though only one type of isotope is measured, the concentration values quoted are for the element inclusive of all isotopes.

ICP-MS data in chapter 4 was performed on Agilent 7800 ICP-MS in the ICP-MS centre of East Anatolia High Technical Application and Research Centre at Ataturk University, Turkey. Additionally, LECO CHNS-932 analyzer was used to determine the quantity of S. The ICP-MS data for chapter 5 was carried out in Chemistry Teaching Laboratory, University of Oxford. Prior to measurement, approximately 10 mg of samples are digested in a Teflon-lined autoclave with 2 mL concentrated HNO_3 and heated to 180 °C for 24 hours. Upon cool down, the samples are diluted to 2 % HNO_3 with 18 MΩ DI water. The calibration curve was obtained separately by dissolving $In(NO_3)_3$ and $ZrCl_4$ into DI water and diluted to 2 ppm, 400 ppb, 80 ppb, 16 ppb, 3.2 ppb, 0.64 ppb and 0.128 ppb as depicted in Figure 2 . 9 below. The calibration curve has adjusted R-square value higher than 0.999 in both ^{115}In and ^{90}Zr.

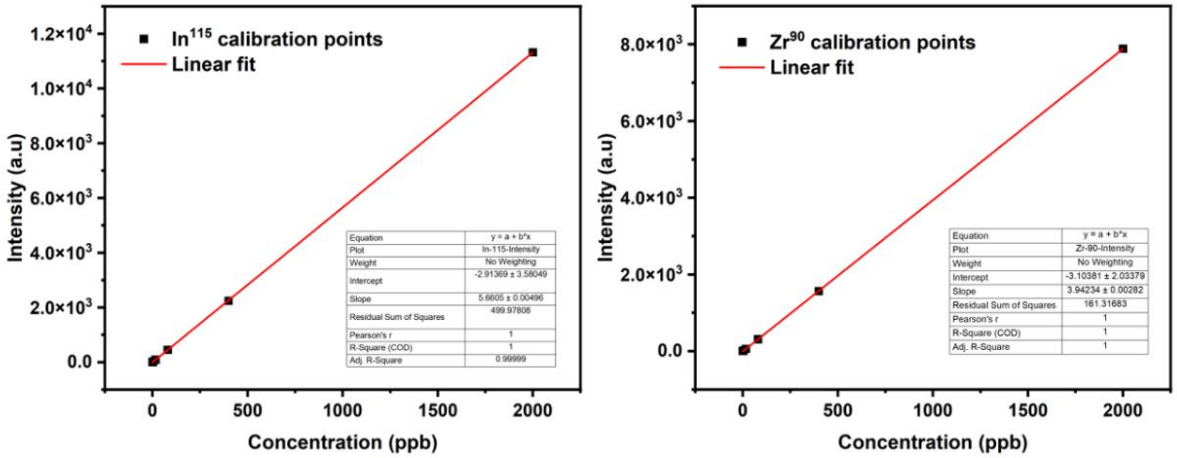


Figure 2 . 9 | Calibration curve for ^{115}In and ^{90}Zr for ICP

2.4.5 N_2 adsorption-desorption experiments

N_2 adsorption-desorption experiments were performed with a Micrometritics Tristar instrument with ultrahigh purity gases (99.999 %) under Surface Analysis Facilities, Chemistry Research Laboratory, University of Oxford. Before the sorption analysis, a sample (~0.1 g)

will be loaded into a sample tube and subject to a vacuum of 10^{-5} Pa at 150 °C overnight. The surface area is calculated by the Brunauer-Emmett-Teller (BET) analysis based on a multilayer adsorption model, which is calculated by the initial slope (0.01 to 0.1 P/P_0) of the N_2 adsorption data[23]. The Pore size distribution was calculated by the DFT method embedded in the Micrometrics software, based on a slit-type pores structure with carbon surface analyzed by N_2 at 77 K. In this thesis, BET analysis was used for the determination of surface area in the UiO-series MOFs.

2.4.6 Thermogravimetric Analysis (TGA)

TGA measures the mass of a sample as a function of increasing temperature. Changes in mass can be due to thermal decomposition or other chemical or physical changes of the sample. For UiO-series MOF materials, increasing the temperature from room temperature will lead to the desorption of any physiosorbed and chemisorbed molecules, and subsequently the breakdown of the electrostatic interaction between the Zr_6 inorganic units and the organic linkers, by extension the porous structure. Since the organic linkers are combustible in air, while the inorganic units stay as oxides, it has been well documented in the literature for the use of TGA in air to determine the ratio of organic linkers and inorganic units for the calculation of missing linker defects. In this thesis, TGA is also used to resolve the amount of missing linker defect present in the synthesized sample of UiO-67-bpydc in Chapter 3. TGA was performed on a TA Instruments SDT Q600 under a constant air flow rate of 60 mL/min in Inorganic Chemistry Laboratory, University of Oxford. Sample of approximately 8 mg was added onto an alumina pan and heated from 30 °C to 900 °C at a rate of 5 °C min^{-1}.

2.4.7 Infra-red Spectroscopy (IR)

Molecular vibrations have energy within the infra-red region of the electromagnetic spectrum. The vibrations can therefore be probed by measuring the IR radiation absorbed. In various

catalysts this can be the O-H stretching, while in the field of MOFs it is commonly the C=O and the C=C stretching present in the organic linker. Absorption only occurs at resonant frequencies of the molecular vibration proportional to $\frac{1}{2\pi c}\sqrt{\frac{k}{\mu}}$, where c is the speed of light, k is the force constant of the bond with units N m^{-1}, while μ the reduced mass of the bond. For convenience, the energy in the field of IR spectroscopy is in wavenumbers, $\tilde{\nu}$ with units cm^{-1}, which is related to the wavelength λ of the IR radiation via $\tilde{\nu} = \frac{1}{\lambda}$. Dispersive IR spectroscopy operates with a rather lengthy time scale, and therefore Fourier-transform infra-red (FT-IR) is generally used for better efficiency along with other advantages.

FTIR (Fourier-transform Infra-red) spectroscopy

Rather than shining monochromatic IR radiation at each wavelength, FT-IR shines light composing of many different frequencies of light at once and measures how much each of the frequencies of light are absorbed by the sample. This process is repeated for different set of frequencies for more data points rapidly over a short period of time. Afterwards, an algorithm takes in all the data points to reverse engineer the amount of absorption at each wavelength. The algorithm mentioned here is a modification of Fourier transform, and hence the name of the spectroscopic technique. The raw data before Fourier transform is called an interferogram.

In this thesis, FTIR spectroscopy were performed in the range of 650-4000 cm^{-1} on a Nicolet iS 50 FT-IR spectrometry using an MCT/A detector at a resolution of 4 cm^{-1} in Inorganic Chemistry Laboratory, University of Oxford. For the Ru/bpy sample in Chapter 3, Approximately 50 mg of Ru/bpy samples was placed in the reaction cell in the glove box to avoid the quenched reactive intermediates to be oxidized by air.

2.4.8 Nuclear Magnetic Resonance (NMR)

Nuclear Magnetic Resonance gives information about the nuclear charge experienced by the nuclei of NMR-active nucleus with spin one half (I = ½), including ^{1}H and ^{13}C which happened

to be building blocks of organic chemistry. Such nuclei has two independent spin states denoted by the spin quantum number m_s = +½ or -½, also known as spin-up and spin-down. These two states are degenerate with the absence of any magnetic field, and hence the population will be equal under the laws of statistical mechanics. However, in the presence of a magnetic field, nuclei with spin pointing in the same direction as the magnetic field will be more energetically stable compared to nuclei with spin opposing the magnetic field due to the magnetic dipole interactions i.e. the degeneracy will be lifted. Consequently, there will be an energy difference ($\triangle E$) between the two states which is proportional to the strength of the magnetic field B_0 according to the equation $\triangle E = \gamma \hbar B_0$, where γ is the gyromagnetic ratio for the nuclei and ħ the reduced Planck's constant. This is summarized in Figure 2 . 10.

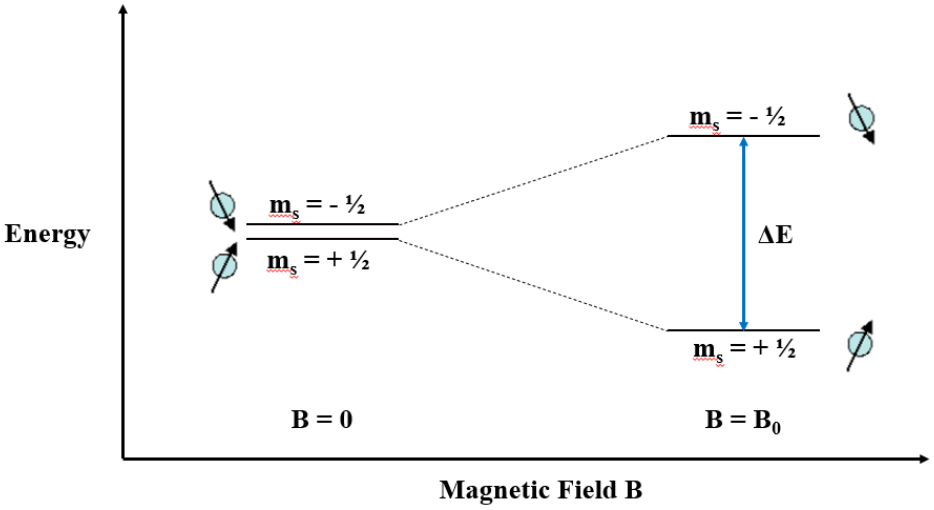


Figure 2 . 10 | Magnetic field lifting degeneracy for nuclei with opposite spin

Similar to the use of wavenumber (cm^{-1}) as units for convenience in IR, chemical shift δ with unit ppm is used in NMR for convenience. Chemical shift is the resonant frequency of a certain NMR-active nucleus relative to a standard with the presence of a magnetic field, and is calculated in Equation 2 . 5.

$$\delta = \frac{\nu_{sample} - \nu_{reference}}{\nu_{reference}} = \frac{1}{h}\frac{\Delta E_{sample} - \Delta E_{reference}}{\Delta E_{reference}}$$

Equation 2 . 5 | Chemical shift calculation in NMR

where ν_{sample} and ΔE_{sample} is the resonant frequency and energy difference due to presence of magnetic field for the sample, and $\nu_{reference}$ and $\Delta E_{reference}$ that for the reference. Since the numerator is often in units Hz, and the denominator in units MHz, δ has units ppm (10^{-6}). Common references used for ^{1}H and ^{13}C tetramethylsilane, $Si(CH_3)_4$, while for other NMR-active nuclei there may be other reference compounds.

Magic Angle Spinning for solid-state NMR

Unfortunately, numerous complications arise when this technique is attempted at solid-state samples, including dipolar interaction, chemical shift anisotropy and quadrupolar interaction. These interactions lead to broad and featureless NMR lines. In solution NMR, most of these interactions can be averaged out due to thermal molecular motion. Thankfully, these problems are partially orientation dependent, and can be mitigated to some extent via Magic Angle Spinning (MAS). The nuclear dipolar interaction, which is the interaction between the magnetic dipole of two neighbouring nuclei. This interaction depends on the angle between the internuclear axis of the sample and the magnetic field with a $3\cos^2\theta - 1$ dependence. As a result, at $\theta = 54.7°$, the dipolar interaction vanishes. Although it is impossible for all the internuclear vectors to be set to this angle, rotating the sample around this axis will produce the same effect. Chemical shift anisotropy is the dependence of chemical shift on the orientation of samples. This can largely be mitigated by magic angle spinning. The quadrupolar interaction arises from the presence of quadrupolar nuclei with spin larger than a half ($I > ½$), such as ^{2}H ($I = 1$). The nuclear electric quadrupole moments from such nuclei can couple with the surrounding electric field gradients. Such interactions are only partially averaged by MAS.

^{1}H-^{1}H Nuclear Overhauser Effect Spectroscopy (NOESY) NMR

Spatial proximity between two NMR-active nuclei can also be probed by the Nuclear Overhauser Effect spectroscopy (NOESY). The NOE effect stems from the transfer of nuclear spin polarization from one spin-active nucleus to another by cross-relaxation. Two-dimensional NMR can be obtained by irradiating the samples with resonant frequency of a certain proton environment and detecting at other frequencies, any intensity detected suggests transfer of nuclear spin polarization through space, and therefore indicating these protons are in spatial proximity. It is possible for this spectroscopy to be applied on any different pairs of NMR-active nuclei (e.g. ^{1}H-^{13}C, ^{1}H-^{31}P, named Heteronuclear Overhauser Effect Spectroscopy HOESY), but only ^{1}H-^{1}H NOESY NMR is used in this thesis.

^{1}H MAS NMR experiments were conducted on a Bruker Avance 400 spectrometer operating at 9.05 T with a 4 mm double-resonance MAS probe, with Larmor frequencies of 495.43 MHz for ^{1}H in Wuhan University, China. Spinning speeds of 12 kHz, 32 scans and 3.9 μs π/2 excitation pulse were used for ^{1}H single-pulse acquisitions. The standard two-dimensional (2D) three-pulse exchange (a.k.a. NOESY) sequence was used to monitor chemical exchange between proton sites in the catalyst, with a dwell time in the indirect dimension set to 20 μs. Typically, 32 scans were acquired for each t_1 increment, with final data sets consisting of 512 t_1 × 2048 t_2. Mixing times is 10 ms. The recycle delay used in the 2D exchange experiments is 5 s with MAS speeds equal to 12 kHz. ^{1}H chemical shift is referenced to adamantane at 1.78 ppm.

2.4.9 Scanning / Transmission Electron Microscopy (S/TEM)

The resolution of optical microscope is limited by the energy of its light source. Electron microscopies are able to reach higher resolution due to the application of high energy focused beam of electrons as energy source. This beam of electrons interacts with the atoms present in the sample to produce signals that contain information about the surface of the sample. The

position combined with the intensity of the detected signals allows an image to be generated. SEM creates images via detecting the electrons which are bounced back from the sample upon projection of the electron beam and can provide a 3-dimensional image of the surface of the sample. On the other hand, in TEM the electrons which passed through the samples are detected, effectively projecting the sample onto a 2-dimensional surface. Generally, the resolution for TEM (up to 50 million times magnification) is better than SEM (up to 2 million times magnification), but the maximum field of view for SEM is better.

In this thesis SEM images were taken using Zeiss Merlin - EBSD with a FEG SEM. Operating voltages are between 20-30 kV and beam current used was up to 40 nA. TEM images were obtained using a JEOL 2100 Transmission electron microscopy (JEOL, Tokyo, Japan) at 200 kV in the Department of Materials, University of Oxford. The sample was placed on an Agar Scientific Holey carbon-supported copper 400 mesh grid.

2.4.10 Energy dispersive X-ray (EDX)

EDX is an analytical technique commonly associated with SEM or TEM for elemental analysis. Elements with different atomic structure will have different electromagnetic emission spectrum upon stimulation by X-ray. The electron beam for microscopic imaging purposes focused on the samples will promote ground state electrons bound to the nucleus to higher energy states, and subsequently generating an electron hole at the original position. An electron with higher energy located at the outer shells can then fill this hole and release the energy difference between the two states in the form of an X-ray. The intensity and energy of such X-rays are measured by an energy-dispersive spectrometer, which allows the elemental composition of the sample to be revealed. As the electron beams used for EDX purposes can be originated from SEM/TEM, EDX data with spatial resolution can be obtained i.e. the position and identity of elements can be exposed.

2.5 Optical Characterization

2.5.1 Ultra-Violet-Visible (UV-Vis)

UV-Vis spectroscopy uses the ultraviolet and the visible range of the electromagnetic spectrum for spectroscopic purposes. As it is relatively inexpensive and easy to execute, it has diverse applications with the only requirement of the sample absorbing light in UV-Vis region. For solution, absorbance of samples is often measured. For solid samples, it is more common to measure the remission (both specular reflection and diffusely back-scattered light) of the sample. Transitions between various electronic states for metals fall in this range of energy and can be probed by UV-Vis spectroscopy. Common transitions present in organic chromophores include π–π*, n–π*, σ–σ*, and n–σ*. In the case of UiO-series MOF, the π–π* and n–π* transitions present in the organic linker can be most usefully investigated with UV-Vis. Moreover, UV-Vis spectroscopy can determine the band gap of semiconductor materials, via the Tauc method[24] according to Equation 2 . 6.

$$(\alpha h\nu)^{\frac{1}{\gamma}} = B\ (h\nu - E_g)$$

Equation 2 . 6 | Tauc equation

where α is the absorption coefficient of the material,

h the Planck's constant,

ν the frequency of the electromagnetic radiation,

B a constant,

E_g the energy of the band gap,

γ a parameter denoting the nature of the transitions.

For indirect transitions considered in the UiO-series materials $\gamma = 2$. Therefore, a plot of $(\alpha h\nu)^{1/2}$ against photon energy $h\nu$, followed by the extrapolation of the linear region onto the x-axis will yield the optical band gap of the sample.

UV-Vis measurements were performed using Shimadzu UV-2600 under diffuse reflectance mode, with barium sulphate pallet used as the white diffuse standard. The measurement is performed from 200 to 900 nm, with a sampling interval of 0.5 nm at 298 K. The slit width of the measurement is set at 5.0 nm and the wavelength of light source change from W halogen lamp to deuterium lamp was set to be 370.

2.5.2 Photoluminescence (PL)

Photoluminescence is the light emission of a material upon photoexcitation. Typically, various relaxation processes can occur upon photoexcitation, as the excited electron and hole can ideally be diffused onto surface of materials for catalytic redox reactions. In the more common scenarios, the excitons will induce molecular motion such as vibrations or rotations present in the MOFs, or recombine radiatively to release light. PL spectroscopy examines the radiative recombination of excitons for the understanding of electron transition behaviours present in semiconductor materials.

A simplified Jablonski diagram is used to explain the electron transition processes (Figure 2 . 11). Upon photoexcitation, electrons can be promoted to higher energies ($S_0 \rightarrow S_2$), and vibrationally relaxed into S_1 energy state, and consequently recombine with the hole in S_0 energy state to radiate a photon. This process of re-emission of photos at a lower energy compared to the incident photon is defined as fluorescence. However, the electron can go through inter-system crossing into triplet states T_1, where it can also recombine with the hole in S_0 to radiate a photon. This process takes a longer time compared to fluorescence due to the re-emission being associated with “forbidden” transitions in quantum mechanics and is termed

phosphorescence instead. There is no distinct boundary between the emission times of fluorescence and phosphorescence, but generally if a substance glows in UV light it is considered fluorescent, while if it glows in the dark it is called phosphorescent. Note it is also possible for the electrons excited to S_2 to fall back to S_0 and radiatively recombine with high intensities. This process is in frequently measured due to its lack of extractable information of the sample.

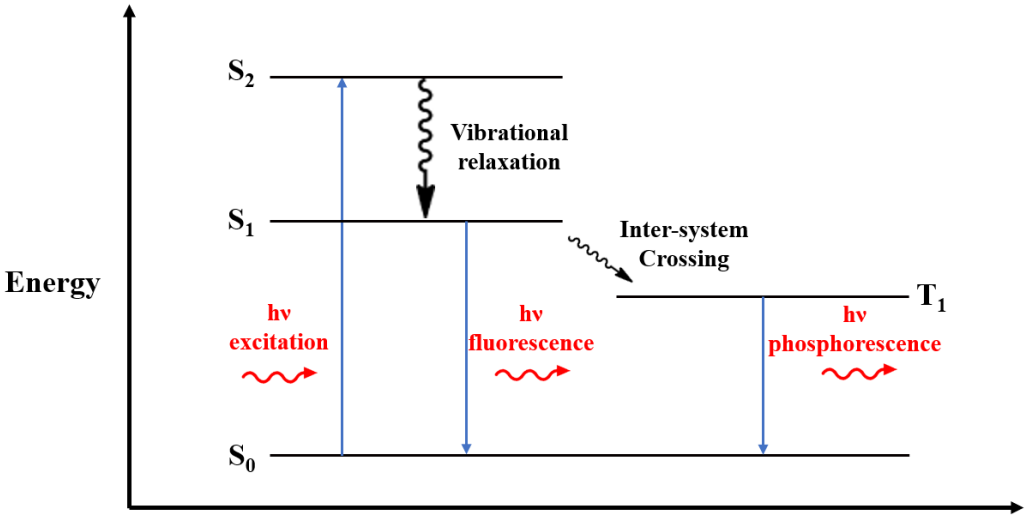


Figure 2 . 11 | Simplified Jablonski diagram showing the light absorption, fluorescence, phosphorescence processes. S_0, S_1 and S_2 are arbitrary singlet states, while T_1 is arbitrary triplet states.

PL spectroscopy can be performed in three modes: Excitation, emission or simultaneous. In excitation mode, the wavelength of detection is held constant, while the excitation wavelength is increased. In Emission mode, the excitation wavelength is held constant, while the wavelength of photons being detected is varied. In simultaneous mode, the difference in wavelength between excitation and emission is held constant and increases simultaneously during measurement. Emission mode is most frequently used for the photoluminescence spectroscopy of MOF materials. In this thesis, the photoluminescence is used as a probe for the interaction between the organic linkers and co-catalysts.

PL data were recorded on Shimadzu RF-6000 spectrofluorophotometer in the Chemistry Teaching Laboratory, University of Oxford. The excitation wavelength is 375 nm with emission wavelength monitored from 400 nm to 700 nm. Data interval was set to be 0.2 nm at a scan rate of 200 nm / min. The bandwidth of excitation and emission are set to be 10 nm. Samples were prepared at a concentration of 1mg/mL with deionised water as solvent at 298K.

2.5.3 Time-resolved photoluminescence (TRPL)

TRPL is a laboratory technique to study the lifetime of PL processes with time resolution. They are used to study the lifetime of excitons in the catalyst. TRPL is a complimentary technique to PL, with the excitation wavelength and emission wavelength identical to the PL peaks used as parameters for measurements with time resolution. The emission of photon due to charge recombination as a function of time will be measured, and the difference in time between the excitation and emission is taken as the lifetime of the exciton. In this thesis, TRPL is done on co-catalyst deposited UiO-series MOFs to measure the lifetime of excitons. TRPL results in chapter 3 are obtained on the FLS1000 fluorescence spectrophotometer with a pulsed laser light source with excitation wavelength 375 nm in Department of Applied Physics, Hong Kong Polytechnic University. The TRPL results in chapter 5 are obtained from a bespoke photoluminescence setup in Department of Physics, University of Oxford. A Ti-Sapphire laser (λ = 266 nm, pulse duration = 150 fs, repetition rate = 76 MHz) is directed onto the sample. The diameter of the laser spot on the sample was approximately 200 μm, and its laser output power was 2 mW, resulting in a power density of 5000 mW cm^{-2}. Time-resolved measurements are performed using a monochromator before passing the signal to a photomultiplier tube detector with an instrument response function width of 150 ps connected to a time-correlated counting module. The TRPL measurements were performed under a pulse-picking mode, with the recorded signals selected with a pulse picker for a long-enough decay of approximately 100 ns for consecutively recorded signals, such that all the excited charge carriers can decay back

to the ground state and avoiding accumulation of charge carriers in the sample. The background-corrected TRPL data are normalized against all samples, and fitted against a mono-exponential ($y = A_1 e^{-\frac{x}{\tau_1}}$) or bi-exponential decay function ($y = A_1 e^{-\frac{x}{\tau_1}} + A_2 e^{-\frac{x}{\tau_2}}$), depending on the presence of one or two kinds of exciton radiative recombination processes. In the equation, y is the observed TRPL data, while x is the time elapsed since excitation. A_1, A_2, τ_1, τ_2 are fitting parameters with τ_1, τ_2 being the lifetime for the PL processes. Errors in the fitting were determined using the least square method. The average lifetime for the sample can be calculated by Equation 2 . 7.

$$t_{avg} = \frac{A_1 t_1^2 + A_2 t_2^2}{A_1 t_1 + A_2 t_2}$$

Equation 2 . 7 | Average lifetime calculation in TRPL.

2.5.4 Transient Absorption Spectroscopy (TAS)

TAS is applied for the study of dynamic photophysical or photochemical processes present in chemical compounds. A laser pulse of a specific wavelength λ (the "pump" pulse) is first used to promote electrons to an excited state, and after a specific time delay τ, another laser pulse (the "probe" pulse) is used to detect the changes in absorbance of the sample, correlated to the population difference between the two states. By subtracting the absorption spectrum of the probe pulse from the pump pulse, a difference absorption (ΔA) spectrum is generated for that specific time delay τ. By repeating the pump-probe analysis at values of τ spanning different orders of magnitude, a comprehensive 2-dimensional ΔA intensity with respect to τ and λ can be obtained. Typically, τ will take values from 1 ps to 1 ms.

The difference of intensity between the two absorption spectra in the pump and probe pulse is measured, and the change in ΔA indicates a change in population difference between the ground state energy level G and excited energy levels A and B (Figure 2 . 12). A positive ΔA

indicates a increased ground state population with respect to the excited state. Examples of such processes include product absorption and further excitation of excited electrons, both reducing the population in the excited state. Conversely, a negative ΔA indicates a reduced ground state population with respect to the excited state. Examples include ground state bleaching, with electrons promoted to the excited states by the pump pulse, or stimulated emissions, electrons fall back to the ground state upon pump pulse with the emission of a photon.

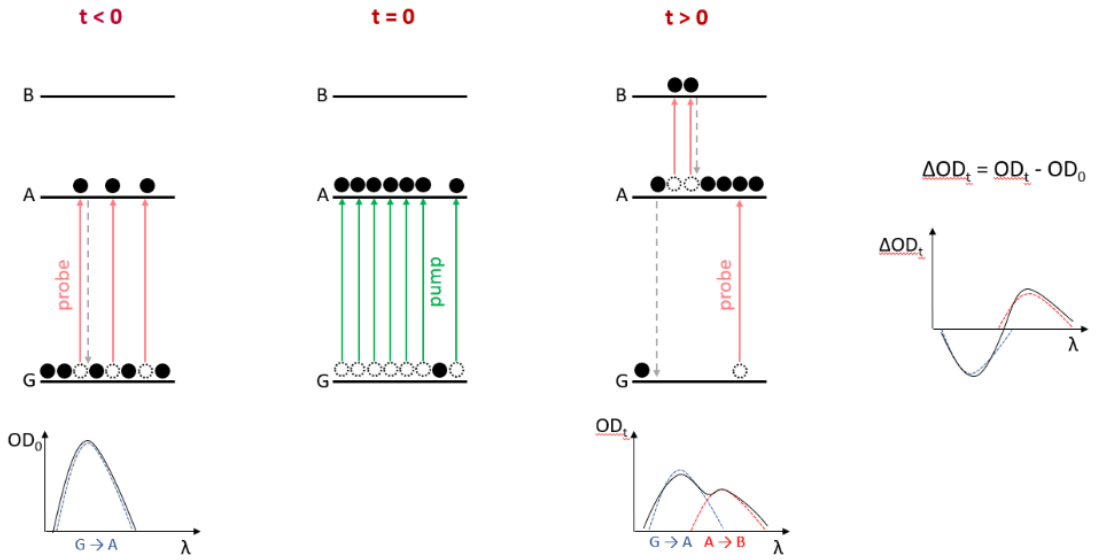


Figure 2 . 12 | Schematic diagram of a Transient Absorption Spectroscopy experiment, reproduced from ref [25].

In this thesis, TAS is used to elucidate the charge transfer processes in the engineered UiO-series MOFs. TAS data in chapter 3 was performed on an Ultrafast Systems Helios Transient Absorption Spectrometer by Shiyanjia, Guangzhou, China. The sample was dispersed in ethane-1,2-diol to reduce the rate of sedimentation and the effect of scattering. TAS data in chapter 4 was performed by using the pump/probe setup in Ultrafast Systems Helios Transient Absorption Spectrometer with an amplified Ti Sapphire femtosecond laser (λ = 800 nm, pulse duration = 50 fs, repetition rate = 1 kHz) in the Department of Applied Physics, Hong Kong

Polytechnic University. The 400 nm pump pulses were obtained by frequency doubling the 800 nm fundamental regenerative amplifier output. The white light continuum probe pulses were generated by focusing a small portion of the regenerative amplifier's fundamental 800 nm laser pulses into a 2 mm sapphire crystal.

2.6 Fuel-forming photocatalysis quantification

2.6.1 Quadrupole Mass Spectrometry (QMS)

Quadrupole mass spectrometry allows the analysis of product according to their mass. As the name implies, the magnetic component consists of four cylindrical rods parallel to each other. The QMS operates similarly to other mass spectrometers, with the incoming samples passing through a capillary heated to 160 °C, and then being atomized and ionized via bombarding with a beam of electrons. The ions are separated in the quadruple based on their trajectories' stability in the oscillating electric fields applied to the rods according to their mass-to-charge (m/z) ratio. Subsequently, they are detected via conversion to electric signal[26].

The QMS measurement was done with the HPR-20 QIC Gas Analysis systems along with the MASsoft software manufactured by Hidden Analytical. The measurement was taken in bar mode for mass number 1 to 5 with the Faraday detector, at sensitivity from 10^{-7} to 10^{-12} Pa. For each scan, the signal from 300 scans is averaged to produce a reliable result. Mass to charge ratio of 3 has been interpreted as signal from hydrogen deuteride[27] for the measurement of catalytic activity in Chapter 3.

2.6.2 Gas chromatography (GC)

Chromatography is the separation of a mixture into its components, which is a technique frequently employed by chemists ranging from organic chemistry to physical chemistry. Depending on the components present in the mixture, the use of different equipment is used for gas chromatography (GC), liquid chromatography (LC), and column chromatography (CC),

and others. The mixture is typically dissolved in either a gaseous or liquid solvent, and termed mobile phase in the context of chromatography. Passing the mobile phase through a stationary phase, which can be composed of a column, a capillary tube, or a sheet, can separate the mixture into the constituent components. This separation against the second law of thermodynamics is achieved via the different affinities of the components in the mobile phase for the stationary phase.

The concept of chromatography can be easily comprehended with a real-life example. An extrovert and an introvert trying to get through a crowd of people. The two people are the mobile phase, while the crowd of people is the stationary phase. The extrovert greets everyone and talks about the weather with every person he/she meets, while the introvert walks straight pass the crowd. As a result, the introvert walks through the crowd faster compared to the extrovert. The separation of the introvert from the extrovert with different retention times (time spent in the stationary phase) is accomplished by their different "affinities" towards strangers.

Gas chromatography is most commonly used in the field of green energy conversion and fuel-forming catalysis for the separation and quantification of gaseous molecules. Depending on the identity of the products, hydrogen, helium or nitrogen can be used as carrier gas (gaseous solvent) for the sample. Fused silica capillaries with inner diameters and length in the range of 100 μm and 10 m are commonly used as stationary phase for GC. The varied affinity for different molecules such as H_2, CO_2, CH_4 and others with the silica allow their separation. Different detectors are used for different molecules, most commonly thermal conductivity detector (TCD) or flame ionization detector (FID).

Thermal conductivity detector (TCD)

Hydrogen and helium have high thermal conductivities and are commonly used as carrier gas complementary to this detector. TCD measures the changes in the thermal conductivity of the mixture upon passing through the stationary phase and compares it to a reference flow of pure

carrier gas. A reduction of thermal conductivity of the separated mixture with respect to pure carrier gas will produce a detectable signal with a certain retention time. All organic or inorganic compounds have some non-zero thermal conductivity that is lower than helium or hydrogen, and therefore virtually all compounds can be detected. Plotting the intensity of signal from the TCD against retention time, the peak position on the baseline indicates the type of compound, while the peak area obtained by integration of the TCD signal over time corresponds to its concentration. In this thesis, the TCD detector with nitrogen as the carrier gas coupled with Agilent 7890 GC is used for the detection of H_2 from photocatalytic water splitting in Chapter 4.

Flame Ionization Detector (FID)

The operating principle of an FID is based on the measurement of ions formed during the combustion of carbon-based compounds in a hydrogen flame via conversion into electrical current[28]. The concentration of generated ions is proportional to their concentration in the gas stream, and the intensity of signal corresponds roughly to the number of carbons present in the compound prior to combustion. Lists of response factors are available in the literature to allow for the divergent current generated by the FID detector[29-31]. FID is widely used in GC systems due to its relatively low cost and wide range for detection. Nevertheless, its limitations stems from the requirement of the presence of C-H bonds which excludes CO and CO_2. The detection of CO and CO_2 can be realized by coupling the FID detector with a methanizer, which is a bed of Ni catalyst to reduce CO and CO_2 to methane for detection by FID. Similar to the TCD detector, if the signal from the FID is plotted against retention time, the peak position on the baseline indicates the type of compound, while the peak area obtained by integration of the FID signal over time corresponds to its concentration. In this thesis, the FID detector with hydrogen as the carrier gas coupled with Agilent 7890 GC is used for the detection of CO and CH_4 from photocatalytic CO_2 reduction in Chapter 5.

2.7 Density Functional Theory (DFT) Calculations

The periodic structures were optimized by performing spin-polarized density functional theory (DFT) calculations using the *Vienna ab initio Simulation Package* (*VASP*)[32-34]. The PBEsol[35] exchange–correlation functional with the D3 dispersion correction of Grimme[36] was applied for geometry optimizations. The core–valence electron interactions were treated by using the projector augmented wave (PAW)[37] method. A kinetic energy cutoff of 500 eV was used for all periodic DFT calculations. A 1×1×1 *k*-point mesh was used for the sampling of the first Brillouin zone. Both atomic positions and the shape of the cell were allowed to relax during optimizations, for which we used a Hellman–Feynman force criterion of 0.05 eV/Å for each ion.

For Chapter 3, the cluster models of the Ru/NH_2 and Ru/bpy structures were constructed by capping the $[RuCl_3(H_2O)_2(BDC\text{-}NH_2)_3]^{6-}$ and $[RuCl_2(H_2O)_2(BPYDC)_3]^{6-}$ anions with protons, respectively. The ground-state structures for models in Chapter 3 and 5 were obtained by a two-step optimization procedure. In the first step, only the proton capping ions were optimized. In the second step, the COOH groups of the carboxylates were fixed to retain periodic constraints, while the other atoms were allowed to fully relax. Time-dependent density functional theory (TDDFT) with the adiabatic linear-response approximation[38] was used for excited-state calculations. The cluster calculations were performed using the *Gaussian 16* program[39]. The B3LYP[40] exchange–correlation functional and the def2-TZVP[41-43] basis set were used for the calculations; for Ru, effective core potential (ECP) was used. Note that B3LYP is the most commonly used functional for Ru-complexes in the reported studies[44-47]. The electron-hole distributions were calculated by using the *Multiwfn*[48,49] and visualized by using the VESTA[50].

The primitive cell was employed to perform spin-polarized periodic DFT calculations by using the Vienna ab initio Simulation Package (VASP). The PBEsol and HSE06 exchange–correlation functionals were applied for geometry optimizations and single point calculations (to obtain energies). We refer to this protocol as HSE06//PBEsol.

The core electrons were treated by using the projector augmented wave (PAW) method with a kinetic energy cutoff of 500 eV. A 1×1×1k –point mesh sampling (i.e., Γ point sampling of the first Brillouin zone) was used for geometry optimizations. The convergence criterion for SCF iterations was 10−5 eV. Both atomic positions and the shape of the cell were allowed to relax during optimization, for which we used a Hellman–Feynman force criterion of 0.05 eV/Å on each ion. The D3 dispersion correction of Grimme was considered in the geometry optimization and calculations of energies.

Calculations on isolated RuCl3-linker type species were performed using Gaussian 16. The isolated linkers were constructed by protonating the RuCl3-NH2-BDC2- or the RuCl3-BPYDC2- anions cut from the optimized periodic models. The ground state (GS) structures of the isolated linkers were optimized by relaxing the proton cappings only. The optimized GS structures were then used to perform excited state (ES) calculations using time-dependent DFT(TD-DFT) with the adiabatic linear-response approximation, that is, we consider vertical transitions. The first 50 excited states were calculated for each isolated linker. For the cluster calculations, we used the b3lyp exchange–correlation functional with the def2-TZVP basis set for C, N, Cl and H and the SDD, MWB28 basis set for Ru. The electron-hole distribution maps were simulated by the Multiwfn.

We tested the M06/B3LYP/HSE06/Cam-b3lyp functionals. As a result, M06/B3LYP/HSE06 show the properties : NH2-UiO-66 (ligand-to-$RuCl_3$ CT excitation can occur while RuCl3-to-ligand CT excitation can’t appear); RuCl3-bpydc-UiO-67 (RuCl3-to-ligand CT excitation can

occur), especially B3LYP. (B3LYP is the most commonly used functional for Ru-complex in the reported studies.)

2.8 References

1 Cavka, J. H., Jakobsen, S., Olsbye, U., Guillou, N., Lamberti, C., Bordiga, S. & Lillerud, K. P. A New Zirconium Inorganic Building Brick Forming Metal Organic Frameworks with Exceptional Stability *J Am Chem Soc* **130**, 13850-13851 (2008).

2 Zhang, K., Hu, H., Shi, L., Jia, B., Huang, H., Han, X., Sun, X. & Ma, T. Strategies for Optimizing the Photocatalytic Water-Splitting Performance of Metal–Organic Framework-Based Materials. *Small Science* **1** (2021).

3 Bragg, W. H. & Bragg, W. L. The Reflection of X-rays by Crystals *Proc. R. Soc. Lond. A* **88**, 428-438 (1913).

4 Rietveld, H. M. A profile refinement method for nuclear and magnetic structures. *J. Appl. Cryst.* **2**, 65-71 (1969).

5 David, W. I. F. Powder Diffraction: Least-Squares and Beyond. *J Res Natl Inst Stand Technol* **109**, 107-123 (2004).

6 Lutterotti, L. & Scardi, P. Simultaneous Structure and Size-Strain Refinement by the Rietveld Method. *J. Appl. Cryst.* **23**, 246-252 (1990).

7 Chalmin, E., Farges, F. & Brown, G. E. A pre-edge analysis of Mn K-edge XANES spectra to help determine the speciation of manganese in minerals and glasses. *Contributions to Mineralogy and Petrology* **157**, 111-126 (2008).

8 Glatzel, P., Bergmann, U., Yano, J., Visser, H., Robblee, J. H., Gu, W., Groot, F. M. F., Christou, G., Pecoraro, V. L., Cramer, S. P. & Yachandra, V. K. The Electronic Structure of Mn in Oxides, Coordination Complexes, and the Oxygen-Evolving Complex of Photosystem II Studied by Resonant Inelastic X-ray Scattering. *J Am Chem Soc* **126**, 9946-9959 (2004).

9 Westre, T. E., Kennepohl, P., DeWitt, J. G., Hedman, B., Hodgson, K. O. & Solomon, E. I. A Multiplet Analysis of Fe K-edge 1s - 3d Pre-edge Features of Iron Complexes. *J Am Chem Soc* **119**, 6297-6314 (1997).

10 Farges, F. Ab initioand experimental pre-edge investigations of the MnK-edge XANES in oxide-type materials. *Physical Review B* **71** (2005).

11 Trummer, D., Searles, K., Algasov, A., Guda, S. A., Soldatov, A. V., Ramanantoanina, H., Safonova, O. V., Guda, A. A. & Coperet, C. Deciphering the Phillips Catalyst by Orbital Analysis and Supervised Machine Learning from Cr Pre-edge XANES of Molecular Libraries. *J Am Chem Soc* **143**, 7326-7341 (2021).

12 Wang, J., Sun, K., Jia, X. & Liu, C.-j. CO2 hydrogenation to methanol over Rh/In2O3 catalyst. *Catalysis Today* **365**, 341-347 (2021).

13 Yang, H., Zhang, X., Yu, Y., Chen, Z., Liu, Q., Li, Y., Cheong, W. C., Qi, D., Zhuang, Z., Peng, Q., Chen, X., Xiao, H., Chen, C. & Li, Y. Manganese vacancy-confined single-atom Ag

in cryptomelane nanorods for efficient Wacker oxidation of styrene derivatives. *Chem Sci* **12**, 6099-6106 (2021).

14 Wang, J., Hsu, C. S., Wu, T. S., Chan, T. S., Suen, N. T., Lee, J. F. & Chen, H. M. In situ X-ray spectroscopies beyond conventional X-ray absorption spectroscopy on deciphering dynamic configuration of electrocatalysts. *Nat Commun* **14**, 6576 (2023).

15 Ressler, T. WinXAS: a program for X-ray absorption spectroscopy data analysis under MS-Windows. *J Synchrotron Radiat* **5**, 118-122 (1998).

16 Figueroa, S. J. A. & Prestipino, C. PrestoPronto: a code devoded to handling large data sets. *J. Phys.: Conf. Ser.* **712** (2016).

17 Klementev, K. V. Package "VIPER (visual processing in EXAFS researches) for windows". *Nuclear Instruments and Methods in Physics Research A* **448**, 299-301 (2000).

18 Martini, A., Guda, S. A., Guda, A. A., Smolentsev, G., Algasov, A., Usoltsev, O., Soldatov, M. A., Bugaev, A., Rusalev, Y., Lamberti, C. & Soldatov, A. V. PyFitit: The software for quantitative analysis of XANES spectra using machine-learning algorithms. *Computer Physics Communications* **250** (2020).

19 Ravel, B. & Newville, M. ATHENA, ARTEMIS, HEPHAESTUS: data analysis for X-ray absorption spectroscopy using IFEFFIT. *J Synchrotron Radiat* **12**, 537-541 (2005).

20 Ng, B. K. Y., Wong, C. C. Y., Niu, W., Garcia, H. P., Li, Y., Ho, P.-L., Kuo, W. C. H., Taylor, R. A., Taniya, K., Wei, Q., Li, M., Stamatakis, M. & Tsang, S. C. E. Molecular layer-by-layer re-stacking of MoS2–In2Se3 by electrostatic means: assembly of a new layered photocatalyst. *Materials Chemistry Frontiers* **7**, 937-945 (2023).

21 Zhang, H., Diao, J., Liu, Y., Zhao, H., Ng, B. K. Y., Ding, Z., Guo, Z., Li, H., Jia, J., Yu, C., Xie, F., Henkelman, G., Titirici, M. M., Robertson, J., Nellist, P., Duan, C., Guo, Y., Riley, D. J. & Qiu, J. In-Situ-Grown Cu Dendrites Plasmonically Enhance Electrocatalytic Hydrogen Evolution on Facet-Engineered Cu(2) O. *Adv Mater* **35**, e2305742 (2023).

22 Held, G., Venturini, F., Grinter, D. C., Ferrer, P., Arrigo, R., Deacon, L., Quevedo Garzon, W., Roy, K., Large, A., Stephens, C., Watts, A., Larkin, P., Hand, M., Wang, H., Pratt, L., Mudd, J. J., Richardson, T., Patel, S., Hillman, M. & Scott, S. Ambient-pressure endstation of the Versatile Soft X-ray (VerSoX) beamline at Diamond Light Source. *J Synchrotron Radiat* **27**, 1153-1166 (2020).

23 Brunauer, S., Emmett, P. H. & Teller, E. Adsorption of Gases in Multimolecular Layers. *J Am Chem Soc* **60**, 309-319 (1938).

24 Tauc, J. Optical Properties and Electronic Structure of Amorphous Ge and Si. *Mat. Res. Bull.* **6**, 37-46 (1968).

25 Instruments, E. *What is Transient Absorption Spectroscopy?*

26 Edmond, H. & Stroobant, V. *Mass Spectrometry: Principles and Applications (Second Edition)*. 65 (John Wiley & Sons, Ltd., 2003).

27 R. E. Ellefson, W. E. M. Hydrogen isotope analysis by quadrupole mass spectrometry. *J. Vac. Sci. Techhnol.* **18(3)** (1981).

28 McWilliam, I. G. & Dewar, R. A. Flame Ionization Detector for Gas Chromatography. *Nature* **181**, 760.

29 Tong, H. Y. & Karasek, F. W. Flame Ionization Detector Response Factors for Compound Classes in Quantitative Analysis of Complex Organic Mixtures. (1984).

30 Dietz, W. A. Response Factors for Gas Chromatographic Analyses. *J Chromatogr Sci* **5**, 68-71 (1967).

31 Marvai, M., Palyka, I. & Molnar-Perl, I. Flame Ionization Detector Response Factors Using the Effective Carbon Number Concept in the Quantitative Analysis of Esters. *J Chromatogr Sci* **30**, 448-452 (1992).

32 Kresse, G. & Joubert, D. From ultrasoft pseudopotentials to the projector augmented-wave method. *Phys Rev B* **59**, 1758 (1999).

33 Kresse, G. & Furthmuller, J. Efficient iterative schemes for ab initio total-energy calculations using a plane-wave basis set. *Phys Rev B* **54**, 11169-11186 (1996).

34 Kresse, G. & Furthmuller, J. Efficiency of ab-initio total energy calculations for metals and semiconductors using a plane-wave basis set. *Comput Mater Sci* **6**, 15-50 (1996).

35 Perdew, J. P., Ruzsinszky, A., Csonka, G. I., Vydrov, O. A., Scuseria, G. E., Constantin, L. A., Zhou, X. & Burke, K. Restoring the density-gradient expansion for exchange in solids and surfaces. *Phys Rev Lett* **100**, 136406 (2008).

36 Grimme, S., Antony, J., Ehrlich, S. & Krieg, H. A consistent and accurate ab initio parametrization of density functional dispersion correction (DFT-D) for the 94 elements H-Pu. *J Chem Phys* **132**, 154104 (2010).

37 Blochl, P. E. Projector augmented-wave method. *Phys Rev B Condens Matter* **50**, 17953-17979 (1994).

38 Casida, M. E., Jamorski, C., Casida, K. C. & Salahub, D. R. Molecular excitation energies to high-lying bound states from time-dependent density-functional response theory: Characterization and correction of the time-dependent local density approximation ionization threshold. *J Chem Phys* **108** (1997).

39 Gaussian 16 Rev. C.01 (Wallingford, CT, 2016).

40 Becke, A. D. Density-functional thermochemistry. III. The role of exact exchange. *J Chem Phys* **98**, 5648-5652 (1993).

41 Weigend, F. Accurate Coulomb-fitting basis sets for H to Rn. *Phys Chem Chem Phys* **8**, 1057-1065 (2006).

42 Weigend, F. & Ahlrichs, R. Balanced basis sets of split valence, triple zeta valence and quadruple zeta valence quality for H to Rn: Design and assessment of accuracy. *Phys Chem Chem Phys* **7**, 3297-3305 (2005).

43 Andrea, D., Hausermann, U., Dolg, M., Stoll, H. & Preus, H. Energy-adjusted ab initio pseudopotentials for the second and third row transition elements. *Theor Chim Acta* **77**, 123-141 (1990).

44 Fantacci, S., De Angelis, F., Sgamellotti, A. & Re, N. A TDDFT study of the ruthenium(II) polyazaaromatic complex [Ru(dppz)(phen)2]2+ in solution. *Chem Phys Lett* **396**, 43-48 (2004).

45 Hughes, T. F. & Friesner, R. A. Systematic investigation of the catalytic cycle of a single site ruthenium oxygen evolving complex using density functional theory. *J Phys Chem B* **115**, 9280-9289 (2011).

46 Askevold, B., Khusniyarov, M. M., Herdtweck, E., Meyer, K. & Schneider, S. A square-planar ruthenium(II) complex with a low-spin configuration. *Angew Chem Int Ed Engl* **49**, 7566-7569 (2010).

47 Fomine, S. & Tlenkopatchev, M. A. Cross-metathesis of dimethyl maleate and ethylene catalyzed by second generation ruthenium carbene complexes: B3LYP and MPW1K comparison study. *J Organomet Chem* **691**, 5189-5196 (2006).

48 Lu, T. & Chen, F. Multiwfn: a multifunctional wavefunction analyzer. *J Comput Chem* **33**, 580-592 (2012).

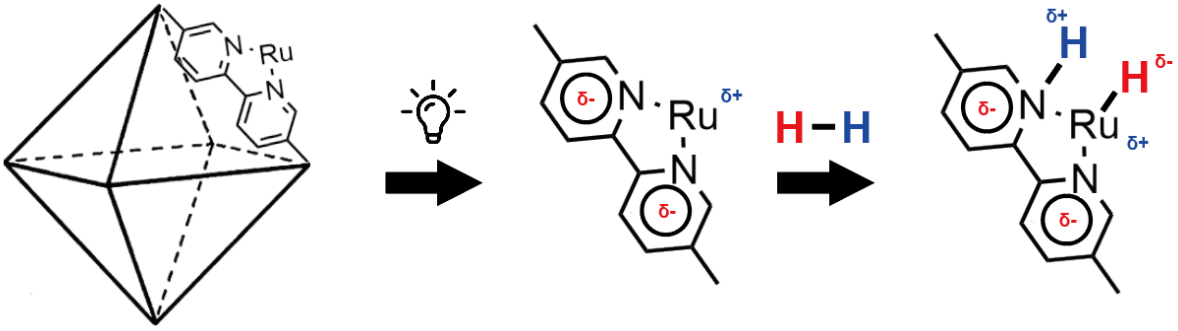
49 Liu, Z., Lu, T. & Chen, Q. An sp-hybridized all-carboatomic ring, cyclo[18]carbon: Electronic structure, electronic spectrum, and optical nonlinearity. *Carbon* **165**, 461-467 (2020).

50 Momma, K. & Izumi, F. VESTA 3for three-dimensional visualization of crystal, volumetric and morphology data. *J Appl Crystallogr* **44**, 1272-1276 (2011).

3 Chapter 3 | Designing UiO-based catalysts for photocatalytic heterolytic hydrogen activation

3.1 Graphical abstract

The work in this chapter has been published in Journal of the American Chemistry Society as "Photo-Induced Active Lewis Acid-Base Pairs in a Metal-Organic Framework for H_2 Activation". The charge transfer from Ru metal to the bipyridine ligands upon light irradiation has polarized the Ru-N Lewis Acid-base pair, for heterolytic activation of the hydrogen molecule.



3.2 Introduction

The activation of H-H bond is challenging in various catalytic process for the production of fuels[1]. Traditional oxidative addition step over electron-rich transition metal center can lead to H-H cleavage into two M-H bonds. Recently, Frustrated Lewis pairs (FLPs) involving synergetic sites can be created from stereo-isolated Lewis acid and base sites in close proximity or derived from a weak intramolecular adduct instead of using single transition metal center to provide an alternative pathway for the heterolytic H-H bond cleavage by the charged, polarized bodies. From the pioneering work of Welch and Stephan, who reported the heterolytic fission of H-H bond by sterically bulky phosphines and boranes[2], the application of FLP in catalysis have been prominent in the activation of different small molecules including CO_2 and alkynes

since the extension of the concept into heterogeneous systems by combining imines and nitriles as Lewis base and the gold surface as Lewis acid[3]. Geometrically separated anion vacancies and hydroxyl groups have then been reported as Lewis basic and acidic sites, respectively[4-6]. However, the majority of such FLP catalysts have the Lewis basic and acidic sites separately introduced, which prohibits the precise control of the location and quantity of the active sites. Further advance in synthesis methods would be required for the improved catalytic application of FLP for small molecule activation by enhanced control of the active sites.

Molecular activation via photochemical means is generally achieved under comparatively milder conditions. Photocatalytic activation of H-H bond would therefore be beneficial towards energy efficiency. Our approach for the design of such photo-active transient but polarized Lewis acid-base sites in metal-organic framework (MOF) materials are inspired by the characteristic superior surface area and porosity of the MOFs and their anchored transition metal(s) with designated linkers of tunable properties to capture light energy with facilitated polarization, which could create the required active Lewis acid and base pair for synergetic activation of substrate[7]. In our previous work, we have utilized various MOFs as supports for design of efficient catalysts thanks to their vast chemical tunability[8]. MOFs are extending frameworks formed by the coordination of metal clusters with polyfunctional organic ligands, specifically the Universitet-i-Oslo (UiO) series[9]. Its incredible chemical stability is credited to the strong electrostatic attraction between highly charged $Zr_6O_4(OH)_4$ clusters and carboxylic acid-based organic linkers[10-12]. Its aforementioned adjustable functional groups and tunable pore sizes[13-15] have attracted considerable attention for applications in adsorption[16], separation[17], sensing[18,19] and catalysis[20-22]. Thanks to such tunability of the UiO series, the ruthenium bipyridine motives can be integrated onto the MOF systems. Ruthenium has been deposited onto MOF UiO-67-bpydc with 2,2'-bipyridine-5,5'-dicarboxylic acid analogous to ruthenium bipyridine complexes[23,24] (denoted Ru/bpy). For comparison, ruthenium-amine

complexes were also synthesised with ruthenium decorated UiO-66-NH_2 (denoted Ru/NH_2), where 2-aminoterephthaclic acid was used as the organic linker.

In this work, we demonstrate the high activity for H_2-D_2 exchange of our photo-induced FLP-like catalyst with ruthenium deposited UiO-67-bpydc (Ru/bpy) under illumination. Our synthesis method give precise control of FLP-like active site location and quantity in the solid catalyst. Synchrotron X-ray absorption and X-ray diffraction measurements were initially performed to determine the structures of the anchored ruthenium complexes onto the frameworks with precision before the theoretical calculations. The optical properties of different Ru-MOFs were also characterized with UV-Vis, PL and TRPL. Excited-state calculations based on time-dependent density functional theory (TDDFT) were particularly performed to rationalize the charge transfer processes and the formation of photo-induced active sites in excited states. IR and 2D NMR indicated the synergetic formation of hydride and proton from dihydrogen via the formation of transient Lewis acid-base pair upon illumination.

3.3 Results and Discussion

3.3.1 Structural Characterization

Ruthenium deposited UiO-67-bpydc (bipyridine linker) and UiO-66-NH_2 (benzylamine linker) were synthesized as prototypes for photo-induced FLP. Inductively-coupled plasma-mass spectrometry (ICP-MS) results on both Ru/bpy and Ru/NH_2 showed similar Ru: Zr ratio of 0.352 and 0.344 (Table 3 . 1).

Sample	Ru (ppm)	Zr (ppm)	Ru:Zr
Ru/NH_2	90.69	257.94	0.352
Ru/bpy	117.74	342.46	0.344

Table 3 . 1 | Amount of Ru and Zr as determined by ICP-MS analysis

Advanced techniques were then utilized to characterize the structures of their Ru loaded samples, namely, Ru/bpy (UiO-67-bpydc with Ru) and Ru/NH_2 (UiO-66-NH_2 with Ru). First, extended X-ray absorption fine structure (EXAFS) was performed on the two ruthenium deposited MOFs to probe their local coordination environment. The scattering paths generated from bulk RuN, RuO_2 and $RuCl_3$ were then used to fit the R-space EXAFS data (Figure 3 . 1 a-b), with the k-space data and fit available in Figure 3 . 1 c-d and fitting parameters available in Table 3 . 2 and Table 3 . 3.

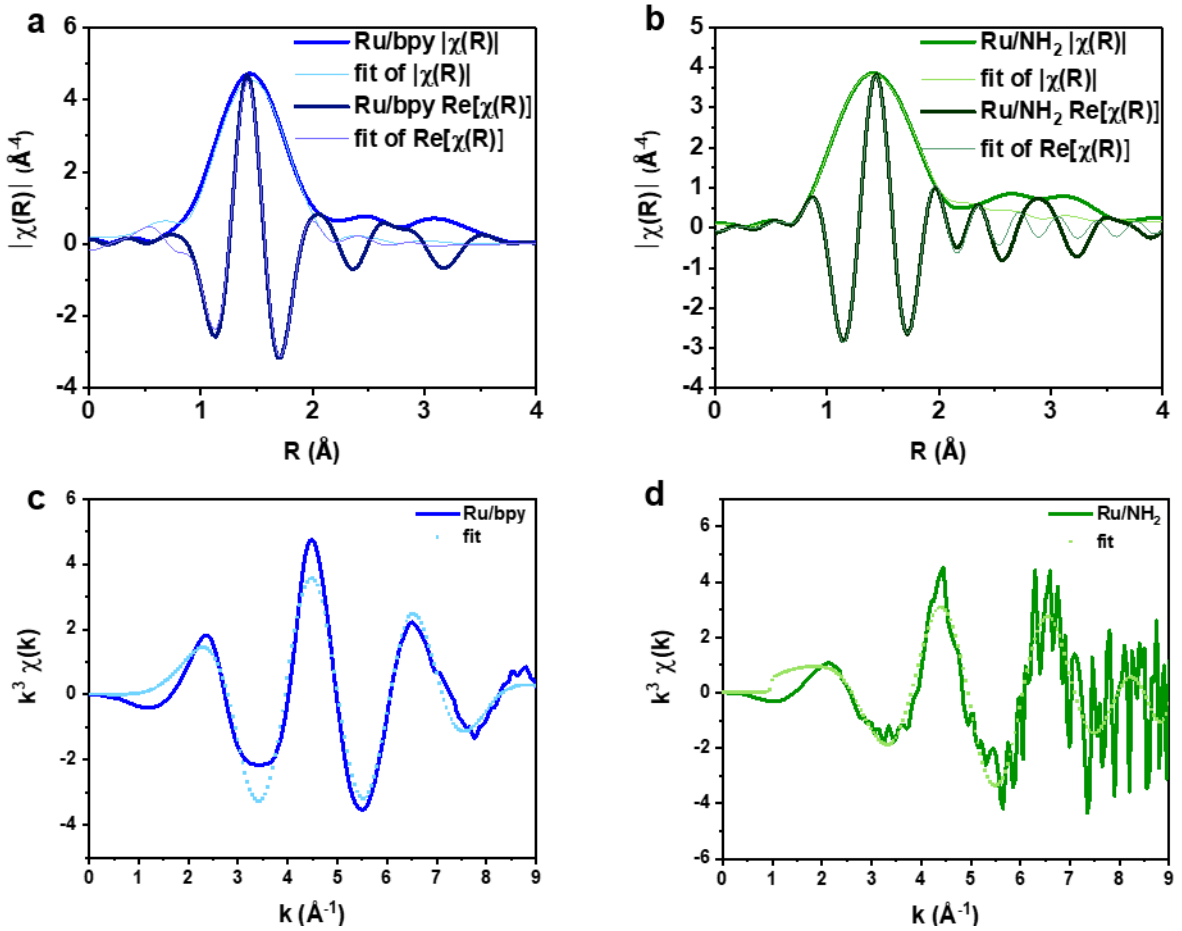


Figure 3 . 1 | Fourier-transformed magnitude of the experimental Ru K-edge k^3-weighted R-space EXAFS data and fit of (a) Ru/bpy and (b) Ru/NH_2, where |χ(R)| and Re[χ(R)] denote the magnitude and real part of the Fourier transformed k-space data. k^3-weighted k-space EXAFS data and fit for (c) Ru/bpy and (d) Ru/NH_2. Dr. Tai-Sing Wu and Prof. Yun-Liang Soo are gratefully acknowledged for their assistance in EXAFS data collection. The EXAFS data fitting was performed by Bryan Ng.

Path	CN	R / Å	D-W factor (σ^2)
Ru-N	2.0 ± 0.2	2.30 ± 0.02	0.003 ± 0.002
Ru-O	2.2 ± 0.3	1.94 ± 0.01	0.003 ± 0.002
Ru-Cl	2.2 ± 0.2	2.28 ± 0.02	0.013 ± 0.003

Table 3 . 2 | EXAFS fitting parameters of Ru/bpy

Fitting was performed with all k^1, k^2, and k^3-weighted R-space data. S_0^2 was fixed as 0.85[25] and ΔE_0 was evaluated as -4.18 ± 0.37 eV. Data ranges $2 \leq k \leq 9$ Å^{-1}, $1.0 \leq R \leq 2.2$ Å. R factor for this fit is 0.59 % (R-factor by k-weight: k^1: 0.54 %, k^2: 0.41 %, k^3:0.81 %).

Path	CN	R / Å	D-W factor (σ^2)
Ru-N	0.9 ± 0.1	1.78 ± 0.04	0.012 ± 0.001
Ru-O	1.9 ± 0.1	2.00 ± 0.01	0.001 ± 0.001
Ru-Cl 1	2.0 ± 0.1	2.24 ± 0.01	0.009 ± 0.001
Ru-Cl 2	1.0 ± 0.2	2.43 ± 0.02	0.015 ± 0.003

Table 3 . 3 | EXAFS fitting parameters of Ru/NH_2

Fitting was performed with all k^1, k^2, and k^3-weighted R-space data. S_0^2 was fixed as 0.85 and ΔE_0 was evaluated as -7.53 ± 0.17 eV. Data ranges $2 \leq k \leq 9$ Å^{-1}, $1.1 \leq R \leq 2.2$ Å with Rbkg set at 1.1 Å. R factor for this fit is 0.04 % (R-factor by k-weight: k^1: 0.02 %, k^2: 0.03 %, k^3:0.06 %).

The goodness of fit in EXAFS data is shown by the low R-factor of 0.59 % and 0.04 % for Ru/bpy and Ru/NH_2, respectively. In both Ru/NH_2 and Ru/bpy, it is unambiguous that there is no aggregation of the ruthenium species in the system, by comparing the data to the scattering paths generated from the bulk references RuN, RuO_2, $RuCl_3$ and Ru foil (Figure 3 . 2).

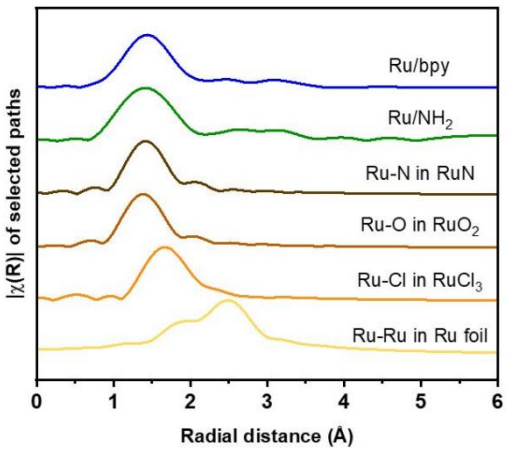


Figure 3 . 2 | Comparison of scattering paths generated by Ru-N, Ru-O, Ru-Cl and Ru-Ru.

In total for the average of ca. 6 coordination (6.4 ± 0.7 for Ru/bpy and 5.8 ± 0.5 for Ru/NH_2). The degeneracy obtained from fitting for Ru/bpy shows value of 2.0(2) Ru-N from the bipyridine linker, 2.2 ± 0.3 Ru-O from adsorbed H_2O and 2.2 ± 0.2 Ru-Cl. For Ru/NH_2, 0.9 ± 0.1 Ru-N from linker, 1.9 ± 0.1 Ru-O and 3.0 ± 0.3 Ru-Cl. To further determine their structures, synchrotron X-ray diffraction (SXRD) was performed on all the samples and is shown in

Figure 3 . 3 a-b. Notice that the positions of Bragg peaks remain unchanged (space group: Fm-3m) for both of samples, implying that the crystalline framework of the host MOF remains mostly unaltered by the Ru incorporation. Further Rietveld refinement of the model was built based on the bond lengths from EXAFS fitting resulted to generate an SXRD pattern and a satisfactory fit (R_{wp} values of 15.46 and 10.58 for Ru/bpy and Ru/NH_2, respectively) with acceptable parameters was obtained through the Rietveld method[26]. The refined structures are shown in Figure 3 . 3 c-d, with the Rietveld refined parameters and fit in Table 3 . 4 and Table 3 . 5. The observed, calculated and difference in peak intensities of SXRD are shown in Figure 3 . 3 e-f.

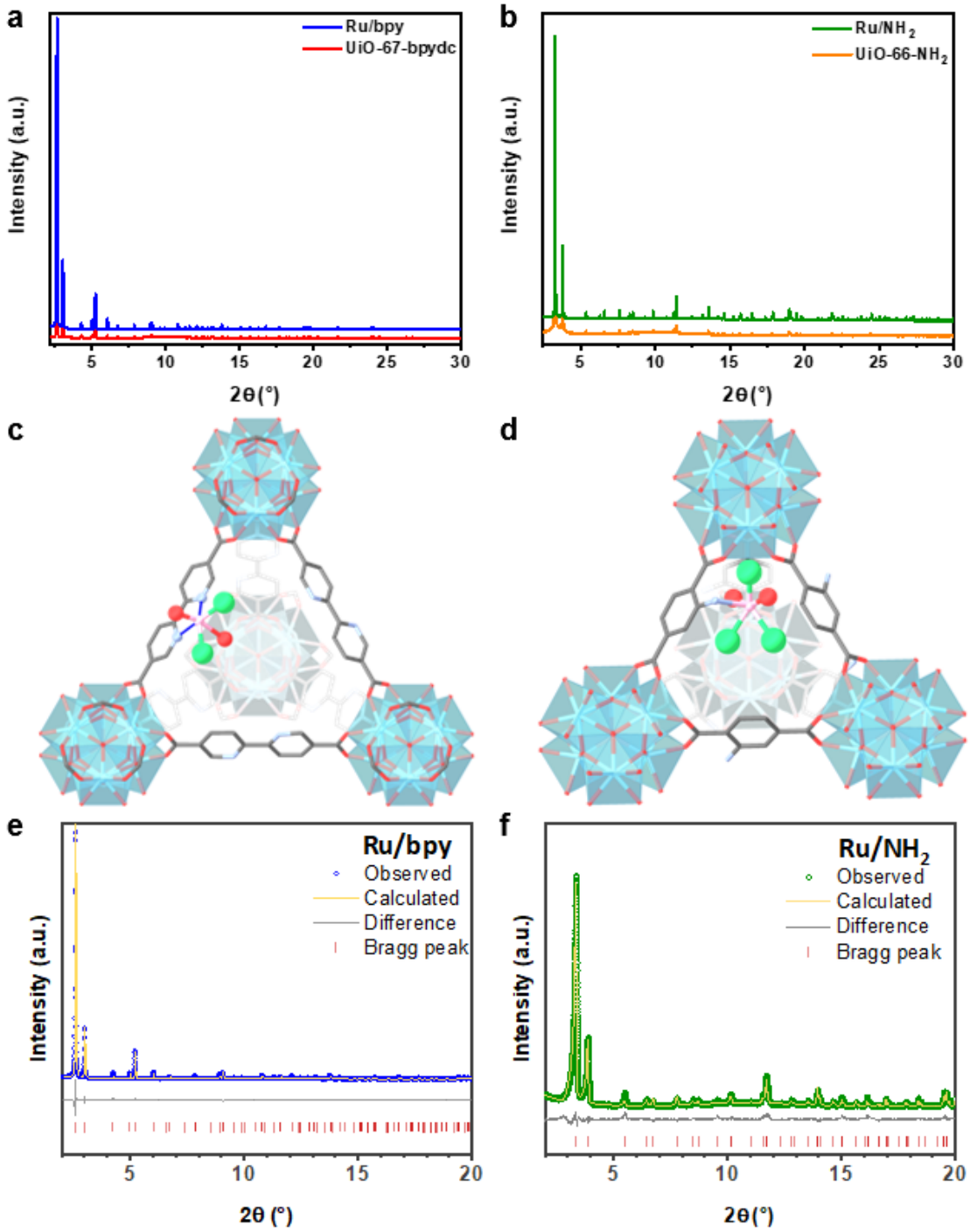


Figure 3 . 3 | High-throughput X-ray diffraction of (a) Ru/bpy and UiO-67-bpydc, (b) Ru/NH_2 and UiO-66-NH_2. Crystal structures built from Rietveld Refinement of SXRD data with EXAFS fitting parameters of (c) Ru/bpy and (d) Ru/NH_2. Colour scheme: Zr = light blue polyhedra, O = red, C = black, N = blue, Ru = pink and Cl = light green. Hydrogen and adsorbed water O-atoms have been omitted for clarity. (e) Rietveld refinement of Ru/bpy and (f)

Rietveld refinement of Ru/NH_2. Assistance from Dr. Tatchamapan Yoskamtorn is gratefully acknowledged for the Rietveld refinement of the SXRD data.

Unit cell of Ru/bpy, Crystal system: Cubic, Space group: Fm-3m

Unit cell parameter: a=b=c=26.5471 ± 0.0005 Å

Unit cell angle: α=β=γ=90°; $R_{wp}/R_p/R_{exp}$(%): 15.46/10.93/0.75. Goodness of fit: 20.52

Atom	Multiplicity	Fractional coordinates			Occupancy	B_{iso} (Å^2)
		X	y	z		
Zr1	24	0.5	0	0.0932	1	0.75117
O1	96	0.42693	0	0.13363	1	0.4992
O2A	32	0.4465	-0.0535	0.0535	0.5	0.0
O2B	32	0.4594	-0.0406	0.0406	0.5	0.0
C4	96	0.3814972	-1.916582e-16	0.1180148	0.56664	3.55441
C5	96	0.3417866	-9.993049e-17	0.1577254	0.56664	3.55441
C8	96	0.2700049	6.40707e17	0.2295072	0.46132	9.92876
C9	192	0.255576	0.002400547	0.1810787	0.23066	9.92876
C10	192	0.292159	0.002373526	0.1452033	0.46132	9.92876
N9	192	0.255576	0.002400547	0.1810787	0.23066	9.92876
H1	32	0.4284	-0.0716	0.0716	0.5	0.0
H9	192	0.2209608	0.004061182	0.172211	0.23066	11.91451
H10	192	0.2828014	0.004049805	0.1106683	0.46132	11.91451
Ru1	192	0.18264	0.00488	0.1894	0.04169	19.96562
Cl1	192	0.09744389	0.007884507	0.19611037	0.04169	19.96562
Cl2	192	0.183064	0.008137123	0.1039509	0.04169	19.96562
Or1	192	0.1796612	-0.07266422	0.1894106	0.04169	19.96562
Or2	192	0.1856311	0.08209076	0.1822214	0.04169	19.96562
O_w1	96	0.31546	-0.07176	0.07176	0.45478	19.99141
O_w2	32	0.39485	-0.10515	0.10515	0.42006	19.99141
O_w3	192	0.33443	0.3354	0.33354	0.29149	19.99141

O_w4	192	0.60942	0.51622	-0.98548	0.01881	19.99141

Table 3 . 4 | Atomic parameters from Rietveld refinement of SXRD measurement for Ru/bpy

Unit cell of Ru/NH_2, Space group Fm-3m

Unit cell parameter: a=b=c=20.8116 ± 0.0001 Å

Unit cell angle: α=β=γ=90°; $R_{wp}/R_p/R_{exp}$(%):10.58/7.59/6.86. Goodness of fit: 1.54

Atom	Multiplicity	Fractional coordinates			Occupancy	B_{iso} ($Å^2$)
		x	y	z		
Zr1	24	0.11898	0	0	1	0.29153
O2A	32	0.0496	0.0496	0.0496	0.5	0.01487
O2B	32	0.07143	0.07143	0.07143	0.5	0.01487
C1	48	0.5	0.20254	0.29746	0.6673	3.37132
C2	192	0.4957595	0.2672635	0.3147305	0.6673	3.37132
C3	48	0.5	0.14971	0.35029	1	0.01487
O1	96	0.5	0.14971	0.35029	1	0.01487
N1	192	0.3043871	-0.0106218	0.1110782	0.166825	3.37132
Ru1	192	0.27891	0.0665	0.08978	0.057	19.7
Cl1	192	0.348658	0.07751482	0.1710116	0.057	19.7
Cl2	192	0.1945092	0.1297852	0.1409389	0.057	19.7
Cl3	192	0.2218596	0.04596427	0.0008517708	0.057	19.7
O5	192	0.24597	-0.01671792	0.129756	0.057	19.7
O6	192	0.3050694	0.1539578	0.05407054	0.057	19.7
O_w1	32	0.13971	0.13971	0.13971	0.65396	6.3672

B_{iso}: Isotropic displacement factor

Table 3 . 5 | Atomic parameters from Rietveld refinement of SXRD measurement for Ru/NH_2

3.3.2 Structure-activity relationship

The hydrogen activation of Ru/bpy and Ru/NH_2 was evaluated by the hydrogen-deuterium exchange. Reactions with and without visible light filtered Xe lamp irradiation were performed at 25 to 100 °C and the results are presented in Figure 3 . 4.

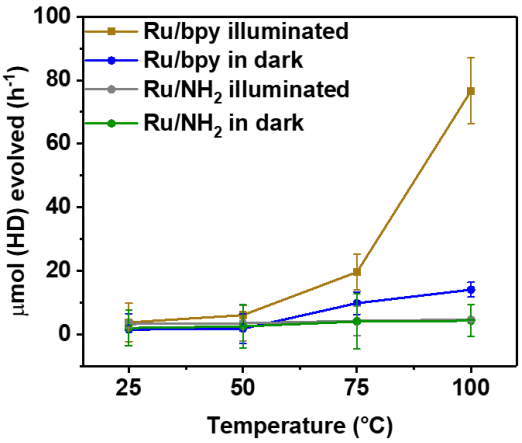


Figure 3 . 4 | Reactivities of Ru/bpy and Ru/NH_2 under illuminated and dark conditions on the hydrogen-deuterium exchange reaction

The conversion factor of the signal of quadruple mass spectrometer was determined by a calibration curve of pure HD gas (Figure 3 . 5).

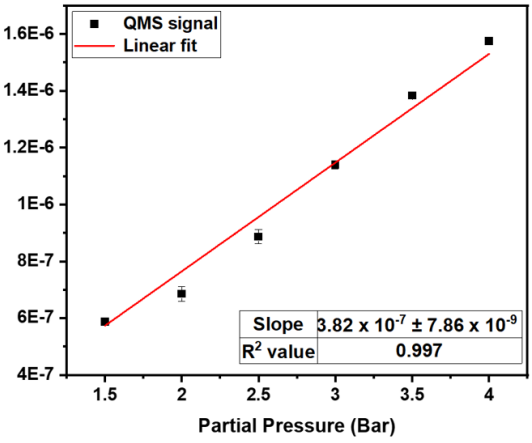


Figure 3 . 5 | Calibration curve of QMS signal with HD gas

There is no noticeable exchange rate with both Ru/bpy and Ru/NH_2 samples at room temperature. At 100 °C, small thermal activation of about 10 μmol HD per hour is formed can be detected over Ru/bpy, due to a thermal partition of the electrons for metal-to-ligand charge transfer to a small degree. Conversely, Ru/NH_2 still does not seem to show any measurable activity in the dark. However, under illumination, there is a dramatic light promotion to the exchange rate with at least ca. 5.5-fold increase in the amount of HD formed in Ru/bpy while Ru/NH_2 still remains catalytically inert. The turnover frequency, with the Ru content based on ICP-MS results is plotted against inverse of temperature to obtain an activation energy of 0.368 eV under light illumination (Figure 3 . 6), attributed to the diffusion of H_2/D_2 molecules into the pores of Ru/bpy.

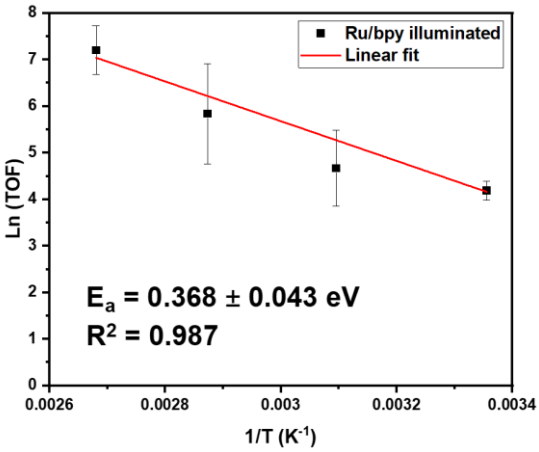


Figure 3 . 6 | Arrheniusm plot of Ru/bpy illuminated of the natural log of catalytic activity against the inverse of temperature

This is much lower than the literature value of 0.672 eV quartz as activated similarly by the Si-O acid-base pair[27], 1.36 eV from the sterically bulky boranes as considered traditional Frustrated Lewis Pairs[28], or without catalyst at 2.59 eV[29]. It is apparent that the two Ru-MOF samples do not seem to be active for H_2 activation via the dissociative means over their metal center at room temperature. In fact, the more extensive conjugated aromatic π* in the bipyridine in Ru/bpy should in principle be able to withdraw electron from Ru by the back donation than

the electron richer Ru from the sigma Ru-N bond in Ru/NH_2 hence attenuating the propensity for the classical H_2 activation. However, this catalyst is clearly shown to be more active under the light at elevated temperature than the Ru/NH_2. The key question is that why H_2 activation can be significantly promoted by light in the Ru/bpy but it does not apply to the related Ru/NH_2.

To understand the mechanistic pathway of the H_2-D_2 exchange reaction, Fourier transformed infra-red (FTIR) spectroscopy at variable temperature was performed on the reaction intermediate (Figure 3 . 7). A simultaneous detection of Ru-H and N-H stretching at 2045 cm^{-1} of Ru-H and at 2973 cm^{-1} of N-H in the quenched sample at 100°C supporting the unconventional heterolytic cleavage of H- H upon illumination is identified[30,31].

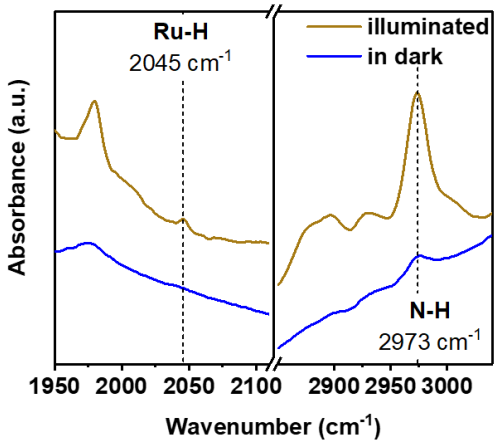


Figure 3 . 7 | FTIR spectra of Ru/bpy in dark and illuminated in reaction conditions

Despite the difficulty in quantification by infra-red, the Ru-H appears to be far smaller in size than that of N-H. It is well known that charge transfer and proton migration can take place simultaneously from transition metal hydride with a proton acceptor in a close proximity. For example, [FeFe]-hydrogenases can catalyse H_2 oxidation to protons exclusively via initiative FLP Fe-N sites and with the further conversion of H^- on Fe by charge transfer to NH^+. Similar chemistry for Ru-H charge transfer and proton migration to $O(H^+)$ on MgO(111) is demonstrated[32]. Thus, Ru^{3+} (2N) can generate Ru^+ and $2NH^+$ with a substantial reduction/elimination of Ru-H peak.

Notice that one dimensional (1D) ^{1}H Solid-state nuclear magnetic resonance (SSNMR) spectra for sample before and after illumination, are shown in Figure 3 . 8 a. Deconvolution of the spectrum of Ru/bpy in dark shows a 1:0.87:0.91 ratio of the peaks at 9.18, 8.30 and 7.14 ppm, respectively of the three H environments on the linker, as depicted in Figure 3 . 8 b and Table 3 . 6[33,34]. The resonances at around 1.20 ppm and 0.18 ppm are attributed to the bridging Zr(μ_3-OH) groups[35] and the linker defects motifs[36], respectively. Interestingly, a peak at 4.1 ppm, characteristic of trapped H_2 in the porous sample is detected before light activation.

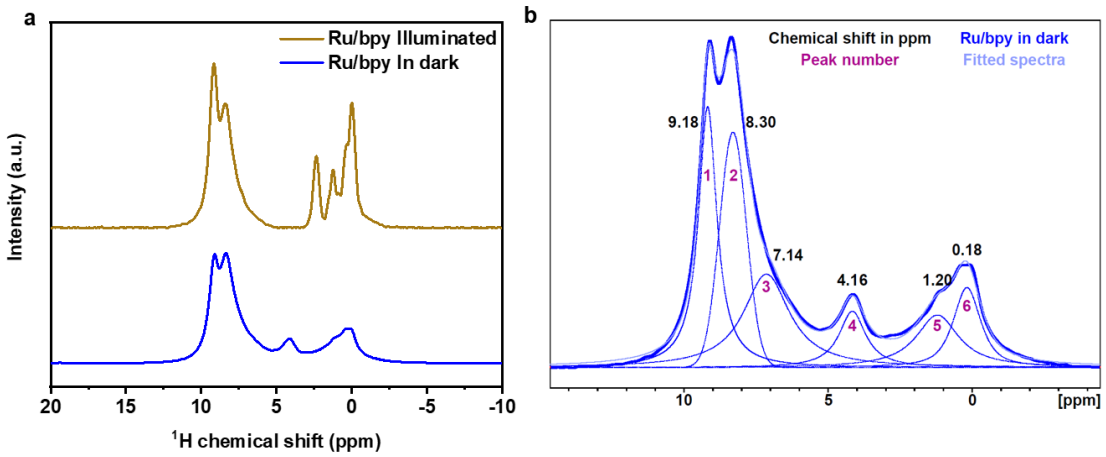


Figure 3 . 8 | (a) ^{1}H NMR spectra of Ru/bpy illuminated and in dark. (b) Deconvoluted 1D ^{1}H SSNMR spectra of Ru/bpy in dark. Assistance from Dr. Guangchao Li for obtaining the solid state-NMR spectra is gratefully acknowledged. The NMR data fitting was performed by Bryan Ng.

Peak number	Iy (10^8)	Chemical shift (ppm)	LB Peak width (Hz)	% of Gaussian	Area of peak
1	8.80	9.18	307	0.000	1
2	7.91	8.30	435	1.000	0.87
3	3.19	7.14	786	0.000	0.91
4	1.88	4.16	445	0.000	0.31
5	1.76	1.20	704	0.000	0.45
6	2.75	0.18	440	0.199	0.42

Table 3 . 6 | Fitting of NMR spectrum of Ru/bpy in dark by a mixture of Gaussian/Lorentz peaks

Best overlap (Parameter quantifying the overlap between data and fit): 94.10%

Iy: Signal intensity parameter, LB: Line broadening parameter

% of Gaussian: A full Lorentz curve has this parameter = 0, whereas a full Gaussian curve has this parameter = 1

For well-flushed and cold-trapped sample after illumination, its NMR spectrum is also deconvoluted and shown in Figure 3 . 9 and Table 3 . 7. Although no similar trace peak of Ru-H as IR is identified, presumably embedded in strong background, a distinctive peak at 2.4 ppm attributable to proton on amine can clearly be seen upon the illumination[37]. The relative proton peak size of bipyridine (7-9ppm) to NH^+ (2.4 ppm) peak of 7.19:1 suggests the near conversion, with the stoichiometric quantity of Ru-N pairs relative to bipyridinic protons determined by ICP and thermogravimetric analysis (TGA, Figure 3 . 10, Table 3 . 8 and Table 3 . 9) as 6.90:1.

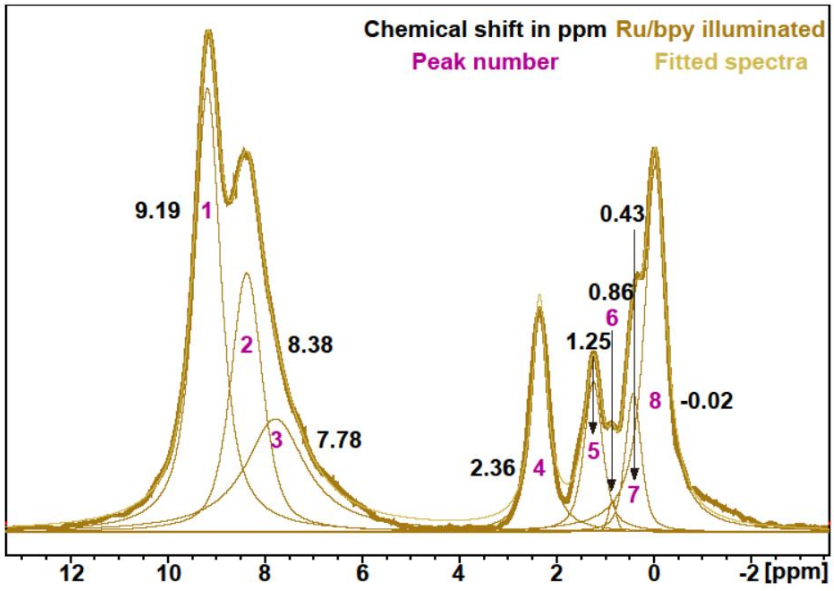


Figure 3 . 9 | Deconvoluted 1D ^{1}H SSNMR spectra of Ru/bpy illuminated

Peak number	Iy (10^8)	Chemical shift (ppm)	LB Peak width (Hz)	% of Gaussian	Area of peak
1	4.88	9.19	261	0.181	1
2	8.69	8.38	307	0.459	0.62
3	3.79	7.78	597	0.000	0.61
4	7.55	2.36	149	0.000	0.31
5	5.04	1.25	178	0.382	0.22
6	1.04	0.86	76.7	0.654	0.02
7	4.65	0.43	154	0.493	0.17
8	2.27	-0.02	211	0.031	0.70

Best overlap (Parameter quantifying the overlap between data and fit): 94.62%

Table 3 . 7 | Fitting of NMR spectrum of Ru/bpy in dark by a mixture of Gaussian/Lorentz peaks

Iy: Signal intensity parameter, LB: Line broadening parameter

% of Gaussian: A full Lorentz curve has this parameter = 0, whereas a full Gaussian curve has this parameter = 1

Relative peak size of bipyridine (7-9 ppm) to N-H^+ (2.4 ppm):

$$\frac{Area\ of\ peak\ 4}{Area\ of\ peak\ 1+2+3} = \frac{0.31}{1+0.62+0.61} = \frac{1}{7.19}$$

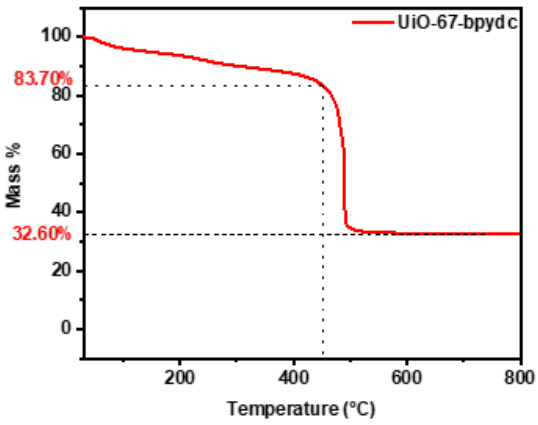


Figure 3 . 10 | Thermogravimetric analysis (TGA) of UiO-67-bpydc

Sample	ZrO_2	Linker
Mass (%)	32.60	83.70-32.60 = 51.10
Molar mass (g mol^{-1})	123.218	244.21
Mol of Zr and linker present	0.265	0.209
To whole number ratio	1	0.791

Table 3 . 8 | Calculation of Linker to Zr ratio based on TGA data

Ru:Zr of Ru/bpy ratio from ICP	0.344
Linker:Zr ratio from TGA	0.791
Ru/linker : linker	(0.791-0.344):0.344 = 0.447:0.344
Simplest ratio	1.30:1
Available pyridinic linker to Ru-N pair ratio	2.30:1
Expected ratio of N(H^+) at 2.4 ppm relative to bipyridine protons*	2.30 x 6 : 1 x 2 6.90:1

Table 3 . 9 | Ratio of N(H^+) proton on Ru-N pair relative to bipyridinic linker protons

* Protons on pyridinic linker = 6

Protons expected from N(H^+) after charge transfer = 2

To correlate their spatial relationship, two dimensional (2D) ^{1}H-^{1}H magic angle spinning (MAS) SSNMR experiment was performed (Figure 3 . 11 a). Besides, the strong cross-diagonal correlation peaks which belong to the equivalent proton sites, both peaks at 4.1 ppm and 2.4 ppm show off-diagonal correlation peak with the bipyridinic protons, indicating their spatial close proximity. Evidently, transient N(H^+) can be identified in H_2 with no reduction to the bipyridine linker during illumination (proton remained in the same positions) after activation and charge transfer characterized by IR and ssNMR. It is thought that light activation is likely to create transient intra-molecular Ru^+-N^- via metal-to-ligand charge transfer (MLCT) for H_2 activation. We therefore propose a photo-induced Ru-N polarization mechanism as depicted in Figure 3 . 11 b. H_2 and D_2 molecules can be exchanged by the light activation.

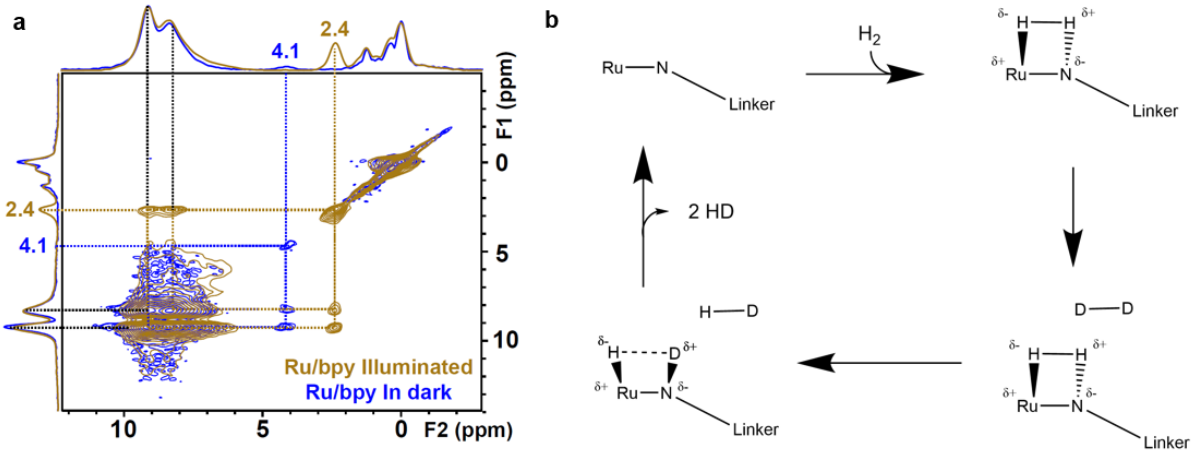


Figure 3 . 11 | (a) ^{1}H-^{1}H COSY NMR spectrum of Ru/bpy in dark (blue) and illuminated (brown). (b) Proposed mechanism of heterolytic activation of H-H bond by transient frustrated Lewis acid-base like pair. The proposed mechanism is speculated based on the addition detection of protonic and hydridic hydrogen upon light illumination on Ru-N acid-base pair by IR and NMR. It is not known the exact mechanism of hydrogen-deuterium exchange.

3.3.3 Optical Characterization

To confirm the importance of MLCT over Ru/bpy over Ru/NH_2 to create the active Lewis acid-base pair, the various charge transfer processes of different energies of the ruthenium-decorated MOFs were investigated by UV-vis spectroscopy (Figure 3 . 12). Observed in both UiO-67-bpydc and Ru/bpy, the absorption peaks at 249 and 283 nm can be attributed the typical π to π* transition of a bipyridinic and the isolated pyridinic rings present in these MOF samples, respectively[38].

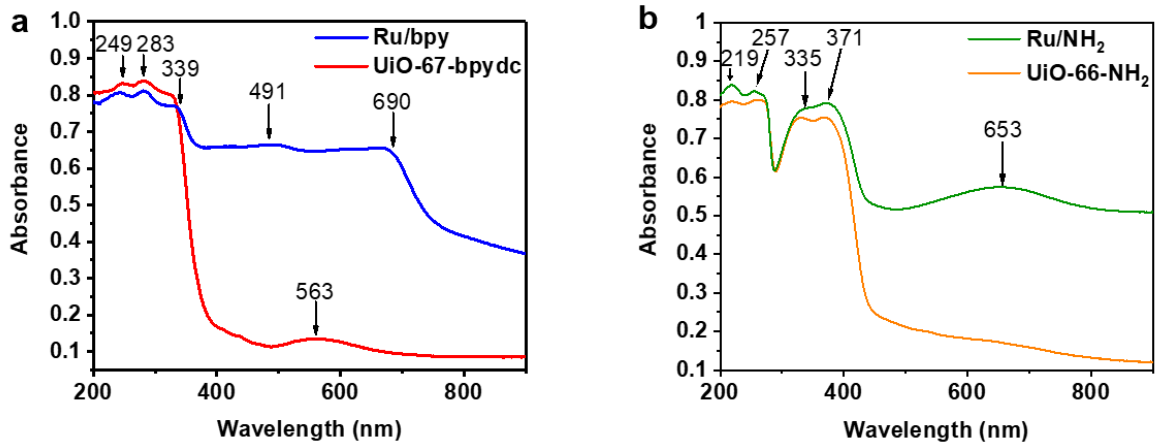


Figure 3 . 12 | UV-Vis absorbance spectra comparison for (a) Ru/bpy, UiO-67-bpydc, (b) Ru/NH_2, UiO-66-NH_2

For the absorption characteristics at visible regime, UiO-67-bpydc without Ru, gives a characteristic peak at 563 nm which can be ascribed to linker-linker charge transfer (LLCT), as it is also detectable in its free linker molecules (Figure 3 . 13).

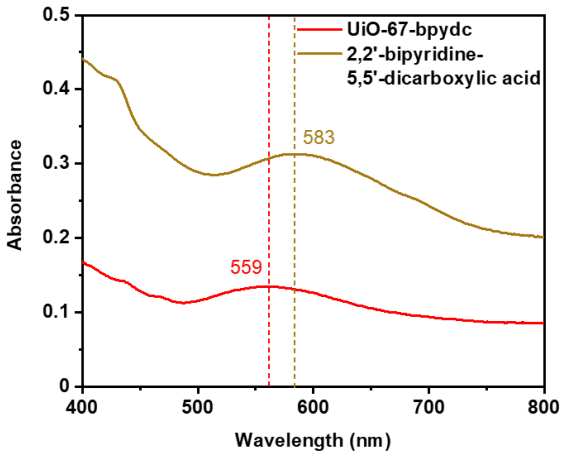


Figure 3 . 13 | UV-Vis spectra of UiO-67-bpydc and 2,2'-bipyridine5,5'-dicarboxylic acid

Interestingly, three distinctive intense broad peaks commonly assigned as MLCT peaks are indeed detectable in Ru/bpy around 339, 491 and 690 nm (Figure 3 . 12)[39-41]. Such strong adsorption peaks cover almost the entire visible region, giving the intense dark color of the sample. On the other hand, in the case of benzyl amine linker (UiO-66-NH_2) with the linker of lesser conjugation, the π to π* absorption peaks are found to be located at 219 and 257 nm,

respectively[38,42]. Additional peaks at 335 and 371 nm can be generally ascribed to the charge transfer processes from amine lone pair to organic linker π* transitions[43], which remain unaltered upon Ru incorporation. With rather isolated conjugated benzyl ring from the sigma M-NH_2 there is no similar broad intense LLCT or MLCT absorption regions at visible region in both samples in contrast to those observed in bipyridine systems. Only a small peak around 653 nm of Ru/NH_2 is detected, which may be attributed to the weak Ru d-d transitions[44,45].

The photophysical processes in the samples were also characterized by photoluminescence (PL) at 375 nm excitation (Figure 3 . 14) to understand the dynamic photo-excitation processes. It is interesting to note that the UiO-66-NH_2 with and without Ru only shows a main broad PL peak but with no vibrational or progression feature, whereas UiO-67-bpydc gives a clear shoulder peak at about 550 nm (triplet state from LLCT) matching with its visible absorption regime. The PL of Ru/bpy and UiO-67-bpydc can be deconvoluted into two Gaussian peaks to quantify the peak shoulder (Figure 3 . 14 a), with the fitting parameters available in Table 3 . 10. Similar to the UV-vis spectrum, there is a further broadening of the PL shoulder in Ru/bpy to capture the most visible regime, presumably to the availability of the additional lower energy triplet intermediate state due to MLCT in metal-bipyridinic system[46].

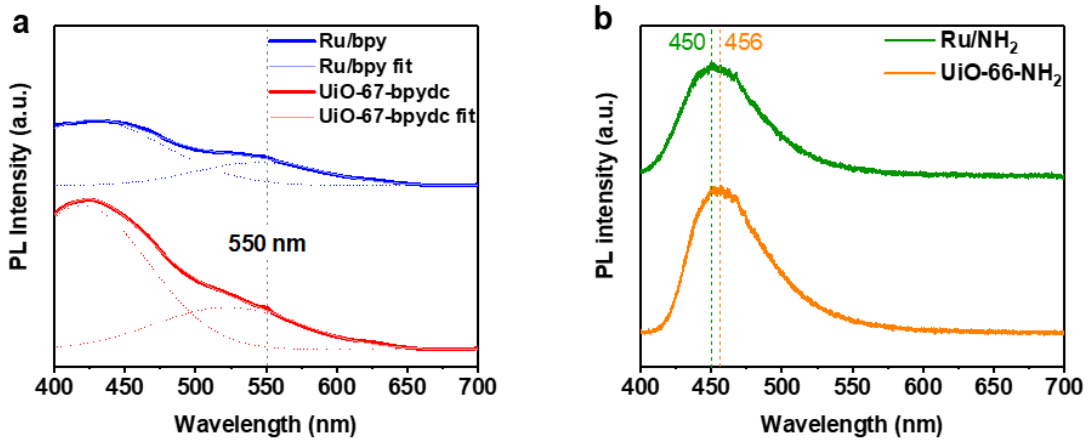


Figure 3 . 14 | Photoluminescence spectra of (a) Ru/bpy and (b) Ru/NH_2 along with their parent MOFs excited at 375 nm.

Sample	Peak centre (nm)	Peak area (10^6)	Peak width
Ru/bpy peak 1	426.3 ± 0.5	2.96 ± 0.07	121 ± 3
Ru/bpy peak 2	544.1 ± 1.9	0.91 ± 0.04	105 ± 2
UiO-67-bpydc peak 1	419.8 ± 0.6	5.93 ± 0.17	110 ± 2
UiO-67-bpydc peak 2	522.2 ± 3.4	1.92 ± 0.13	121 ± 4

Table 3 . 10 | Gaussian fitting parameters of PL of Ru/bpy and UiO-67-bpydc

Time-resolved photoluminescence (TRPL) was also employed at the energy of PL peak to examine the kinetics of such charge transfer processes (Figure 3 . 15), and the data is fitted against a bi-exponential decay function (Table 3 . 11). For the extensive conjugation in bipyridine without Ru, the dominant charge transfer process is shown to be the higher energetic LLCT, as stated. The introduction of Ru offers another lower energy pathway, which would quench the LLCT transition. Notice that the average lifetime of Ru/bpy was calculated to be 0.110 ns, which is significantly shorter compared to 0.450 ns of UiO-67-bpydc[47]. Such sharp attenuation in excitons lifetime suggests that an relaxation pathway is via the MLCT process,

which is alternative to radiative recombination of LLCT. Alternatively, for the isolated benzyl amine systems, it is acceptable that the high energetic process involves transfer of lone pair electrons in N to the linker molecule (n → π*, see TDDFT calculations below), the Ru could thus facilitate the polariation by further coupling with its orbtials hence prolonging the average lifetime of UiO-66-NH_2 and from 0.668 to 1.696 ns in the case of Ru/NH_2. Thus, Ru is thus shown to suppress the rate of charge recombination for increased lifetime of charge carriers in this case[48].

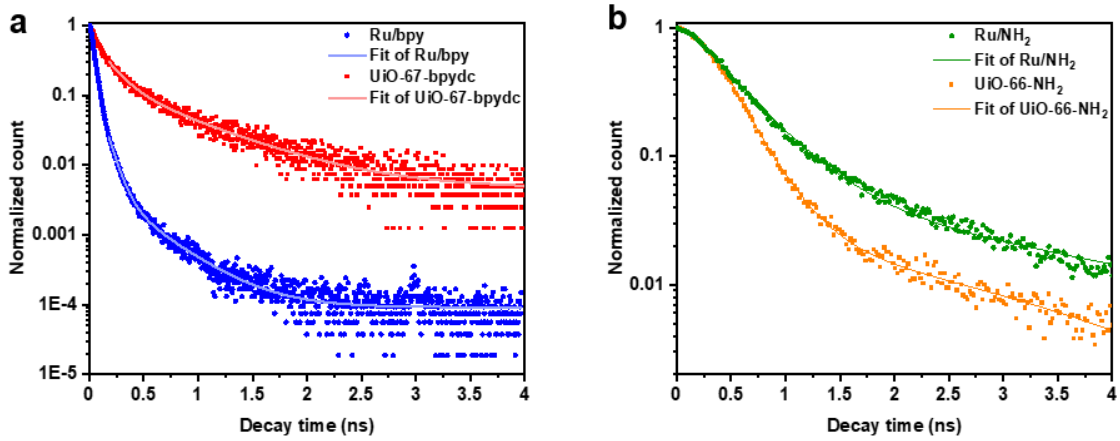


Figure 3 . 15 | TRPL of (a) UiO-67-bpydc and Ru/bpy. (b) UiO-66-NH_2 and Ru/NH_2. Assistance from Dr. Yiyang Li for collecting the TRPL spectra is gratefully acknowledged. The TRPL data fitting was performed by Bryan Ng.

Samples	A_1	t_1	A_2	t_2	Average lifetime	R^2 value
UiObpy	0.565 ± 0.020	0.155 ± 0.007	0.162 ± 0.010	0.684 ± 0.031	0.450 ± 0.150	0.984
Ru/bpy	0.233 ± 0.004	0.076 ± 0.001	0.006 ± 0.001	0.375 ± 0.010	0.110 ± 0.057	0.998
$UiONH_2$	2.39 ± 0.06	0.262 ± 0.004	0.036 ± 0.004	3.012 ± 0.202	0.668 ± 0.200	0.998
Ru/NH_2	1.19 ± 0.01	0.437 ± 0.004	0.061 ± 0.005	4.228 ± 0.453	1.70 ± 0.22	0.998

Table 3 . 11 | Fitting parameters of TRPL data against a bi-exponential decay function

To further understand the evaluate the charge carrier dynamics, transient absorption spectroscopy (TAS) was performed on the Ru/bpy sample (Figure 3 . 16). Intriguingly, a positive peak of 423 nm can be observed, which is close to the PL peak determined at 426 nm. This is indicative of excited state absorption (ESA) on top of the radiative process probed by PL, echoing our proposed model for Ru/bpy. Both the broadening of the PL peaks and the ESA suggests there are various available triplet energy intermediate state due to MLCT in the Ru/bpy system, whose lifetime peaks at 2 ps.

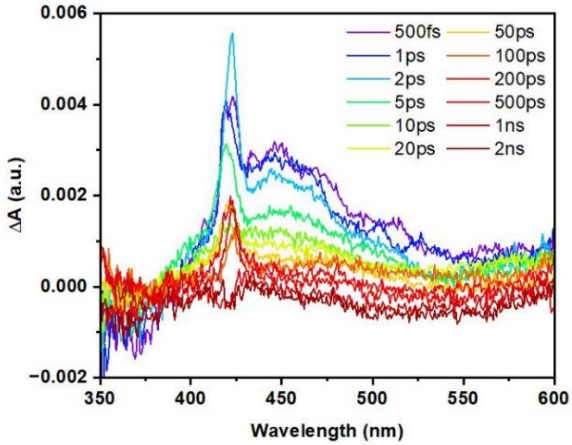


Figure 3 . 16 | Transient Absorption Spectroscopy (TAS) of Ru/bpy

3.3.4 Excited-state Calculations

From the optical characterization, the MLCT processes of the Ru/bpy catalyst have been seen by UV-Vis and PL spectroscopy, while the charge transfer kinetics have indicated a decreased lifetime of Ru/bpy compared to its parent UiO-67-bpydc. To confirm the above charge transfer processes and the nature of polarization in the Ru-MOFs, excited-state calculations were performed based on TDDFT. The Ru/bpy and Ru/NH_2 structures were constructed by anchoring the corresponding Ru species on the linkers of the UiO-67-bpydc and UiO-66-NH_2 frameworks, respectively (Figure 3 . 17). To reduce the computational cost, the UiO-67-bpydc and UiO-66-NH_2 frameworks were presented by their truncated clusters (Figure 3 . 18), which has been proved to be effective in previous studies[49,50].

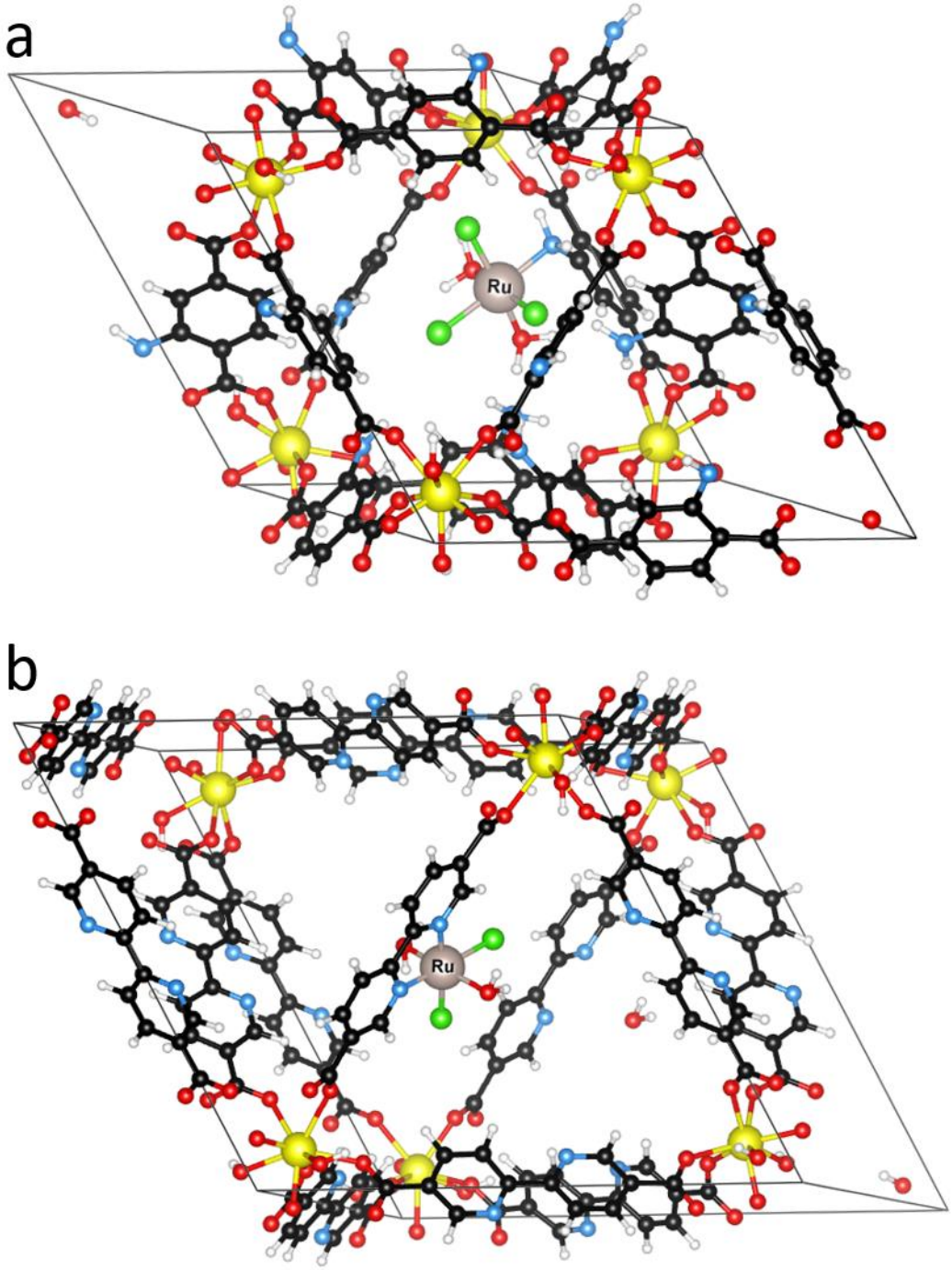


Figure 3 . 17 | Optimized structures of (a) the UiO-66-NH_2 and (b) UiO-67-bpydc frameworks with Ru species anchored on the linkers. Prof. Xin-Ping Wu is gratefully acknowledged for the DFT optimization of the structures.

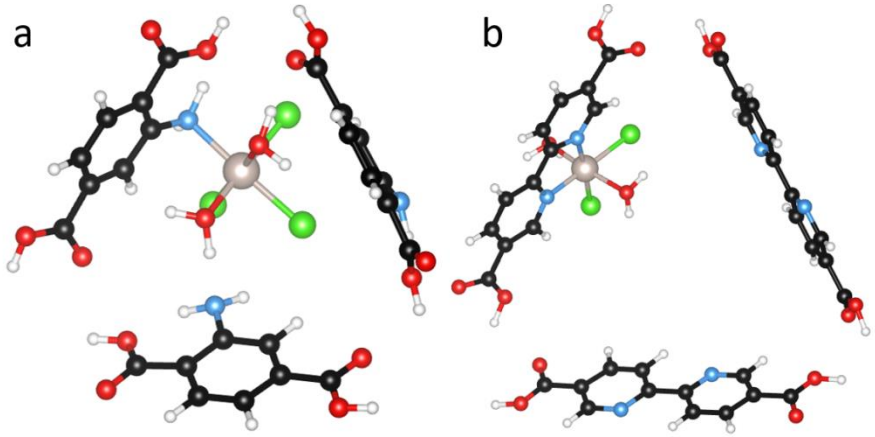


Figure 3 . 18 | Cluster models of (a) the Ru/NH_2 and (b) Ru/bpy structures

The calculated most stable spin states of the cluster models of the Ru/bpy and Ru/NH_2 are closed-shell singlet and doublet, respectively (Table 3 . 12 and Table 3 . 13).

Multiplicity	ΔE (eV)
Singlet	0
Triplet	0.83
Quintet	1.67

Table 3 . 12 | Relative energies (ΔE) of the cluster model of the Ru/bpy with various spin states

Multiplicity	ΔE (eV)
Doublet	0
Quartet	0.74
Sextet	1.25

Table 3 . 13 | Relative energies (ΔE) of the cluster model of the Ru/NH_2 with various spin states

The electronic transitions in these two clusters (with the most stable spin state) were further explored with the aid of TDDFT. The first 50 excited states were calculated for each cluster model, and those with an oscillator strength (*f*) being larger than 0.01 are presented in Figure 3 . 19 and Table 3 . 14. The oscillator strength quantifies the probability of absorption or emission of electromagnetic radiation in transitions between energy levels. In the cluster of the Ru/bpy, the $S_0 \rightarrow S_3$ (f = 0.030), $S_0 \rightarrow S_{20}$ (f = 0.019), $S_0 \rightarrow S_{22}$ (f = 0.052), and $S_0 \rightarrow S_{23}$ (f = 0.129) transitions are relatively strong. Interestingly, the $S_0 \rightarrow S_3$ transition of MLCT in origin identified at 732 nm, corresponds well to the experimental 690 nm peak in UV-Vis. Similarly, the calculated $S_0 \rightarrow S_{20}$ transition (415 nm) is correlated to the MLCT peak at 487 nm of UV-Vis, while the energetically close $S_0 \rightarrow S_{22}$ and $S_0 \rightarrow S_{23}$ transitions (398 and 371 nm, respectively) are correlated with the absorption region at 339 nm of the UV-Vis. Such transitions indeed feature the excited electron and hole being localized on the linker and Ru, respectively, confirming the generation of the photoinduced but transient Ru–N Lewis acid-base pair as the dominant transition under illumination. It is well known that excited states, in particular charge-transfer excited states, are challenging to model accurately[51-53 54]. In the framework of TDDFT, the mean absolute error of electronic transition energies calculated using the decent B3LYP functional[55] (which is also the functional used in the present study) is approximately 0.5 eV, as reported in previous benchmark studies[56,57]. Therefore, in the state-of-the-art TDDFT, the obtained transition energies agree well with the experimental results. On the other hand, the absence of low energy available π overlap between Ru-N in Ru/NH_2, with isolated benzyl amine and poor mixing with Ru orbitals is evident, there are only two relatively strong electronic transitions, i.e., $D_0 \rightarrow D_{29}$ (f = 0.053) and $D_0 \rightarrow D_{32}$ (f =0.023). The $D_0 \rightarrow D_{29}$ transition at 413 nm is dominated by the electron from lone pair n in N → aromatic π* configuration, with minimal involvement with Ru metal, which agrees well with the

experimentally observed absorption peak at 371 nm in the spectrum of the Ru/NH_2. The peak may also have the contribution from $D_0 \rightarrow D_{32}$ transition, which is generally localized within the Ru complex, reinforcing the absence of charge transfer between Ru and the linker (no polarization).

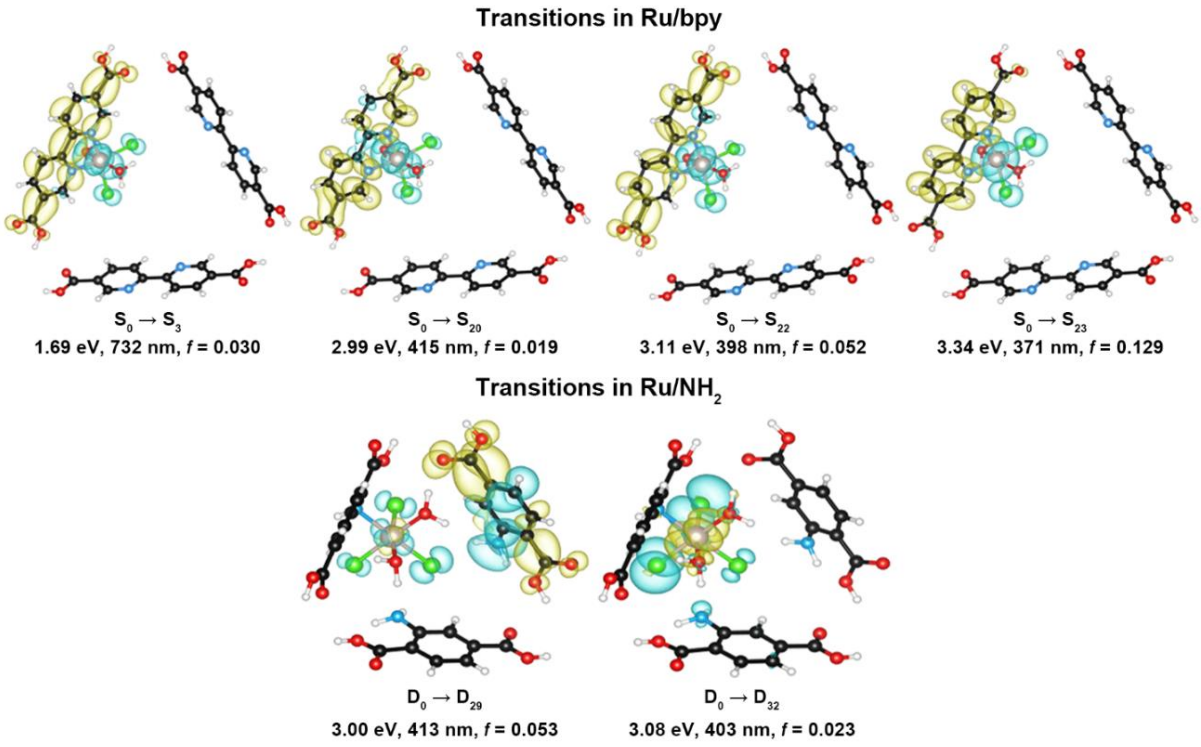


Figure 3 . 19 | Electron-hole distributions (isosurface:0.001 e/Å^3) of the electronic transitions with oscillator strength being larger than 0.01 in the cluster models of Ru/bpy and Ru/NH_2 structures. S and D denote singlet and doublet, respectively. Structure colour scheme: C = black, N = blue, O = red, H = white, Ru = grey, Cl = green. Isosurface colour scheme: Electron = yellow, hole = blue

Transition	Energy	Oscillator Strength, *f*
Ru/bpy		
$S_0 \rightarrow S_3$	1.69 eV, 732 nm	0.030
$S_0 \rightarrow S_{20}$	2.99 eV, 415 nm	0.019
$S_0 \rightarrow S_{22}$	3.11 eV, 398 nm	0.052
$S_0 \rightarrow S_{23}$	3.34 eV, 371 nm	0.129
Ru/NH_2		
$D_0 \rightarrow D_{29}$	3.00 eV, 413 nm	0.053
$D_0 \rightarrow D_{32}$	3.08 eV, 403 nm	0.023

Where S and D denote singlet and doublet, respectively

Table 3 . 14 | Electronic transitions with oscillator strength being larger than 0.01 in the cluster models of Ru/bpy and Ru/NH_2 structures

3.4 Conclusion

In conclusion, a photo-induced frustrated Lewis pair like active sites is, for the first time, reported in the Ru/bpy catalyst as a proof of concept. Its design combines the high chemical tunability of MOF and the strong metal-to-ligand charge transfer ability of ruthenium complexes. The successful anchoring of Ru onto MOFs is shown with EXAFS and Rietveld refinement on SXRD data, while the optical processes are characterized by UV-Vis, PL and TRPL. Upon light irradiation, the Ru-N Lewis acid-base pair in Ru/bpy is polarized as indicated by the TDDFT calculations, beneficial to the photo catalysis of hydrogen-deuterium gas exchange reaction. We believe our approach for catalyst design can become transferable to the wider application of light induced FLP-like chemistries on the activation of small molecules.

3.5 References

1 Albero, J., Peng, Y. & García, H. Photocatalytic CO2 Reduction to C2+ Products. *ACS Catal* **10**, 5734-5749 (2020).

2 Welch, G. C. S., D. W. Facile Heterolytic Cleavage of Dihydrogen by Phosphines and Boranes. *J Am Chem Soc* **129**, 1880-1881 (2007).

3 Lu, G., Zhang, P., Sun, D., Wang, L., Zhou, K., Wang, Z.-X. & Guo, G.-C. Gold catalyzed hydrogenations of small imines and nitriles: enhanced reactivity of Au surface toward H2via collaboration with a Lewis base. *Chem. Sci.* **5**, 1082-1090 (2014).

4 Liang, X., Wang, X., Zhang, X., Lin, S., Ji, M. & Wang, M. Frustrated Lewis Pairs on In(OH)3–x Facilitate Photocatalytic CO2 Reduction. *ACS Catal.* **13**, 6214-6221 (2023).

5 Chen, Z., Ye, Y., Feng, X., Wang, Y., Han, X., Zhu, Y., Wu, S., Wang, S., Yang, W., Wang, L. & Zhang, J. High-density frustrated Lewis pairs based on Lamellar Nb(2)O(5) for photocatalytic non-oxidative methane coupling. *Nat. Commun.* **14**, 2000 (2023).

6 Ma, J., Zhang, Q., Chen, Z., Kang, K., Pan, L., Wu, S., Chen, C., Wu, Z., Zhang, J. & Wang, L. Design of frustrated Lewis pair in defective TiO2 for photocatalytic non-oxidative methane coupling. *Chem Catal.* **2**, 1775-1792 (2022).

7 Cannizzo, A., van Mourik, F., Gawelda, W., Zgrablic, G., Bressler, C. & Chergui, M. Broadband femtosecond fluorescence spectroscopy of [Ru(bpy)3]2+. *Angew Chem Int Ed Engl* **45**, 3174-3176 (2006).

8 Xue, Q., Zhang, Z., Ng, B. K. Y., Zhao, P. & Lo, B. T. W. Recent Advances in the Engineering of Single-Atom Catalysts Through Metal-Organic Frameworks. *Top Curr Chem (Cham)* **379**, 11 (2021).

9 Cavka, J. H., Jakobsen, S., Olsbye, U., Guillou, N., Lamberti, C., Bordiga, S. & Lillerud, K. P. A New Zirconium Inorganic Building Brick Forming Metal Organic Frameworks with Exceptional Stability *J Am Chem Soc* **130**, 13850-13851 (2008).

10 He, J., Wang, J., Chen, Y., Zhang, J., Duan, D., Wang, Y. & Yan, Z. A dye-sensitized Pt@UiO-66(Zr) metal-organic framework for visible-light photocatalytic hydrogen production. *Chem Commun (Camb)* **50**, 7063-7066 (2014).

11 Shen, L., Liang, R., Luo, M., Jing, F. & Wu, L. Electronic effects of ligand substitution on metal-organic framework photocatalysts: the case study of UiO-66. *Phys Chem Chem Phys* **17**, 117-121 (2015).

12 Pu, S., Xu, L., Sun, L. & Du, H. Tuning the optical properties of the zirconium–UiO-66 metal–organic framework for photocatalytic degradation of methyl orange. *Inorg Chem Commun* **52**, 50-52 (2015).

13 Lee, J., Farha, O. K., Roberts, J., Scheidt, K. A., Nguyen, S. T. & Hupp, J. T. Metal-organic framework materials as catalysts. *Chem Soc Rev* **38**, 1450-1459 (2009).

14 Mo, S., Wang, G., Ng, B. K. Y. & Zhao, P. Investigating porous catalysts with synchrotron X-rays and neutrons. *Chem Catalysis* (2022).

15 Wei, Y. S., Zhang, M., Zou, R. & Xu, Q. Metal-Organic Framework-Based Catalysts with Single Metal Sites. *Chem Rev* **120**, 12089-12174 (2020).

16 Yoskamtorn, T., Zhao, P., Wu, X. P., Purchase, K., Orlandi, F., Manuel, P., Taylor, J., Li, Y., Day, S., Ye, L., Tang, C. C., Zhao, Y. & Tsang, S. C. E. Responses of Defect-Rich Zr-Based Metal-Organic Frameworks toward NH3 Adsorption. *J Am Chem Soc* **143**, 3205-3218 (2021).

17 Cui, W. G., Hu, T. L. & Bu, X. H. Metal-Organic Framework Materials for the Separation and Purification of Light Hydrocarbons. *Adv Mater* **32**, e1806445 (2020).

18 Xue, Q., Chan, K. H., Yim, C. K., Ng, B. K. Y., Chen, T., Day, S. J., Tang, C., Kawaguchi, S., Wong, K.-Y. & Lo, T. W. B. Guest-Anion-Induced Rotation-Restricted Emission in UiO-66-NH2 and Advanced Structure Elucidation. *Chem Mater* **33**, 5422-5429 (2021).

19 Qiu, S., Xue, M. & Zhu, G. Metal-organic framework membranes: from synthesis to separation application. *Chem Soc Rev* **43**, 6116-6140 (2014).

20 Xue, Q., Ng, B. K. Y., Man, H. W., Wu, T. S., Soo, Y. L., Li, M. M., Kawaguchi, S., Wong, K. Y., Tsang, S. C. E., Huang, B. & Lo, T. W. B. Controlled synthesis of Bi- and tri-nuclear Cu-oxo nanoclusters on metal-organic frameworks and the structure-reactivity correlations. *Chem Sci* **13**, 50-58 (2021).

21 Niu, Z., Bhagya Gunatilleke, W. D. C., Sun, Q., Lan, P. C., Perman, J., Ma, J.-G., Cheng, Y., Aguila, B. & Ma, S. Metal-Organic Framework Anchored with a Lewis Pair as a New Paradigm for Catalysis. *Chem* **4**, 2587-2599 (2018).

22 Zhu, B., Zou, R. & Xu, Q. Metal–Organic Framework Based Catalysts for Hydrogen Evolution. *Adv Energy Mater* **8** (2018).

23 Katz, M. J., Brown, Z. J., Colon, Y. J., Siu, P. W., Scheidt, K. A., Snurr, R. Q., Hupp, J. T. & Farha, O. K. A facile synthesis of UiO-66, UiO-67 and their derivatives. *Chem Commun (Camb)* **49**, 9449-9451 (2013).

24 Xu, L., Luo, Y., Sun, L., Pu, S., Fang, M., Yuan, R. X. & Du, H. B. Tuning the properties of the metal-organic framework UiO-67-bpy via post-synthetic N-quaternization of pyridine sites. *Dalton Trans* **45**, 8614-8621 (2016).

25 König, C. F. J., van Bokhoven, J. A., Schildhauer, T. J. & Nachtegaal, M. Quantitative Analysis of Modulated Excitation X-ray Absorption Spectra: Enhanced Precision of EXAFS Fitting. *The Journal of Physical Chemistry C* **116**, 19857-19866 (2012).

26 Rietveld, H. M. A profile refinement method for nuclear and magnetic structures. *J. Appl. Cryst.* **2**, 65-71 (1969).

27 Lee, R. W., Frank, R. C. & Swets, D. E. Diffusion of Hydrogen and Deuterium in Fused Quartz. *J Chem Phys* **36**, 1062-1071 (1962).

28 Sultana, M., Paul, A. & Roy, L. Computational Investigation of the Mechanism of FLP Catalyzed H2 Activation and Lewis Base Assisted Proton Transfer. *Chemistry Select* **5**, 13397-13406 (2020).

29 Boato, G., Careri, G., Cimino, A., Molinari, E. & Volpi, G. G. Homogeneous Exchange Reaction Between Hydrogen and Deuterium. *J Chem Phys* **24**, 783-791 (1956).

30 Choi, J. H., Heim, L. E., Ahrens, M. & Prechtl, M. H. Selective conversion of alcohols in water to carboxylic acids by in situ generated ruthenium trans dihydrido carbonyl PNP complexes. *Dalton Trans* **43**, 17248-17254 (2014).

31 Hansen, P. E., Vakili, M., Kamounah, F. S. & Spanget-Larsen, J. NH Stretching Frequencies of Intramolecularly Hydrogen-Bonded Systems: An Experimental and Theoretical Study. *Molecules* **26** (2021).

32 Armstrong, F. A. & Hirst, J. Reversibility and efficiency in electrocatalytic energy conversion and lessons from enzymes. *Proc Natl Acad Sci U S A* **108**, 14049-14054 (2011).

33 Fei, H. & Cohen, S. M. A robust, catalytic metal-organic framework with open 2,2'-bipyridine sites. *Chem Commun (Camb)* **50**, 4810-4812 (2014).

34 Yuan, N., Church, T. L., Brandt, E. G., Hedin, N., Zou, X. & Bernin, D. Insights into Functionalization of Metal-Organic Frameworks Using In Situ NMR Spectroscopy. *Sci Rep* **8**, 17530 (2018).

35 Devautour-Vinot, S., Maurin, G., Serre, C., Horcajada, P., Paula da Cunha, D., Guillerm, V., de Souza Costa, E., Taulelle, F. & Martineau, C. Structure and Dynamics of the Functionalized MOF Type UiO-66(Zr): NMR and Dielectric Relaxation Spectroscopies Coupled with DFT Calculations. *Chem Mater* **24**, 2168-2177 (2012).

36 Lawrence, M. C., Schneider, C. & Katz, M. J. Determining the structural stability of UiO-67 with respect to time: a solid-state NMR investigation. *Chem Commun (Camb)* **52**, 4971-4974 (2016).

37 Limbach, H. H., Pery, T., Rothermel, N., Chaudret, B., Gutmann, T. & Buntkowsky, G. Gas phase (1)H NMR studies and kinetic modeling of dihydrogen isotope equilibration catalyzed by Ru-nanoparticles under normal conditions: dissociative vs. associative exchange. *Phys Chem Chem Phys* **20**, 10697-10712 (2018).

38 Wu, S.-H., Wang, S., Fang, W.-L., Guo, X.-F. & Wang, H. An exceptionally stable Zr-based fluorescent metal–organic framework for highly selective detection of pH. *Anal Method* **11**, 36-43 (2019).

39 An, Y., Liu, Y., Bian, H., Wang, Z., Wang, P., Zheng, Z., Dai, Y., Whangbo, M.-H. & Huang, B. Improving the photocatalytic hydrogen evolution of UiO-67 by incorporating Ce4+-coordinated bipyridinedicarboxylate ligands. *Sci Bull* **64**, 1502-1509 (2019).

40 Gonzalez, M. I., Bloch, E. D., Mason, J. A., Teat, S. J. & Long, J. R. Single-crystal-to-single-crystal metalation of a metal-organic framework: a route toward structurally well-defined catalysts. *Inorg Chem* **54**, 2995-3005 (2015).

41 Hidalgo-Acosta, J. C., Mendez, M. A., Scanlon, M. D., Vrubel, H., Amstutz, V., Adamiak, W., Opallo, M. & Girault, H. H. Catalysis of water oxidation in acetonitrile by iridium oxide nanoparticles. *Chem Sci* **6**, 1761-1769 (2015).

42 Mu, X., Jiang, J., Chao, F., Lou, Y. & Chen, J. Ligand modification of UiO-66 with an unusual visible light photocatalytic behavior for RhB degradation. *Dalton Trans* **47**, 1895-1902 (2018).

43 Gomes Silva, C., Luz, I., Llabres i Xamena, F. X., Corma, A. & Garcia, H. Water stable Zr-benzenedicarboxylate metal-organic frameworks as photocatalysts for hydrogen generation. *Chemistry* **16**, 11133-11138 (2010).

44 Subbaiyan, S. & Ponnusamy, I. Biological investigations of ruthenium(III) 3-(Benzothiazol-2-liminomethyl)-phenol Schiff base complexes bearing PPh3 / AsPh3 coligand. *Curr. Chem. Lett.* **8**, 145-156 (2019).

45 Kureshy, R. I. & Khan, N. H. Studies on Mixed Ligand Complexes of Ruthenium (II) Chiral Schiff Bases with Nitrogen Donors. *Polyhedron* **12**, 2395-2401 (1993).

46 Xu, K., Zhao, J. & Moore, E. G. Photo-induced electron transfer in a diamino-substituted Ru(bpy)3[PF6]2 complex and its application as a triplet photosensitizer for nitric oxide (NO)-activated triplet-triplet annihilation upconversion. *Photochem Photobiol Sci* **15**, 995-1005 (2016).

47 Wu, Y., Shi, J., Li, D., Zhang, S., Gu, B., Qiu, Q., Sun, Y., Zhang, Y., Cai, Z. & Jiang, Z. Synergy of Electron Transfer and Electron Utilization via Metal–Organic Frameworks as an Electron Buffer Tank for Nicotinamide Regeneration. *ACS Catal* **10**, 2894-2905 (2020).

48 Wang, X., Yang, G., Chai, G., Nasir, M. S., Wang, S., Zheng, X., Wang, C. & Yan, W. Fabrication of heterostructured UIO-66-NH2 /CNTs with enhanced activity and selectivity over photocatalytic CO2 reduction. *Int J Hydrog Energy* **45**, 30634-30646 (2020).

49 Wu, X. P., Gagliardi, L. & Truhlar, D. G. Cerium Metal-Organic Framework for Photocatalysis. *J Am Chem Soc* **140**, 7904-7912 (2018).

50 Wu, X. P., Choudhuri, I. & Truhlar, D. G. Computational Studies of Photocatalysis with Metal–Organic Frameworks. *Energy Environ Mater* **2**, 251-263 (2019).

51 Maitra, N. T. Charge transfer in time-dependent density functional theory. *J Phys Condens Matter* **29**, 423001 (2017).

52 Dreuw, A. & Head-Gordon, M. Failure of Time-Dependent Density Functional Theory for Long-Range Charge-Transfer Excited States: The Zincbacteriochlorin-Bacteriochlorin and Bacteriochlorophyll-Spheroidene Complexes. *J Am Chem Soc* **126**, 4007-4016 (2004).

53 Jacquemin, D., Wathelet, V., Perpete, E. A. & Adamo, C. Extensive TD-DFT Benchmark: Singlet-Excited Statese of Organic Molecules. *J Chem Theory Comput* **5**, 2420-2435 (2009).

54 Laurent, A. D. & Jacquemin, D. TD-DFT benchmarks: A review. *Int J Quantum Chem* **113**, 2019-2039 (2013).

55 Becke, A. D. Density-functional thermochemistry. III. The role of exact exchange. *J Chem Phys* **98**, 5648-5652 (1993).

56 Toffoli, D., Quarin, M., Fronzoni, G. & Stener, M. Accurate Vertical Excitation Energies of BODIPY/Aza-BODIPY Derivatives from Excited-State Mean-Field Calculations. *J Phys Chem A* **126**, 7137-7146 (2022).

57 Sarkar, R., Boggio-Pasqua, M., Loos, P. F. & Jacquemin, D. Benchmarking TD-DFT and Wave Function Methods for Oscillator Strengths and Excited-State Dipole Moments. *J Chem Theory Comput* **17**, 1117-1132 (2021).

4 Chapter 4 | Designing UiO-based catalysts for photocatalytic CO_2 reduction

4.1 Introduction

Metal-organic frameworks (MOFs) have received considerable attention in the field of photocatalysis[1,2]. They are a class of porous inorganic compound with high surface area, whose assembly of organic linker molecules and metal-oxalate clusters results in high chemical stability along with wide structural tuneability. The organic linker present in the MOF can act as chromophore to extract light energy for catalysis[3-5], while its highly porous nature provides plentiful adsorption site for reactant molecules[6,7]. It is also useful for a wide-range of application such as sensing[8], separation and adsorption[9]. The Universitet i Oslo (UiO) series is a family of MOFs well known for its chemical stability, which stems from the strong electrostatic force between Zirconium-oxo clusters $Zr_6O_4(OH)_4$ and 1,4-benzenedicarboxylic acid (commonly known as terephthalic acid) for the most basic UiO-66 MOF. The UiO series have demonstrated good potential as photocatalysts. However, the application of unmodified as photocatalyst suffers from quick exciton recombination upon light induction, which originates from the high energy difference between highly cationic Zr^{4+} and anionic carboxylic acid[10,11]. The light energy harvested by organic linkers cannot be efficiently transferred to the catalytic reaction. Coupling with co-catalysts allow the structural stability, light-harvesting ability and porosity of MOFs to be further exploited.

Semiconductors are often used in the decoration of photocatalysts for improved light-harvesting performance. The interaction in the semiconductor/catalyst interface has strong influence on their fuel-forming catalytic performances, such as water splitting and CO_2 reduction[12,13]. Well-designed catalytic heterojunction is shown to suppress the recombination

of photo-excited electron-hole by spatial separation[13,14]. Charge-transfer between semiconductor and support can alter the bandgap of the catalysts, which enhances the quantum yield of incoming light[15]. Moreover, the semiconductor/catalyst interface can provide extra adsorption sites for reactant molecules, hence achieving a higher rate of conversion[16]. The interplay between band energies and diffusion of separated charges to reactants determines the performance of the photocatalysts. Nevertheless, the decoration of semiconductor onto support materials requires cost and energy intensive methods such as photodeposition, and may need various solvent or surfactant for optimal control of size or shape[17-19].

In light of this, we attempt to anchor In_2S_3 particles of different ratio controlled by hard soft acid-base chemistry under room temperature in a bottom-up approach[20]. An amine group is introduced to the organic linker of UiO-66 (as UiO-66-NH_2) via isoreticular synthesis to enhance contact of MOF and In_2S_3 particles[21]. Different from studies of similar system of coupling sulphide materials with UiO series of MOF, which mainly focus on the optical aspects of improved interfacial charge transfer[22-26], our system offers a more thorough understanding of the mechanism of improvement on rate of photocatalysis. Structurally the external In_2S_3 particles are characterized by X-ray diffraction, absorption techniques along with microscopy images, which reveal the diffusion of In^{3+} into the pores and formation of In_2S_3 on UiO-66-NH_2. Our In_2S_3 doped catalyst has more than doubled compared to parent UiO-66-NH_2 in photocatalytic CO_2 reduction, attributed to the increase in adsorption sites arose from the interface between In_2S_3 and UiO-66-NH_2, as quantified by Brunauer-Emmett-Teller (BET) analysis. Optically, the charge transfer from MOF to In_2S_3 was demonstrated by photoluminescence (PL) and increased light absorption in the visible region have promoted the photocatalytic CO_2 reduction.

4.2 Results and Discussion

4.2.1 Photocatalytic CO_2 Reduction

A series of In_2S_3/UiO-66-NH_2 nanocomposites were fabricated through a one-step solvothermal method, with the synthesis methods detailed in Supporting Information. The In and Zr content present in the series of catalysts are quantified by Inductively-coupled plasma-mass spectroscopy (ICP-MS) in

Table 4 . 1, with an increasing trend in In_2S_3 component. The samples are labelled as In-1, In-2, In-3, In-4 and In-5 according to the increasing amount of In present in the sample.

Sample	In / ppm	Zr / ppm	In/Zr ratio
UiO-66-NH_2	0.0201	460	0
In-1	13.4	477	0.02
In-2	105	557	0.2
In-3	339	576	0.7
In-4	778	298	2.82
In-5	1140	135	8.44

Table 4 . 1 | Amount of In and Zr present in series of In_2S_3/UiO-66-NH_2 catalysts quantified by ICP

Photocatalytic CO_2 reduction over the series of In_2S_3/UiO-66-NH_2 materials were tested with 1:3 CO_2/H_2 mixture at 180 °C, with the results shown in Figure 4 . 1. A volcano trend of catalytic activity for both the amount of CH_4 and CO detected against amount of In species present can be observed. The pristine UiO-66-NH_2 exhibits poor photocatalytic performance with CO and CH_4 production of 60.7 and 54.1 μmol $h^{-1}g^{-1}$. The catalytic activities peaks at In-2, with 257.0 and 139.7 μmol $h^{-1}g^{-1}$ of CO and CH_4, corresponding to a 323 % and 158 %

increase from the pristine UiO-66-NH_2 MOF. With higher loading of In species, the catalytic activity decreases to 50.5 and 40.3 μmol $h^{-1}g^{-1}$, respectively for In-5.

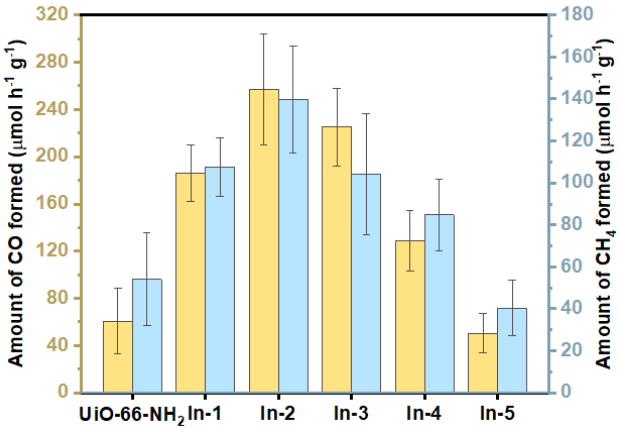


Figure 4 . 1 | Photocatalytic activity of CO_2 reduction for the series of UiO-66-NH_2 and InS-deposited UiO-66-NH_2. The yellow and blue bars correspond to the amount of CO and CH_4 formed in μmol h^{-1} g_{cat}^{-1}, respectively. The CO_2 reduction was performed with 1:3 CO_2/H_2 mixture at 180 ºC. The catalytic activity was measured with the assistance of Miss. Xiyu Zhang.

Control experiments with no light and with N_2 gas flowing in place of CO_2/H_2 mixture, with no products observed as shown in Figure 4 . 2. With the dependence of the catalytic reaction on CO_2 and light confirmed, the series of catalysts are subjected to further characterization for the elucidation of reaction mechanism.

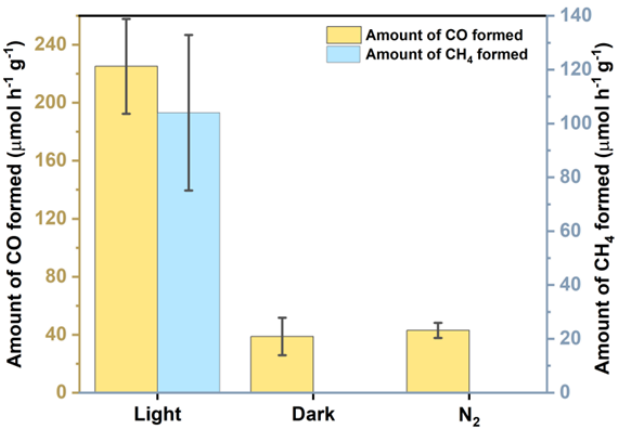


Figure 4 . 2 | Control experiments of In-2 sample with light, dark (without light) and under N_2 (in place of CO_2). The catalytic activity was measured with the assistance of Miss. Xiyu Zhang.

A comparison of the catalytic performance of our catalysts as compared to the literature on CO_2 reduction to CH_4 is available in Table 4 . 2. The series of In_2S_3 anchored UiO-66-NH_2 catalysts are characterized structurally and optically to reveal the reasons behind the high catalytic activity compared to the state-of-the-art.

MOF used	Hydrogen Source	Production rate of CH_4 /μmol $h^{-1}g^{-1}$	Ref
Mn-MOF	H_2O	75	[27]
MIL-100(Fe)	TEOA	49	[28]
PCN-601	H_2O	10.1	[29]
Zn/PMOF	H_2O	8.7	[30]
NH_2-MIL-125(Ti)	H_2O+TEOA	1.01	[31]
Ti/Zr-MOF-525	H_2O	0.36	[32]
Co-MOF-525	TEOA	36.76	[33]
Cu_2O@MOF(Zn)-1	H_2	10	[34]
In_2S_3@UiO-66-NH_2 (In-2)	H_2	139.7	This work

Table 4 . 2 | Catalytic performance of In-2 in CO_2 reduction to CH_4 compared to the literature.

4.2.2 Structural Characterization

To understand the crystallinity of the series of In_2S_3/UiO-66-NH_2 samples, X-ray diffraction (XRD) has been performed and are shown in Figure 4 . 3. The diffraction pattern of the as-synthesised UiO-66-NH_2 corresponds well to the literature[35]. The narrow and sharp peaks for In-1 to In-4 indicates high crystallinity and consequently a preserved structure upon In_2S_3 decoration. With further loading of In species, In-5 shows a complete disruption of crystallinity. The additional peaks observed in In-5 at 2θ of 27.5°, 33.3° and 48.2°, as labelled with Figure 4 . 3, correspond to the diffractions of the (311), (400) and (440) planes of In_2S_3 (JCPDS 73-1366)[36]. The In_2S_3 species present in In-1 to In-4 are of much smaller particle sizes to be detected by XRD.

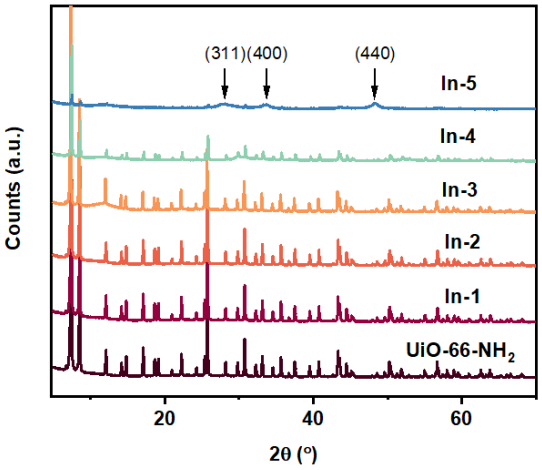


Figure 4 . 3 | X-ray diffraction pattern of the series of catalysts, with the peaks of In_2S_3 phases in In-5 labelled.

Additionally, synchrotron X-ray diffraction (SXRD) was performed to quantify the structural change to the unit cell for the series of catalysts. Le Bail refinements of the SXRD data suggests a face-centred topology with an Fm-3m symmetry. As the In_2S_3 content increases, the lattice parameter of the cubic unit cell decreases slightly by 0.0422% for In-1 to 0.244% for In-5 compared to 20.814665 ± 0.000075 Å obtained for UiO-66-NH_2, as shown in

Sample	Lattice parameter/ Å	Rwp
UiO-66-NH2	20.814665 ± 0.000075	10.65
In-1	20.805876 ± 0.000076	10.22
In-2	20.802218 ± 0.000063	10.93
In-3	20.800429 ± 0.000076	10.29
In-4	20.804362 ± 0.000298	17.28
In-5	20.763923 ± 0.003212	20.74

Table 4 . 3. The contraction of lattice parameter can be explained by the increase in electrostatic force within the framework[37].

Sample	Lattice parameter/ Å	R_{wp}
UiO-66-NH_2	20.814665 ± 0.000075	10.65
In-1	20.805876 ± 0.000076	10.22
In-2	20.802218 ± 0.000063	10.93
In-3	20.800429 ± 0.000076	10.29
In-4	20.804362 ± 0.000298	17.28
In-5	20.763923 ± 0.003212	20.74

Table 4 . 3 | Lattice parameters from Le Bail refinement of SXRD

X-ray photoelectron spectroscopy (XPS) is performed to study the chemical interaction of the In_2S_3/UiO-66-NH_2 interface. High-resolution In 3d spectrum of the series of catalysts (Figure 4 . 4 a) shows binding energies for $3d_{3/2}$ and In $3d_{5/2}$ summarized in Table 4 . 4. Normalizing the $3d_{5/2}$ peak of the series of catalysts demonstrates a clear shift towards lower binding energy (Figure 4 . 4 b), from 452.9 eV for In-1 to 452.3 eV for In-5. This demonstrates a reduction of nuclear charge on In, which can be explained by the transition of coordination environments from In-N to In-S.

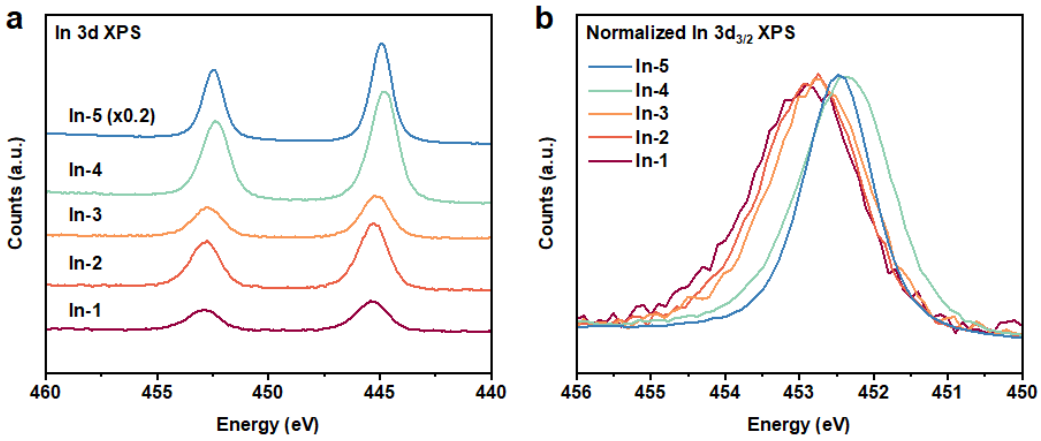


Figure 4 . 4 | (a) High-resolution In 3d XPS spectra, (b) Normalized $3d_{5/2}$ peak of In-1 to In-5

Sample	$3d_{5/2}$	$3d_{3/2}$
In_2S_3[38]	445.5	452.9
In-1	445.4	452.9
In-2	445.2	452.8
In-3	445.2	452.7
In-4	444.9	452.3
In-5	444.8	452.5

Table 4 . 4 | Peak binding energy of In $3d_{5/2}$ and $3d_{3/2}$ XPS for the series of catalyst

On another hand, the S 2p spectrum shown in Figure 4 . 5 is more complex. Peaks around 169.0 eV corresponds to the sulphate states, while peaks around 162.0 eV corresponds to sulphide states. For In-1 to In-3, peaks centred at 169.0 eV can be seen clearly, indicating the presence of sulphate species which are likely due to the oxidation of thiourea added during the synthesis process. The sole existence of $2p_{3/2}$ and $2p_{1/2}$ peaks for In-4 and In-5, at 161.5 eV and 162.7 eV, respectively, indicates the formation of In_2S_3 species present combined with In XPS. The co-

existence of peaks at 162.0 eV and 169.0 eV for In-2 and In-3 suggests the presence of both sulphate and sulphide species.

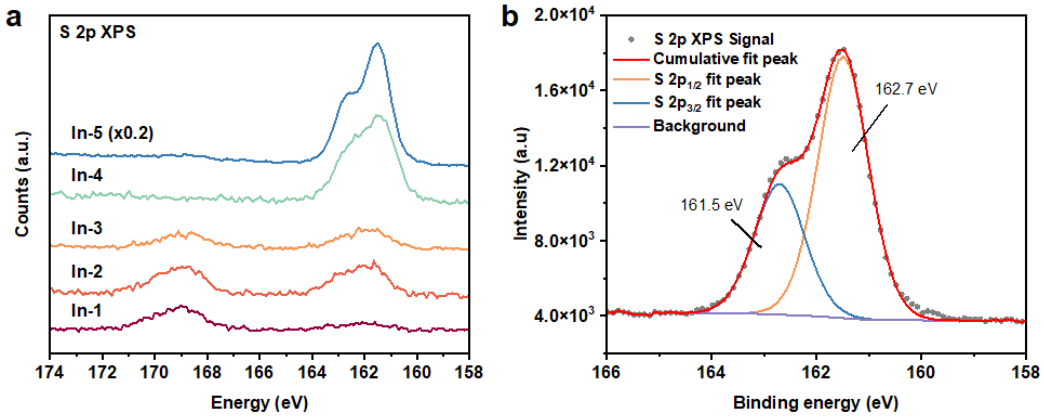


Figure 4 . 5 | (a) S 2p XPS of In-1 to In-5 samples, (b) In-5 S 2p XPS fitted with two Gaussian peaks corresponding to $2p_{1/2}$ and $2p_{3/2}$ peaks.

The nitrogen present on the -NH_2 amine group of the 2-aminoterephthalic acid organic linker has a value of 399.2 eV from the literature. Interestingly, there is a consistent shift of N 2p binding energy to 399.7 eV for In-2 to In-4 catalysts (Figure 4 . 6 a), showing the close chemical interaction between the Lewis basic -NH_2 and the Lewis acidic In^{3+} in the synthesis. A Gaussian fit is performed on the data for clarity in comparison as presented in Figure 4 . 6 b, with the peak position and R-factor of Gaussian fit summarized in Table 4 . 5. The shift in the In-1 sample is less pronounced due to the reduced In^{3+} present in the catalyst, while that for In-5 is likely due to aggregation of In_2S_3 particles before penetrating into the porous UiO-66-NH_2. Either way, more of the -NH_2 sites on the organic linker are untouched and has a binding energy closer to free 2-aminoterephthalic acid organic linker.

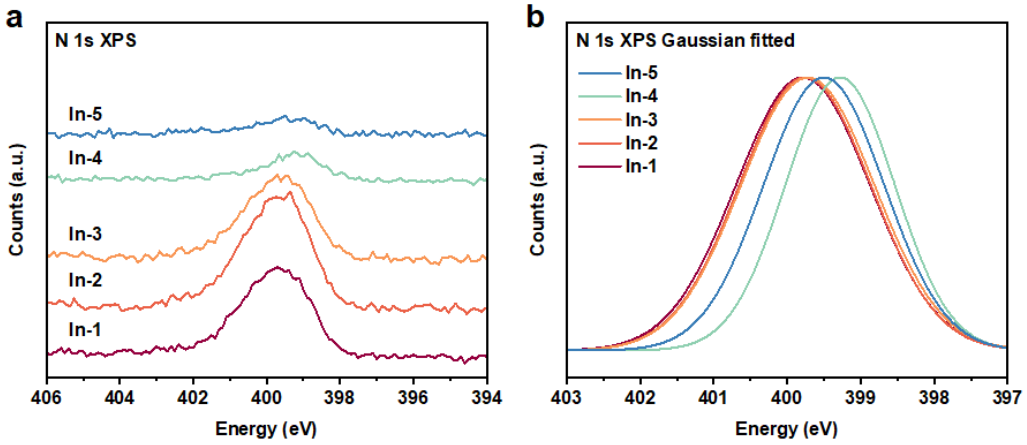


Figure 4 . 6 | (a) N 2p XPS of In-1 to In-5 samples, (b) Normalized N 2p XPS fitted with a Gaussian peak. The lower R-factor obtained for In-4 and In-5 is due to the lower signal-to-noise ratio.

Sample	N 1s / eV	R-factor of Gaussian Fit
UiO-66-NH_2[39]	399.2	
In-1	399.8	0.977
In-2	399.8	0.978
In-3	399.7	0.977
In-4	399.3	0.878
In-5	399.5	0.764

Table 4 . 5 | Peak binding energy of N 2p XPS, and the R-factor of Gaussian Fit for the series of catalyst

FT-IR was further applied to inspect the structural changes of the catalysts as shown in Figure 4 . 7 a. The intense bands between 1700 to 1100 cm^{-1} are associated to the vibration of the organic linker present in the samples, with the most intense bands at 1382 cm^{-1} and 1484 cm^{-1} relating to the symmetric and asymmetric stretching of the -C(O)O carboxylic group. Such bands unaltered upon In_2S_3 incorporation indicates a retained crystal structure of UiO-66-NH_2 MOF, echoing with findings from XRD. Interestingly, The IR peak of 1656

cm^{-1} is attributing to the bending motion for the two N-H bonds in the -NH_2 group (Figure 4 . 7 b). A significant decrease in intensity of this peak is observed for all In-1 to In-5 compared to pristine UiO-66-NH_2, suggesting that the interaction between the -NH_2 group and In species restricts the bending motion around N atom[40].

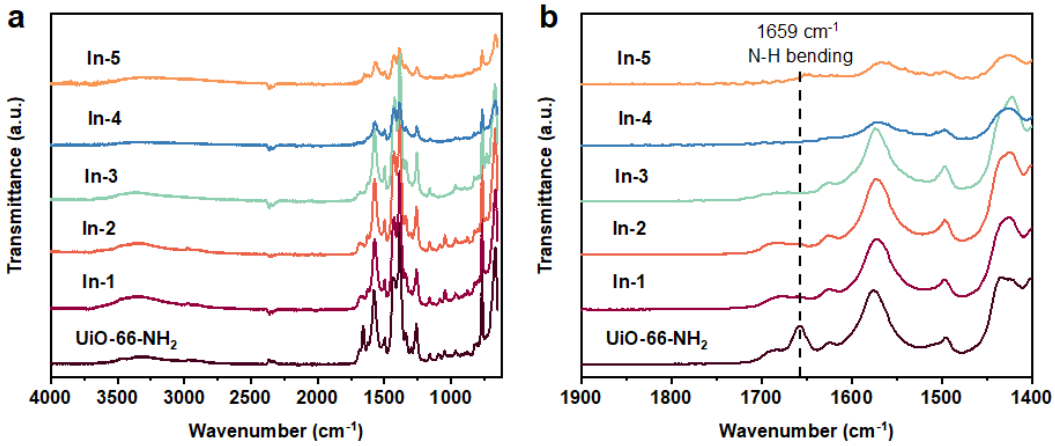


Figure 4 . 7 | (a) FT-IR full spectra of the series of catalyst and (b) N-H bending at 1659 cm^{-1}

To confirm the local coordination structure and the interaction on heterojunction interface of In_2S_3/UiO-66-NH_2, Indium K-edge X-ray absorption spectroscopy (XAS) has been performed. As shown in Figure 4 . 8, the normalised peak intensity at the absorption edge (27,948 eV) gradually decreases as the In and S loading increases, representing an increase in electron density in indium present in the catalysts. This is attributed to the gradual decrease of electronegativities of first shell neighbours in the In species[41].

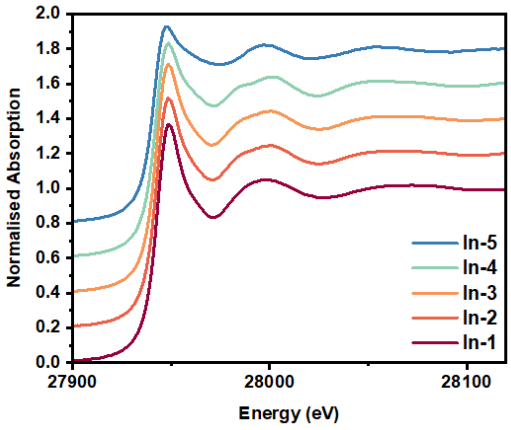


Figure 4 . 8 | In K-edge X-ray Absorption Spectra of In-1 to In-5. Dr. Tai-Sing Wu and Prof. Yun-Liang Soo are gratefully acknowledged for their assistance in XAS data collection. The XAS data fitting is consequently performed by Bryan Ng.

Similarly, Wavelet transform (WT, Figure 4 . 9) of the EXAFS data further proves it by demonstrating a gradual shift of peak position from 5.81 $Å^{-1}$, 1.61 Å for In-1 (Figure 4 . 9 a), to 6.06 $Å^{-1}$, 1.99 Å for In-5 (Figure 4 . 9 e) in both k (atomic number) and R (radial distances) of the first shell neighbours relative to In. Based on the reagents added during our synthesis procedures, the decrease of intensity at the absorption edge along with the shift in WT peak are attributed to the change in coordination environment from mainly In-O or In-N to In-S.

Furthermore, the second shell scattering for In-3 and In-5, wavelet transform intensity with R higher than 3Å shows an increase in cluster size as shown by the In-In scattering.

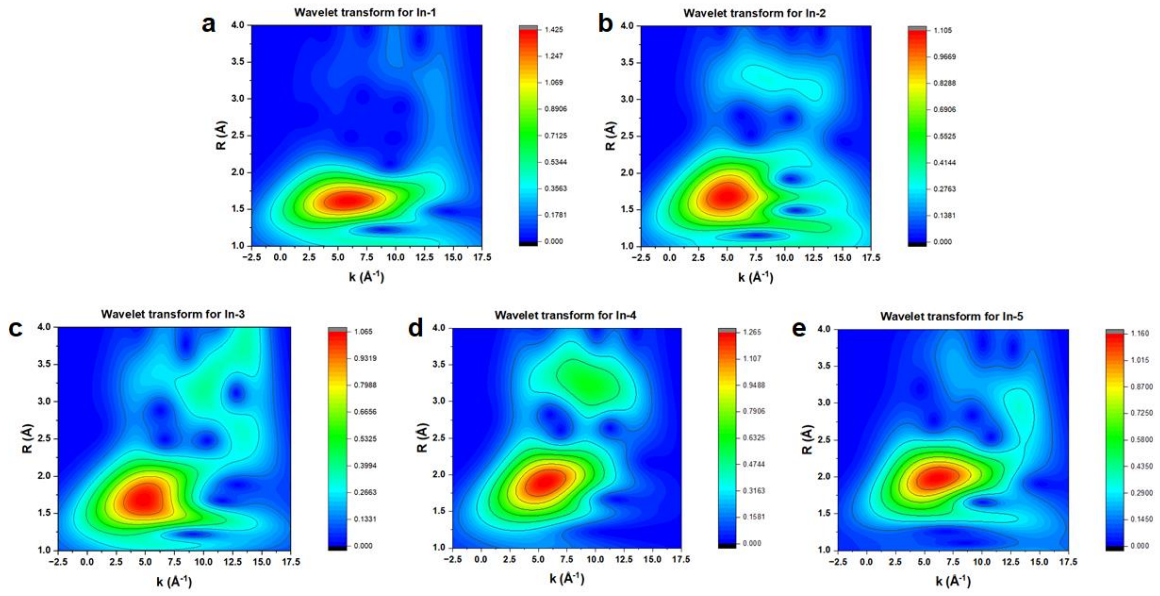


Figure 4 . 9 | Wavelet analysis of XAS data for (a) In-1, (b) In-2, (c) In-3, (d), In-4, and (e) In-5

A fit of the Fourier-transform extended X-ray absorption fine structure (FT-EXAFS) data is performed to further quantify the coordination environment, with all k^1, k^2, and k^3-weighted spectra been fitted in R-space for optimal reliability (Figure 4 . 10 a). More details on k-space EXAFS data are shown in Figure 4 . 10 b and the fitting parameters are summarised in Table 4 . 6.

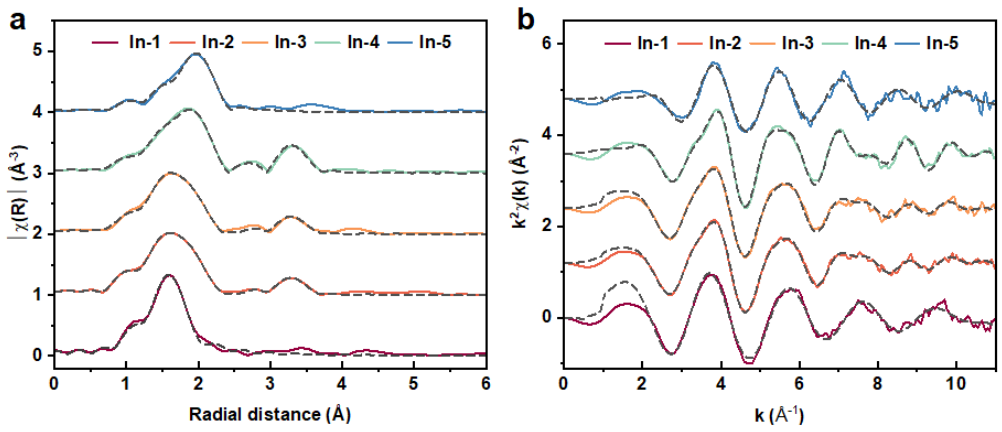


Figure 4 . 10 | Data and fit of (a) R-space and (b) k-space of In K-edge EXAFS data for In-1 to In-5

Sample	Scattering Paths	Coordination number	Radial distance / Å	D-W factor / 10^{-3}	ΔE / eV	R-factor of fit
In-1	In-O/N	5.99 ± 0.53	2.17 ± 0.01	6.2 ± 1.5	1.86 ± 1.19	1.82
In-2	In-O/N	4.65 ± 0.33	2.164 ± 0.009	9.4 ± 1.5	-0.89 ± 0.66	0.26
	In-S	2.48 ± 0.31	2.504 ± 0.009	9.4 ± 1.5		
	In-In (from InS)	4.94 ± 0.69	3.51 ± 0.01	13.4 ± 1.8		
In-3	In-O/N	4.33 ± 0.49	2.16 ± 0.01	8.4 ± 2.4	-1 ± 1.06	0.94
	In-S	2.39 ± 0.46	2.51 ± 0.01	8.4 ± 2.4		
	In-In (from InS)	5.07 ± 1.16	3.52 ± 0.02	13.4 ± 3.0		
In-4	In-O/N	2.21 ± 0.24	2.16 ± 0.02	7.5 ± 1.6	-0.31	0.86
	In-S	4.07 ± 0.57	2.51 ± 0.007	7.5 ± 1.6		
	In-In (from InS)	6.84 ± 0.95	3.52 ± 0.01	11.1 ± 1.5		
In-5	In-O/N	0.51 ± 0.59	2.16 ± 0.02	9.4 ± 2.6	2.09 ± 1.18	1.33

Table 4 . 6 | EXAFS fitting parameters for In-1 to In-5

The first coordination around In originates from amino group of the organic linker and O in hydroxide. The similarity between In-N and In-O scattering hinders the ability to discriminate between them so the following content will discuss In-N/O together. For the lowest loading of In-1, a coordination number of 5.99 ± 0.53 based on the In-N/O scattering path can be obtained.

Hexa-aqua indium ions must have been washed away during the synthesis procedures, and therefore the indium ions present in In-1 must at least have coordinated to one amino group from the $–NH_2$ as probed by XPS and FT-IR previously. As the loading of In is increased, a reduction in In-N/O coordination is observed from 5.99 ± 0.53 in In-1 to 0.51 ± 0.59 in In-5, corresponding to the formation of In_2S_3, similar to our findings in XRD. This can also be seen by an increase in In-S scattering from 2.48 ± 0.31 for In-2 gradually to 5.08 ± 1.07 for In-5. Interestingly, a rather longer range order of In-In second shell scattering at around 3.51 ± 0.01 Å appears for In-2 with coordination number 6.84 ± 0.95, and gradually increases to 5.07 ± 1.16 for In-3 and 6.84 ± 0.95 for In-4. This increase in second shell In-In scattering can be attributed to the aggregation of In_2S_3 particles present in the catalysts.

In order to study the morphology upon In_2S_3 decoration, transmission electron microscopy (TEM) was conducted to study the microstructures of UiO-66-NH_2 with In_2S_3 decoration. As confirmed in TEM image (Figure 4 . 11), UiO-66-NH_2 display a cubic morphology with truncated octahedra which gives (100) and (111) facet[42].

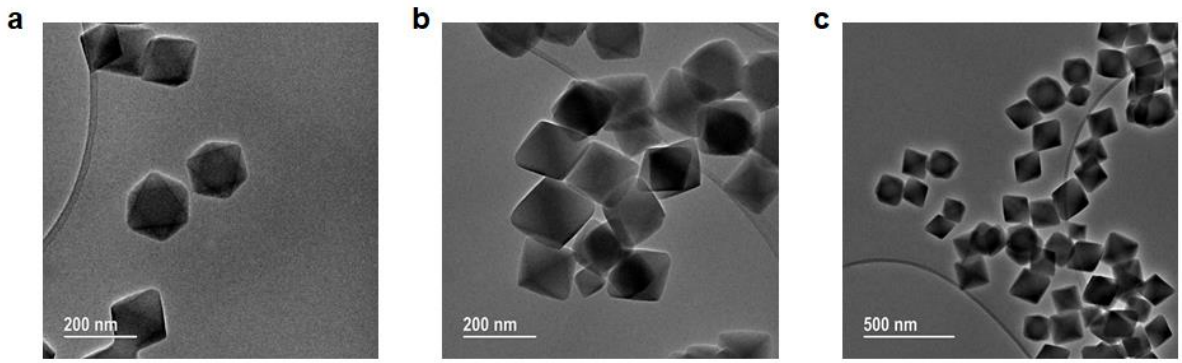


Figure 4 . 11 | TEM image of UiO-66-NH_2. Mr. Ping-Luen Ho is gratefully acknowledged for his assistance in collecting the TEM images and their EDX mappings.

Such morphologies are retained as shown by the TEM images. For In-1 to In-3 (Figure 4 . 12, Figure 4 . 13, Figure 4 . 14, respectively), the cubic morphology with truncated octahedra remains unchanged, with no clear deposition of In_2S_3 species on the surface likely due to the small cluster size being under the detection limit.

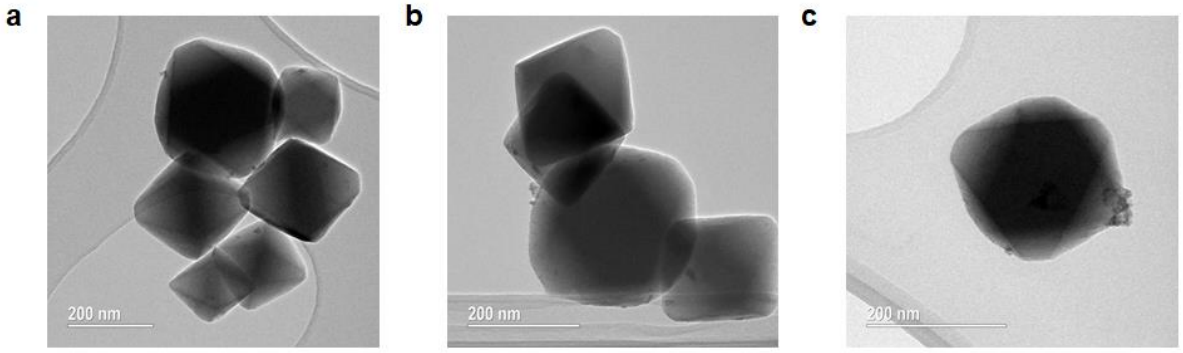


Figure 4 . 12 | TEM image of In-1.

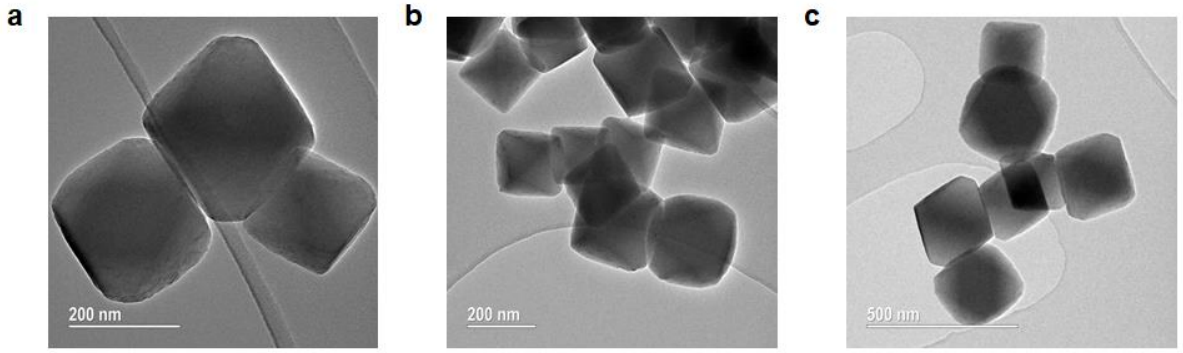


Figure 4 . 13 | TEM image of In-2.

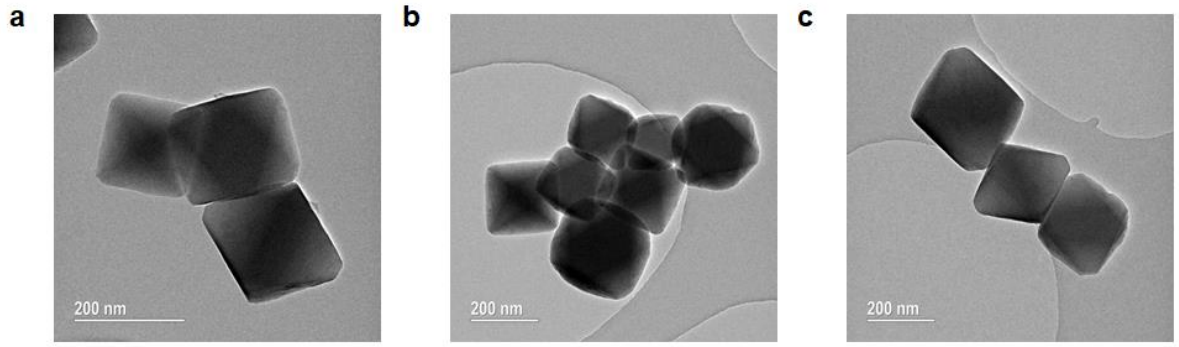


Figure 4 . 14 | TEM image of In-3.

Energy dispersive X-ray (EDX) elemental mappings of In-3 (Figure 4 . 15) illustrates the evenly distributed Zr, C, N and O from UiO-66-NH_2 octahedra, with In and S evenly scattered in.

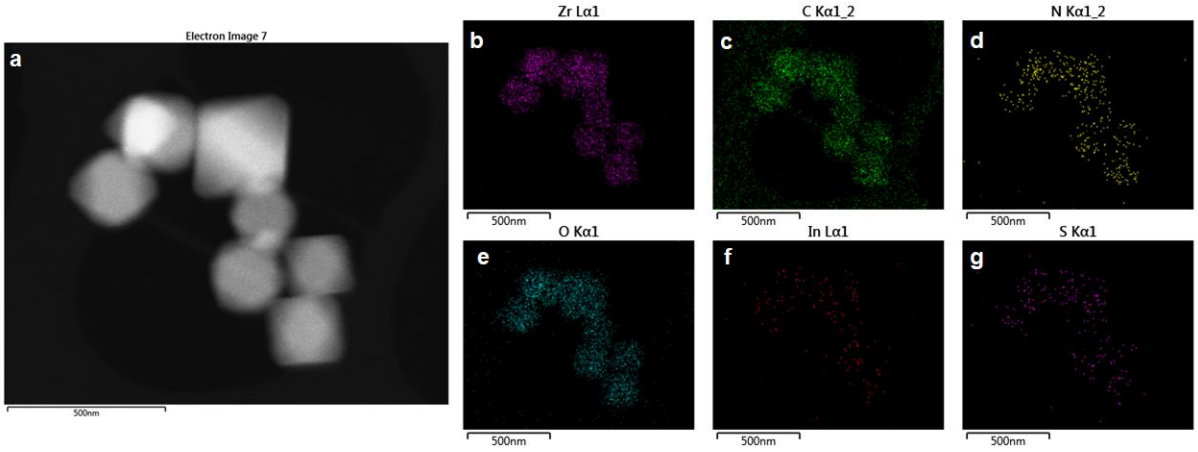


Figure 4 . 15 | (a) TEM image of In-3 and its EDX mapping of (b) Zr, (c) C, (d) N, (e) O, (f) In and (g) S.

The In_2S_3 clustering can be clearly observed in the In-4 sample (Figure 4 . 16), whose effect is magnified in In-5 where the octahedral UiO-66-NH_2 particles are fully wrapped inside an aggregated In_2S_3 bulk (Figure 4 . 17).

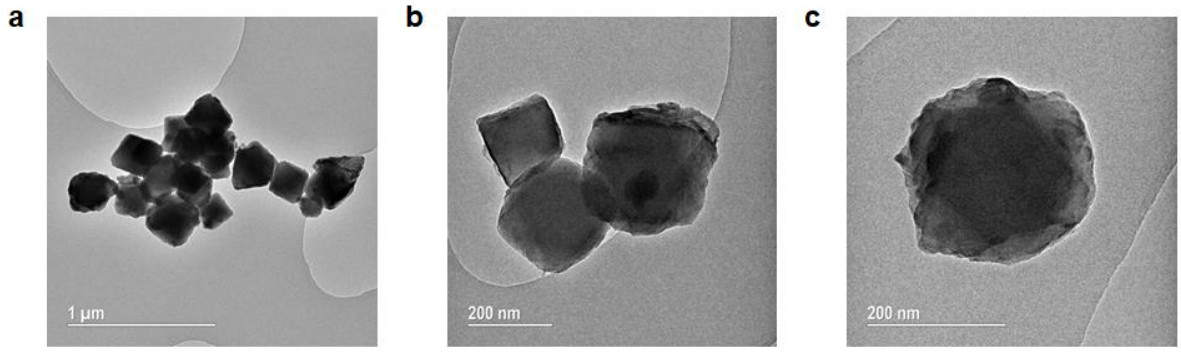


Figure 4 . 16 | TEM image of In-4.

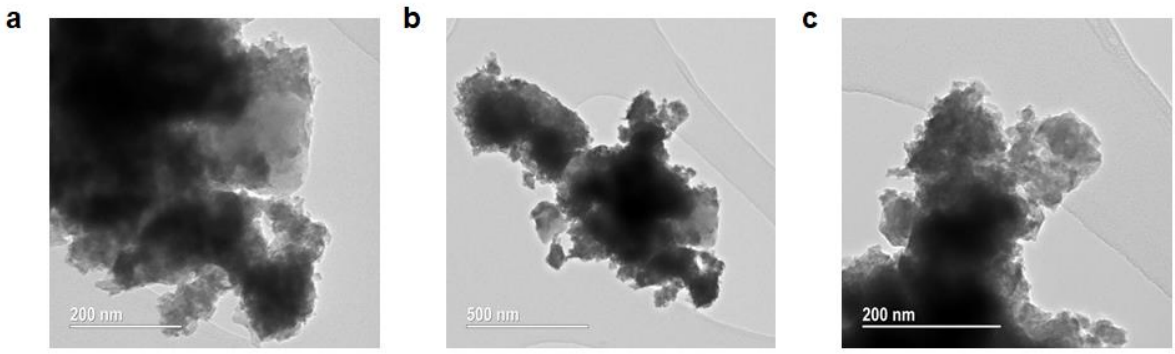


Figure 4 . 17 | TEM image of In-5.

The surface area and adsorption behaviour of catalysts upon the introduction of In species were analysed by N_2 adsorption−experiments. UiO-66-NH_2 was found to possess a BET surface area of 790 ± 3.6 m^2 g^{-1} which agree with values in the literature[43]. The same surfacea area for In-1, In-2 and In-3 were found to be 959 ± 4.3, 958 ± 3.7 and 848 ± 3.4 m^2 g^{-1} (Figure 4 . 18), respectively, higher than that for the parent UiO-66-NH_2. The increase in surface area can be explained by the gate-opening effect of the In_2S_3 species on UiO-66-NH_2, whose observation were reported in the literature. On another hand, In-4 and In-5 exhibit considerably lower adsorption capability towards N_2, with a BET surface area of 526 ± 2.8 and 296 ± 0.8 m^2 g^{-1} for In-4 and In-5, respectively. The decrease in BET surface area is undoubtedly due to the aggregation of In_2S_3 on the surface of the UiO-66-NH_2, hence restricting the access of adsorbate to the internal channels or pores within the structure.

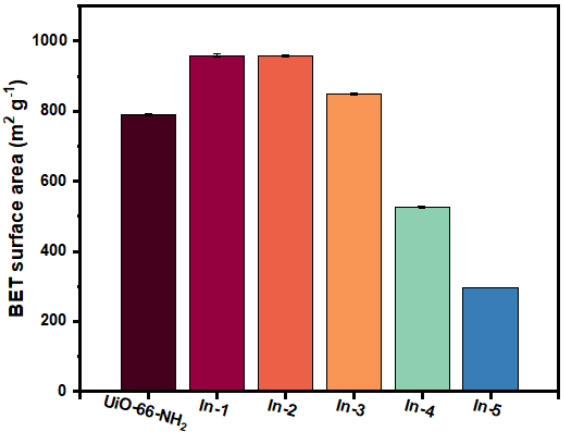


Figure 4 . 18 | BET Surface area of In-1 to In-5 compared with UiO-66-NH_2

The adsorption-desorption isotherms of the series of samples (Figure 4 . 19 a) for UiO-66-NH_2, In-1 to In-4 demonstrate type-I isotherm, suggesting a microporous (pore size < 20Å) structure in line with the literature[44]. However, the type-IV isotherm exhibited by In-5 shows a characteristic hysteresis loop between a relative pressure of 0.5 to 1.0 due to secondary process of capillary condensation. It has been reported that such similar type IV physisorption isotherm can also be observed in pure In_2S_3[45], suggesting that In-5 with excess loading over the surface predominantly retains the properties of In_2S_3. The BET surface area plot for all samples are also provided in Figure 4 . 19 b.

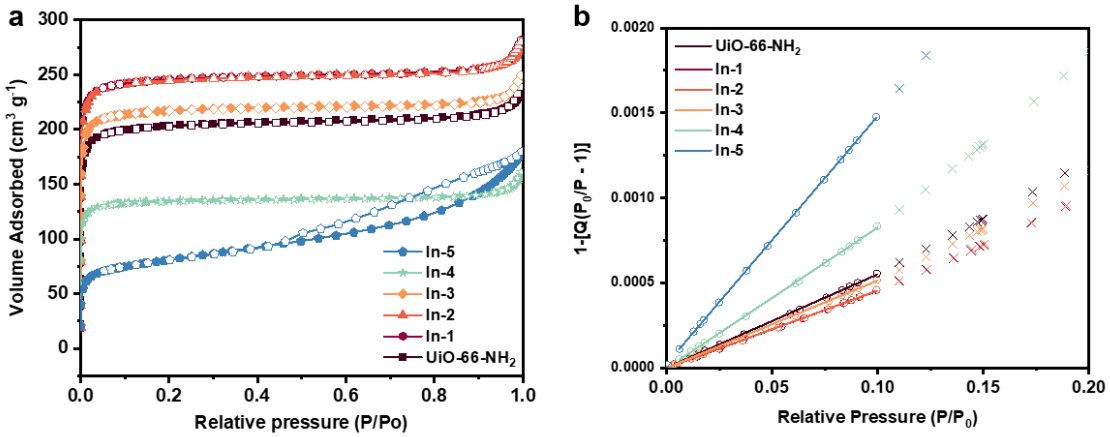


Figure 4 . 19 | (a) N_2 Adsorption-Desorption isotherm of In-1 to In-5 compared to UiO-66-NH_2, (b) BET surface area plot of In-1 to In-5 and UiO-66-NH_2

4.2.3 Structure-Reactivity Relationship

The volcano trend of catalytic reduction of CO_2 against increasing In_2S_3 content can now be explained by the variance in their structural properties. Evidently, the 323 % and 158 % increase of CO and CH_4 observed for In_2S_3 coupled UiO-66-NH_2 (In-2) compared to the pristine MOF is due to synergy between the anchored In_2S_3 species and UiO-66-NH_2 MOF. The chemical interaction between the amino group on the organic linker of UiO-66-NH_2 and In_2S_3 has been evidenced by XPS, IR and EXAFS fitting. In the case of In-1, mainly In-O/N was detected from EXAFS fitting. This suggests the coordination environment around In is mainly aqua ion or hydroxide ion, and will behave electronically more like In_2O_3. With marginally more In loading in In-2, the observed mixture of In-O/N and In-S allows the In species to behave more like a semiconductor In_2S_3 electronically. It is widely known oxide materials possess a larger band gap compared to sulphide materials and for indium it is no exception. With more S next to In, more efficient charge carrier transport can be allowed due to the lower energy of the sulphur bonded In compared to oxygen bonded In. However, an excess of In_2S_3 can have a negative effect as seen in In-4 and In-5, where the aggregation of In_2S_3 will block the UiO-66-NH_2 as a whole as seen by the reduced surface area and TEM

images. Consequently, the optimal balance between In-O and In-S bonds in In-2 or In-3 leads to the formation of a well-defined interface between UiO-66-NH_2 and In_2S_3 and allow for efficient charge carrier transport for gate-opening mechanisms similar to the previous chapter for photocatalytic performance enhancement.

4.2.4 Optical Characterization

Having clarified the structure-reactivity relationship, optical characterization is then performed to examine the light induced response of the series of catalysts. The absorption features of synthesised photocatalysts were measured by UV-vis diffuse reflectance spectra (DRS). As illustrated in Figure 4 . 20, the optical spectrum of pristine UiO-66-NH_2 shows two absorption bands at 200-280 nm and 300-400 nm corresponds to the π to π^* electron transfer within the organic linker, and -NH_2 n to π^* ligand-to-metal charge transfer, respectively[46]. Upon the modification with In_2S_3, the absorption bands in composites In-1 to In-4 remain at similar energies, reflecting the preserved crystal structures of UiO-66-NH_2 as shown by other aforementioned structural characterization techniques. The enhancement in the intensity of visible absorbance and a slight redshift of the absorption edge has been recognized as the loading of In_2S_3 components increases.

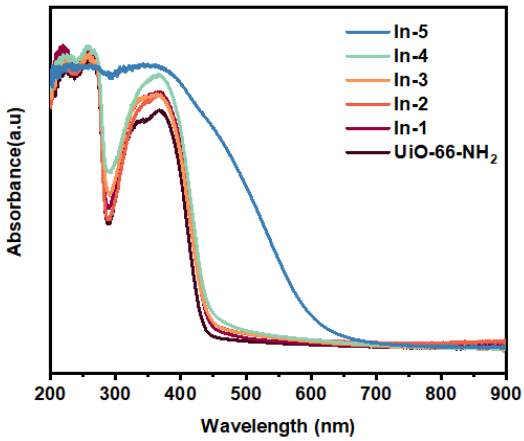


Figure 4 . 20 | UV-Vis Spectra of UiO-66-NH_2, In-1 to In-5

Tauc analysis (Figure 4 . 21) was subsequently conducted to probe the electronic band structure of the samples. The band gaps exhibited similar energies to the parent UiO-66-NH_2 with values ranging from 2.89-2.91 eV, suggesting that the introduction of In_2S_3 into the MOF framework has minimal impact on the band gap. This is likely because of the relatively small size of In_2S_3 cluster relatively to UiO-66-NH_2 compared to a close contact between intimate layer-by-layer In_2Se_3 and MoS_2 previously reported in the literature. In-5 with excess amount of In_2S_3 has an absorption edge appears at around 600 nm and a band gap of 2.25 eV, which are highly similar to bulk In_2S_3[47,48].

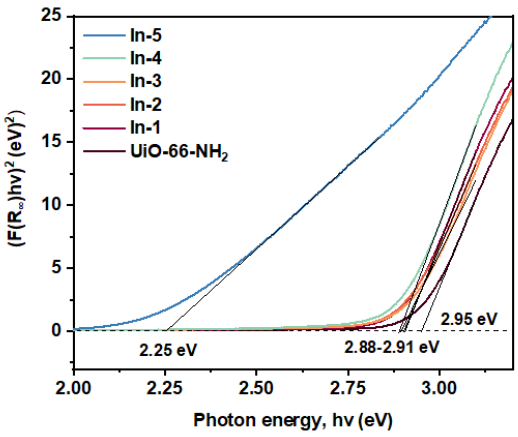


Figure 4 . 21 | Tauc plot of In-1 to In-5 compared to UiO-66-NH_2

The stability of photoexcited electron-hole pairs was further supported by solid-state photoluminescence spectroscopy (PL), which was carried out at room temperature with an excitation wavelength of 266 nm. Figure 4 . 22 presents the PL spectra of the whole series of catalysts. In-2 displays the highest PL intensity centered at 475 nm, with In-1 and In-3 exhibiting peak intensities comparable to each other. A noticeable reduction in PL intensity is observed In-4 and In-5, accompanied by a shift in peak to 480 nm and 505 nm, respectively, which corresponds to the redshift of the adsorption edge in UV-vis results. Intriguingly, the order of PL intensity also resembles the trend in photocatalytic activity. PL intensity could be influenced by several factors, and one of them is the exciton binding energy E_b. Excitonic effects arise from the Coulombic interactions between electrons and holes, which strongly enhance the oscillator strength between them[49]. The electron in the conduction band experience less attraction towards the localised hole due to the repulsive Coulomb forces generated by large numbers of electrons which surround the hole and excited electron. These repulsive forces provide a stabilizing energy balance. According to Gotoh and coworkers, it is theoretically suggested that the intensity of PL spectra is considerably enhanced by electron–hole Coulomb interaction[50]. This suggests that In-2 exhibits the highest E_b which allow the photoexcited free carriers bind together to form stable excitons. Consequently, the electron and hole can remain

spatially close, and the resonance stabilization from the overlap of the electron and hole wave functions limits the recombination and decay of the excitons[49,51]. The results provide adequate evidence of effective exciton separation and suppressed recombination of electron−hole pairs after the introduction of In_2S_3 in UiO-66-NH_2 due to interfacial interaction by heterojunction formation.

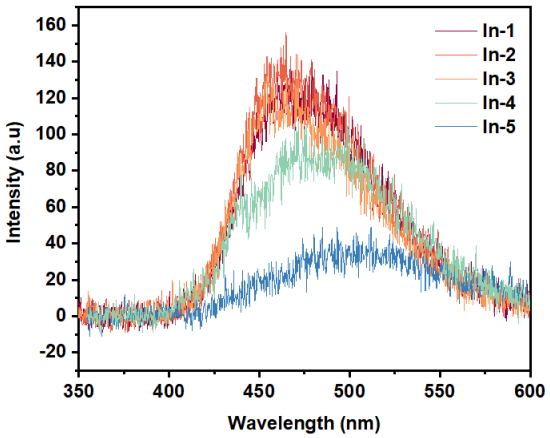


Figure 4 . 22 | PL spectra of In-1 to In-5. Dr. Yiyang Li and Prof. Robert Taylor are gratefully acknowledged for his help in collecting the PL spectra.

In addition, time resolved photoluminescence (TRPL) analysis were carried out to study the emission lifetime of photoexcited electrons as shown in Figure 4 . 23 and the average excited state lifetimes were found to be 0.090, 0.089, 0.087, 0.073 and 0.080 ns for In-1 to In-5, respectively. The fitting parameters are provided in Table 4 . 7. The shortest lifetime of In-4 is 19 % shorter than the longest lifetime observed in In-1. Both t_1 and t_2 present a decreasing trend as the In_2S_3 loading raises. The longer lifetimes of photo-generated excitons further support a better prevention of electron-hole pair recombination and more electrons could participate in CO_2 reduction, leading to potentially enhanced photocatalytic performance.

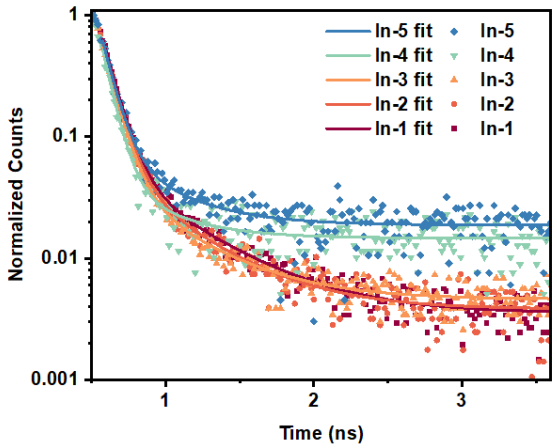


Figure 4 . 23 | TRPL spectra for In-1 to In-5. Dr. Yiyang Li is gratefully acknowledged for his assistance in collecting the TRPL spectra. The TRPL data fitting was performed by Bryan Ng.

Sample	y_0	A_1	t_1	A_2	t_2	R-factor
In-1	0.0035 ± 0.0008	0.174 ± 0.063	0.488 ± 0.081	372 ± 58	0.089 ± 0.002	0.998
In-2	0.0038 ± 0.0007	0.181 ± 0.080	0.449 ± 0.083	358 ± 65	0.088 ± 0.003	0.998
In-3	0.0046 ± 0.0007	0.143 ± 0.077	0.452 ± 0.103	388 ± 73	0.087 ± 0.003	0.998
In-4	0.0147 ± 0.0006	0.151 ± 0.134	0.360 ± 0.114	1217 ± 323	0.073 ± 0.003	0.986
In-5	0.0188 ± 0.0007	0.278 ± 0.129	0.374 ± 0.063	739 ± 158	0.080 ± 0.003	0.991

Table 4 . 7 | Fitting parameters of TRPL on a bi-exponential decay function for In-1 to In-5.

4.2.5 Mechanism of photocatalytic CO_2 reduction

The addition of In_2S_3 into UiO-66-NH_2 system has significantly increased its photocatalytic CO_2 reduction activity, indicating the usefulness of In_2S_3 phase in the MOF in the activation of H_2 and CO_2 molecules in reducing the activation energy barrier of the reaction. The chemistry underlying such activation is postulated towards the photo-excitation of electrons from valence band into conduction band of In_2S_3[52]. Upon such excitation, the charge transfer processes from InS clusters to the terephthalic acid organic linker via the amino group will put δ+ charges on the In orbitals, while there will be δ- charges on the N of the amino group and the S orbitals. As such, H_2 can be dissociative activated in heterolytic way via an FLP-like manner, similar to the descriptions in the Ru/bpy in Chapter 3[53]. The hydridic hydrogen atom associated with Indium and protonic hydrogen atom with sulphur will assist the catalytic reduction of CO_2 (presumably binding on similar sites or -NH_2 sites) towards the formation of CO and CH_4. It remains unclear the exact reaction pathway between the H_2 and CO_2 to form CO and CH_4.

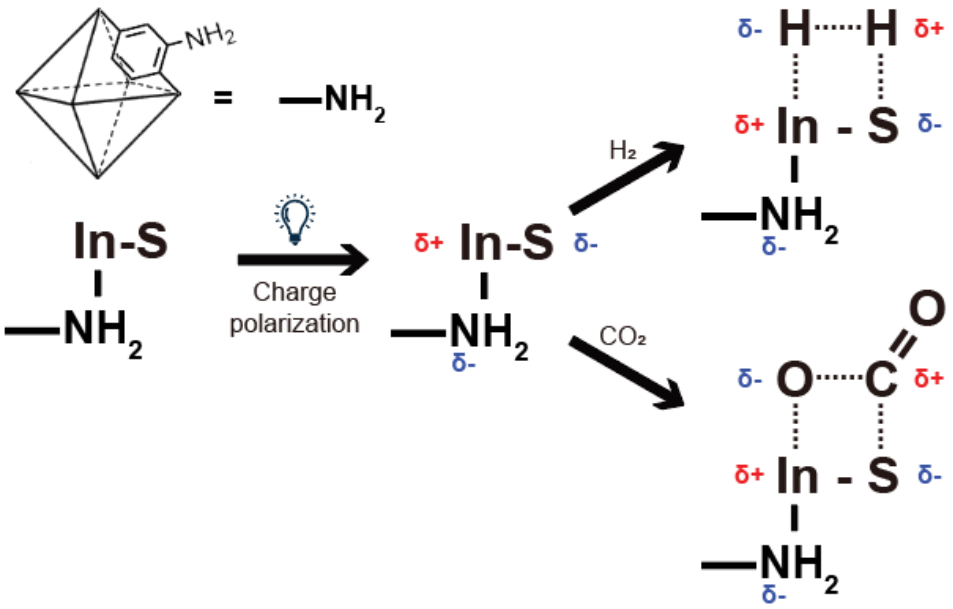


Figure 4 . 24 | Activation of H_2 and CO_2 via an FLP-like manner by In_2S_3 materials upon light irradiation

On top of that, the overall trend of catalysis is correlated with the increased BET surface area observed in the series of In_2S_3-anchored catalysts. This is likely due to the synergistic opening of the organic linker, termed "Gate-Opening Effect" of the MOFs[54,55], for improved access into the pores of UiO-66-NH_2. The origins of the Gate-Opening Effect are postulated to be related to the charge transfer processes from the In_2S_3 towards UiO-66-NH_2 at the interface between the two materials. More characterization of the dihedral angles of the organic linker before and after In_2S_3 incorporation will be needed for reliable conclusions to be drawn.

4.3 Conclusion

A one-pot synthesis method of In_2S_3-decorated UiO-66-NH_2 with different loadings of In_2S_3 was devised. The deposition of In_2S_3 on the amino group of the organic linker in UiO-66-NH_2 was evidenced by IR and XPS. An increase of BET surface area was observed, which can be correlated with the increase in photocatalytic CO_2 reduction activity via increase in adsorption sites in the In_2S_3/UiO-66-NH_2 interface. This work can shed light on devising new synthesis methods for the design of interface between MOFs and co-catalysts for more efficient photocatalysts.

4.4 Reference

1 Xue, Q., Zhang, Z., Ng, B. K. Y., Zhao, P. & Lo, B. T. W. Recent Advances in the Engineering of Single-Atom Catalysts Through Metal-Organic Frameworks. *Top Curr Chem (Cham)* **379**, 11 (2021).

2 Xue, Q., Ng, B. K. Y., Man, H. W., Wu, T. S., Soo, Y. L., Li, M. M., Kawaguchi, S., Wong, K. Y., Tsang, S. C. E., Huang, B. & Lo, T. W. B. Controlled synthesis of Bi- and tri-nuclear Cu-oxo nanoclusters on metal-organic frameworks and the structure-reactivity correlations. *Chem Sci* **13**, 50-58 (2021).

3 Wang, Q., Gao, Q., Al-Enizi, A. M., Nafady, A. & Ma, S. Recent advances in MOF-based photocatalysis: environmental remediation under visible light. *Inorg Chem Front* **7**, 300-339 (2020).

4 Liu, H., , C. X. & , D. L., and Hai-Long Jiang. Photocatalytic Hydrogen Production Coupled with Selective Benzylamine Oxidation over MOF Composites. *Angewandte Chemie* **130**, 5477-5481 (2018).

5 Zhang, M., Wang, L., Zeng, T., Shang, Q., Zhou, H., Pan, Z. & Cheng, Q. Two pure MOF-photocatalysts readily prepared for the degradation of methylene blue dye under visible light. *Dalton Trans* **47**, 4251-4258 (2018).

6 Ploskonka, A. M. & DeCoste, J. B. Tailoring the Adsorption and Reaction Chemistry of the Metal-Organic Frameworks UiO-66, UiO-66-NH2, and HKUST-1 via the Incorporation of Molecular Guests. *ACS Appl Mater Interfaces* **9**, 21579-21585 (2017).

7 Zhai, Z., Zhang, X., Wang, J., Li, H., Sun, Y., Hao, X., Qin, Y., Niu, B. & Li, C. Washable and flexible gas sensor based on UiO-66-NH2 nanofibers membrane for highly detecting SO2. *Chemical Engineering Journal* **428** (2022).

8 Xue, Q., Chan, K. H., Yim, C. K., Ng, B. K. Y., Chen, T., Day, S. J., Tang, C., Kawaguchi, S., Wong, K.-Y. & Lo, T. W. B. Guest-Anion-Induced Rotation-Restricted Emission in UiO-66-NH2 and Advanced Structure Elucidation. *Chem Mater* **33**, 5422-5429 (2021).

9 Yoskamtorn, T., Zhao, P., Wu, X. P., Purchase, K., Orlandi, F., Manuel, P., Taylor, J., Li, Y., Day, S., Ye, L., Tang, C. C., Zhao, Y. & Tsang, S. C. E. Responses of Defect-Rich Zr-Based Metal-Organic Frameworks toward NH3 Adsorption. *J Am Chem Soc* **143**, 3205-3218 (2021).

10 Sun, D., Fu, Y., Liu, W., Ye, L., Wang, D., Yang, L., Fu, X. & Li, Z. Studies on photocatalytic CO(2) reduction over NH2 -Uio-66(Zr) and its derivatives: towards a better understanding of photocatalysis on metal-organic frameworks. *Chemistry* **19**, 14279-14285 (2013).

11 Shen, L., Liang, S., Wu, W., Liang, R. & Wu, L. Multifunctional NH2-mediated zirconium metal-organic framework as an efficient visible-light-driven photocatalyst for selective

oxidation of alcohols and reduction of aqueous Cr(VI). *Dalton Trans* **42**, 13649-13657 (2013).

12 Laskowski, F. A. L., Oener, S. Z., Nellist, M. R., Gordon, A. M., Bain, D. C., Fehrs, J. L. & Boettcher, S. W. Nanoscale semiconductor/catalyst interfaces in photoelectrochemistry. *Nat Mater* **19**, 69-76 (2020).

13 Ng, B. K. Y., Wong, C. C. Y., Niu, W., Garcia, H. P., Li, Y., Ho, P.-L., Kuo, W. C. H., Taylor, R. A., Taniya, K., Wei, Q., Li, M., Stamatakis, M. & Tsang, S. C. E. Molecular layer-by-layer re-stacking of MoS2–In2Se3 by electrostatic means: assembly of a new layered photocatalyst. *Materials Chemistry Frontiers* **7**, 937-945 (2023).

14 Low, J., Yu, J., Jaroniec, M., Wageh, S. & Al-Ghamdi, A. A. Heterojunction Photocatalysts. *Adv Mater* **29**, 1601694 (2017).

15 Ioannides, T. & Verykios, X. E. Charge Transfer in Metal Catalysts Supported on Doped TiO2: A Theoretical Approach Based on Metal–Semiconductor Contact Theory. *Journal of Catalysis* **161**, 560-569 (1996).

16 Das, A., Kumar, P. M., Bhagavathiachari, M. & Nair, R. G. Hierarchical ZnO-TiO2 nanoheterojunction: A strategy driven approach to boost the photocatalytic performance through the synergy of improved surface area and interfacial charge transport. *Applied Surface Science* **534**, 147321 (2020).

17 Zhou, M., Wang, S., Yang, P., Huang, C. & Wang, X. Boron Carbon Nitride Semiconductors Decorated with CdS Nanoparticles for Photocatalytic Reduction of CO2. *ACS Catalysis* **8**, 4928-4936 (2018).

18 Simon, T., Bouchonville, N., Berr, M. J., Vaneski, A., Adrovic, A., Volbers, D., Wyrwich, R., Doblinger, M., Susha, A. S., Rogach, A. L., Jackel, F., Stolarczyk, J. K. & Feldmann, J. Redox shuttle mechanism enhances photocatalytic H2 generation on Ni-decorated CdS nanorods. *Nat Mater* **13**, 1013-1018 (2014).

19 Xiao, F. X., Hung, S. F., Miao, J., Wang, H. Y., Yang, H. & Liu, B. Metal-cluster-decorated TiO2 nanotube arrays: a composite heterostructure toward versatile photocatalytic and photoelectrochemical applications. *Small* **11**, 554-567 (2015).

20 Sun, W., Li, H., Li, H., Li, S. & Cao, X. Adsorption mechanisms of ibuprofen and naproxen to UiO-66 and UiO-66-NH2: Batch experiment and DFT calculation. *Chemical Engineering Journal* **360**, 645-653 (2019).

21 Garibay, S. J. & Cohen, S. M. Isoreticular synthesis and modification of frameworks with the UiO-66 topology. *Chem Commun (Camb)* **46**, 7700-7702 (2010).

22 Shen, L., Liang, S., Wu, W., Liang, R. & Wu, L. CdS-decorated UiO–66(NH2) nanocomposites fabricated by a facile photodeposition process: an efficient and stable visible-

light-driven photocatalyst for selective oxidation of alcohols. *Journal of Materials Chemistry A* **1**, 11473-11482 (2013).

23 Liang, Q., Cui, S., Liu, C., Xu, S., Yao, C. & Li, Z. Construction of CdS@UIO-66-NH2 core-shell nanorods for enhanced photocatalytic activity with excellent photostability. *J Colloid Interface Sci* **524**, 379-387 (2018).

24 Xu, H.-Q., Yang, S., Ma, X., Huang, J. & Jiang, H.-L. Unveiling Charge-Separation Dynamics in CdS/Metal–Organic Framework Composites for Enhanced Photocatalysis. *ACS Catalysis* **8**, 11615-11621 (2018).

25 Zhou, J.-J., Wang, R., Liu, X.-L., Peng, F.-M., Li, C.-H., Teng, F. & Yuan, Y.-P. In situ growth of CdS nanoparticles on UiO-66 metal-organic framework octahedrons for enhanced photocatalytic hydrogen production under visible light irradiation. *Applied Surface Science* **346**, 278-283 (2015).

26 Mao, S., Zou, Y., Sun, G., Zeng, L., Wang, Z., Ma, D., Guo, Y., Cheng, Y., Wang, C. & Shi, J. W. Thio linkage between CdS quantum dots and UiO-66-type MOFs as an effective transfer bridge of charge carriers boosting visible-light-driven photocatalytic hydrogen production. *J Colloid Interface Sci* **581**, 1-10 (2021).

27 Qin, J. H., Xu, P., Huang, Y. D., Xiao, L. Y., Lu, W., Yang, X. G., Ma, L. F. & Zang, S. Q. High loading of Mn(ii)-metalated porphyrin in a MOF for photocatalytic CO(2) reduction in gas-solid conditions. *Chem Commun (Camb)* **57**, 8468-8471 (2021).

28 Dao, X.-Y., Guo, J.-H., Zhang, X.-Y., Wang, S.-Q., Cheng, X.-M. & Sun, W.-Y. Structure-dependent iron-based metal–organic frameworks for selective CO2-to-CH4photocatalytic reduction. *J Mater Chem A* **8**, 25850-25856 (2020).

29 Fang, Z. B., Liu, T. T., Liu, J., Jin, S., Wu, X. P., Gong, X. Q., Wang, K., Yin, Q., Liu, T. F., Cao, R. & Zhou, H. C. Boosting Interfacial Charge-Transfer Kinetics for Efficient Overall CO(2) Photoreduction via Rational Design of Coordination Spheres on Metal-Organic Frameworks. *J Am Chem Soc* **142**, 12515-12523 (2020).

30 Sadeghi, N., Sharifnia, S. & Sheikh Arabi, M. A porphyrin-based metal organic framework for high rate photoreduction of CO2 to CH4 in gas phase. *J Co2 Util* **16**, 450-457 (2016).

31 Cheng, X.-M., Dao, X.-Y., Wang, S.-Q., Zhao, J. & Sun, W.-Y. Enhanced Photocatalytic CO2 Reduction Activity over NH2-MIL-125(Ti) by Facet Regulation. *Acs Catal* **11**, 650-658 (2020).

32 Gao, W. Y., Ngo, H. T., Niu, Z., Zhang, W., Pan, Y., Yang, Z., Bhethanabotla, V. R., Joseph, B., Aguila, B. & Ma, S. A Mixed-Metal Porphyrinic Framework Promoting Gas-Phase CO(2) Photoreduction without Organic Sacrificial Agents. *ChemSusChem* **13**, 6273-6277 (2020).

33 Zhang, H., Wei, J., Dong, J., Liu, G., Shi, L., An, P., Zhao, G., Kong, J., Wang, X., Meng, X., Zhang, J. & Ye, J. Efficient Visible-Light-Driven Carbon Dioxide Reduction by a Single-

Atom Implanted Metal-Organic Framework. *Angew Chem Int Ed Engl* **55**, 14310-14314 (2016).

34 Cabrero-Antonino, M., Remiro-Buenamanana, S., Souto, M., Garcia-Valdivia, A. A., Choquesillo-Lazarte, D., Navalon, S., Rodriguez-Dieguez, A., Minguez Espallargas, G. & Garcia, H. Design of cost-efficient and photocatalytically active Zn-based MOFs decorated with Cu(2)O nanoparticles for CO(2) methanation. *Chem Commun (Camb)* **55**, 10932-10935 (2019).

35 Kandiah, M., Nilsen, M. H., Usseglio, S., Jakobsen, S., Olsbye, U., Tilset, M., Larabi, C., Quadrelli, E. A., Bonino, F. & Lillerud, K. P. Synthesis and Stability of Tagged UiO-66 Zr-MOFs. *Chem Mater* **22**, 6632-6640 (2010).

36 Zheng, Z. M., Yu, J. L., Cheng, S. Y., Lai, Y. F., Zheng, Q. & Pan, D. M. Investigation of structural, optical and electrical properties of Cu doped beta-In2S3 thin films. *J Mater Sci-Mater El* **27**, 5810-5817 (2016).

37 Xue, Q., Chan, K. H., Yim, C. K., Ng, B. K. Y., Chen, T., Day, S. J., Tang, C., Kawaguchi, S., Wong, K.-Y. & Lo, T. W. B. Guest-Anion-Induced Rotation-Restricted Emission in UiO-66-NH2 and Advanced Structure Elucidation. *Chemistry of Materials* **33**, 5422-5429 (2021).

38 Chen, J., Liu, W. & Gao, W. Tuning photocatalytic activity of In2S3 broadband spectrum photocatalyst based on morphology. *Appl Surf Sci* **368**, 288-297 (2016).

39 Wang, H., Wang, S., Wang, S., Tang, J., Chen, Y. & Zhang, L. Adenosine-functionalized UiO-66-NH2 to efficiently remove Pb(II) and Cr(VI) from aqueous solution: Thermodynamics, kinetics and isothermal adsorption. *Journal of Hazardous Materials* **425**, 127771 (2022).

40 Zhao, F., Su, C. Y., Yang, W., Han, Y. Q., Luo, X., Li, C. M., Tang, W., Yue, T. & Li, Z. In-situ growth of UiO-66-NH2 onto polyacrylamide-grafted nonwoven fabric for highly efficient Pb(II) removal. *Appl Surf Sci* **527**, 146862 (2020).

41 Altman, A. B., Pemmaraju, C. D., Camp, C., Arnold, J., Minasian, S. G., Prendergast, D., Shuh, D. K. & Tyliszczak, T. Theory and X-ray Absorption Spectroscopy for Aluminum Coordination Complexes - Al K-Edge Studies of Charge and Bonding in (BDI)Al, (BDI)AlR2, and (BDI)AlX2 Complexes. *J Am Chem Soc* **137**, 10304-10316 (2015).

42 Zheng, L., Dong, Y. J., Chi, B., Cui, Z., Deng, Y., Shi, X., Du, L. & Liao, S. UiO-66-NH2-derived Mesoporous Carbon Catalyst Co-Doped with Fe/N/S as Highly Efficient Cathode Catalyst for PEMFCs. *Small* **15**, 1803520 (2019).

43 Luu, C. L., Nguyen, T. T. V., Nguyen, T. & Hoang, T. C. Synthesis, characterization and adsorption ability of UiO-66-NH2. *Adv Nat Sci-Nanosci* **6** (2015).

44 Thommes, M., Kaneko, K., Neimark, A. V., Olivier, J. P., Rodriguez-Reinoso, F., Rouquerol, J. & Sing, K. S. W. Physisorption of gases, with special reference to the evaluation of surface

area and pore size distribution (IUPAC Technical Report). *Pure Appl Chem* **87**, 1051-1069 (2015).

45 Kumar, N., Mishra, D., Kim, S. Y., Na, T. & Jin, S. H. Directly grown two dimensional In2S3 nanoflakes via one-step solvothermal method: Material properties on In2S3 and performance data for supercapacitors. *Data Brief* **32** (2020).

46 Wang, Y., Penas-Garzon, M., Rodriguez, J. J., Bedia, J. & Belver, C. Enhanced photodegradation of acetaminophen over Sr@TiO2/UiO-66-NH2 heterostructures under solar light irradiation. *Chem Eng J* **446** (2022).

47 Zhang, X. L., Zhang, N., Gan, C. X., Liu, Y. F., Chen, L., Zhang, C. & Fang, Y. Z. Synthesis of In2S3/UiO-66 hybrid with enhanced photocatalytic activity towards methyl orange and tetracycline hydrochloride degradation under visible-light irradiation. *Mat Sci Semicon Proc* **91**, 212-221 (2019).

48 Dong, W. B., Wang, D. B., Wang, H., Li, M. K., Chen, F., Jia, F. Y., Yang, Q., Li, X. M., Yuan, X. Z., Gong, J. L., Li, H. L. & Ye, J. Facile synthesis of In2S3/UiO-66 composite with enhanced adsorption performance and photocatalytic activity for the removal of tetracycline under visible light irradiation. *J Colloid Interf Sci* **535**, 444-457 (2019).

49 Li, F. M., Yang, L., Cai, Z. X., Wei, K., Lin, F. Y., You, J., Jiang, T., Wang, Y. R. & Chen, X. Enhancing exciton binding energy and photoluminescence of formamidinium lead bromide by reducing its dimensions to 2D nanoplates for producing efficient light emitting diodes. *Nanoscale* **10**, 20611-20617 (2018).

50 Gotoh, H. & Ando, H. Excitonic quantum confinement effects and exciton electroabsorption in semiconductor thin quantum boxes. *J Appl Phys* **82**, 1667-1677 (1997).

51 Wu, S. D., Cheng, L. W. & Wang, Q. Excitonic effects and related properties in semiconductor nanostructures: roles of size and dimensionality. *Mater Res Express* **4** (2017).

52 Wang, H. L., Zhang, L. S., Chen, Z. G., Hu, J. Q., Li, S. J., Wang, Z. H., Liu, J. S. & Wang, X. C. Semiconductor heterojunction photocatalysts: design, construction, and photocatalytic performances. *Chem Soc Rev* **43**, 5234-5244 (2014).

53 Ng, B. K. Y., Zhou, Z.-J., Liu, T.-T., Yoskamtorn, T., Li, G., Wu, T. S., Soo, Y.-L., Wu, X. P. & Tsang, S. C. E. Photo-Induced Active Lewis Acid-Base Pairs in a Metal-Organic Framework for H2 Activation. *J Am Chem Soc* **145**, 19312-19320 (2023).

54 Craig, G. A., Larpent, P., Kusaka, S., Matsuda, R., Kitagawa, S. & Furukawa, S. Switchable gate-opening effect in metal-organic polyhedra assemblies through solution processing. *Chem Sci* **9**, 6463-6469 (2018).

55 Sun, X., Ma, Y., Zhao, J., Li, D. S., Li, G., Zhang, L. & Liu, Y. Tuning the gate opening pressure of a flexible doubly interpenetrated metal-organic framework through ligand functionalization. *Dalton Trans* **47**, 13158-13163 (2018).

5 Chapter 5 | Enhancing photocatalytic water splitting via Gate-Opening Effect of UiO MOFs

5.1 Introduction

Metal-organic frameworks (MOFs) have received considerable attention in the field of photocatalysis[1,2]. They are a class of porous inorganic compound with high surface area, whose assembly of organic linker molecules and metal-oxalate clusters results in high chemical stability along with wide structural tuneability. The organic linker present in the MOF can act as chromophore to extract light energy for catalysis[3-5], while its highly porous nature provides plentiful adsorption site for reactant molecules[6,7]. It is also useful for a wide-range of application such as sensing[8], separation and adsorption[9]. The Universitet i Oslo (UiO) series is a family of MOFs well known for its chemical stability, which stems from the strong electrostatic force between Zirconium-oxo clusters $Zr_6O_4(OH)_4$ and 2-aminoterephthalic acid for UiO-66-NH_2. The UiO series have demonstrated good potential as catalysts due to their high porosity with plentiful adsorption sites for reactant molecules, with UiO-66-NH_2 possessing surface area ranging from 600-1200 $m^2\ g^{-1}$ from various reports[10-12]. This is higher than zeolites (200-400 $m^2\ g^{-1}$)[13] or metal oxides materials (10-200 $m^2\ g^{-1}$)[14].

Recent works in the field of UiO-series MOFs as porous catalytic materials have reported increased surface area upon post-synthetic modifications. Cao and coworkers have synthesized a composite material containing UiO-66 and graphene oxide (GO), with the graphene oxide added along with the $ZrCl_4$ and terephthalic acid and heated under 120°C for 24 hours. Despite the retained crystal structure, a surge in BET surface from 838 $m^2\ g^{-1}$ to 1184 $m^2\ g^{-1}$ upon GO incorporation have been reported[15]. More recently, Li reported a significant enhancement of BET surface area of UiO-66 from 579 $m^2\ g^{-1}$ to 1530 $m^2\ g^{-1}$ upon BiOCl decoration[16]. However,

hypothesis given by various authors without strong experimental or theoretical evidence appear to be insufficient in explaining the reasons behind the increment of BET surface area.

It is well-known that flexibility in zeolite frameworks alters their structures in response to incorporation of exo-skeleton species[17-20]. On another hand, it has also been accepted that in the literature that the heteronuclear species can induce a gate-opening effect of MOF materials, altering its crystal structure in a similar manner[21-23]. In light of this, we report an increase of BET surface area of UiO-66-NH_2 upon CdS particles introduction, shown to be strongly beneficial towards photocatalytic water splitting. Different from various studies of similar system of coupling CdS with UiO-series MOF, mainly focusing on the optical aspects of improved interfacial charge transfer[24-28], our system offers a fundamental atomic understanding in the improvement of photocatalytic activity. We report that the rotational flexibility of the organic linkers in UiO-66-NH_2 can be controlled via the amount of CdS present, experimentally via Rietveld refined SXRD data, and theoretically by DFT calculations. The organic linkers have shown to open synchronously for an increased surface area, as termed by the Gate-opening effect of MOFs[23]. Optically, the charge transfer from CdS to MOF as probed by UV-Vis spectroscopy has shown to stablize the open form of the organic linkers.

5.2 Results and Discussion

A series of one-pot synthesis of CdS/UiO-66-NH_2 was performed with a constant Cd source (Cadmium nitrate, $Cd(NO_3)_2$) and increasing sulphur source (thioacetamide, TAA) with water as a solvent. In this synthesis method, the aggregation of CdS is a consequence from the reaction between Cd and thiol upon hydrolysis of TAA[29,30]. Inductively-coupled plasma-mass spectrometry (ICP-MS) is performed on the series of samples to quantify the loading of CdS onto UiO-66-NH_2 (Table 5 . 1), with the increasing trend of the loading of Cd increasing in line with the amount of TAA added. It is interesting to observe the high affinity for Cd towards

S, as predicted by the hard soft acid-base theory[31], illustrated by the enhanced loading of Cd onto MOF conditional with TAA.

Sample	Cadmium wt%	Sulphur wt%	Cd:S ratio
UiO-66-NH_2	0.018	0	-
0.1Cd/UiO-66-NH_2	0.112	0	-
0.2Cd/UiO-66-NH_2	0.247	0	-
1.8Cd/UiO-66-NH_2	1.835	0.351	1.491
2.3Cd/UiO-66-NH_2	2.309	0.592	1.113

Table 5 . 1 | ICP-MS results for Cd and S in the series of catalyst

The samples are then named according to the percentage by weight of Cd present in the sample (0.1Cd, 0.2Cd, 1.8Cd and 2.3Cd/UiO-66-NH_2). In subsequent paragraphs the UiO-66-NH_2 suffix in the sample names is omitted for clarity. More structural characterization is performed to determine the identity of such Cd-containing species present in the catalysts.

5.2.1 Photocatalytic performance

To study the effect of the different Cd species towards catalysis, photocatalytic testing for water splitting reaction at 120 °C was conducted for the series of catalysts with 10% v/v triethanolamine (TEOA) as sacrificial reagent (Figure 5 . 1). Interestingly, the catalytic activity does not follow linearly the Cd concentration present in the catalysts. For the parent UiO-66-NH_2, a catalytic activity of 12.2 $\mu mol_{H2}\ h^{-1}g^{-1}$ is observed. At low loading of 0.1Cd and 0.2Cd, their catalytic activity seems to be similar to the unmodified UiO-66-NH_2 within experimental error, at 11.4 and 10.5 $\mu mol_{H2}\ h^{-1}g^{-1}$, respectively. However, catalysts with more CdS particles on the surface, 1.8Cd and 2.3Cd samples, are found to have higher catalytic activities compared

to the parent UiO-66-NH_2 at 26.9 and 20.4 μmol_{H2} $h^{-1}g^{-1}$, respectively. The 1.8Cd sample has the highest activities, more than double than that for UiO-66-NH_2. The differences in the influence of CdS at low and high loadings are worth in-depth investigation. A comparison of the catalytic activities of hydrogen production with MOF photocatalysts in the literature is available in Table 5 . 2. It can be seen that the performance of CdS/UiO-66-NH_2 photocatalyst in this work is among the better performances available in the literature.

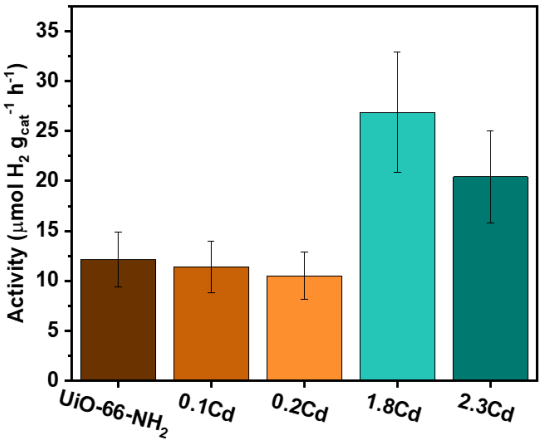


Figure 5 . 1 | Photocatalytic water splitting activities performed at 120°C with 10% v/v TEOA. The catalytic activity was measured with the assistance of Mr. Daniel Woodside.

MOF used	Sacrificial Reagent	Co-catalysts added	Production rate of H_2 /μmol $h^{-1}g^{-1}$	Ref
MIL-101	TEOA	Erythrosin B, $Ni(NO_3)_2$	125	[32]
UiO-66/CdS	Na_2SO_3 + Na_2S	1 wt% Pt	85	[33]
MIL-167	TEA	N/A	7.7	[34]
Ti-MOF-NH_2	TEOA	Pt	5.2	[35]
ZIF-67	TEOA	RuN_3	4.85	[36]
RhB/UiO-66	TEOA	N/A	2.7	[37]
Ti-MOF-$Ru(tpy)_2$	TEOA	H_2PtCl_6	1.82	[38]
UiO-66	Na_2SO_3 + Na_2S	1 wt% Pt	0	[33]
CdS/UiO-66-NH_2 (1.8Cd)	TEOA	N/A	26.9	This work

Table 5 . 2 | Catalytic performance of 1.8CdS/UiO-66-NH_2 in photocatalytic water splitting compared to the literature.

The adsorption onto the highly porous catalyst can contribute significantly towards catalytic activity. With that in mind, the effect of CdS species towards the porosity is investigated with adsorption with N_2. The nitrogen adsorption and desorption isotherms (Figure 5 . 2 a) all show characteristics of type II isotherms, indicative of the presence of large number of micropores[41]. The BET surface area plot for all samples are also provided in Figure 5 . 2 b.

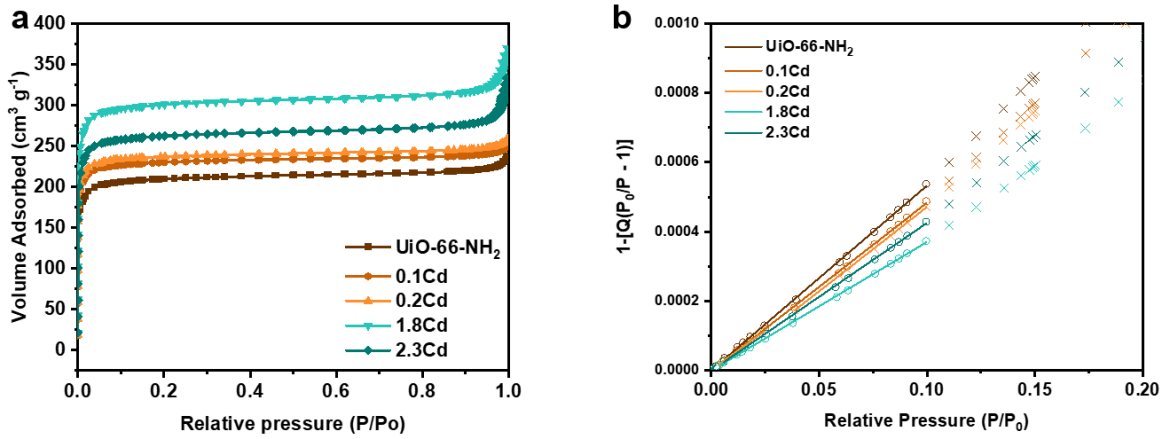


Figure 5 . 2 | (a) Adsorption and desorption isotherm of the series of catalysts. (b) BET plot based on the adsorption isotherm of the series of catalysts.

The surface areas obtained from the BET plot are presented in Figure 5 . 3 a. Interestingly, All CdS loaded UiO-66-NH_2 samples are found to bear higher surface area compared to UiO-66-NH_2 of 818.8 ± 2.7 m^2 g^{-1} which agrees with values in the literature[39,40]. The 1.8Cd and 2.3Cd samples are found to possess significantly higher surface area of 1176.3 ± 4.7 and 1025.0 ± 4.1 m^2 g^{-1} respectively. The total pore volume follows the identical trend (Figure 5 . 3 b).

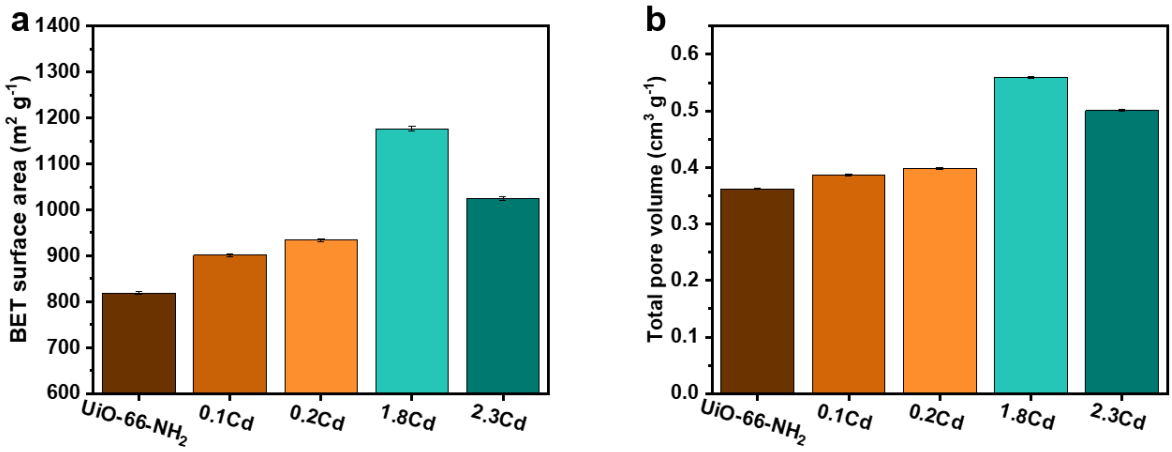


Figure 5 . 3 | (a) BET surface area and (b) Total pore volume of the series of catalysts

More importantly, resemblance between the trend in BET surface area and the photocatalytic activity can be noticed, and such correlation is quantified by a plot of photocatalytic activity against the BET surface area (Figure 5 . 4). Fascinatingly, the points corresponding to low

loading (0.1Cd, 0.2Cd) and high loading (1.8Cd, 2.3Cd) can both be independently fit linearly with high R factors (0.946 and 0.999, respectively) with the fitting parameters available in Table 5 . 3. The negative slope for low loading (brown line) indicates that the slight improvement in BET surface area due to Cd^{2+} dispersed in the pores worsen the photocatalytic activity. Conversely, the improvement in the BET surface area for high loading (blue line), due to the sulphide of Cd in contact with UiO-66-NH_2 benefits photocatalysis greatly. The introduction of CdS and UiO-66-NH_2 has introduced additional sites for adsorption[42]. The fact that 1.8Cd outperforms 2.3Cd in the photocatalysis can be further explained by the higher BET surface area.

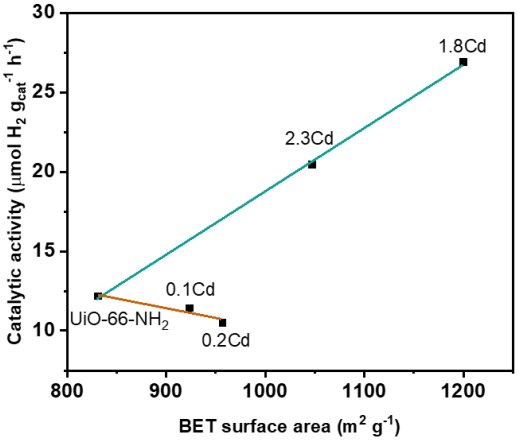


Figure 5 . 4 | Plot of photocatalytic activity against BET surface area for the series of catalysts

Line	Slope	Intercept	R-factor
Brown line (0.1, 0.2Cd)	$(-1.21 \pm 0.41) \times 10^{-2}$	$(2.23 \pm 0.37) \times 10^{1}$	-0.946
Blue line (1.8, 2.3Cd)	$(3.97 \pm 0.11) \times 10^{-2}$	$(-2.10 \pm 0.12) \times 10^{1}$	0.999

Table 5 . 3 | Parameters for the linear fit of catalytic activity against BET surface area

5.2.2 Structural Characterization

Structural characterization is performed to elucidate the Cd species present in the catalysts and their interactions with the MOF support. The structural integrity and the identity of Cd species deposited on MOF was studied with X-ray diffraction (XRD, Figure 5 . 5). The diffraction pattern of the synthesised UiO-66-NH_2 is consistent with the literature, and the sharp and narrow peaks indicate again that the high crystallinity has been maintained upon Cd and S decoration the series of catalysts. Synchrotron XRD (SXRD) is performed on UiO-66-NH_2 along with the 1.8Cd and 2.3Cd samples. The lattice parameter decreases from 20.832011 ± 0.000055 Å to 20.811634 ± 0.000061 Å and 20.805626 ± 0.000064 Å for 1.8CdS and 2.3CdS respectively, as the loading of Cd increases due to the Cd species improving the electrostatic force within the framework (Table 5 . 4)[8].

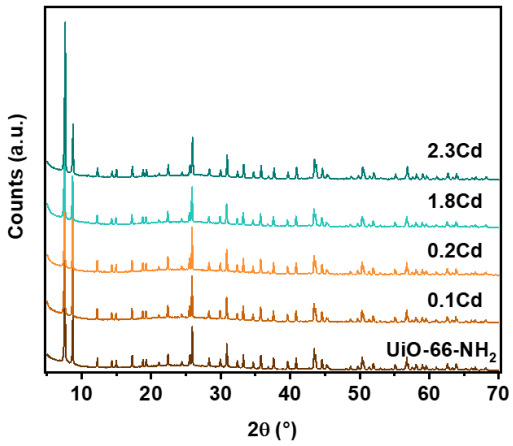


Figure 5 . 5 | XRD pattern for the series of catalysts

Sample	Lattice parameter / Å
UiO-66-NH_2	20.832011 ± 0.000055
1.8Cd/UiO-66-NH_2	20.811634 ± 0.000061
2.3Cd/UiO-66-NH_2	20.805626 ± 0.000064

Table 5 . 4 | Lattice parameter of UiO-66-NH_2, 1.8CdS/UiO-66-NH_2 and 2.3CdS/UiO-66-NH_2 obtained from SXRD.

The oxidation states of Zr present in the series of samples are analysed by X-ray photoelectron spectroscopy (XPS, Figure 5 . 6 and Table 5 . 5). The spin-orbit coupling $3d_{3/2}$ and $3d_{5/2}$ peaks for Zr of all the samples emerge at 185.1 and 182.6 eV respectively, which correlates well with the literature[43]. This suggests the $Zr_6O_4(OH)_4$ pillars of UiO-66-NH_2 remained untouched that the Cd species did not coordinate to the hydroxyl group in place of the inherent missing linker defects[44], as the introduction of metal species on Zr-oxo clusters have shown to shift the binding energy for Zr probed by XPS[45]. The Cd species present in the pores can therefore be concluded to be chemically unrelated to the Zr-oxo cluster. The Cd^{2+} ions must therefore have coordinated to the amino group on the organic linkers as expected from various reports in the literature of deposition of metal species onto UiO-66-NH_2[2,46].

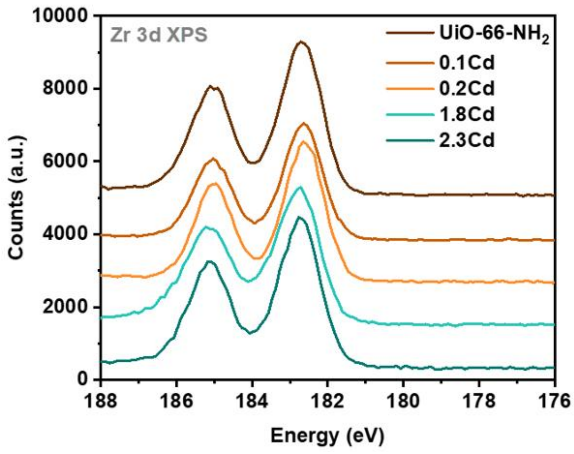


Figure 5 . 6 | Zr 3d XPS data. The Zr 3d data is offset by 1000 units in the y-axis

Sample	Zr $3d_{3/2}$ (eV)	Zr $3d_{5/2}$ (eV)
UiO-66-NH_2	185.1	182.7
0.1Cd	185.0	182.6
0.2Cd	185.1	182.7
1.8Cd	185.1	182.8
2.3Cd	185.1	182.8

Table 5 . 5 | Binding energy determined by Zr XPS

Thermogravimetric analysis (TGA, Figure 5 . 7 a) is used to further explore the effect of Cd species on the stability of UiO-66-NH_2. Specifically, focusing the weight derivative in the 280-380 °C region, the temperature with highest rate of mass loss decreases with increasing Cd present from 339.7 °C in UiO-66-NH_2 to 322.6 °C in 2.3Cd (Figure 5 . 7 b). This indicates a weakened structure of UiO-66-NH_2 upon Cd incorporation. Cd^{2+} (in the case of low loading) or CdS (high loading) coordinated to the amino group of the organic linker draws electron density away from it, hence weakening the electrostatic interaction between the anionic linker and cationic Zr^{4+}-based metal-oxo clusters.

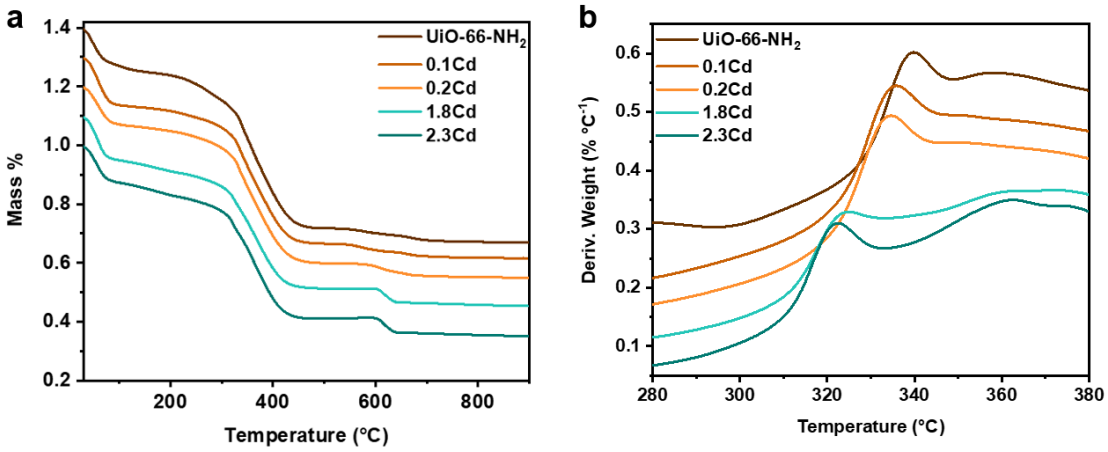


Figure 5 . 7 | (a) TGA analysis and (b) Weight derivative at 280-380 °C obtained from TGA

Cd K-edge X-ray absorption spectroscopy (XAS) has been performed to investigate the coordination shell of the Cd species present in the catalysts (Figure 5 . 8). Based on our synthesis method, the possible elements coordinating to Cd are only N from amino group of the organic linkers, O from aqua or hydroxide, or S from TAA. The similarity in their X-ray scattering factor inhibits the discrimination between N and O. With this in mind, the discussion thereafter will focus on N/O together and S as the possible first shell neighbours of Cd. As the loading of Cd increases, the intensity of the white line near absorption edge has decreased, signalling an increase in electron density of Cd present in the catalysts, and is attributed to a change from mainly Cd-O to Cd-S coordination.

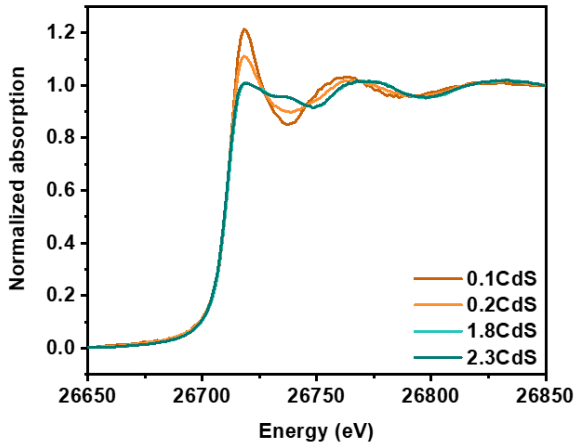


Figure 5 . 8 | Cd K-edge X-ray absorption Spectroscopy of the series of catalysts. Dr. Tai-Sing Wu and Prof. Yun-Liang Soo are gratefully acknowledged for their assistance in collection of XAS spectra. The XAS data fitting was performed by Bryan Ng.

Wavelet transform (WT) of the Extended X-ray absorption fine structures (EXAFS) data showed a gradual shift of peak position from 5.25 $Å^{-1}$, 1.67 Å for 0.1Cd , to 6.90 $Å^{-1}$, 2.04 Å for 2.3Cd (Figure 5 . 9). The progressive change from Cd-O to Cd-S coordination is manifested by the increase in both k (atomic number) and R (radial distances) of the first shell neighbours with respect to Cd.

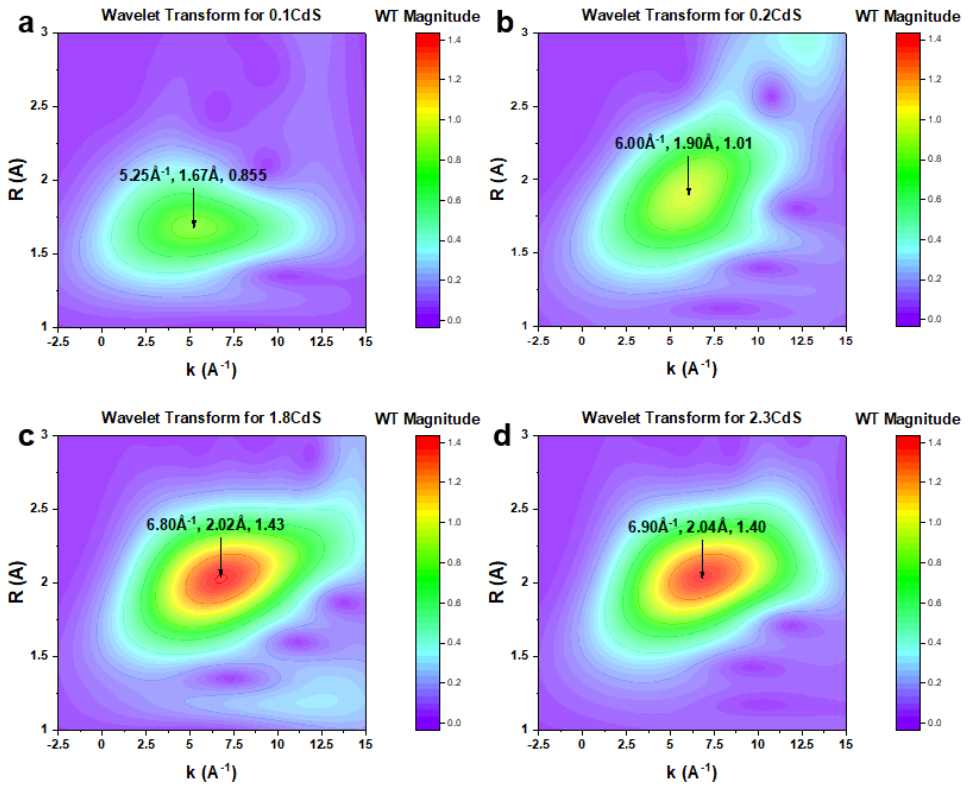


Figure 5 . 9 | Wavelet transform for (a) 0.1Cd, (b) 0.2Cd, (c) 1.8Cd, and (d) 2.3Cd

Additionally, data fitting performed on the EXAFS data reveals a gradual shift from Cd-O to Cd-S bonds quantitatively as the loading of Cd increases. For optimal reliability, k^1, k^2, and k^3-weighted spectra are simultaneously fitted in R-space, with more details on fitting method available in Chapter 2. The R-space EXAFS data and fit are shown in Figure 5 . 10 a, with the k-space data and their fitting parameters available in Figure 5 . 10 b and Table 5 . 6.

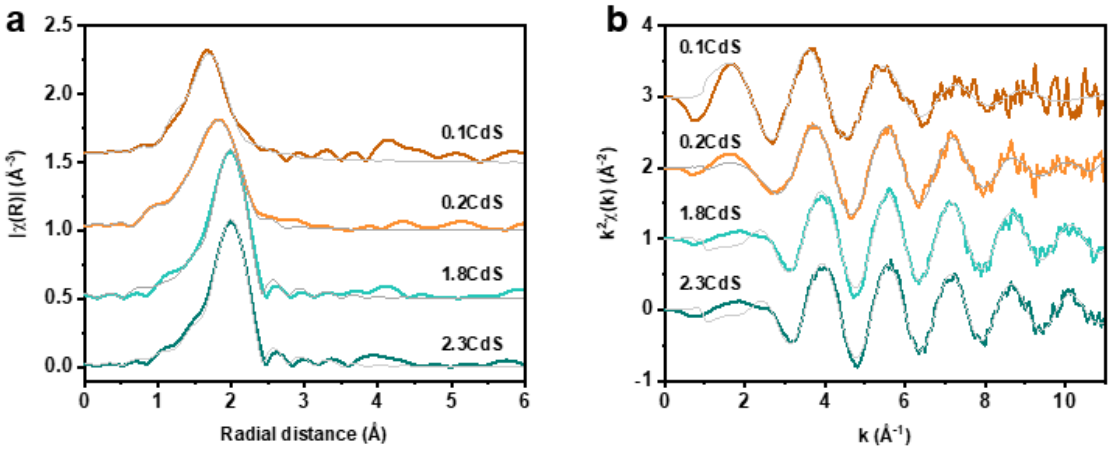


Figure 5 . 10 | k^2-weighted (a) R-space and (b) k-space data and fit for the series of catalyst

Sample	Path	CN	R (Å)	D-W (10^{-3})	ΔE (eV)	R-k^1	R-k^2	R-k^3	R-factor
0.1Cd	Cd-O	5.44 ± 0.77	2.27 ± 0.01	11.5 ± 2.9	2.05 ± 1.03	0.39	1.28	4.24	2.03
0.2Cd	Cd-O Cd-S	1.96 ± 0.45 1.51 ± 0.69	2.22 ± 0.03 2.54 ± 0.03	1.0 ± 4.3 1.0 ± 4.3	0.20 ± 3.89 1.92 ± 3.17	0.55	0.72	1.59	0.96
1.8Cd	Cd-S	4.05 ± 0.39	2.52 ± 0.01	5.4 ± 1.3	1.88 ± 0.80	1.48	0.93	1.07	1.40
2.3Cd	Cd-S	3.93 ± 0.35	2.52 ± 0.01	5.3 ± 1.2	2.91 ± 0.73	1.55	0.69	0.50	1.00

Table 5 . 6 | Fitting parameters for Cd K-edge EXAFS

Fitting parameters: CN, Coordination number; R, Radial distance; D-W, Debye-Waller factor; ΔE, Difference of edge energy used in data reduction compared to the theoretical edge energy; R-k^1, R-factor by fitting the k^1-weighted R-space data; R-k^2, R-factor by fitting the k^2-weighted

R-space data; R-k^3, R-factor by fitting the k^3-weighted R-space data; R-factor, Final R-factor computed by Artemis fitting software.

Amplitude reduction factor is set to 0.855 from fitting Cd reference. k-range of fitting is 2-11$Å^{-1}$ while R-range of fitting is 1-3Å except for 0.1CdS sample at 1.2-3Å, whose R_{bkg} was set to 1.15 for optimal background removal.

For 0.1Cd sample, Cd-O coordination environment with a coordination number of 5.44 ± 0.77 at 2.27 ± 0.01 Å from Cd was observed. Isolated Cd^{2+} species would have been washed away during the synthesis procedures, and therefore the Cd species present in the catalyst must have coordinated to amine group from the 2-aminoterephthalic acid. With no sulphur source added during synthesis, single site Cd^{2+} coordinated to amine or hydroxyl group from MOF and H_2O molecules or OH^- for charge balancing is observed. The 0.2Cd sample sees a reduction in Cd-O coordination to 1.96 ± 0.45 at 2.22 ± 0.03 Å, along with the emergence of Cd-S scattering to a coordination number of 1.51 ± 0.69 at 2.54 ± 0.03 Å. This shift in bonding environment marks the formation of CdS particles alongside the single site previous mentioned. For catalysts with higher Cd loading, the size and amount of CdS increases compared to 0.2Cd as indicated by increased Cd-S scattering, with 4.05 ± 0.39 at 2.52 ± 0.01 Å and 3.93 ± 0.35 at 2.52 ± 0.01 Å for 1.8 and 2.3Cd respectively. Compellingly, the change from octahedral to tetrahedral coordination favoured by d-p mixing in Cd^{2+} can be recognised[47].

Scanning and transmission electron microscopy (S/TEM) were then utilized to probe the morphologies of UiO-66-NH_2 before and after Cd decoration. The cubic morphology of UiO-66-NH_2 is confirmed with SEM, indicated by the truncated octahedra showing (100) and (111) facet (Figure 5 . 11).

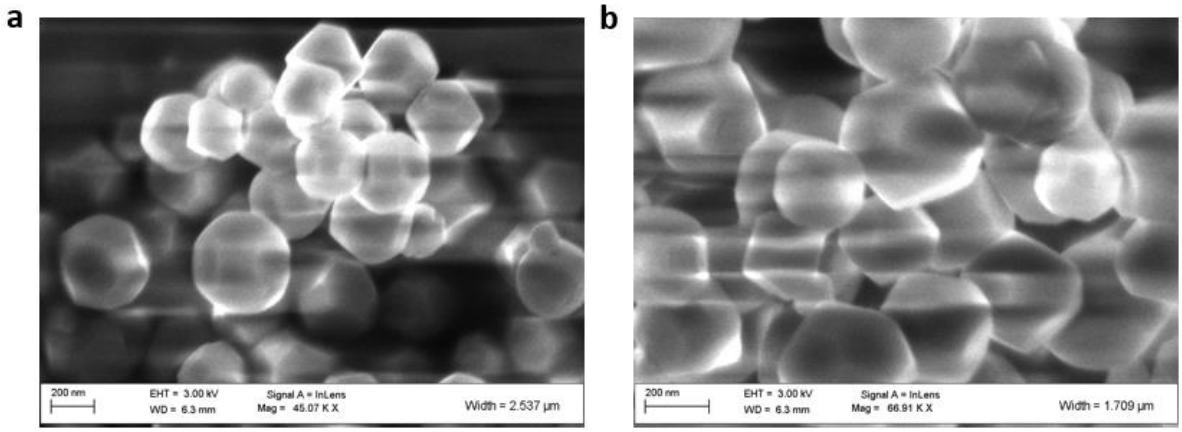


Figure 5 . 11 | SEM images for UiO-66-NH_2. Mr. Zhiyang Zhong is gratefully acknowledged for his assistance in obtaining the SEM images.

Such morphologies are retained in 0.2Cd, 1.8Cd and 2.3Cd as shown by their high-resolution TEM image (Figure 5 . 12,

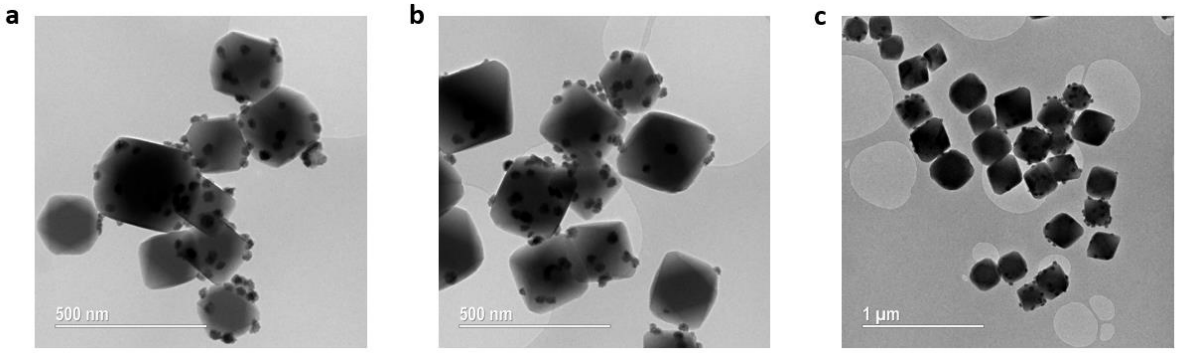


Figure 5 . 13 and Figure 5 . 14). Additionally, clear dark spots on the surface can be seen in the 1.8Cd and 2.3Cd samples.

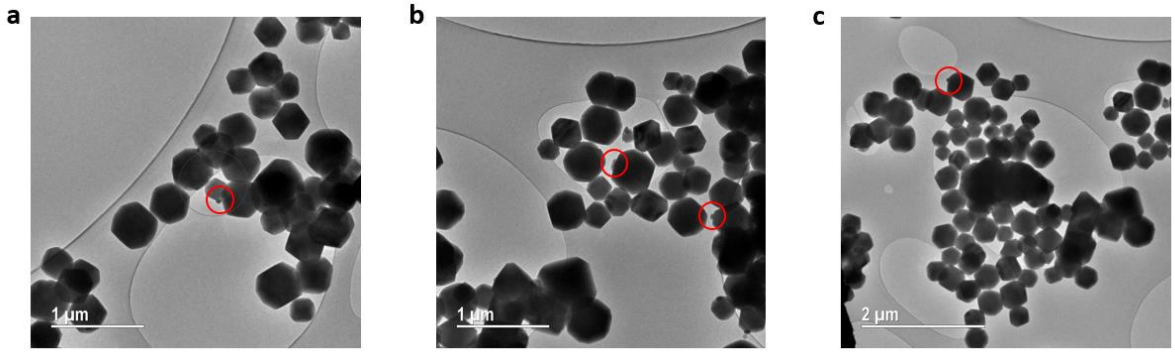


Figure 5 . 12 | TEM images for 0.2Cd. Mr. Ping-Luen Ho is gratefully acknowledged for his assistance in obtaining the TEM images and their EDX mappings.

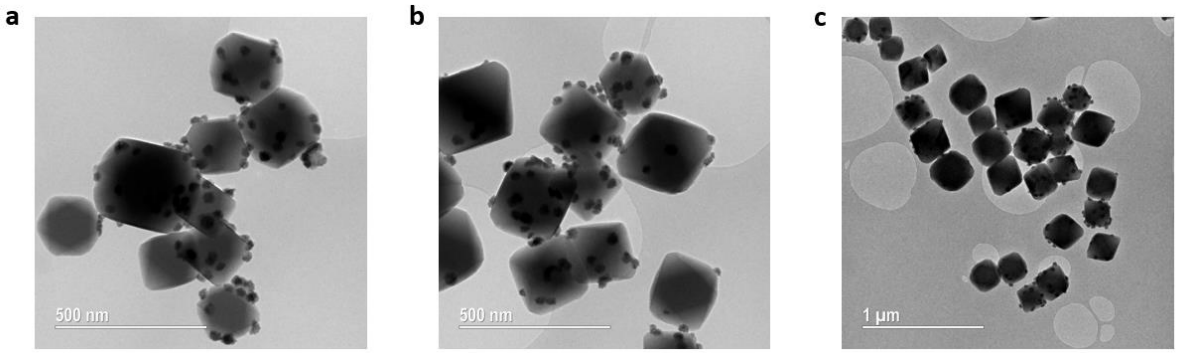


Figure 5 . 13 | TEM images for 1.8Cd

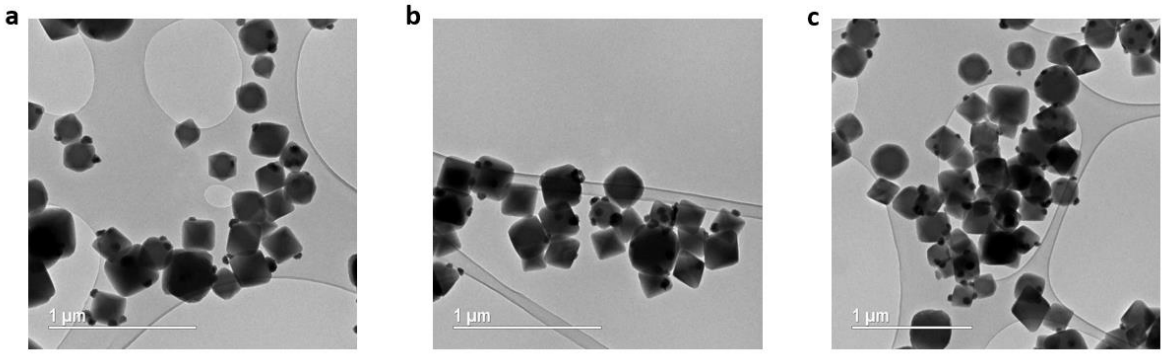


Figure 5 . 14 | TEM images for 2.3Cd

Zooming in to the surface spots a fringe spacing of 3.3 Å can be observed, which is consistent with the CdS(111) plane in its cubic form (Figure 5 . 15)[46].

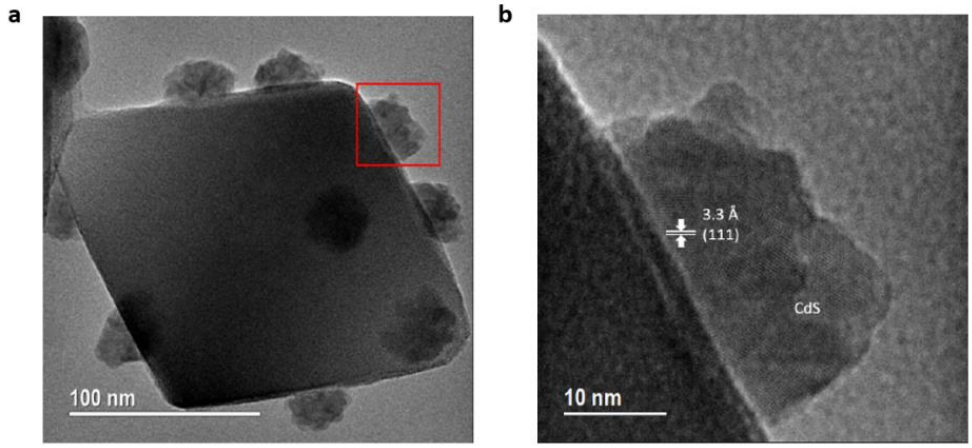


Figure 5 . 15 | TEM image of 1.8CdS at higher resolution, showing CdS particles on the surface of UiO-66-NH_2, with the fringes clearly seen with spacing corresponds to the [111] face of CdS at 3.3Å.

Moreover, energy dispersive X-ray (EDX) elemental mapping all show well dispersion of such elements present in the samples (Figure 5 . 16, Figure 5 . 17 and Figure 5 . 18). Particularly, in the 1.8Cd and 2.3Cd sample, the Cd and S clusters can be seen clearly on the surface of the UiO-66-NH_2 framework. For improved clarity the EDX mapping was subjected to a 40 % increase in both brightness and contrast.

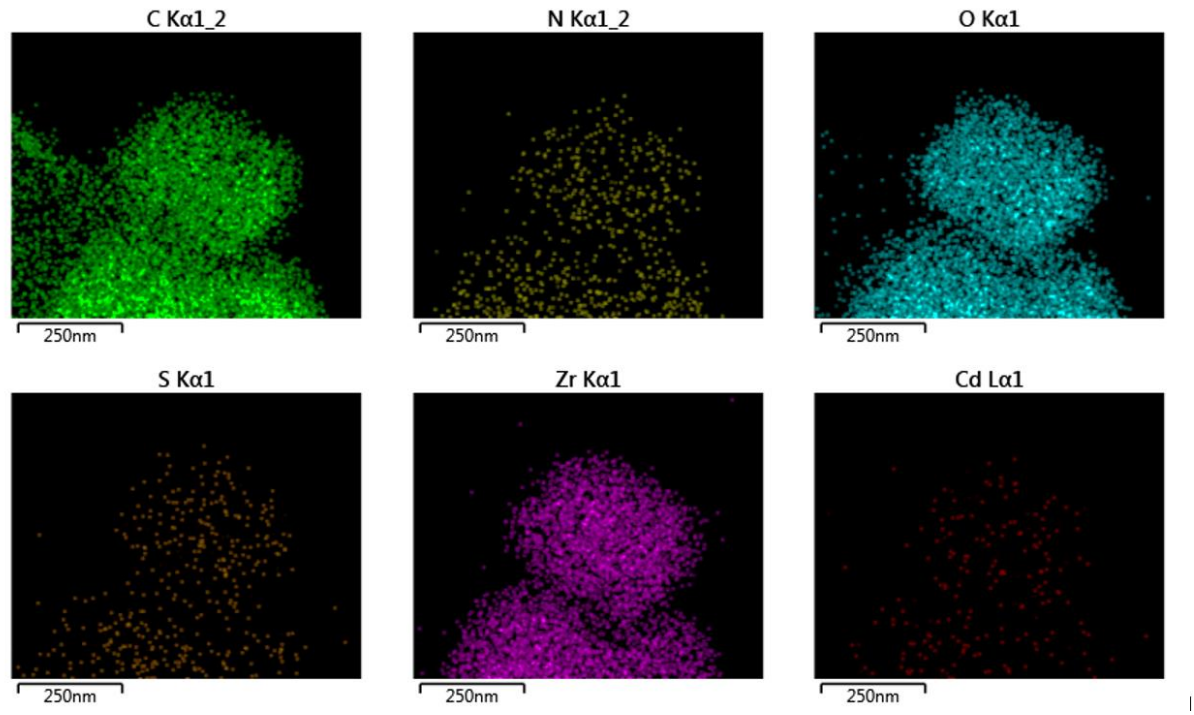


Figure 5 . 16 | EDX mapping of 0.2Cd/UiO-66-NH_2

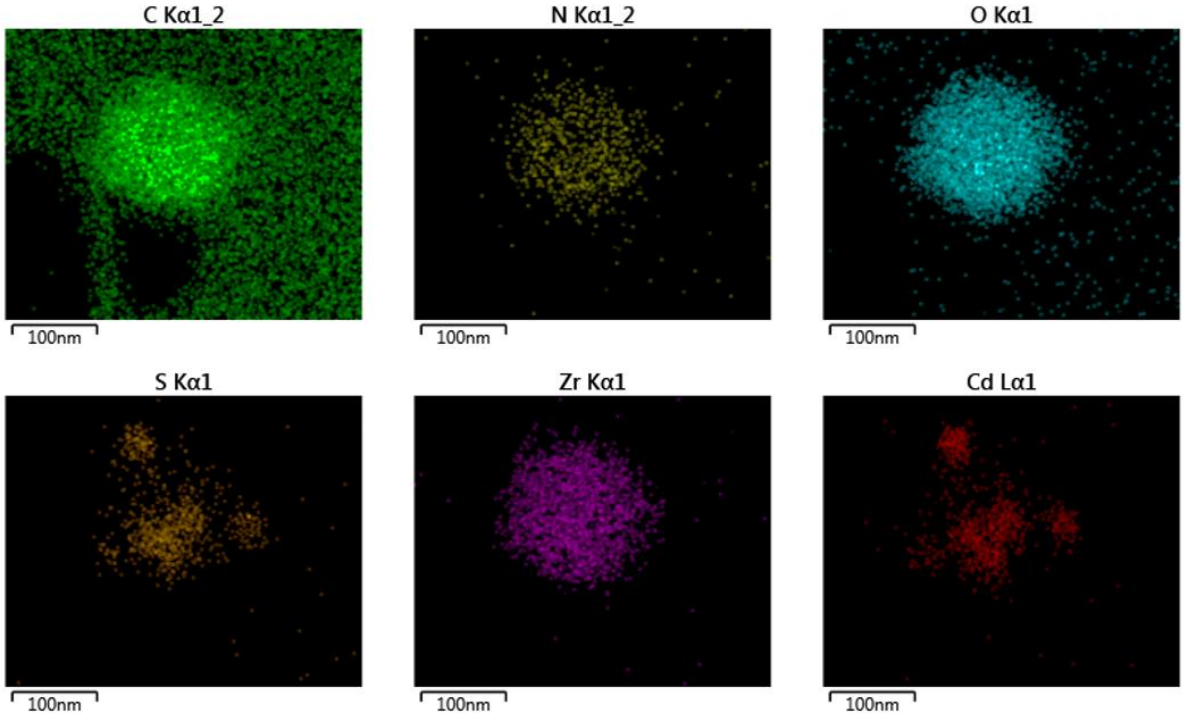


Figure 5 . 17 | EDX mapping of 1.8Cd/UiO-66-NH_2

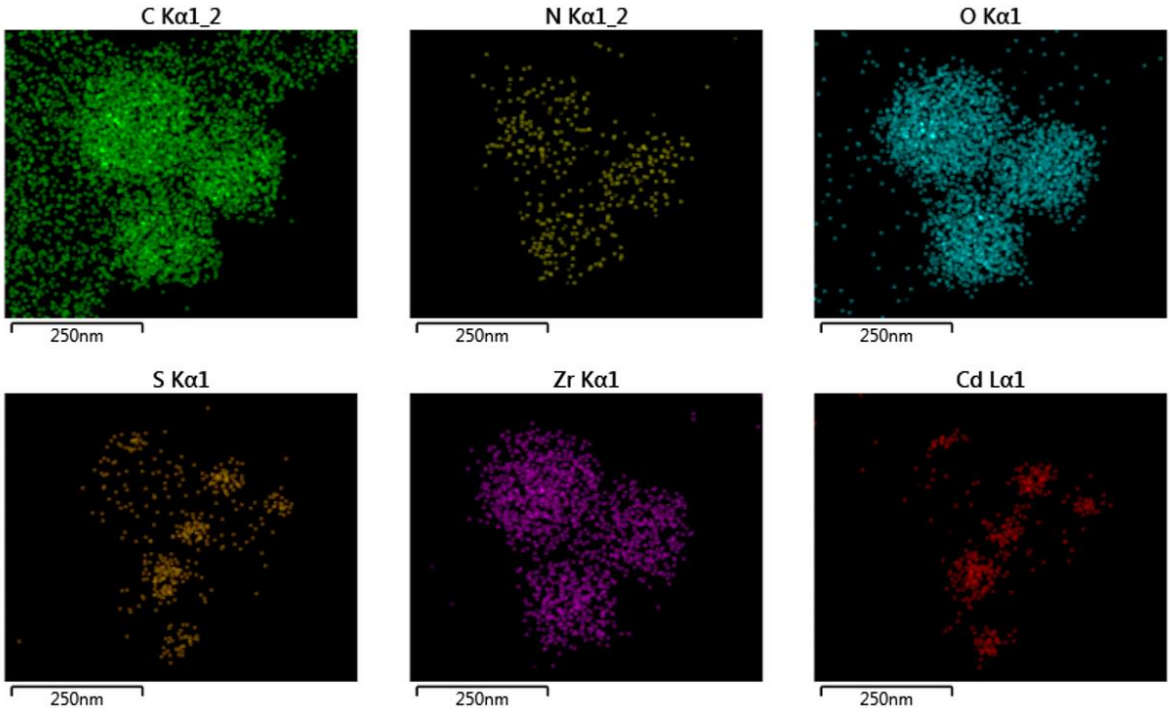


Figure 5 . 18 | EDX mapping for 2.3Cd/UiO-66-NH_2

The fact that such CdS particles generate no new XRD peaks, and the R-space EXAFS data show no peaks at radial distance larger than 3 Å, demonstrate the amorphous nature of the CdS particles with no long-range order. Such CdS particles on the surface are frequently observed for 1.8Cd and 2.3Cd samples, whose statistical analysis results in an average particle diameter of 30.9 ± 6.1 and 57.4 ± 14.1 nm, respectively (Figure 5 . 19). Despite only little TAA is added in the 0.2Cd sample, CdS surface spots can still be rarely observed (Figure 5 . 12, 4 CdS spots has been circled in red out of >100 UiO-66-NH_2), resonate with the Cd-S scattering recognized by EXAFS fitting.

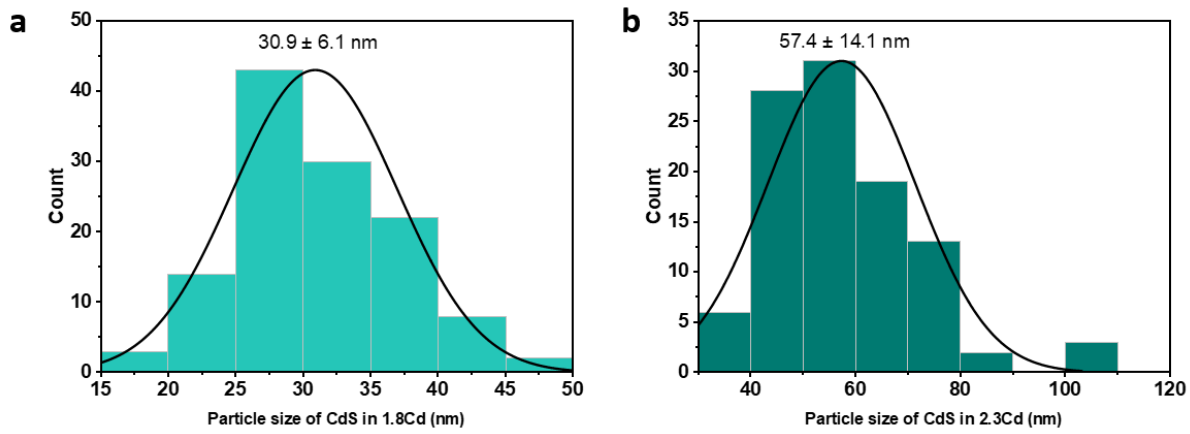


Figure 5 . 19 | Particle size distribution of CdS in (a) 1.8Cd and (b) 2.3Cd

5.2.3 Structure-reactivity relationship

A consistently increased BET surface area upon CdS decoration can be observed, different to post-synthetic modified UiO-66 series MOF reported in the literature. It is widely believed that any modification will alter the connectivity between metal node and organic linkers to increase the amount of defects, or blocking the pores present in MOFs. However, it has been reported twice in the literature that the surface area of UiO-66 series MOFs can increase upon post-synthetic modification[15,16]. On another hand, it has been accepted that in the literature that the heteronuclear species can induce a gate-opening effect of MOF materials, altering its crystal structure[21-23]. Previously presented synchrotron X-ray diffraction (SXRD) data has been subjected to Rietveld Refinement for understanding the structural changes upon CdS deposition for the pristine UiO-66-NH_2 and the CdS deposited 1.8Cd samples. Interestingly, it has been observed that the dihedral angles of the organic linkers present in the MOF vary according to the loading of Cd present in the samples. In this Rietveld refinement, the $Zr_6O_4(OH)_4$ clusters have been held untouched, with the only degrees of freedom allowed for the rotation of the organic linker. The crystallographic data and details of UiO-66-NH_2 and 1.8Cd are shown in Table 5 . 7.

Sample	**UiO-66-NH_2**	**1.8Cd**
Space group	Fm-3m	Fm-3m
2θ range for refinement (°)	2-60	2-60
Number of independent parameters	43	43
Number of hkls	747	747
Refinement method(s)	Rietveld	Rietveld
a (Å)	20.83207 (5)	20.81147(2)
b (Å)	20.83207 (5)	20.81147(2)
c (Å)	20.83207 (5)	20.81147(2)
V ($Å^3$)	9040.602(6)	9013.810(6)
R_{wp} / R_p / R_{exp} (%)	3.43/3.39/0.22	4.30/4.52/0.211
GOF($\chi 2$)	15.52	20.36
Wavelength (Å)	0.70826(1)	0.70826(1)
2θ zero point(°)	-0.00189(3)	-0.00189(3)

Table 5 . 7 | Crystallographic data and details of UiO-66-NH_2 and 1.8Cd based on SXRD. The assistance of Dr. Guangchao Li is gratefully acknowledged in the Refinement.

For pristine UiO-66-NH_2, a dihedral angle of 0° can be observed. The observed, calculated and difference in SXRD intensity is presented in Figure 5 . 20 and the structure is present in Figure 5 . 21. Figure 5 . 21 a shows the tetrahedral pores of Rietveld refined UiO-66-NH_2, while Figure 5 . 21 b focuses on the rotation of the organic linker. The atomic parameters from Rietveld refinement of SXRD measurement for UiO-66-NH_2 is shown in Table 5 . 8.

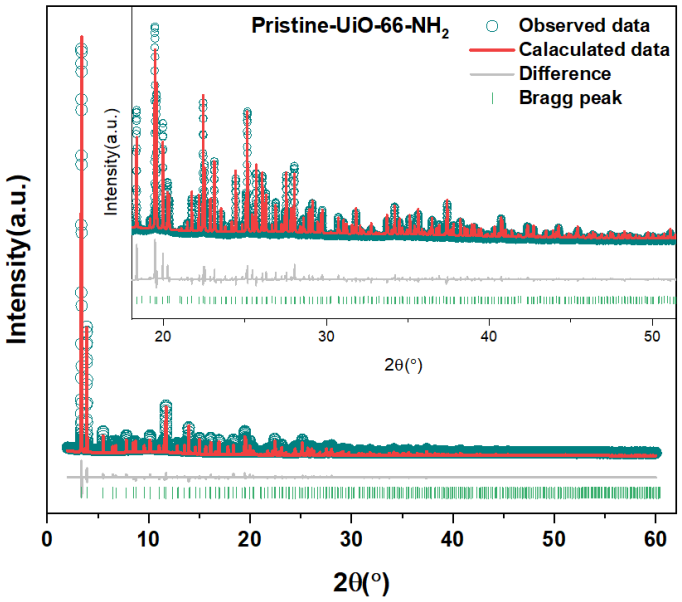


Figure 5 . 20 | Observed, calculated and difference in SXRD intensity for Rietveld Refinement of pristine UiO-66-NH_2

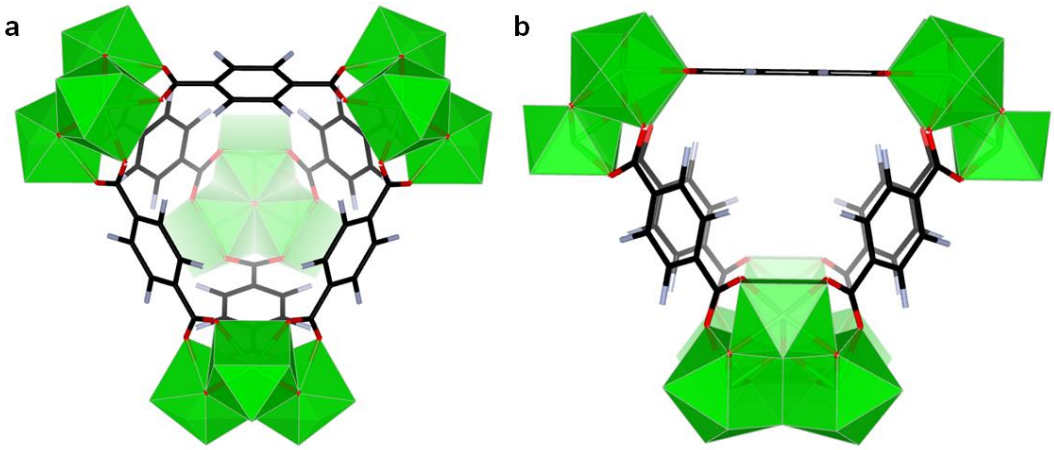


Figure 5 . 21 | Rietveld refined UiO-66-NH_2, showing (a) the tetrahedral pore and (b) the rotation viewed in the plane of the carboxylate of the organic linker on top. Colour scheme: Zr = light green polyhedra, O = red, C = black, N = blue. Hydrogen and adsorbed water O-atoms have been omitted for clarity.

Species	Atom	x	y	z	SOF[a]	Beq[b](Å2)
Framework	Zr1	0.1198(5)	0	0	1	1.2458(5)
	O1	0.1733(2)	0	0.0951(1)	1	3.3599(9)
	O2	0.0598(7)	0.0598(7)	0.0598(7)	1	3.3599(9)
	C1	0.1500(0)	0.00000	0.1500	1	9.0860(1)
	C2	0.2000(0)	-0.00000	0.2000	1	9.0860(1)
	C3	0.2630(5)	0.00000	0.1844	1	9.0860(1)
	N1	0.2783(1)	0.00000	0.1217	1	9.0860(1)
Water species	Od1	0.1650(9)	2.1646(0)	0.8617(1)	0.1508(5)	20
	Od2	-0.0445(0)	2.1206(1)	0.4379(3)	0.2225(4)	20
	Od3	-0.0449(5)	2.2289(3)	0.5002(3)	0.0902(5)	20
	Od4	-0.3792(4)	2.1207(6)	0.8121(3)	0.1504(1)	20
	Od5	-0.2606(8)	2.1882(5)	1.1602(7)	0.2419(2)	20

Table 5 . 8 | Atomic parameters from Rietveld Refinement of UiO-66-NH_2

[a]Beq refers to the isotropic displacement factor or the thermal parameter.
[b]SOF represents the site occupancy factor per asymmetric unit.

A similar Rietveld refinement analysis is performed on the SXRD data for 1.8Cd, with two distinct crystallographic sites for both Cd and S. The observed, calculated and difference in SXRD intensity is shown in Figure 5 . 22 and the structure is present in Figure 5 . 23. Similarly, Figure 5 . 23 a shows the tetrahedral pores of Rietveld refined 1.8Cd, while Figure 5 . 23 b focuses on the rotation of the organic linker. The atomic parameters from Rietveld refinement

of SXRD measurement for UiO-66-NH_2 is shown in Table 5 . 9. Interestingly, a rotation of the organic linker by 25.8º can be observed.

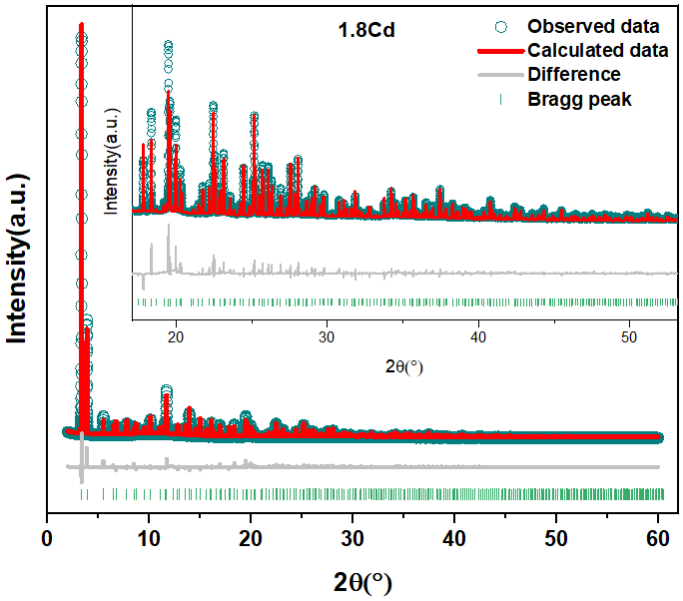


Figure 5 . 22 | Observed, calculated and difference in SXRD intensity for Rietveld Refinement of 1.8Cd

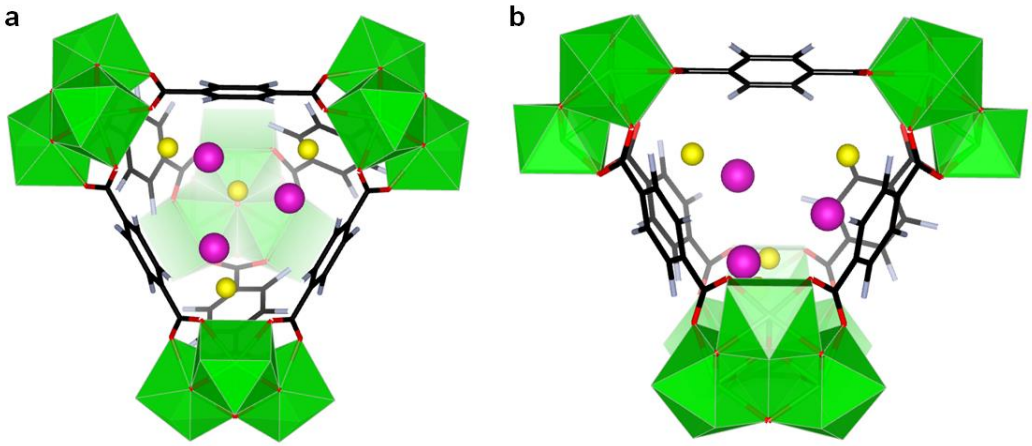


Figure 5 . 23 | Rietveld refined 1.8Cd, showing (a) the tetrahedral pore and (b) the rotation viewed in the plane of the carboxylate of the organic linker on top. Colour scheme: Zr = light green polyhedra, O = red, C = black, N = blue, Cd = pink, S = yellow. Hydrogen and adsorbed water O-atoms have been omitted for clarity.

Species	Atom	x	y	z	SOF[a]	Beq[b](Å2)
Framework	Zr1	0.1198(5)	0	0	1	1.2458(5)
	O1	0.1733(2)	0	0.0951(1)	1	3.3599(9)
	O2	0.0598(7)	0.0598(7)	0.0598(7)	1	3.3599(9)
	C1	0.1500(0)	0.00000	0.1500	1	9.0860(1)
	C2	0.2000(0)	-0.00000	0.2000	1	9.0860(1)
	C3	0.2630(5)	0.00000	0.1844	1	9.0860(1)
	N1	0.2783(1)	0.00000	0.1217	1	9.0860(1)
CdS	Cd1	0.1199(1)	1.4857 (8)	1.5044(7)	0.0525(5)	2.6086(8)
	Cd2	-0.1802(7)	0.7414(1)	0.6798(7)	0.0328(6)	3.8078(8)
	S1	-0.3578(1)	0.6421(9)	0.8305(1)	0.0652(8)	12.1511(5)
	S2	0.0612(8)	0.5695(8)	0.8656(5)	0.1054(8)	20

Table 5 . 9 | Atomic parameters from Rietveld Refinement of 1.8Cd

[a]B_{eq} refers to the isotropic displacement factor or the thermal parameter.
[b]SOF represents the site occupancy factor per asymmetric unit.

Density Functional Theory (DFT) calculations were performed to further explore the underlying cause of the difference in dihedral angles observed in the optimized Rietveld refined models. Structures were subjected to geometry relaxation, with its average dihedral angle and energy calculated shown in Figure 5 . 24 and tabulated in Table 5 . 10. The optimal structure was found to possess a dihedral angle of 4.66° and have an energy of -925.26 eV.

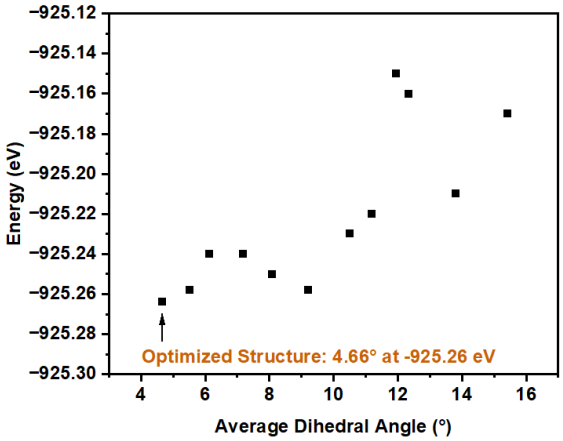


Figure 5 . 24 | Energy of UiO-66-NH_2 with varying dihedral angles. The assistance of Prof. Xin-Ping Wu on the DFT calculations are gratefully acknowledged.

Average Dihedral Angle (°)	Energy (eV)
23.9	-922.33
24	-922.45
1.82	-922.46
15.74	-922.48
8.87	-922.56
14.36	-923.29
11.96	-925.15
12.34	-925.16
15.43	-925.17
13.8	-925.21
11.2	-925.22
10.5	-925.23
7.19	-925.24
6.14	-925.24
8.08	-925.25
9.21	-925.26
5.51	-925.26
4.66	-925.26

Table 5 . 10 | Energy of UiO-66-NH_2 with varying dihedral angles

A structural model of CdS-deposited UiO-66-NH_2 is created by the incorporation of a Cd_4S_4 cluster onto UiO-66-NH_2 as depicted in Figure 5 . 25.

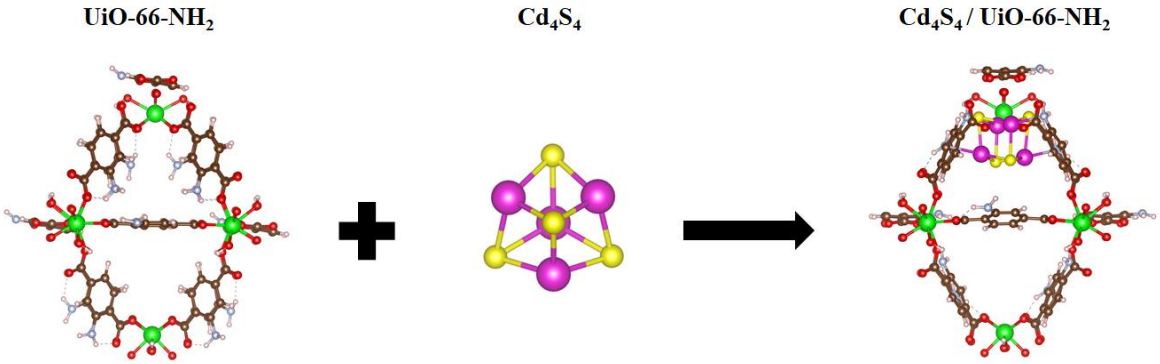


Figure 5 . 25 | Addition of Cd_4S_4 cluster onto UiO-66-NH_2 for Cd_4S_4/UiO-66-NH_2, a structural model for CdS-deposited UiO-66-NH_2.

The Cd_4S_4/UiO-66-NH_2 is also subjected to geometry relaxation and calculation of the average dihedral angle. The top five most stable structures and their structural model of Cd_4S_4/UiO-66-NH_2 are presented in Table 5 . 11. The most optimal structure was found to bear an average dihedral angle of 28.25°, similar to the observation from Rietveld refined SXRD data for 1.8Cd.

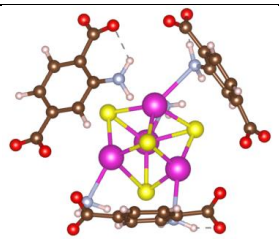
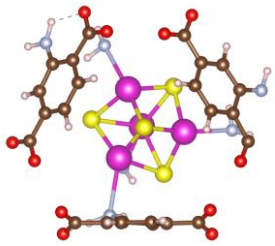
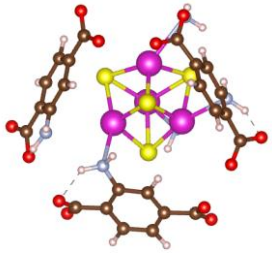
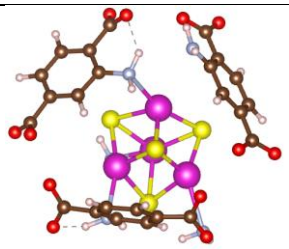
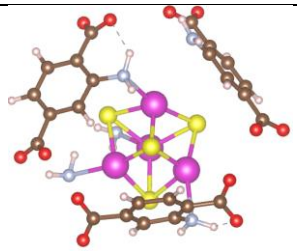
Average Dihedral Angle	Energy	Structural model
28.25	-942.61	
22.03	-942.46	
26.46	-942.44	
25.1	-942.43	
27.1	-942.4	

Table 5 . 11 | Energy of Cd_4S_4/UiO-66-NH_2 with varying dihedral angles, and their structural model

Optical characterisation is then implemented to inspect the response of series of catalysts to light. UV-Vis spectroscopy was conducted on all samples (Figure 5 . 26 a). The organic linker-based π to π* transition from 200-260 nm region and the n to π* transition in the 300-400 nm region has stayed at similar energies[48], reflecting again the mostly retained crystal structures of UiO-66-NH_2. Interestingly, gradual improvement of light absorption between 400-550 nm region has been recognized as the loading of Cd increases, signifying the improvement in adsorption of light from both Cd^{2+} within the pores and CdS on the surface. Tauc plots were then generated to probe the band structure of the samples (Figure 5 . 26 b). It is found that the CdS decorated catalysts have similar band gap energies to the parent UiO-66-NH_2 at 2.94 eV, indicating the band gap is virtually unaffected by the introduction of CdS into the framework. It is likely that the size of the CdS particles have been too small for an efficient heterojunction to form, and therefore a relatively constant band gap is seen.

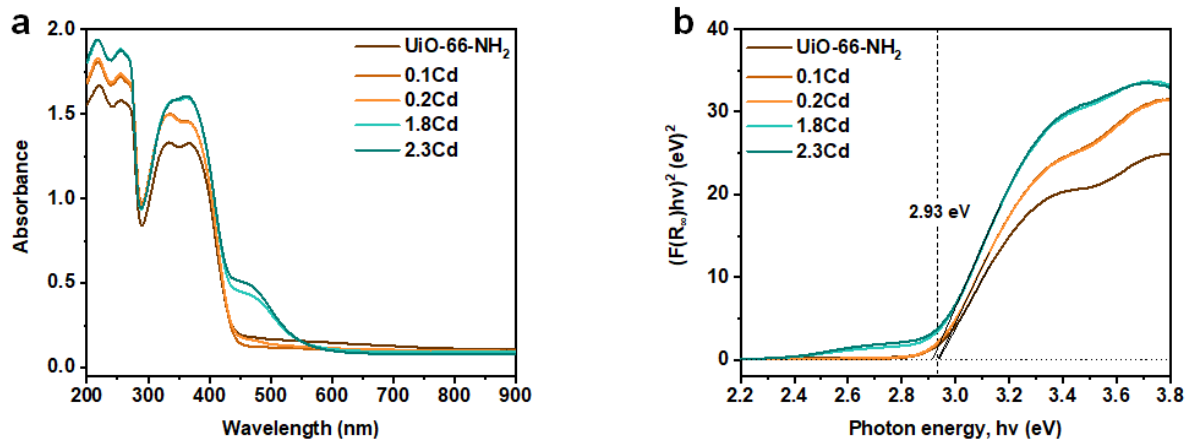


Figure 5 . 26 | (a) UV-Vis absorbance spectra and (b) Tauc plot of the series of catalyst

To confirm the reliability of the DFT optimized structural models of Cd_4S_4/UiO-66-NH_2, the excited states of UiO-66-NH_2 and Cd_4S_4/UiO-66-NH_2 are simulated via Time Dependent-DFT to compare with the experimentally obtained UV-Vis. The simulated absorption spectra of UiO-66-NH_2 and Cd_4S_4/UiO-66-NH_2 are presented in Figure 5 . 27 below. For UiO-66-NH_2, strong simulated absorption peaks at 328 and 357 nm are in the range of the n to π* transitions

measured experimentally. On the other hand, the similarly strong absorption peaks of the n to π* seems to have shifted to 388 and 403 nm. Interestingly, new absorption peaks can be observed in 420, 428 and 455 nm. The 10 excited states of lowest energies, which gave rise to the new absorption peaks are summarized in Table 5 . 12.

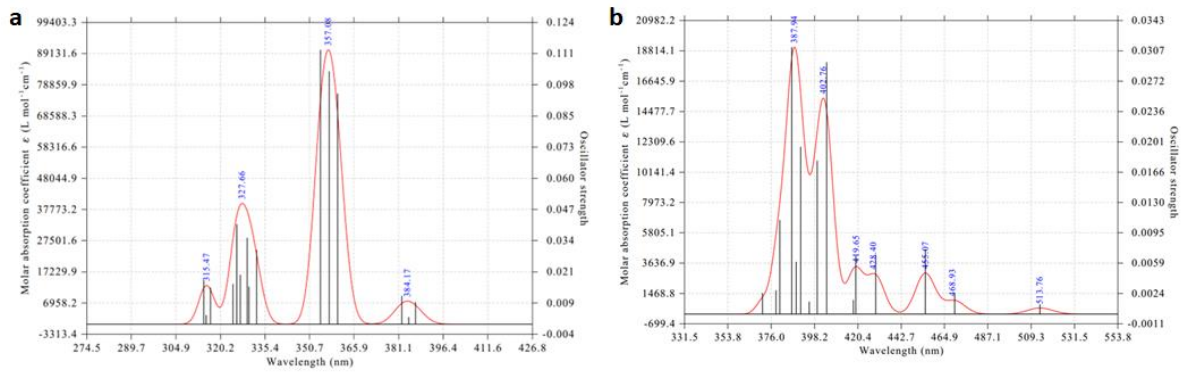


Figure 5 . 27 | Simulated Absorption Spectra of (a) UiO-66-NH_2 and (b) Cd_4S_4/UiO-66-NH_2

Excited State	Excitation Energy (eV)	Excitation Energy (nm)	Oscillator Strength
S_1	2.41	513.77	0.001
S_2	2.64	470.05	0.002
S_3	2.72	455.02	0.008
S_4	2.89	429.58	0.007
S_5	2.96	419.33	0.007
S_6	2.97	418.14	0.002
S_7	3.07	404.42	0.029
S_8	3.10	399.61	0.018
S_9	3.14	395.49	0.001
S_{10}	3.17	391.15	0.020

Table 5 . 12 | First 10 excited states in Cd_4S_4/UiO-66-NH_2 simulated by TD-DFT.

The UV-Vis spectra of UiO-66-NH_2 and 2.3Cd were normalized and their difference calculated to better visualize the effect of the CdS species on the UV-Vis absorption spectra (Figure 5 . 28). The difference of the two spectra peaks at 457 nm as labelled. Interestingly, this correlates well with the three excited states of S_3, S_4 and S_5 with excitation energy of 419, 430 and 455 nm and high oscillator strength of 0.007, 0.007 and 0.008 respectively (Table 5 . 12).

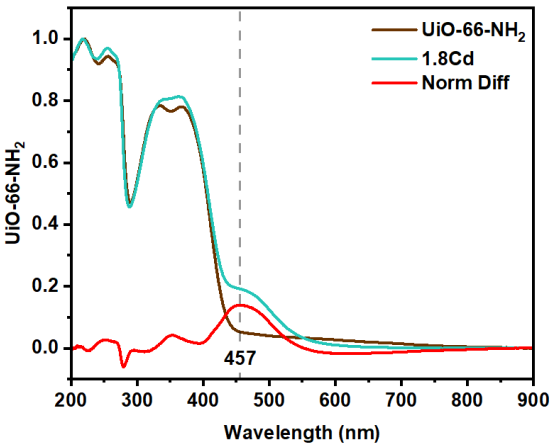


Figure 5 . 28 | Normalized UV-Vis spectra of UiO-66-NH_2 and 2.3Cd, and their normalized difference

The photoluminescence (PL) peak at 455 nm for UiO-66-NH_2 has been ascribed to the amine n to organic linker π* charge transfer[8]. As shown by the decreasing PL intensity in Figure 5 . 29 a, the incorporated Cd^{2+} and CdS gradually perturb this n to π* transition, reducing electron density on the amine lone pair. This is further evidenced by a Stern-Volmer plot of I_0/I against combined mol% of Cd from ICP, which gives a linear trend with a high R-factor of 0.995 (Figure 5 . 29 b)[49,50]. The slope of the linear fit is calculated to be 0.385 ± 0.019, with the y-intercept at 1.017 ± 0.028. This observation is in line with the reduction of electrostatic interactions between organic linkers and Zr-oxo clusters probed by TGA in Figure 5 . 7 b.

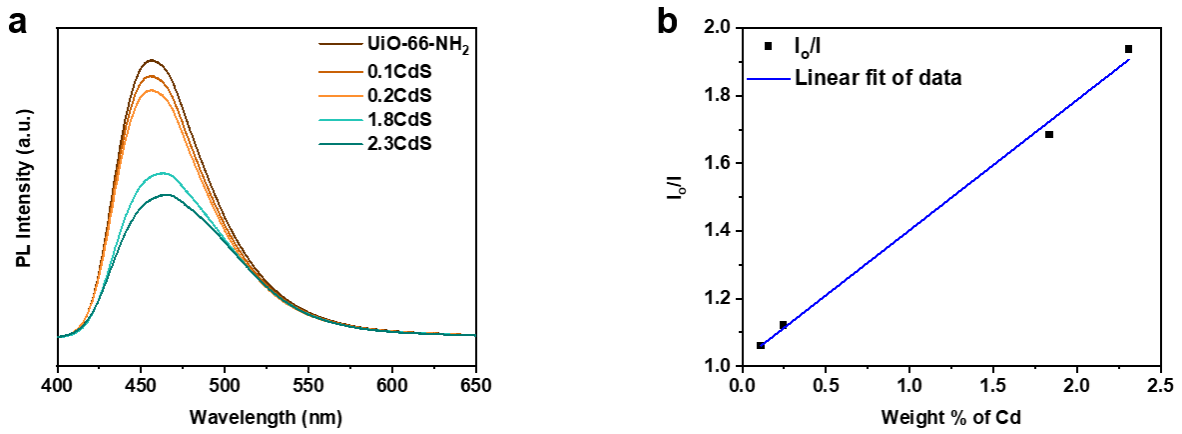


Figure 5 . 29 | (a) PL intensity of the series of catalyst and (b) Stern-Volmer plot of I_0/I against combined mol% of Cd from ICP

Normalization of the PL data in Figure 5 . 30 reveals charge transfer processes present in the catalysts. The normalized PL spectra of 0.1Cd and 0.2Cd overlaps with that for UiO-66-NH_2 with no observable difference. Adversely, for 1.8Cd and 2.3Cd, the peak of the n to π* transition at 455 nm gradually shifts to the right to 466 nm, along with the formation of a peak shoulder at around 500 nm[51].

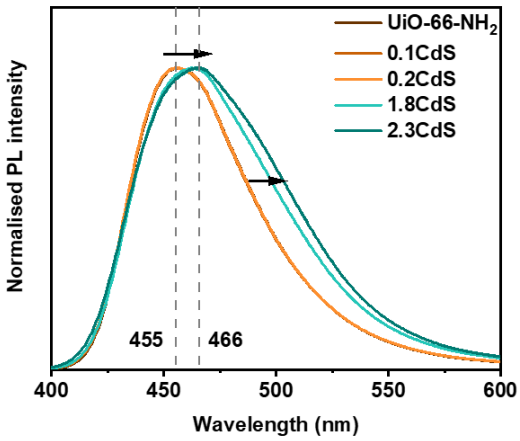


Figure 5 . 30 | Normalized PL spectra for series of catalyst

To quantify the effect of the peak shoulder, two Gaussian peaks at 455 nm and 492 nm are used to fit the Normalized PL data for 1.8Cd and 2.3Cd (Figure 5 . 31), with the fitting parameters available at Table 5 . 13. The 492 nm peak was ascribed to charge recombination after charge

transfer from UiO-66-NH_2 to CdS. The % area for the 492 nm peak rose to 56.1 % for 1.8Cd and 61.1 % for 2.3Cd, indicating much increased charge transfer from UiO-66-NH_2 to CdS particles, but not to the Cd^{2+} present in the pores. In this system, it is possible for the MOF to act as antennas to transfer charge towards the surface CdS particles.

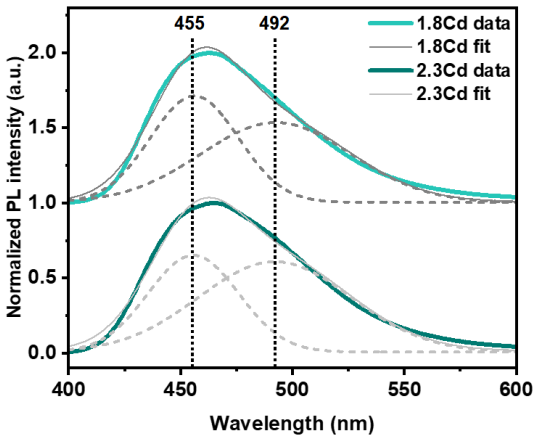


Figure 5 . 31 | Deconvoluted Gaussian peaks from PL data for 1.8Cd and 2.3Cd

Sample	Peak position (nm)	Area (%)	Peak position (nm)	Area (%)	R^2 value
1.8CdS	456.2	43.9	492.6	56.1	0.993
2.3CdS	455.7	38.9	492.1	61.1	0.994

Table 5 . 13 | Gaussian peak fitting parameters for PL data of 1.8Cd and 2.3Cd

To further examine the charge transfer processes in the CdS/UiO-66-NH_2 interface, femtosecond transient absorption spectroscopy (fs-TAS) is conducted (Figure 5 . 32). The peak positions and peak intensities appear to be relatively similar, with the only difference being a reduction of peak intensity for 200 fs for 0.2Cd, 1.8Cd and 2.3Cd compared to UiO-66-NH_2 (Figure 5 . 33). This peak is ascribed to the ligand-to-cluster transfer based on its short lifetime[52], and its reduction is indicative of charge transfer from UiO-66-NH_2 to both the CdS particles present in the catalysts, instead of the metal clusters.

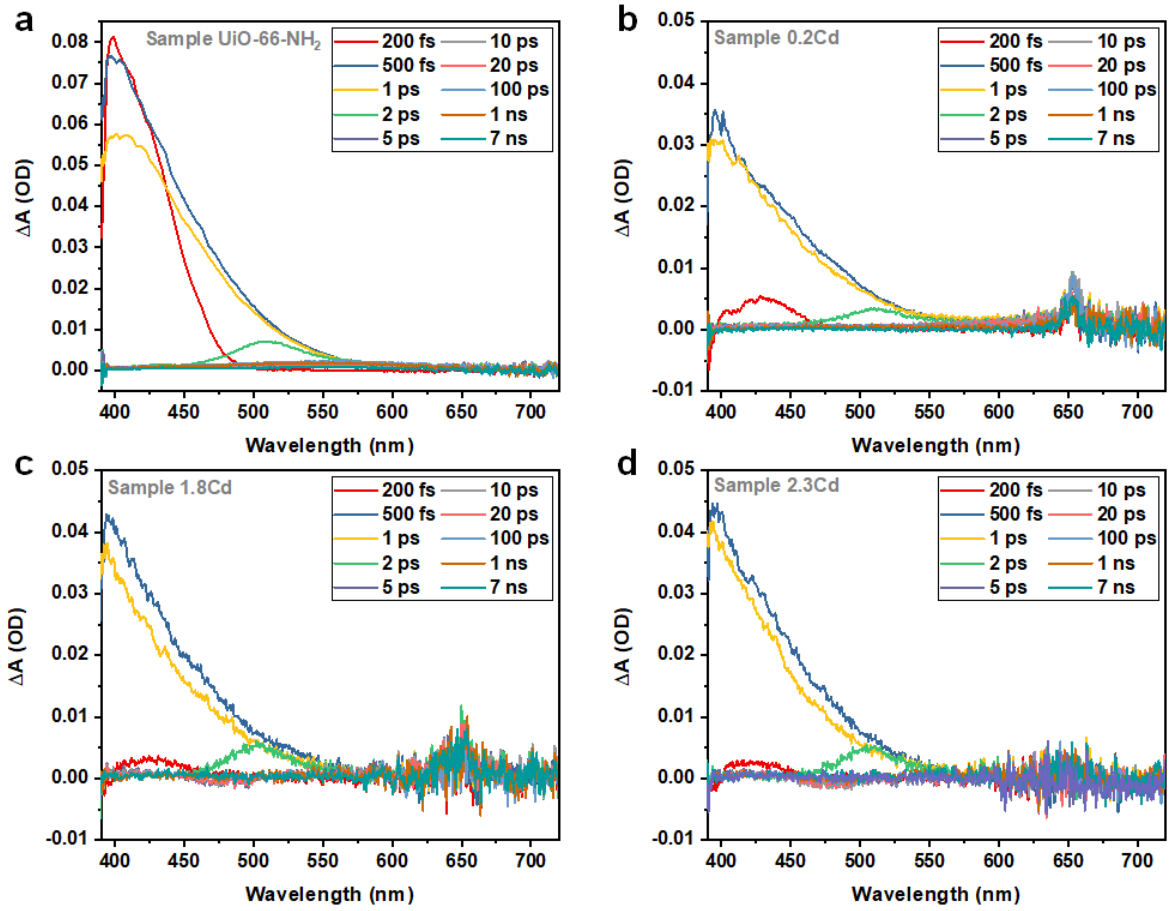


Figure 5 . 32 | Transient Absorption Spectroscopy (TAS) for selected catalysts. Dr. Mingjie Li and Mr. Qi Wei are gratefully acknowledged for their assistance in collection of TAS spectra.

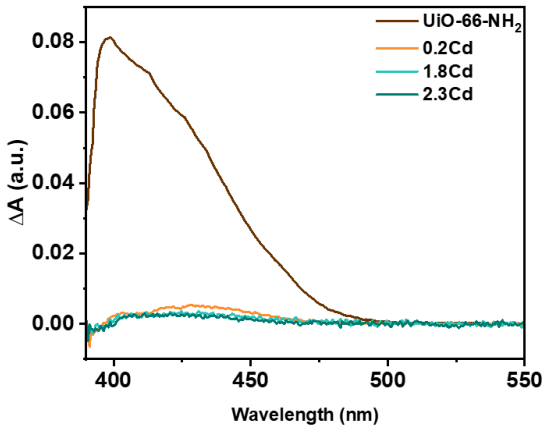


Figure 5 . 33 | TAS for selected catalysts probed at 200fs

5.2.4 Mechanism of photocatalytic water splitting

As similar to In_2S_3 modification, the incorporation of CdS into UiO-66-NH_2 has also shown increased BET surface area (Gate-Opening Effect). The chemistries underlying the activation of H_2O molecules to reduce the activation energy barrier of water splitting is postulated towards the photo-induced charge separation in CdS. Upon such excitation, the charge transfer processes from CdS clusters to the terephthalic acid organic linker via the amino group will put δ+ charges on the Cd orbitals, while there will be δ- charges on the N of the amino group and the S orbitals. H_2O molecules can then be heterolytically activated via an FLP-like manner as depicted in Figure 5 . 34. It remains unclear the mechanistic pathway for the hydrogen production from water and would be worth investigating in the future. Moreover, the BET surface area increase is this time shown to be correlated with the increase in dihedral angle of the organic linkers, experimentally observed via Rietveld Refinement of the SXRD data. The

origins of such change in the dihedral angles of the organic linkers were explored with DFT calculations, which reveals charge transfer processes from CdS particles towards UiO-66-NH_2.

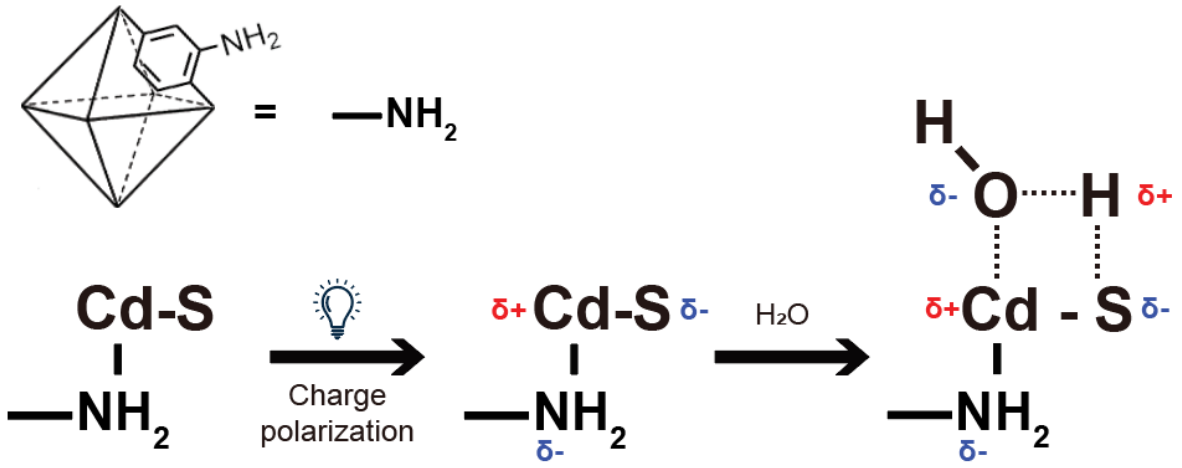


Figure 5 . 34 | Activation of H_2O via an FLP-like manner by Cd-S acid-base pair upon light irradiation.

5.3 Conclusion

Surface area enhancement of UiO-66-NH_2 upon CdS incorporation was reported, and shown to be strongly beneficial towards photocatalytic water splitting. The underlying chemistries of increased surface area was explored with Rietveld refinements of the SXRD data, which revealed increasing dihedral angles of the organic linkers present in UiO MOFs. DFT calculations expose the charge transfer processes from CdS towards aromatic rings favours the gate-opening effect of organic linkers, with robust correlations between simulated and experimental UV-Vis spectra. This work presents a new nanotechnology skill for controlling rotational dynamics of MOF materials using light-induced charge transfer processes, valuable to the field of photocatalyst design.

5.4 References

1 Xue, Q., Zhang, Z., Ng, B. K. Y., Zhao, P. & Lo, B. T. W. Recent Advances in the Engineering of Single-Atom Catalysts Through Metal-Organic Frameworks. *Top Curr Chem (Cham)* **379**, 11 (2021).

2 Xue, Q., Ng, B. K. Y., Man, H. W., Wu, T. S., Soo, Y. L., Li, M. M., Kawaguchi, S., Wong, K. Y., Tsang, S. C. E., Huang, B. & Lo, T. W. B. Controlled synthesis of Bi- and tri-nuclear Cu-oxo nanoclusters on metal-organic frameworks and the structure-reactivity correlations. *Chem Sci* **13**, 50-58 (2021).

3 Wang, Q., Gao, Q., Al-Enizi, A. M., Nafady, A. & Ma, S. Recent advances in MOF-based photocatalysis: environmental remediation under visible light. *Inorg Chem Front* **7**, 300-339 (2020).

4 Liu, H., , C. X. & , D. L., and Hai-Long Jiang. Photocatalytic Hydrogen Production Coupled with Selective Benzylamine Oxidation over MOF Composites. *Angewandte Chemie* **130**, 5477-5481 (2018).

5 Zhang, M., Wang, L., Zeng, T., Shang, Q., Zhou, H., Pan, Z. & Cheng, Q. Two pure MOF-photocatalysts readily prepared for the degradation of methylene blue dye under visible light. *Dalton Trans* **47**, 4251-4258 (2018).

6 Ploskonka, A. M. & DeCoste, J. B. Tailoring the Adsorption and Reaction Chemistry of the Metal-Organic Frameworks UiO-66, UiO-66-NH2, and HKUST-1 via the Incorporation of Molecular Guests. *ACS Appl Mater Interfaces* **9**, 21579-21585 (2017).

7 Zhai, Z., Zhang, X., Wang, J., Li, H., Sun, Y., Hao, X., Qin, Y., Niu, B. & Li, C. Washable and flexible gas sensor based on UiO-66-NH2 nanofibers membrane for highly detecting SO2. *Chemical Engineering Journal* **428** (2022).

8 Xue, Q., Chan, K. H., Yim, C. K., Ng, B. K. Y., Chen, T., Day, S. J., Tang, C., Kawaguchi, S., Wong, K.-Y. & Lo, T. W. B. Guest-Anion-Induced Rotation-Restricted Emission in UiO-66-NH2 and Advanced Structure Elucidation. *Chem Mater* **33**, 5422-5429 (2021).

9 Yoskamtorn, T., Zhao, P., Wu, X. P., Purchase, K., Orlandi, F., Manuel, P., Taylor, J., Li, Y., Day, S., Ye, L., Tang, C. C., Zhao, Y. & Tsang, S. C. E. Responses of Defect-Rich Zr-Based Metal-Organic Frameworks toward NH3 Adsorption. *J Am Chem Soc* **143**, 3205-3218 (2021).

10 Saleem, H., Rafique, U. & Davies, R. P. Investigations on post-synthetically modified UiO-66-NH 2 for the adsorptive removal of heavy metal ions from aqueous solution. *Micropor Mesopor Mat* **221**, 238-244 (2016).

11 Peterson, G. W., DeCoste, J. B., Fatollahi-Fard, F. & Britt, D. K. Engineering UiO-66-NH2 for Toxic Gas Removal. *Industrial & Engineering Chemistry Research* **53**, 701-707 (2014).

12 Luu, C. L., Nguyen, T. T. V., Nguyen, T. & Hoang, T. C. Synthesis, characterization and adsorption ability of UiO-66-NH2. *Advances in Natural Sciences: Nanoscience and Nanotechnology* **6** (2015).

13 Batonneau-Gener, I. & Sachse, A. Determination of the Exact Microporous Volume and BET Surface Area in Hierarchical ZSM-5. *The Journal of Physical Chemistry C* **123**, 4235-4242 (2019).

14 Ma, Y., Tong, W., Zhou, H. C. & Suib, S. L. A review of zeolite-like porous materials. *Micropor Mesopor Mat* **37**, 243-252 (2000).

15 Cao, Y., Zhao, Y., Lv, Z., Song, F. & Zhong, Q. Preparation and enhanced CO2 adsorption capacity of UiO-66/graphene oxide composites. *Journal of Industrial and Engineering Chemistry* **27**, 102-107 (2015).

16 Li, X., Almatrafi, E., Wang, H., Liu, X., Yang, Y., Zhou, C., Tang, X., Ren, X., Yin, L., Zeng, G. & Wang, D. Novel synthesis strategy for Z-scheme BiOCl/UiO-66 photocatalyst: Enhanced surface area and improved Cr(VI) removal efficiency. *Chemical Engineering Journal* **457** (2023).

17 Heard, C. J., Grajciar, L., Rice, C. M., Pugh, S. M., Nachtigall, P., Ashbrook, S. E. & Morris, R. E. Fast room temperature lability of aluminosilicate zeolites. *Nat Commun* **10**, 4690 (2019).

18 Sartbaeva, A., Wells, S. A., Treacy, M. M. & Thorpe, M. F. The flexibility window in zeolites. *Nat Mater* **5**, 962-965 (2006).

19 Pugh, S. M., Wright, P. A., Law, D. J., Thompson, N. & Ashbrook, S. E. Facile, Room-Temperature (17)O Enrichment of Zeolite Frameworks Revealed by Solid-State NMR Spectroscopy. *J Am Chem Soc* **142**, 900-906 (2020).

20 Xiong, H., Liu, Z., Chen, X., Wang, H., Qian, W., Zhang, C., Zheng, A. & Wei, F. In situ imaging of the sorption-induced subcelltopological flexibility of a rigid zeolite framework. *Science* **376**, 491-496 (2022).

21 Craig, G. A., Larpent, P., Kusaka, S., Matsuda, R., Kitagawa, S. & Furukawa, S. Switchable gate-opening effect in metal-organic polyhedra assemblies through solution processing. *Chem Sci* **9**, 6463-6469 (2018).

22 Sun, X., Ma, Y., Zhao, J., Li, D. S., Li, G., Zhang, L. & Liu, Y. Tuning the gate opening pressure of a flexible doubly interpenetrated metal-organic framework through ligand functionalization. *Dalton Trans* **47**, 13158-13163 (2018).

23 Wang, W., Wang, G.-D., Zhang, B., Li, X.-Y., Hou, L., Yang, Q.-Y. & Liu, B. Discriminatory Gate-Opening Effect in a Flexible Metal-Organic Framework for Inverse CO2/C2H2 Separation. *Small* **19**, 2302975 (2023).

24 Shen, L., Liang, S., Wu, W., Liang, R. & Wu, L. CdS-decorated UiO–66(NH2) nanocomposites fabricated by a facile photodeposition process: an efficient and stable visible-light-driven

photocatalyst for selective oxidation of alcohols. *Journal of Materials Chemistry A* **1**, 11473-11482 (2013).

25 Liang, Q., Cui, S., Liu, C., Xu, S., Yao, C. & Li, Z. Construction of CdS@UIO-66-NH2 core-shell nanorods for enhanced photocatalytic activity with excellent photostability. *J Colloid Interface Sci* **524**, 379-387 (2018).

26 Xu, H.-Q., Yang, S., Ma, X., Huang, J. & Jiang, H.-L. Unveiling Charge-Separation Dynamics in CdS/Metal–Organic Framework Composites for Enhanced Photocatalysis. *ACS Catalysis* **8**, 11615-11621 (2018).

27 Zhou, J.-J., Wang, R., Liu, X.-L., Peng, F.-M., Li, C.-H., Teng, F. & Yuan, Y.-P. In situ growth of CdS nanoparticles on UiO-66 metal-organic framework octahedrons for enhanced photocatalytic hydrogen production under visible light irradiation. *Applied Surface Science* **346**, 278-283 (2015).

28 Mao, S., Zou, Y., Sun, G., Zeng, L., Wang, Z., Ma, D., Guo, Y., Cheng, Y., Wang, C. & Shi, J. W. Thio linkage between CdS quantum dots and UiO-66-type MOFs as an effective transfer bridge of charge carriers boosting visible-light-driven photocatalytic hydrogen production. *J Colloid Interface Sci* **581**, 1-10 (2021).

29 Butler, E. A., Peters, D. G. & Swift, E. H. Hydrolysis Reactions of Thioacetamide in Aqueous Solutions. *Analytical Chemistry* **30**, 1379-1383 (1958).

30 Bowersox, D. F. & Swift, E. H. Precipitation of Cadmium Sulfide from Acid Solutions by Thioacetamide. *Analytical Chemistry* **30**, 1288-1291 (1958).

31 Ayers, P. W. An elementary derivation of the hard/soft-acid/base principle. *J Chem Phys* **122**, 141102 (2005).

32 Liu, X.-L., Wang, R., Zhang, M.-Y., Yuan, Y.-P. & Xue, C. Dye-sensitized MIL-101 metal organic frameworks loaded with Ni/NiOx nanoparticles for efficient visible-light-driven hydrogen generation. *APL Materials* **3** (2015).

33 Lin, R., Shen, L., Ren, Z., Wu, W., Tan, Y., Fu, H., Zhang, J. & Wu, L. Enhanced photocatalytic hydrogen production activity via dual modification of MOF and reduced graphene oxide on CdS. *Chem Commun (Camb)* **50**, 8533-8535 (2014).

34 Assi, H., Pardo Perez, L. C., Mouchaham, G., Ragon, F., Nasalevich, M., Guillou, N., Martineau, C., Chevreau, H., Kapteijn, F., Gascon, J., Fertey, P., Elkaim, E., Serre, C. & Devic, T. Investigating the Case of Titanium(IV) Carboxyphenolate Photoactive Coordination Polymers. *Inorg Chem* **55**, 7192-7199 (2016).

35 Toyao, T., Saito, M., Horiuchi, Y., Mochizuki, K., Iwata, M., Higashimura, H. & Matsuoka, M. Efficient hydrogen production and photocatalytic reduction of nitrobenzene over a visible-light-responsive metal–organic framework photocatalyst. *Catalysis Science & Technology* **3** (2013).

36 Yang, S., Pattengale, B., Kovrigin, E. L. & Huang, J. Photoactive Zeolitic Imidazolate Framework as Intrinsic Heterogeneous Catalysts for Light-Driven Hydrogen Generation. *Acs Energy Lett* **2**, 75-80 (2016).

37 He, J., Wang, J., Chen, Y., Zhang, J., Duan, D., Wang, Y. & Yan, Z. A dye-sensitized Pt@UiO-66(Zr) metal-organic framework for visible-light photocatalytic hydrogen production. *Chem Commun (Camb)* **50**, 7063-7066 (2014).

38 Toyao, T., Saito, M., Dohshi, S., Mochizuki, K., Iwata, M., Higashimura, H., Horiuchi, Y. & Matsuoka, M. Development of a Ru complex-incorporated MOF photocatalyst for hydrogen production under visible-light irradiation. *Chem Commun (Camb)* **50**, 6779-6781 (2014).

39 Mehta, J., Dhaka, S., Paul, A. K., Dayananda, S. & Deep, A. Organophosphate hydrolase conjugated UiO-66-NH2 MOF based highly sensitive optical detection of methyl parathion. *Environ Res* **174**, 46-53 (2019).

40 Xu, X.-Y., Chu, C., Fu, H., Du, X.-D., Wang, P., Zheng, W. & Wang, C.-C. Light-responsive UiO-66-NH2/Ag3PO4 MOF-nanoparticle composites for the capture and release of sulfamethoxazole. *Chemical Engineering Journal* **350**, 436-444 (2018).

41 Brunauer, S., Deming, L. S., Deming, W. E. & Teller, E. On a Theory of the van der Waals Adsorption of Gases. *J Am Chem Soc* **62**, 1723-1732 (1940).

42 Cao, Y., Zhang, H., Song, F., Huang, T., Ji, J., Zhong, Q., Chu, W. & Xu, Q. UiO-66-NH(2)/GO Composite: Synthesis, Characterization and CO(2) Adsorption Performance. *Materials (Basel)* **11**, 589 (2018).

43 Zhang, X., Huang, P., Liu, A. & Zhu, M. A metal–organic framework for oxidative desulfurization: UIO-66(Zr) as a catalyst. *Fuel* **209**, 417-423 (2017).

44 Abdel-Mageed, A. M., Rungtaweevoranit, B., Parlinska-Wojtan, M., Pei, X., Yaghi, O. M. & Behm, R. J. Highly Active and Stable Single-Atom Cu Catalysts Supported by a Metal-Organic Framework. *J Am Chem Soc* **141**, 5201-5210 (2019).

45 Xu, C., Pan, Y., Wan, G., Liu, H., Wang, L., Zhou, H., Yu, S. H. & Jiang, H. L. Turning on Visible-Light Photocatalytic C-H Oxidation over Metal-Organic Frameworks by Introducing Metal-to-Cluster Charge Transfer. *J Am Chem Soc* **141**, 19110-19117 (2019).

46 Wang, L., Zheng, P., Zhou, X., Xu, M. & Liu, X. Facile fabrication of CdS/UiO-66-NH2 heterojunction photocatalysts for efficient and stable photodegradation of pollution. *Journal of Photochemistry and Photobiology A: Chemistry* **376**, 80-87 (2019).

47 Filgueiras, C. A. L. & Carazza, F. Electronic Transitions as a probe of tetrahedral versus octahedral coordination in Nickel (II) Complexes. *Journal of Chemical Education* **57**, 826-827 (1980).

48 Mu, X., Jiang, J., Chao, F., Lou, Y. & Chen, J. Ligand modification of UiO-66 with an unusual visible light photocatalytic behavior for RhB degradation. *Dalton Trans* **47**, 1895-1902 (2018).

49 He, Y., Shi, L., Wang, J., Yan, J., Chen, Y., Wang, X., Song, Y. & Han, G. UiO-66-NDC (1,4-naphthalenedicarboxilic acid) as a novel fluorescent probe for the selective detection of Fe3+. *Journal of Solid State Chemistry* **285**, 121206 (2020).

50 Boaz, H. & Rollefson, G. K. The quenching of Fluorescence. Deviations from the Stern-Volmer Law. *J Am Chem Soc* **72**, 3435-3443 (1950).

51 Sun, C. Y., Wang, X. L., Qin, C., Jin, J. L., Su, Z. M., Huang, P. & Shao, K. Z. Solvatochromic behavior of chiral mesoporous metal-organic frameworks and their applications for sensing small molecules and separating cationic dyes. *Chemistry* **19**, 3639-3645 (2013).

52 Gutierrez, M., Cohen, B., Sanchez, F. & Douhal, A. Photochemistry of Zr-based MOFs: ligand-to-cluster charge transfer, energy transfer and excimer formation, what else is there? *Phys Chem Chem Phys* **18**, 27761-27774 (2016).

6 Chapter 6 | Conclusion & Future Works

6.1 Conclusion

This thesis has systematically demonstrated various strategies for modification of UiO-series Metal-Organic Frameworks for fuel-forming photocatalysis. UiO-series MOFs, photocatalysis were introduced, and the reported strategies for modifying UiO-series MOFs structurally for photocatalytic applications reviewed thoroughly in Chapter 1. The experimental techniques, including the synthesis methods and theories behind structural, optical and dynamic characterization capabilities were provided in Chapter 2. These two chapters provided contextual information for the 3 forthcoming experimental chapters.

In Chapter 3, a photo-induced frustrated Lewis pair like active sites is, for the first time, reported in the Ru/bpy catalyst as a proof of concept. Its design combines the high chemical tunability of MOF and the strong metal-to-ligand charge transfer ability of ruthenium complexes. The successful anchoring of Ru onto MOFs is shown with EXAFS and Rietveld refinement on SXRD data, while the optical processes are characterized by UV-Vis, PL and TRPL. Upon light irradiation, the Ru-N Lewis acid-base pair in Ru/bpy is polarized as indicated by the TDDFT calculations, beneficial to the photo catalysis of hydrogen-deuterium gas exchange reaction. We believe our approach for catalyst design can become transferable to the wider application of light induced FLP-like chemistries on the activation of small molecules.

In Chapter 4, a one-pot synthesis method of In_2S_3-decorated UiO-66-NH_2 with different loadings of In_2S_3 was devised. The deposition of In_2S_3 on the amino group of the organic linker in UiO-66-NH_2 was evidenced by IR and XPS. An increase of BET surface area was observed, which can be correlated with the increase in photocatalytic CO_2 reduction activity via increase in adsorption sites in the In_2S_3/UiO-66-NH_2 interface. The H_2 and CO_2 are postulated to be activated in an FLP-like manner similar to that demonstrated in Chapter 3. This work can shed

light on devising new synthesis methods for the design of interface between MOFs and co-catalysts for more efficient photocatalysts.

In Chapter 5, Surface area enhancement of UiO-66-NH_2 upon CdS incorporation was reported, and shown to be strongly beneficial towards photocatalytic water splitting. The underlying chemistries of increased surface area were explored with Rietveld refinements of the SXRD data, which revealed increasing dihedral angles of the organic linkers present in UiO MOFs. DFT calculations expose the charge transfer processes from CdS towards aromatic rings favours the gate-opening effect of organic linkers, with robust correlations between simulated and experimental UV-Vis spectra. This work presents a new nanotechnology skill for controlling rotational dynamics of MOF materials using light-induced charge transfer processes, valuable to the field of photocatalyst design.

6.2 Future Work

6.2.1 Catalytic testing

The study of photocatalytic activities across the different reactions can be done more thoroughly. For example, the hydrogen-deuterium exchange activity for the catalysts can be explored at a larger temperature range to ensure the role of thermal activation in the process. On top of that, it will be beneficial to understand the activity at different time scales, to understand whether there is an activation period is presence. Similarly, the catalytic CO_2 reduction and water splitting can be tried in different temperatures for optimization of the catalytic activities. The pressure of gas in the autoclave may have a higher inhibition effect to the production of hydrogen from water splitting, compared to the reduction of CO_2 by H_2, and such parameters influencing the catalytic activity can be worth examining. On top of that, the recyclability of the catalysts should be tested for application in industrial chemistry context.

The rate of utilization of light as calculated by the quantum efficiency can be helpful towards comparing the efficiency of catalysts across different systems.

6.2.2 Mechanistic studies

The mechanistic details on the pathway of both the CO_2 reduction and water splitting for H_2 production are lacking. Catalytic testing with different quenching reagents can be helpful towards the determination of reactive intermediates in the process. Repeating the catalysis reactions with limiting conditions can also be helpful towards determining the rate determining step, providing an indirect evidence of the mechanism. Additionally, DFT simulations are commonly employed for establishing the pathways available for the catalytic process.

6.2.3 Post mortem analysis

Changes to the catalyst after catalytic testing can also clarify the usefulness of the catalysts in a longer time scale. Structural changes to the MOFs, such as monitoring with XRD the changes in crystallinity, or with TGA the changes in thermal stability, can provide insight on the pathway towards deactivation. Moreover, the amount of semiconductors / metals present in the MOF supports before and after catalysts can be compared using ICP, to understand the extend of leaching during reaction. The analysis of catalysts post reaction allows the design of longer lifetime catalysts to be generated.

6.2.4 In-situ characterization

Future work can also focus on further *in-situ* characterization of the catalytic processes explored in this thesis. For example, the *in-situ* XANES or XPS of the Ru/bpy system under light illumination should give indication of *in-situ* reduction of Ru species. *In-situ* SXRD of the In_2S_3/UiO-66-NH_2 or CdS/UiO-66-NH_2 samples can explore how the structural variety contributes to the catalytic activity. Unfortunately, it is well-known that *in-situ* beam times in synchrotrons around the world are notoriously hard to get hold of. Therefore, such

characterizations can only be done when more beam time resources are available around synchrotrons in the world.

6.2.5 Applying MOFs as photocatalysts at industrial scales

The synthesis procedures used in this thesis are at small scale compared to industry applications. There are rooms for optimization related to the synthesis procedures, and how the use of the organic solvent (DMF) can be reduced per unit mass of MOF produced. It is known that the particle size of MOFs can depend significantly in the synthesis condition. The difference in particle size may influence the catalytic rate. For more efficient contact of the photocatalyst with the light source, it may be helpful to consider other forms of deposition, other than the suspension of catalyst in water / solvent as used in this thesis. The particle size with respect to the catalytic activity can also be optimized at a larger scale for its industrial application.